

Painting a Picture of the Ovarian Cancer *N*-Glycome

A thesis submitted for the degree of

Doctor of Philosophy

as a portfolio of publications by

Matthew Thomas Briggs



**The University of Adelaide
School of Biological Sciences
Adelaide Proteomics Centre**

Supervisors

Professor Peter Hoffmann

Professor Nicolle Packer

Professor Martin Oehler

December 2018

This page is intentionally left blank

Table of Contents

Declaration	v
Acknowledgements	vii
List of Publications	ix
Abbreviations.....	xi
Abstract	xiii
Chapter 1 Introduction: Setting the Stage.....	2
1.1 Summary	2
1.2 Statement of Authourship	4
Translating <i>N</i> -Glycan Analytical Applications into Clinical Strategies for Ovarian Cancer.....	8
1.3 Aims	24
Chapter 2 Materials and Methods	26
2.1 Summary	26
2.2 Statement of Authourship	28
<i>N</i> -Glycan matrix-assisted laser desorption/ionization mass spectrometry imaging protocol for formalin-fixed paraffin-embedded tissues	32
Chapter 3 Developing <i>N</i> -Glycan MALDI Mass Spectrometry Imaging for FFPE Knee Osteoarthritis Tissue.....	50
3.1 Summary	50
3.2 Statement of Authourship	52
MALDI mass spectrometry imaging of <i>N</i> -glycans on tibial cartilage and subchondral bone proteins in knee osteoarthritis.....	56
3.3 Supplementary Information	62
Chapter 4 Investigating the Intrapatient Variation of Late-Stage Ovarian Cancer Tissues using <i>N</i> -Glycan MALDI Mass Spectrometry Imaging.....	64
4.1 Summary	64
4.2 Statement of Authourship	66
<i>N</i> -glycan MALDI Imaging Mass Spectrometry on Formalin-Fixed Paraffin-Embedded Tissue Enables the Delineation of Ovarian Cancer Tissues	68
4.3 Supplementary Information	82
Chapter 5 Investigating the Interpatient Variation of Early- and Late-Stage Ovarian Cancer Tissues using <i>N</i> -Glycan MALDI Mass Spectrometry Imaging.....	84
5.1 Summary	84
5.2 Statement of Authourship	86
MALDI Mass Spectrometry Imaging of Early- and Late-Stage Serous Ovarian Cancer Tissue Reveals Stage-Specific <i>N</i> -Glycans.....	90
5.3 Supplementary Information	120
Chapter 6 Discussion.....	132

Chapter 7 Conclusion: Striking the Stage.....	140
Chapter 8 References.....	142
Chapter 9 Appendices	146
9.1 Statement of Authourship	146
The Glycomic Quest for the Holy Grail: An Early Stage Biomarker for Ovarian Cancer.....	148
9.2 Statement of Authourship	152
Applications of Mass Spectrometry Imaging to Cancer	155

Declaration

I certify that this work contains no material which has been accepted for the award of any other degree or diploma in my name, in any university or other tertiary institution and, to the best of my knowledge and belief, contains no material previously published or written by another person, except where due reference has been made in the text. In addition, I certify that no part of this work will, in the future, be used in a submission in my name, for any other degree or diploma in any university or other tertiary institution without the prior approval of the University of Adelaide and where applicable, any partner institution responsible for the joint-award of this degree.

I give consent to this copy of my thesis when deposited in the University Library, being made available for loan and photocopying, subject to the provisions of the Copyright Act 1968.

I acknowledge that copyright of published works contained within this thesis resides with the copyright holder(s) of those works.

I also give permission for the digital version of my thesis to be made available on the web, via the University's digital research repository, the Library Search and also through web search engines, unless permission has been granted by the University to restrict access for a period of time.

I acknowledge the support I have received for my research through the provision of an Australian Government Research Training Program Scholarship.

Matthew Thomas Briggs

Signature		Date	06/07/18
-----------	--	------	----------

This page is intentionally left blank

Acknowledgements

Writing a thesis is hard, but no harder than writing my acknowledgements. So, I decided to take an unconventional approach to writing them.

2009. I was undecided on what I should study after year 12. Should I choose EcoChemistry or Molecular Biology? From an early age, I had a strange fascination with rocks. I had a collection that I would scrutinize. But in the end, I decided I should study Molecular Biology.

2010. First year of university. I studied biology and chemistry. I also decided to study geology as an elective. Oh boy, what a mistake that was! Good thing I didn't do EcoChemistry. I was also studying a Diploma of Languages in Indonesian. My grades were average.

2011. Second year of university. My interest in performing arts had grown. I took an interest in stage management. I volunteered as a stage manager for IndoFest. I also volunteered as a stage manager for my old high school. My grades improved.

2012. Third year of university. I then stage managed *Sepia* by award-winning playwright, Emily Steel. *Sepia* won the Tour Ready Award for the 2012 Adelaide Fringe. I was unable travel with the cast and creative team because I had exams. However, I received the opportunity to stage manage Emily Steel's *Rocket Town* several months later. My grades improved again.

2013. Last year of university. I turned 21. I came out of the closet. I got a boyfriend. But then, I lost a boyfriend. I lost a boyfriend during exam period. I spent days in bed when I should have been studying for my exams. My grades were the best they've ever been. *Weird.*

2014. Honours. I arrived at the Adelaide Proteomics Centre. I entered a meeting with Professor Peter Hoffmann and Dr. Johan Gustafsson to discuss my project. I was excited by the prospects of my project. *Skip forward.* I published my first scientific paper. I finished writing my thesis. I submitted my thesis. I graduated with first class honours.

2015. First year of my PhD. **2016.** Second year of my PhD. **2017.** Third year of my PhD.

2018. Last year of my PhD. Stress. Conference. Stress. 2018 Adelaide Fringe. Stress. Writing my thesis. Stress. New job. Stress. Finished writing my thesis. *Relief.*

2009-2018. University is a path to be discovered. The path can be long and an often unknown, but more often than not, taking the unknown path can be rewarding.

I would like to thank following people who have made this thesis possible.

- 1 | My supervisors, Professor Peter Hoffmann, Professor Nicolle Packer and Professor Martin Oehler, who have been instrumental in this project's success. Without their insight and wisdom, this project would not be the success it is today.
- 2 | My mentors, Dr. Arun Everest-Dass, Dr. Yin Ying Ho, Dr. Mark Condina, Dr. Manuela Klinger-Hoffmann and Dr. Georgia Arentz. Without their countless hours of critical analysis of my writing and experimental design, this thesis would not be possible.
- 3 | My colleague, Professor Gurjeet Kaur, who has been invaluable to this project through her annotation of my ovarian cancer tissue samples. Without her expertise, my data could not be analysed and published.
- 4 | My collaborators, Dr. Julia Kuliwaba, Dr. Dzenita Muratovic and Professor David Findlay, for their insight and wisdom into the knee osteoarthritis project. I am looking forward to continuing our collaboration into the future and beyond.
- 5 | My colleagues, Parul Mittal, Chao Zhang, Mitchell Acland, Brooke Dilmetz and Christopher Cursaro. Thank you for your professionalism and continual collaboration.
- 6 | My institutions, The University of Adelaide, the Adelaide Proteomics Centre, the Institute of Photonics and Advanced Sensing (IPAS), the Centre of Excellence in Nanoscale BioPhotonics (CNBP), and Macquarie University. Thank you for the memories.
- 7 | My family. Roslyn, my mother. Jeffrey, my father. Samuel, my brother. Thank you for your unconditional love and endless support. Without it, I would have broken down in tears a lot more often.
- 8 | My partner, Joshua Belperio. Thank you. *Just thank you.*

List of Publications

Chapter 1 | Introduction

Matthew T. Briggs, Mark R. Condina, Arun V. Everest-Dass, Yin Ying Ho, Gurjeet Kaur, Martin K. Oehler, Nicolle H. Packer, Peter Hoffmann: *From Analytical to Clinical: The Ovarian Cancer N-Glycome*. *Proteomics – Clinical Applications* 10/2018; DOI:10.1002/prca.201800099.

Chapter 2 | Materials and Methods

Matthew T Briggs, Yin Ying Ho, Gurjeet Kaur, Martin K Oehler, Arun V Everest-Dass, Nicolle H Packer, Peter Hoffmann: *N-glycan matrix-assisted laser desorption/ionization mass spectrometry imaging protocol for formalin-fixed paraffin-embedded tissues*. *Rapid Communications in Mass Spectrometry* 03/2017; DOI:10.1002/rcm.7845

Chapter 3 | Developing N-Glycan MALDI Mass Spectrometry Imaging for FFPE Knee Osteoarthritis Tissue

Matthew T. Briggs, Julia S. Kuliwaba, Dzenita Muratovic, Arun V. Everest-Dass, Nicolle H. Packer, David M. Findlay, Peter Hoffmann: *MALDI mass spectrometry imaging of N-glycans on tibial cartilage and subchondral bone proteins in knee osteoarthritis*. *Proteomics* 03/2016; 16(11) DOI:10.1002/pmic.201500461

Chapter 4 | Investigating the Intrapatient Variation of Late-Stage Ovarian Cancer Tissues using N-Glycan MALDI Mass Spectrometry Imaging

Matthew T. Briggs, Arun V. Everest-Dass, Gurjeet Kaur, Martin K. Oehler, Peter Hoffmann, Nicolle H Packer: *N -Glycan MALDI Imaging Mass Spectrometry on Formalin-Fixed Paraffin-Embedded Tissue Enables the Delineation of Ovarian Cancer Tissues*. *Molecular & Cellular Proteomics* 07/2016; 15(9):mcp.M116.059816, DOI:10.1074/mcp.M116.059816

Chapter 5 | Investigating the Interpatient Variation of Early- and Late-Stage Ovarian Cancer Tissues using N-Glycan MALDI Mass Spectrometry Imaging

Matthew T. Briggs, Yin Ying Ho, Mark R. Condina, Arun V. Everest-Dass, Gurjeet Kaur, Martin K. Oehler, Nicolle H. Packer, Peter Hoffmann: *MALDI Mass Spectrometry Imaging of Early- and Late-Stage Serous Ovarian Cancer Tissue Reveals Stage-Specific N-Glycans* (unsubmitted).

Chapter 9 | Appendices

M Briggs, A Everest-Dass, M Oehler, N Packer, P Hoffmann: *The Glycomic Quest for the Holy Grail: An Early Stage Biomarker for Ovarian Cancer*.

G. Arentz, P. Mittal, C. Zhang, Y.-Y. Ho, M. Briggs, L. Winderbaum, M.K. Hoffmann, P. Hoffmann: *Applications of Mass Spectrometry Imaging to Cancer*. *Advances in Cancer Research* 01/2017; 134, DOI:10.1016/bs.acr.2016.11.002

This page is intentionally left blank

Abbreviations

μL	Microlitre
ACN	Acetonitrile
CID	Collision induced dissociation
Da	Dalton
DE	Delayed extraction
DHB	2,5-Dihydroxybenzoic acid
ECM	Extracellular matrix
ESI	Electro-spray ionization
ETD	Electron transfer dissociation
EtOH	Ethanol
FA	Formic acid
FF	Fresh frozen
FFPE	Formalin-fixed paraffin-embedded
FIGO	International federation of gynaecology and obstetrics
H&E	Haematoxylin and eosin
HCl	Hydrochloric acid
HPLC	High performance liquid chromatography
IT	Ion trap
LC	Liquid chromatography
LCM	Laser capture micro-dissection
m/z	Mass to charge ratio
MALDI	Matrix-assisted laser desorption/ionization
MeOH	Methanol
MCP	Micro plate detector
MS	Mass spectrometry
MSI	Mass spectrometry imaging
MS/MS	Tandem mass spectrometry
PNGase F	Peptide- <i>N</i> -glycosidase
PTMs	Post-translational modifications
PVDF	Polyvinylidene fluoride
Q	Quadrupole
qTOF/QTOF	Quadrupole time-of-flight
RP	Reverse phase
S/N	Signal to noise ratio
t	Time
TFA	Trifluoroacetic acid
TMA	Tissue micro-array
TOF	Time-of-flight
YAG	Yttrium aluminium garnet

This page is intentionally left blank

Abstract

Our story begins with the current clinical strategies that are used by clinicians today to (1) screen and detect ovarian cancer in the early-stages, (2) monitor treatment effectiveness, (3) detect ovarian cancer recurrence and (4) stratify ovarian cancer patients. However, these current strategies utilise FDA-approved ovarian cancer biomarkers, such as CA125 and HE4, which are relatively unsuccessful and lack specificity, especially for early stage patients. In the introduction, it is highlighted that these ovarian cancer biomarkers and other disease biomarkers are typically glycoproteins, but their glycan structure-protein function relationship remains unknown.

Protein glycosylation is one of the most complex post-translational modifications (PTMs) found in humans, with *N*-linked glycans playing a significant role in protein folding and conformation, protein stability and activity, cell-cell interaction, and cell signalling pathways. The best approach to study and analyse *N*-glycans so far has been to structurally characterise them by firstly, releasing them from complex glycoprotein mixtures using PNGase F, and secondly, identifying specific structures using analytical strategies that may potentially translate into clinical strategies. Ultimately, this thesis focuses on analytical techniques, primarily mass spectrometry, that are available to qualitatively and quantitatively assess *N*-glycosylation while successfully characterising compositional, structural and linkage features with high specificity and sensitivity.

Analytical techniques that were explored include liquid chromatography electrospray ionisation tandem mass spectrometry (LC-ESI-MS/MS) and matrix-assisted laser desorption/ionisation time-of-flight mass spectrometry (MALDI-TOF-MS). These analytical techniques have previously been implemented in the clinic for other diseases, however, not yet for ovarian cancer. It may be possible to implement either LC-ESI-MS/MS or MALDI-TOF-MS in the clinic for ovarian cancer using *N*-glycomic-based approaches since aberrant *N*-glycosylation patterns have been observed consistently between clinical samples, such as serum, plasma, ascites and tissue.

MALDI mass spectrometry imaging (MSI) has emerged as a platform to visualise *N*-glycans in tissue-specific regions. Outlined in this thesis, our group studied the inpatient and interpatient variability between early- and late-stage ovarian cancer patients. From our studies, specific *N*-glycan differences were identified between the early- and late-stage tumour microenvironment that could lead to the development of ovarian cancer diagnosis and prognosis strategies for the clinic.

This page is intentionally left blank

Chapter 1 | Introduction: Setting the Stage



1.1 | Summary

This review article provides readers with a brief summary about the current clinical strategies that are available to clinicians today and the common lack of specificity for disease biomarkers, particularly the ovarian cancer biomarker, CA125. It is highlighted in this review that CA125 is a glycoprotein that is relatively uncharacterised, thereby opening the door to discuss analytical strategies that are available to scientists today to structurally characterise *N*-glycans. Characterisation is important because these *N*-glycan structures have previously been observed to be aberrant when analysed from clinically-relevant ovarian cancer samples including serum, plasma, ascites and tissue. This review emphasises the use of mass spectrometry as an analytical strategy and highlights the potential the technique has to translate into a clinical setting. More specifically, matrix-assisted laser desorption/ionisation (MALDI) mass spectrometry imaging (MSI) has shown much promise in the analysis of clinical samples, such as formalin-fixed paraffin-embedded (FFPE) tissues.

This page is intentionally left blank

1.2 | Statement of Authorship

Title of Paper	Translating N-Glycan Analytical Applications into Clinical Strategies for Epithelial Ovarian Cancer
Publication Status	<input checked="" type="checkbox"/> Published <input type="checkbox"/> Accepted for Publication <input type="checkbox"/> Submitted for Publication <input type="checkbox"/> Unpublished and Unsubmitted work written in manuscript style
Publication Details	<u>Matthew T. Briggs</u> , Mark R. Condina, Arun V. Everest-Dass, Yin Ying Ho, Gurjeet Kaur, Martin K. Oehler, Nicolle H. Packer, Peter Hoffmann: <i>From Analytical to Clinical: The Ovarian Cancer N-Glycome</i> . <i>Proteomics – Clinical Applications</i> 10/2018;, DOI:10.1002/prca.201800099.

Principal Author

Name of Principal Author (Candidate)	Matthew T. Briggs	
Contribution to the Paper	Conceived the project Data collection and analysis Prepared figures and wrote the main manuscript text	
Overall percentage (%)	40%	
Certification:	This paper reports on original research I conducted during the period of my Higher Degree by Research candidature and is not subject to any obligations or contractual agreements with a third party that would constrain its inclusion in this thesis. I am the primary author of this paper.	
Signature		Date 05/07/18

Co-Author Contributions

By signing the Statement of Authorship, each author certifies that:

- i. the candidate's stated contribution to the publication is accurate (as detailed above);
- ii. permission is granted for the candidate to include the publication in the thesis; and
- iii. the sum of all co-author contributions is equal to 100% less the candidate's stated contribution.

Name of Co-Author	Mark R. Condina		
Contribution to the Paper	Conceived the project Wrote sections of the main manuscript text Contributed equally to this work		
Signature		Date	13/12/17

Name of Co-Author	Manuela Klingler-Hoffmann		
Contribution to the Paper	Conceived the project Wrote sections of the main manuscript text		
Signature		Date	05/07/18

Name of Co-Author	Georgia Arentz		
Contribution to the Paper	Conceived the project Wrote sections of the main manuscript text		
Signature		Date	05/07/18

Name of Co-Author	Arun V. Everest-Dass		
Contribution to the Paper	Conceived the project Wrote sections of the main manuscript text		
Signature		Date	20/12/17

Name of Co-Author	Gurjeet Kaur		
Contribution to the Paper	Annotated the H&E stained FFPE sections		
Signature		Date	13/12/17

Name of Co-Author	Martin K. Oehler		
Contribution to the Paper	Provided the ovarian tissue samples		
Signature		Date	12/12/17

Name of Co-Author	Nicolle H. Packer		
Contribution to the Paper	Conceived the project Designed the experiments and supervised the research		
Signature		Date	18/04/18

Name of Co-Author	Peter Hoffmann		
Contribution to the Paper	Conceived the project Designed the experiments and supervised the research		
Signature		Date	20/12/17

This page is intentionally left blank

Translating N-Glycan Analytical Applications into Clinical Strategies for Ovarian Cancer

Matthew T. Briggs, Mark R. Condina, Manuela Klingler-Hoffmann, Georgia Arentz, Arun V. Everest-Dass, Gurjeet Kaur, Martin K. Oehler, Nicolle H. Packer, and Peter Hoffmann*

Protein glycosylation, particularly N-linked glycosylation, is a complex posttranslational modification (PTM), which plays an important role in protein folding and conformation, regulating protein stability and activity, cell–cell interaction, and cell signaling pathways. This review focuses on analytical techniques, primarily MS-based techniques, to qualitatively and quantitatively assess N-glycosylation while successfully characterizing compositional, structural, and linkage features with high specificity and sensitivity. The analytical techniques explored in this review include LC–ESI–MS/MS and MALDI time-of-flight MS (MALDI-TOF-MS), which have been used to analyse clinical samples, such as serum, plasma, ascites, and tissue. Targeting the aberrant N-glycosylation patterns observed in MALDI–MS imaging (MSI) offers a platform to visualize N-glycans in tissue-specific regions. The studies on the intra-patient (i.e., a comparison of tissue-specific regions from the same patient) and inter-patient (i.e., a comparison of tissue-specific regions between different patients) variation of early- and late-stage ovarian cancer (OC) patients identify specific N-glycan differences that improve understanding of the tumor microenvironment and potentially improve therapeutic strategies for the clinic.

1. Introduction

Ovarian cancer (OC) is the most fatal gynecological malignancy in adult women with an estimated 1613 new cases diagnosed and 1069 deaths in Australia during 2018.^[1] Early OC is asymptomatic in most cases, leading to late-stage diagnosis of patients that have developed metastatic stage III or IV cancer based on the International Federation of Gynecology and Obstetrics (FIGO) staging system (see **Table 1**).

Surgery combined with chemotherapy is the current standard treatment for advanced OC. However, prognosis for FIGO stage III and IV is poor and the 5-year overall survival rate is only 30%.^[2] Novel clinical strategies that address 1) screening/early-detection, prediction and monitoring of treatment response, and 3) detection of cancer recurrence are therefore warranted.

M. T. Briggs
Adelaide Proteomics Centre
School of Biological Sciences
University of Adelaide
Adelaide, 5005, Australia

M. T. Briggs
ARC Centre for Nanoscale BioPhotonics (CNBP)
University of Adelaide
Adelaide, 5005, Australia


M. T. Briggs, Dr. M. R. Condina, Dr. M. Klingler-Hoffmann, Dr. G. Arentz, Prof. P. Hoffmann
Future Industries Institute
Mawson Lakes Campus
University of South Australia
5095, Mawson Lakes
E-mail: peter.hoffmann@unisa.edu.au

Dr. A. V. Everest-Dass, Prof. N. H. Packer
Institute for Glycomics Gold Coast Campus
Griffith University
Gold Coast, 4215, Australia

Dr. A. V. Everest-Dass, Prof. N. H. Packer
ARC Centre for Nanoscale BioPhotonics (CNBP)
Macquarie University
Sydney, 2109, Australia

Prof. G. Kaur
Institute for Research in Molecular Medicine (INFORMM)
Universiti Sains Malaysia
Pulau Pinang, Malaysia

Prof. M. K. Oehler
Department of Gynaecological Oncology
Royal Adelaide Hospital
Adelaide, 5000, South Australia, Australia
Prof. M. K. Oehler
Robinson Institute
University of Adelaide
Adelaide, 5005, Australia

 The ORCID identification number(s) for the author(s) of this article can be found under <https://doi.org/10.1002/prca.201800099>

DOI: 10.1002/prca.201800099

Table 1. FIGO stages of ovarian cancer and the extent of tumor spread.

FIGO stage	Tumor spread
I	Confined to ovaries
II	Pelvic extension
III	Extrapelvic intra-abdominal spread and/or lymph node involvement
IV	Distant metastasis (i.e., lung or liver)

2. Current Clinical Strategies for Ovarian Cancer

In 2014, the World Health Organization (WHO) published a now widely used strategy to classify OC in parallel with the already established FIGO staging.^[3] Histological information is used to classify OC into five subtypes (serous, mucinous, endometrioid, clear cell, and transitional cell cancer). These subtypes can be further subdivided into tumor grades, for example, serous low-grade carcinoma and serous high-grade carcinoma. This review focuses on the most common and widely studied form of OC that is serous high-grade carcinoma.

The two most common clinical strategies used to screen and monitor women for OC include pelvic ultrasonography, such as transabdominal and transvaginal ultrasound (TVUS),^[4] and the cancer antigen 125 (CA125) blood test.^[5] However, these current strategies lack specificity and sensitivity that can lead to unnecessary treatment and an increase of burden on the health system.^[6] The failure of such screening strategies is thought to be due to the complexity of OC, largely caused by genetic diversity and tumor heterogeneity.^[7] This review aims to address this complexity by focusing on *N*-glycans since they possess high structural complexity relative to other biomolecules and altered *N*-glycosylation is a universal feature of cancer cells.

This review also focuses on addressing the shortfalls of the current classification system, and how screening, monitoring, and stratification strategies may be improved by the introduction of novel analytical capability into clinical practice.

2.1. TVUS and CA125

Transabdominal and TVUS provide a snapshot of the reproductive organs, such as the uterus, ovaries, fallopian tubes, and cervix, which can lead to the visualization of a mass, potentially tumor.^[8] There are multiple benefits associated with this approach, such as shorter examination times, visualization of tumor size, and assessment of morphologic characteristics (i.e., presence of septae or cyst wall regularity).^[9] However, there are also limitations associated as it is not possible to determine whether the mass is cancerous or benign, and therefore further tests, such as the CA125 blood test, are required.

CA125, or more formally known as mucin 16 (MUC16), is a glycoprotein that has been Food and Drug Administration (FDA)-approved as a blood biomarker for the detection of recurrent OC.^[10] CA125 is also used to monitor treatment response in patients that have undergone tumor debulking surgery and chemotherapy.^[11] However, CA125 has been relatively unsuccessful as an ovarian cancer biomarker, as it lacks the specificity in premenopausal women, and has low sensitivity at early ovarian



Matthew Briggs submitted his PhD thesis in 2018 at the University of Adelaide, which focused on MALDI mass spectrometry imaging of *N*-glycans on FFPE ovarian cancer tissue. He is now a postdoc researcher at the Future Industries Institute, University of South Australia, under the supervision of Prof. Peter Hoffmann where he focuses on the use of MS for cancer,

biopharma, food and environmental research.



Mark Condina received his PhD in 2011 at the University of Adelaide, which focused on the development of sensitive approaches for tyrosine phosphorylation characterisation. Mark spent 7 years in industry-based roles; 5 years as an applications specialist for Bruker MALDI and ESI mass spectrometry platforms across Australia and 2 years at CSL Ltd as a manager of the protein

characterisation group in recombinant protein development. In 2017, Mark accepted a senior research fellow role at the Future Industries Institute, University of South Australia, where he focuses on the use of MS for cancer, biopharma, food and environmental research.



Peter Hoffmann received his PhD 19 years ago in 1999 from the University Saarland, Germany in Analytical Chemistry. In 2005, Peter established the Adelaide Proteomics Centre at the University of Adelaide. After 12 years at the Adelaide Proteomics Centre, Peter is now the Strand Leader of Biomaterials Engineering and Nanomedicine and the Lloyd Sansom Chair at the Future

Industries Institute, University of South Australia, where he focuses on the use of MS for cancer, biopharma, food and environmental research.

cancer stages. Recent results from the UK Collaborative Trial of Ovarian Cancer Screening (UKCTOCS), which separately used CA125 levels and TVUS screening to monitor the development of OC in a large cohort of post-menopausal women over a period of 11 years, found neither test to be of significant benefit in the monitoring of OC.^[12] CA125 is thought to lack specificity due to its production in multiple tissues derived from coelomic epithelia, such as the ovaries, fallopian tube, peritoneum, pleura, pericardium, colon, kidney, and stomach.^[10]

There have been several attempts to improve CA125 as a screening biomarker for OC by combining ultrasound studies with the algorithm-based data of patient age, rate of change of CA125 over time, and the absolute quantitation of CA125.^[13] With no success, CA125 studies have also utilized other unique

techniques such as radio-imaging, radio-immunotherapy, and targeted delivery of cytotoxic agents.^[14] It has been discovered that 20% of high-grade OCs have little or no expression of CA125, leading to the need to identify novel biomarkers for OC diagnosis or monitoring.^[15] Over 30 other biomarkers have been evaluated in conjunction with CA125, including human epididymis protein 4 (HE4), mesothelin, macrophage colony-stimulating factor (MCSF), osteopontin, kallikrein, soluble epidermal growth factor (EGF) receptor, and inhibin, however, the search for an improved OC biomarker continues.^[16]

In 2009, an immunoassay based on the glycoprotein HE4 was approved by the FDA for the monitoring of OC recurrence and progression.^[17] However, this assay was not approved for the screening of early-stage OC in asymptomatic women. Therefore, a combined CA125 and HE4 test was established to assess the probability of detecting OC in women with a pelvic mass. The Risk of Ovarian Cancer Algorithm (ROMA) was applied to generate a score from 0 to 10. ROMA utilized clinical information, such as CA125 and HE4 concentration, and menopausal status, to determine the probability of the patient having OC. Women with ROMA scores above the predetermined cutoff were deemed to have an increased risk of OC and are referred to a gynecological oncologist. However, ROMA scores require further patient information, such as a women's menstrual status. It recently has been reported that at 75% specificity, pre-menopausal women are at 77–81% sensitivity and post-menopausal women are at 90–92% sensitivity.^[17]

In 2016, an American bioanalytical solutions company, Vermillion, released a statement about a second-generation FDA-approved biomarker for determining OC risk in conjunction with clinical information provided prior to surgery.^[18] Ova2, also known as OVA2, replaced two of the five biomarkers from the first-generation test to improve specificity. The five OVA2 biomarkers include CA125-II, HE4, apolipoprotein A-1, follicle stimulating hormone, and transferrin. However, these biomarkers are currently only used to monitor patients, not diagnose them due to the lack of specificity and sensitivity as already mentioned.

2.2. CA125: A Glycoprotein Biomarker

MUC16 is overexpressed in OC and plays important roles in invasion and metastasis. MUC16 is cleaved at a specific location, thus, releasing CA125 into the extracellular space. CA125 is a glycoprotein and its O-linked glycosylation is critical for both structure and function. More recently the focus of analysis has shifted to N-linked glycosylation, which regulates stability and function of CA125. The majority of glycans observed in the tumor microenvironment are N-glycans. Furthermore, N-glycosylation patterns have been observed to be aberrant in various cancers, including OC and other gynecological cancers, which highlights the importance and relevance of this review.

Protein glycosylation can be divided into two main classes; N-linked glycans, which are attached to asparagine residues, and O-linked glycans, which are attached to serine/threonine residues.^[19] N-glycans are the most common and complex type of protein glycosylation with 90% of glycoproteins presenting N-glycan structures. N-glycans are also of particular interest in

OC because structural alterations have been observed in the tumor microenvironment, which contributes to tumor invasion and metastasis.^[20] A structural alteration of interest is the formation of bisecting N-acetylglucosamine (GlcNAc) on several N-glycosylated glycoproteins from ovarian cancer samples. Previous studies have found that CA125 contains monofucosylated and bisecting GlcNAc N-glycans, however, this was not evaluated in a large patient cohort.^[21] See **Figure 1** for a brief summary of the N-glycan biosynthesis pathway.

As already discussed, altered N-glycan compositions and structures have been identified as a unique characteristic of tumorigenesis, tumor cell invasion, and metastasis and thus are an attractive target for monitoring and patient sample classification. This review outlines the current understanding of the OC N-glycome and the analytical strategies that have been used to characterise the N-glycome.

3. Analytical Applications for N-Glycan Characterization

The analytical strategies currently used to characterize N-glycans provide an important insight into their structural identity by obtaining monosaccharide composition, branching and linkage information.^[23] Initially, N-glycans are released from glycoproteins using an enzyme, peptide-N-glycosidase (PNGase F), which cleaves the GlcNAc residue from the asparagine residue (except in cases where fucose is attached at the core GlcNAc via an α -1,3 linkage).^[24] These N-glycans can then be characterized using an array of techniques that have been developed over the past few decades.

3.1. Nuclear Magnetic Resonance

NMR is currently considered the best approach to analyze N-glycans, due to its ability to assign all structural features, such as composition, branching, and linkage.^[25] However, large quantities of highly purified N-glycans are required to obtain such results.^[23] Therefore, this analytical strategy might not be feasible for analyzing clinically relevant samples due to the low abundance of complex N-glycans.

3.2. Ultraviolet–Visible Spectroscopy

Ultraviolet–visible spectroscopy (UV/Vis) measures the absorbance or reflectance of the molecules in the visible range. However, N-glycans are poorly detected by UV/Vis absorption due to their lack of a chromophore.^[26] Instead, N-glycans are initially separated by HPLC or ultra-HPLC (UHPLC) using modes such as ion exchange, hydrophilic interaction LC (HILIC), or porous graphitized carbon (PGC) columns. HILIC utilizes polar interactions between the glycome and the stationary phase instead of separating specific glycans via alternative methods (i.e., lectin affinity chromatography).^[27] In PGC chromatography as well as reversed phase (RP) chromatography, increased number of hydrocarbons results in a proportional increase in

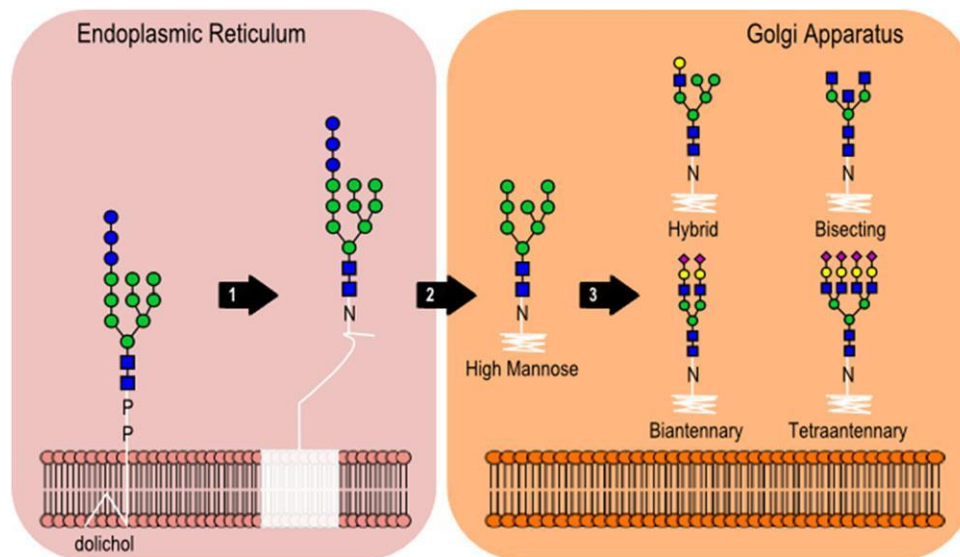


Figure 1. The *N*-linked glycan biosynthesis pathway. In the endoplasmic reticulum (ER), a glycan precursor composed of 14 monosaccharides is synthesized and attached to dolichol. **1)** This precursor is then transferred onto an asparagine residue of a nascent polypeptide also located in the ER. Oligosaccharyltransferase (OST) protein complex, consisting of several protein subunits, transfers this precursor. **2)** The glycan precursor is trimmed in the ER before being transferred to the Golgi apparatus on the nascent polypeptide. **3)** Golgi mannosidases cleave mannose residues, followed by branching and chain extension by various glyco-enzymes, for example glycosyltransferase-III (GnT-III) attaches a GlcNAc in the β 1,4 linkage at the β -mannose of the mannosyl core and glycosyltransferase-IV (GnT-IV) is responsible for β 1,6 branching. Adapted from the Essentials of Glycobiology: Chapter 8 *N*-glycans.^[22]

retention time.^[28] However, it is still unknown how PGC separates *N*-glycans based on their isomeric structure and charge. UHPLC is fast becoming more popular than conventional HPLC, since UHPLC utilizes a smaller particle size, can withstand higher pressures, and provides better resolution while reducing the separation time down to 30 min or less.^[29] Glycan separation is then combined with a charged aerosol detector (CAD), providing a platform to quantitatively analyze glycans cleaved from glycoproteins.^[30] The CAD converts these glycans into dry particles, where a stream of positively charged gas collides, transferring its charge onto the particles. These particles are then transferred to a collector, where the charge is measured by a highly sensitive electrometer, thereby generating a signal, which is directly proportional to the quantity to the glycan measured. CAD offers a better performance than other detectors, such as refractive index (RI), low wavelength UV, and evaporative light scattering (ELS). Alternatively, high-performance anion exchange (HPAE) coupled with pulsed amperometric detection (PAD) has also emerged to quantitatively analyze glycans cleaved from glycoproteins.^[31] HPAE-PAD is capable of measuring glycans in the low picomole range.

3.3. Capillary Electrophoresis

Another common technique used is capillary electrophoresis with laser induced fluorescence (CE-LIF), which is also suitable for profiling labeled glycans.^[32] An electric field mediates the migration of glycans, resulting in high resolution separation. Although CE-LIF is reproducible and highly sensitive, the approach lacks identification capabilities that MS and MS/MS

strategies can offer. Ruhaak and colleagues are at the forefront of innovation by introducing multi-capillary formats for high-throughput profiling of glycan changes.^[33] However, the main issue regarding this technology is identifying peaks, which currently is being addressed by setting up a CE database using an 8-aminopyrene-1,3,6-trisulfonate (APTS) maltrin ladder to normalize data. Studies have compared CE-LIF with UPLC to determine full characterization of *N*-glycans released from human IgG.^[34] It was determined that CE-LIF is a suitable profiling, characterization, and detailed structural analysis tool, when an internal standard ladder and a database is applied. This technology has now been used for clinical applications, such as detecting chronic liver disease.^[35]

3.4. Microarray-Based Approaches

N-glycans can be immobilized in glycan binding assays (i.e., microarrays or microtitration plates) by binding either covalently or non-covalently. Specific carbohydrate-binding proteins (CBPs), such as animal or plant lectins or immunoglobulins, are applied. The bound-CBPs are then detected via fluorescence by either direct labeling or secondary antibody strategies.^[36] This application is useful in determining which *N*-glycans interact with which CBPs, but the technique lacks specificity in identifying the exact *N*-glycan structure required for binding. Additionally, *N*-glycan antibodies are rare, with only 25 found in the Database of Anti-Glycan Reagents (DAGR). A total of 15 of these 25 antibodies were extracted from HIV patients.^[37] Further disadvantages of *N*-glycan antibodies include their commercial unavailability, and their failure to recognize distinct

structural features, with only recognizing *N*-glycan families. Multiple antibodies, for example, recognize multiple high mannose *N*-glycans, such as Man7, Man8, and Man9.^[38] The challenge regarding *N*-glycan antibody recognition lies with the high degree of homology within the *N*-glycan structures, even though they are considered one of the most complex PTMs.

Anti-glycan antibodies against 203 chemically synthesized glycans were detected in serum of adult women with ovarian carcinomas at different stages in 2012.^[39] Following cluster analysis, repetitive patterns were identified revealing specific carbohydrate structures including 11 *N*-glycans. However, these were atypical *N*-glycan structures ranging from linear lactosamine and glucosamine structures to single core lactosamine structures. More recently, a multiplex glycan bead array (MGBA) was conducted on 961 ovarian cancer serum samples where natural anti-glycan IgM and IgG antibodies were analyzed, resulting in the discovery of potential anti-glycan biomarkers for OC.^[40]

These traditional characterization techniques are isolated examples of how *N*-glycan analysis has previously been conducted on a range of biological samples. However, these approaches can often be tedious, unreliable, and difficult to use. Alternative methodologies for detecting *N*-glycans from OC patient samples can potentially assist in improving screening, monitoring, and stratification strategies. In order to be of use, however, such methodology would need to offer a high level of molecular information that can be generated in short timeframes for subsequent patient assessment and treatment.

4. *N*-Glycan Characterization using MS

MS is a rapid and highly sensitive technique with the potential to address such clinical obstacles. Prior to MS analysis, *N*-glycan samples may be subjected to a separation technique in order to construct a more comprehensive library of characterized structures. Complex *N*-glycan mixtures are separated by capillary- or nano-LC prior to analysis with ESI. There are several advantages to this approach, such as the ability to measure and characterize *N*-glycans with high sensitivity and reproducibility from low sample amounts. However, current *N*-glycan structural analysis can still be difficult due to the lack of high-throughput analysis software available. In addition to LC-ESI-MS, the other routinely used ionization method for the analysis of *N*-glycans is MALDI. MALDI-MS is an advantageous technique that can rapidly analyze *N*-glycans directly from biological samples, such as tissue sections, using higher-energy collision-induced dissociation (CID). Additionally, MALDI favors singly charged species that make annotation simpler.

4.1. Electrospray Ionization Mass Spectrometry

ESI is a soft ionization technique that involves the application of a needle voltage to force the liquid analyte from the needle as a Taylor Cone.^[41] A filament forms at the tip of the Taylor Cone until the surface tension and electrostatic repulsion are equal (i.e., Rayleigh limit). Once reached, the filament breaks away and the highly charged droplets are attracted to a voltage supply from

the mass analyzer entrance. In this transition, the Coulombic repulsion exceeds the surface tension, leading to an explosive formation of smaller droplets. Nitrogen nebulizing gas is also used to help produce a fine spray. As the ions fly towards the mass analyzer entrance, the charge density on the surface increases, thereby producing a mixture of singly and multiply charged ions.

There are several different types of mass analyzers available to analyze *N*-glycans, including ion trap (IT), time-of-flight (TOF), quadrupole (Q), and Fourier-transform ion cyclotron resonance (FTICR) analyzers.^[42] These mass analyzers play an important role in mass sensitivity, mass accuracy, mass resolution, and data acquisition. For example, an IT mass analyzer possesses ideal MS fragmentation capabilities, but low mass resolution capabilities. Conversely, Q-TOF mass analyzers are capable of higher mass resolution and accuracy, therefore enabling detailed and comprehensive structural characterization of *N*-glycans.

As already discussed, these complex *N*-glycan mixtures are first separated using fractionation techniques, such as HPAE chromatography, HILIC, RP chromatography, and PGC chromatography, prior to ESI. PGC chromatography possesses specific features that are valuable when analyzing complex *N*-glycan mixtures that contain *N*-glycans of different isomeric structures. For example, Anugraham et al. investigated the *N*-glycome of the SKOV 3 cell line as well as the IGROV 1, A2780, and OV-CAR 3 OC cell lines.^[43] These *N*-glycan profiles were compared to the noncancerous ovarian surface epithelial cell lines, HOSE 6.3 and HOSE 17.1. Through PGC-LC-ESI-MS of *N*-glycans released from membrane glycoproteins, bisecting, α 2-6 linked sialylated, and LacdiNAc *N*-glycans were found to be highly abundant in membrane glycoproteins of the cancerous cell lines relative to the noncancerous HOSE cell lines. Further validation was completed by studying the gene transcript levels of glycosyltransferases, *MGAT3*, *ST6GAL1*, and *B4GALNT3*. For the first time, there was evidence that *MGAT3* gene expression levels may be epigenetically regulated by DNA hypomethylation, leading to the synthesis of bisecting *N*-glycans.

4.2. Matrix-Assisted Laser Desorption/Ionization Mass Spectrometry

MALDI was first introduced by Karas and Hillenkamp.^[44] A typical MALDI-TOF-MS instrument uses an yttrium aluminum garnet (YAG) pulse laser under high vacuum conditions to stimulate an explosive transition from solid to gaseous phase. Ions are produced through a combination of charge neutralization and proton transfer reactions.^[45] Gaseous phase ions, typically singly charged, are accelerated via ion source voltages into a TOF mass analyzer. In terms of published *N*-glycan MALDI-TOF-MS studies, there are multiple which is evident in a series of reviews published by Harvey.^[46] Classically, complex *N*-glycan mixtures are prepared for MALDI-TOF-MS analysis by pipetting the mixture onto a target plate followed by a matrix solution. The matrix co-crystallizes with the *N*-glycan mixture resulting in dried spots, which now possesses strong absorption in the UV range. The most widely used matrix for *N*-glycan analysis is 2,5-dihydroxybenzoic acid (DHB) where $[M + Na]^{1+}$ adducts are typically formed in positive ion mode.

However, sialylated *N*-glycans are quite labile due to the MALDI source operating under vacuum and the TOF mass analyzer operating in reflectron mode as opposed to linear mode.^[47] This caveat has been addressed using several different approaches, such as permethylating the *N*-glycan mixture, prior to pipetting on the target plate, to dissipate the energy in an intermediate pressure MALDI source. Another solution to this limitation has been addressed by derivatizing the sialic acids using the reagent 4-(4,6-dimethoxy-1,3,5-triazin-2-yl)-4-methylmorpholinium chloride (DMT-MM).^[48] This reagent in combination with methanol creates an esterification reaction resulting in α 2–3 linked sialic acid lactones and α 2–6 linked sialic acids that are esterified. This creates a 32 Da mass difference between the two linkages while also stabilizing the sialic acids for MALDI–TOF–MS analysis.

In 2011, the first MALDI-based profiling study was conducted looking at the *N*-glycosylation patterns of glycoproteins from the OC cell line, SKOV 3, and more specifically a recombinantly expressed glycoprotein, erythropoietin (EPO).^[49] The released *N*-glycans were analyzed by HPAE chromatography with PAD and MALDI–TOF–MS. From the total glycoproteins, high mannose and proximally fucosylated *N*-glycans were identified, with EPO containing predominantly core fucosylated tetra-antennary *N*-glycans that partially lacked one or two galactose residues, partially containing the LacdiNAc motif.

Although OC cell lines, such as IGROV 1, A2780 OVCAR 3, and SKOV 3, provide an important insight into the *N*-glycosylation patterns behind OC progression, there are multiple caveats with analyzing these particular sample types. For example, it has been well documented that the most frequently used OC cell lines do not represent high-grade serous OC, based on their genomes.^[50] On the other hand, tissue samples are clinically relevant, but require invasive means to excise from patients. With the limitations discussed regarding cell lines and tissue, many studies are now utilizing serum and plasma from patients due its less invasive nature, and wealth of biological and clinical information.

5. The Ovarian Cancer *N*-Glycome Characterised using Mass Spectrometry

5.1. Serum and Plasma

In 2007, Saldova et al. collected serum from healthy and stage III OC patients to identify which glycoproteins were contributing to changes in the serum *N*-glycome.^[51] Normal-phase HPLC (NPH-PLC) fluorescence was performed to separate *N*-glycan species that were released from serum glycoproteins. See **Table 2** for a brief history of *N*-glycans identified and characterized by MS from ovarian cancer serum, cell line, ascites, and tissue samples. *N*-glycan structures were confirmed by a combination of exoglycosidase digestions, NPHPLC, and MALDI–TOF MS. The relative percentage areas of mono-sialylated, di-sialylated, tri-sialylated, and tetra-sialylated *N*-glycans were calculated and compared between patients. It was concluded that mono-sialylated *N*-glycans were lower on average compared with control while tri-sialylated *N*-glycans were high on average. Immunoglobulin (IgG) was isolated from all of the serum samples by affinity chromatography

on a Protein G column. Previously, core fucosylated *N*-glycan levels have been found to be twofold higher in patients with ovarian cancer, compared to healthy controls, and this was found to be consistent with these samples. 2D SDS–PAGE was employed to the ovarian cancer serum samples, and then the differential protein spots were excised for subsequent *N*-glycan profiling by ESI–MS/MS. Haptoglobin β -chain, α 1-acid glycoprotein, and α 1-antichymotrypsin were represented as examples of the glycoproteins with major *N*-glycosylation differences.

In 2008, Leiserowitz et al. used MALDI–Fourier-transform ion cyclotron resonance (FTICR)–MS again to study the serum glycoproteins of OC patients, utilizing patient information such as grade and mucin 16 (CA125) expression.^[52] Serum samples from 48 ovarian cancer patients and 24 healthy controls were used. Out of the 48 OC patients, 23 patients had CA125 levels with less than 35 U mL^{−1} and 25 patients had CA125 levels with more than 150 U mL^{−1}. It was determined that 44 patients out of 48 OC patients had detectable glycan signals with CA125 values between 2 and 17 044 U mL^{−1}. Conversely, 23 out of 24 healthy controls had no detectable glycans with CA125 values between 10 and 64. Therefore, the sensitivity and specificity was determined to be 91.6% and 95.8% respectively for the classification of OC from controls.

In 2013, Saldova et al. collected serum from mice that had been injected with OVCAR3 adenocarcinoma cell lines.^[53] *N*-glycans were released from serum samples and analyzed by HILIC– and weak anion exchange (WAX)–HPLC, combined with exoglycosidase digestions to assign structural information. A total of 19 peaks were identified by HILIC–HPLC while only five peaks were detected by WAX–HPLC. Mice treated with the pro-inflammatory drugs, thioglycolate (TG), and chlorite-oxidized oxyamylose (COAM), were shown to have increased sialylated and branching *N*-glycans. The same authors' explored the glycosylation patterns of CA125 extracted from healthy and OC patient serum using SDS–PAGE and LC–ESI–MS/MS.^[53] The *N*-glycans identified and characterized included mono-sialylated, di-sialylated, core-fucosylated, bisected, and high-mannosylated *N*-glycans. It was concluded that core-fucosylated bi-antennary mono-sialylated *N*-glycans were highly abundant in OC patients, while bisecting bi-antennary and non-fucosylated *N*-glycans were highly abundant in healthy patients.

Hua et al. investigated isomeric differences of *N*-glycans released from OC serum samples compared with healthy controls.^[54] Nano-PGC–LC–ESI–MS/MS revealed 250 *N*-glycan compound peaks and over 100 distinct *N*-glycan compositions. The *N*-glycans were grouped into complex, hybrid, high mannose, sialylated, and fucosylated *N*-glycans, and then compared based on their average relative abundances and standard errors. Complex, hybrid and high mannose *N*-glycans were recorded to be lower intensity in OC serum samples relative to healthy controls while fucosylation and sialylation were found to be consistently higher in the OC serum. This study provides a valuable insightful into the complexity of *N*-glycans in serum.

A comparison of the serum *N*-glycome from 63 preoperative primary OC patients and 33 age-matched healthy patients used MALDI–TOF–MS and MS/MS analysis to identify 11 *N*-glycan biomarkers; four high mannose and seven

Table 2. A brief history of *N*-glycans identified and characterized by MS from ovarian cancer serum, cell line, ascites, and tissue samples.

Year	Publication Title	Author	Biological Sample	Sample Information	Species	Mass Spectrometry	Journal	Results
2007	Ovarian cancer is associated with changes in glycosylation in both acute-phase proteins and IgG	Saldova et al.	Serum	Stage IIIC serous and endometrioid carcinoma prior to surgery, stage III serous carcinoma at the time of relapse with advanced disease, and healthy controls	Human	MALDI-TOF ESI-QTOF	Glycobiology	Serum ↑Core-fucosylated ↑Tri-sialylated ↓Mono-sialylated
2008	Glycomics analysis of serum: a potential new biomarker for ovarian cancer?	Leiserowitz et al.	Serum	Less than 35 IU mL ⁻¹ (low CA125) and greater than 150 (high CA125)	Human	MALDI-FT	International Journal of Gynaecological Cancer	Serum <i>N</i> -glycans not stated
2011	<i>N</i> -Glycosylation of total cellular glycoproteins from the human ovarian carcinoma SKOV3 cell line and of recombinantly expressed human erythropoietin	Machado et al.	Cell Line	SKOV 3 ovarian carcinoma	Human	MALDI-TOF	Glycobiology	Cell Line ↑High mannosylated ↑Fucosylated
2013	Increase in sialylation and branching in the mouse serum <i>N</i> -glycome correlates with inflammation and ovarian tumour progression	Saldova et al.	Serum	OVCAR 3 adenocarcinoma injected into mice and analysis	Mouse	ESI-QTOF	PLoS One serum extracted for	Serum ↑Sialylated and branching in TG and COAM-treated mice
2013	Exploring the glycosylation of serum CA125	Saldova et al.	Serum	Advanced ovarian cancer	Human	ESI-QTOF	International Journal of Molecular Sciences	Serum ↑Core-fucosylated ↑Mono-sialylated ↓Bisected ↓Non-fucosylated
2013	Isomer-specific chromatographic profiling yields highly sensitive and specific potential <i>N</i> -glycan biomarkers for epithelial ovarian cancer	Hua et al.	Serum	Stage I-IV epithelial ovarian cancer and healthy controls	Human	ESI-chip-TOF	Journal of Chromatography	Serum ↑Sialylated ↑Core-fucosylated ↓High mannosylated ↓Complex/hybrid
2013	Serum glycome profiling: a biomarker for diagnosis of ovarian cancer	Biskup et al.	Serum	Stage I-IV primary ovarian cancer patients and age-matched controls	Human	MALDI-TOF	Journal of Proteome Research	Serum ↑Sialylated ↑Core-fucosylated ↓High mannosylated
2014	The serum glycome to discriminate between early-stage epithelial ovarian cancer and benign ovarian diseases	Biskup et al.	Serum	Stage I-III primary serous ovarian cancer, benign ovarian diseases and healthy controls	Human	MALDI-TOF	Disease Markers	Serum ↑Sialylated ↑Fucosylated ↑Tri- and tetra-antennary ↓High mannosylated
2014	Mass spectrometric screening of ovarian cancer with serum glycans	Jae-Han et al.	Serum	Stage I-IV ovarian cancer and healthy controls	Human	MALDI-TOF	Disease Markers	Serum ↑Sialylated ↑Core-fucosylated ↓High mannosylated
2014	Evaluation of glycomic profiling as a diagnostic biomarker for epithelial ovarian cancer	Kim et al.	Serum	Epithelial ovarian cancer, serous low malignant potential tumours, and healthy controls	Human	ESI-chip-TOF	Cancer, Epidemiology, Biomarkers & Prevention	Serum ↓High mannosylated ↓Bisected ↓Hybrid
2014	Discovery of specific metastasis-related <i>N</i> -glycan alterations in epithelial ovarian cancer based on quantitative glycomics	Zhang et al.	Cell Line	SKOV 3 serous ovarian cancer and its high metastatic derivative SKOV 3-ip	Human	MALDI-QIT-TOF	PLoS One	Cell Line ↓Bisected in secretome of SKOV 3-ip (highly metastatic)

(Continued)

Table 2. Continued.

Year	Publication Title	Author	Biological Sample	Sample Information	Species	Mass Spectrometry	Journal	Results
2014	Specific glycosylation of membrane proteins in epithelial ovarian cancer cell lines: Glycan structures reflect gene expression and DNA methylation status	Anugraham et al.	Cell Line	Serous ovarian cancer (SKOV 3, IGROV 1, A2780 and OVCAR 3), and non-cancerous ovarian surface epithelial (HOSE 6.3, HOSE 17.1)	Human	ESI-QIT	Molecular and Cellular Proteomics	Cell Line ↑Bisected ↑ α 2–6 Sialylated ↑LacdiNAc
2015	Relative quantification and higher-order modeling of the plasma glycan cancer burden ratio in ovarian cancer case-control samples	Hecht et al.	Plasma	Stage I-IV endometriosis, benign ovarian tumours, cysts, and tubal disease	Human	ESI-QIT	Journal of Proteome Research	N/A
2015	Glycomic analysis of membrane glycoproteins with bisecting glycosylation from ovarian cancer tissues reveals novel structures and functions	Allam et al.	Tissue	Fresh frozen endometrioid ovarian cancer, serous ovarian cancer, and normal ovaries	Human	ESI-QIT	Journal of Proteome Research	Tissue ↑Bisected
2016	<i>N</i> -glycan MALDI imaging mass spectrometry on formalin-fixed paraffin-embedded tissue enables the delineation of ovarian cancer tissues	Everest-Dass et al.	Tissue	FFPE stage IIIC serous ovarian cancer	Human	MALDI-TOF and ESI-QIT	Molecular and Cellular Proteomics	Tissue ↑High mannosylated
2017	The ascites <i>N</i> -glycome of epithelial ovarian cancer patients	Biskup et al.	Ascites	Ascitic fluid from primary serous epithelial ovarian cancer versus serum of healthy controls	Human	MALDI-TOF	Journal of Proteomics	Ascites ↑Antennarity ↑Branched ↑Sialylated ↑Lewisx
2017	Simultaneous analyses of <i>N</i> -linked and <i>O</i> -linked glycans of ovarian cancer cells using solid-phase chemoenzymatic method	Yang et al.	Cell Line	OVCAR 3	Human	MALDI-TOF and ESI-QIT	Clinical Proteomics	Cell Line ↓High mannosylated in BAG-treated OVCAR 3
2017	Mass spectrometric profiling reveals association of <i>N</i> -glycan patterns with epithelial ovarian cancer progression	Chen et al.	Tissue	FFPE stage I-III epithelial ovarian cancer and normal ovaries	Human	MALDI-TOF	Tumor Biology	Tissue ↑High mannosylated ↑Fucosylated
2017	Altered (neo-) lacto series glycolipid biosynthesis impairs α 2-6 sialylation on <i>N</i> -glycoproteins in ovarian cancer cells	Alam et al.	Cell Line	IGROV 1 and SKOV 3	Human	ESI-QTOF	Scientific Reports	Cell Line ↓ α 2–6 Sialylated in the B3GNT5 mutant
2017	Tissue glycomics distinguish tumour sites in women with advanced serous adenocarcinoma	Anugraham et al.	Tissue and Cell Line	Fresh frozen serous ovarian and serous peritoneal cancer IGROV 1, A2780, SKOV 3, EFO27, and OVCAR 3	Human	ESI-QIT	Molecular Oncology	Tissue ↑LacdiNAc ↑Bisected ↑Branched ↑ α 2–6 Sialylated

complex fucosylated and sialylated.^[55] The high mannose *N*-glycans were found to be downregulated in OC serum relative to the healthy controls while the complex fucosylated and sialylated *N*-glycans were upregulated. These results generated a sensitivity of 97% and a specificity of 98.4% whereas CA125 results showed a sensitivity of 97% and a specificity of 88.9%.

The serum of OC and healthy patients had been extensively studied between 2007 and 2013, so Biskup et al. investigated the *N*-glycome of serum from early-stage OC patients and benign ovarian diseases.^[56] The serum was collected from 33 healthy, 20 benign OC, and 20 OC patients for *N*-glycan release and analysis by MALDI-TOF-MS. A total of 47 *N*-glycan structures were detected with sialylated fucosylated tri- and tetra-antennary

N-glycans being highly expressed in early-stage OC compared to benign and healthy samples. Alternatively, high mannose *N*-glycans were seen to decrease in early-stage OC patients relative to benign and healthy samples.

In 2014, Jae-Han et al. screened the serum of 40 OC patients and 40 healthy controls for aberrant *N*-glycans.^[57] MALDI-TOF-MS analysis provided a multibiomarker panel composed of 15 peaks which results in an AUC of 0.89, 80–90% sensitivity, and 70–83% specificity in the training set. This panel was then tested against another 23 healthy controls and 37 OC patients, which generated 81–84% sensitivity and 83% specificity. The sensitivity and specificity of CA125 in these patients were 74% and 78%, respectively.

In 2014, Zhang et al. also used the secretome of the SKOV 3 cell line and highly metastatic derivative, SKOV 3-ip, to profile the *N*-glycome using a quantitative glycomics approach based on a metabolic stable isotope labeling strategy.^[58] A total of 17 *N*-glycans were identified with bisecting *N*-glycans being significantly decreased in the SKOV 3-ip cell lines relative to SKOV. This observation was further validated by the measurement of glycosyltransferase levels using real-time PCR, western blotting, transwell assays, lectin blotting, and immunohistochemistry analyses.

In a study by Kim et al., 147 OC and 52 low malignant potential (LMP) serum samples were processed for *N*-glycan release and analyzed by ESI-chip-TOF-MS.^[59] It was concluded that high mannose, hybrid, and bisecting *N*-glycans were decreased on OC samples compared to healthy controls.

In 2015, plasma was studied for the first time in 82 case-control samples, with 27% stage I, 12% stage II, 46% stage III, and 15% stage IV OC.^[60] The released *N*-glycans were analyzed by labeling with hydrazide tags for signal enhancement in LC-ESI-MS/MS. A total of 71 *N*-glycans were identified and reduced to 63 using the following parameters; *N*-glycans in greater than or equal to 90% of spectra and detected above an abundance of 1×10^5 . The glycan cancer burden ratios (GBRs) were calculated as the log ratio of specific structure abundance between cancer and control patients (i.e., stage I) and they were averaged over each triplicate MS injection. Fucosylated and sialylated *N*-glycans were found to be not significant while seven other varying *N*-glycans were identified to be significantly different relative to stage I ovarian cancer patients.

Since 2007, the OC serum and plasma *N*-glycome has extensively been investigated with common *N*-glycan families showing a similar trend, such as sialylated structures increasing, core-fucosylated structures increasing, high mannose structures decreasing, and complex/hybrid structures decreasing. While studying the entire *N*-glycome of serum and plasma provides a valuable opportunity to potentially discover a novel OC biomarker, there is also the possibility this novel biomarker may be found in another fluid that is currently underutilized in clinical studies.

5.2. Ascites

Ascites is localized within the peritoneal cavity that can often result in abdominal pain and compromised respiratory, gastrointestinal, and urinary systems. This can lead to

further complications, thereby making it difficult to treat OC patients. At the time of writing this review, there has only ever been one MS-based publication that investigates *N*-glycans derived from ascites. *N*-glycans were released from ascites of 18 epithelial OC patients and serum of 20 age-matched healthy controls.^[61] Following MALDI-TOF-MS analysis, it was revealed that the ascites *N*-glycome consisted of increased antennarity, branching, sialylation and Lewis^x motives relative to the healthy serum.

Since this is the only documentation of the ascites *N*-glycome so far, there is potential for more studies in the future. Although serum, plasma, and ascites fluid are extracted from OC patients with minimal invasiveness, there are still limitations, for example, storage timeframes must be short due to biomolecular degradation over time.

5.3. Tissue

The first tissue-based study into the *N*-glycome of OC emerged in 2015 where a lectin capture strategy coupled to nano-LC-ESI-MS/MS was used to isolate and identify *N*-glycans from membrane glycoproteins.^[62] It was concluded that bisecting *N*-glycans were highly abundant in both serous and endometrioid OC tissue and this was further validated by amplification of GnT-III mRNA expression compared to normal ovarian tissue.

An investigation into the *N*-glycome of women with advanced serous adenocarcinoma identified α 2–6 sialylated structures in both OC and peritoneal cancer, with the majority displaying bi-antennary mono- and di-sialylation as well as bisecting.^[63] PGC-LC-ESI-MS/MS revealed that Lac-diNAc motifs were unique to serous OC only and correlated with the elevated gene expression of the glycosyltransferases, B4GALNT3 and B4GALNT4, in patients. A total of 13 *N*-glycans were found to be significantly discriminatory between tumor sites with LacdiNAc, bisecting, and branched *N*-glycans being upregulated.

More recently, *N*-glycosylation patterns of OC tissue, with different pathological grades, and healthy controls were studied.^[64] A total of 80 *N*-glycan compositions were detected with high mannose *N*-glycans found to be elevated in the OC samples, whilst hybrid *N*-glycans were reduced, relative to the healthy controls. Receiver operating characteristic (ROC) analysis showed that combining four high mannose and three fucosylated complex neutral *N*-glycans provided good discrimination between cancer and noncancer samples. In addition, it was discovered that two high mannose, two fucosylated and sialylated, and ten fucosylated complex neutral *N*-glycans change abundance across different OC grades.

While applicable to multiple OC sample types, including serum, plasma, ascites, and tissue, LC-ESI-MS and MALDI-TOF-MS have limitations with respect to glycoprotein and glycan distribution, as spatial information is removed through tissue disruption. This is of interest for disease classification using changes in molecular information with tissue morphology, and in particular, surgical pathology annotations. To address this analytical shortfall, MALDI-MSI is a relatively new spatially sensitive technique that directly analyzes analytes across tissue sections, including proteins and released *N*-glycans.

6. Mass Spectrometry Imaging

MSI typically employs a MALDI-TOF-MS instrument for acquisition of mass spectra in a 2D grid across tissue sections (see **Figure 2**).^[65] This allows visualization of the tissue-specific spatial distribution of the measured analytes (i.e., intact proteins, peptides, lipids, metabolites, small molecules, and *N*-glycans) across multiple samples at the same time (e.g., tissue microarrays). Compared with conventional immunohistochemistry (IHC), hundreds of molecules and multiple molecule classes can be measured in a single experiment without the need for antibodies.^[66]

Many MSI studies utilize fresh frozen tissue samples. Most of these studies used small sample numbers due to the expense and difficulty of maintaining large native tissue archives for long periods of time. To address low sample numbers, multiple groups are turning to archival storage forms such as formalin-fixed paraffin-embedded (FFPE) tissue samples. Hundreds to

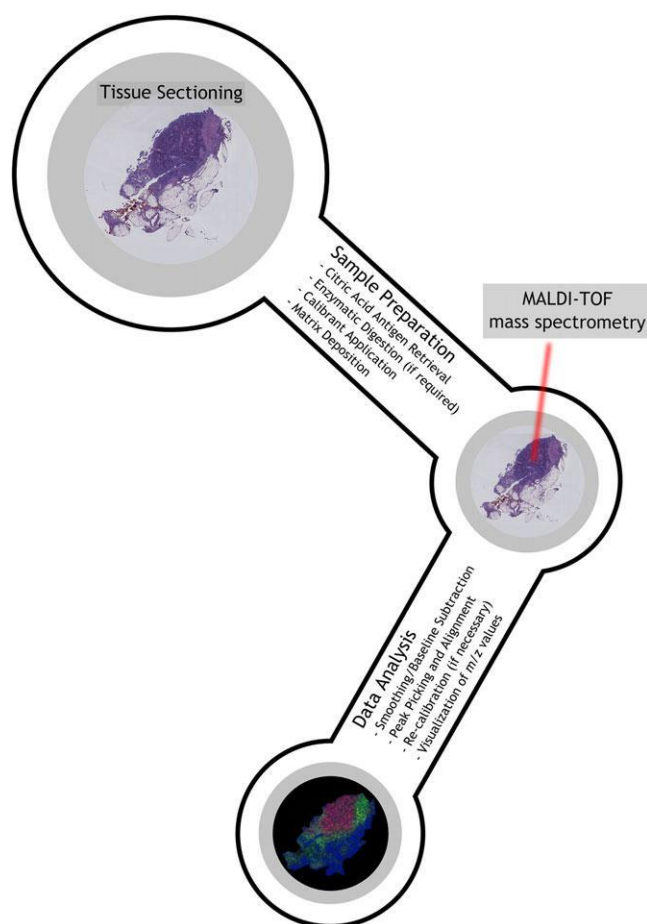


Figure 2. A conventional MALDI-TOF-MS imaging workflow for FFPE tissue sections. Briefly, FFPE tissue is sectioned onto indium tin oxide (ITO)-coated slides, treated with citric acid antigen retrieval (CAAR) and digested with an enzyme, depending on the analyte of interest. Next, calibrants are applied and matrix is deposited across the tissue section. Then, mass spectra are acquired in a two-dimensional array using a YAG pulse laser from a MALDI-TOF-MS instrument. Lastly, the data is analyzed using software such as flexImaging (Bruker Daltonics) or SciLS Lab (Bruker Daltonics) by overlaying the annotated histological stained image.

thousands of FFPE tissue samples, from healthy and diseased individuals, are stored in large repositories world-wide.^[67] These FFPE tissue samples are annotated with clinical information such as patient diagnosis, treatment, and outcome. The formalin-fixation process conserves tissue samples by cross-linking proteins.^[68] As a result, FFPE tissues can be stored under ambient conditions for long periods of time.

ESI and MALDI are complementary soft ionization techniques, such that some analytes have preferential ionization in one or the other. For released glycans, ionization efficiency and thus detection relies on the composition, which affects ionization efficiency depending on the MS mode of analysis (i.e., positive ion or negative ion mode). Furthermore, ESI- and MALDI-MS platforms offer different analyte fragmentation mechanisms, affecting the ability for connectivity evaluation of glycopeptides and/or released glycans. As such, comprehensive *N*-glycome characterization typically requires a combined MS strategy, exploiting ESI- and MALDI-MS platforms. However, maintaining spatial distribution of *N*-glycans improves the ease of correlation with tissue morphology and IHC to better understand the mechanisms behind OC progression.

Our group recently published the first application of an *N*-glycan MALDI-MSI method to FFPE OC tissue.^[69] The tissue analyzed in this study had been annotated by a pathologist, and it was found that specific *N*-glycan structures were differentially detected in specific tissue regions, such as tumor, stroma, adipose, and necrotic tissue (see **Figure 3**). Analysis of stage III OC tissues resulted in the discovery of high mannose structures relatively abundant in the tumor regions, while tri-antennary complex structures in the cancer-associated stromal regions. This observation was consistent between not only the three patients investigated, but also between previous publications from the literature.

We also compared early-stage (see **Figure 4**, Panels A, B and C) and late-stage (see **Figure 4**, Panels D, E and F) serous OC tissue sections by applying *N*-glycan MALDI-MSI and laser capture microdissecting (LCM) tumor-specific regions for PGC-LC-ESI-MS/MS analysis. A total of 14 *N*-glycans were visualized as ion intensity maps by MALDI-MSI whereas 42 *N*-glycans (including structural and compositional isomers) were identified and structurally characterized in the LCM tissue sections by ESI. The spatial distribution of high man-nose, complex neutral, bisecting (see **Figure 4**) and sialylated *N*-glycan families were only observed to be localized to the tumor regions of late-stage OC patients relative to early-stage patients. Potential *N*-glycans diagnostic markers that emerged include the high mannose structure, (Hex)₆ + (Man)₃(GlcNAc)₂, the bisecting structure, (Hex)₁ (HexNAc)₃ (Deoxyhexose)₁ + (Man)₃(GlcNAc)₂, and the sialylated structure, (Hex)₂ (HexNAc)₂ (NeuAc)₁ + (Man)₃(GlcNAc)₂.

In **Figure 4** Panel I, the Z1 ion at *m/z* 350.11 and the Y2 ion at *m/z* 571.16 from the MS/MS fragmentation provide evidence for the presence of the chitobiose core fucose. Another diagnostic ion of significant importance is the D-ion. The D-ion arises from the loss of the chitobiose core (C ion cleavage between Man β 1-4GlcNAc), and the Z ion cleavage between Man α 1-3Man forming the 3-antennae; thus, the D-ion mass corresponds to the composition of the six-arm antenna plus the two remaining branching core mannoses.^[70] Furthermore, the D and [D-18] ions

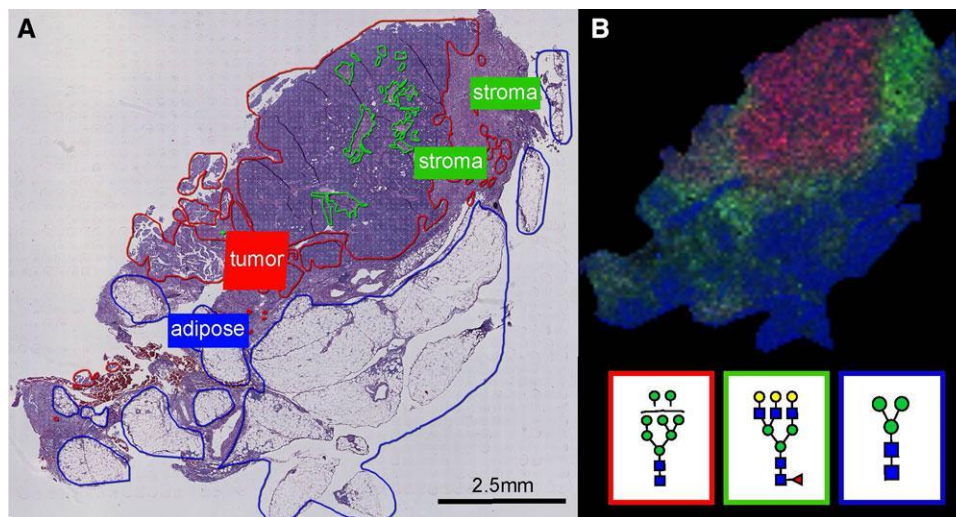


Figure 3. Glycan analysis of ovarian cancer (OC). The formalin-fixed paraffin-embedded stage III OC section was treated with antigen retrieval prior to printing of 15 nL per spot dialyzed PNGase F with 250 μm spacing. 2,5-DHB (20 mg/mL) was sprayed onto the sections and MS spectra were acquired by oversampling at 100 μm intervals using a MALDI-TOF/TOF MS instrument. A) Hematoxylin and eosin stain of the OC section with tumour (red), stroma (green), and adipose (blue) regions annotated by a pathologist. B) An ion intensity map of m/z 1743.7 (red), m/z 2174.9 (green), and m/z 933.3 (blue) on the OC section. Yellow circle, galactose (Gal); green circle, mannose (Man); blue square, *N*-acetylglucosamine (GlcNAc); red triangle, fucose (Fuc).

have been used to identify the composition of the *N*-glycan 6-antenna. If the *N*-glycan has a bisecting GlcNAc residue, the additional loss of this bisecting β 1–4-linked GlcNAc gives rise to the D–221 ion. Figure 4 Panel I shows the MS/MS fragmentation contains the D–221 ion corresponding to m/z 507.88.

In summary, all publications focusing on OC tissue found a relative increase in high mannose, bisecting, fucosylated, Lac-diNAc, and α 2–6 sialylated *N*-glycans. The normal *N*-glycan biosynthetic pathway in the ER and Golgi membranes involves mannosidases cleaving mannose residues to only three mannose residues. However, it has been found, that on the tumor cell surface and on secreted glycoproteins, there are complex high mannose structures with more than three mannose residues. It has also been discovered that there are auto-antibodies specific to high mannose structures within the sera from cancer and other diseased patients, although it is unclear why high mannose structures are transported to the cell surface or secreted on glycoproteins in the tumor microenvironment.

7. Translating Analytical Applications to Clinical Strategies: The Current Challenges

Based on the analytical information collated for this review, it is evident that there are several limitations with analytical applications focused on MS alone. Therefore, to tackle this caveat, recent studies have incorporated other well-established techniques with MS to further understand the biological mechanisms behind OC progression and search for clinically relevant biomarkers. Such approaches include the use of antibodies and lectins to spatially visualize *N*-glycans in situ, molecular biology to correlate gene expression levels with specific *N*-glycan structures, and glyproteomics to obtain site-specific information.

7.1. Antibodies and Lectins

Specific lectins and anti-carbohydrate antibodies are routinely used to evaluate the spatial localization of *N*-glycans and other carbohydrates in situ. For example, the carbohydrate antigen CA19-9 is measured in the clinic to determine the prognosis of pancreatic and other gastrointestinal cancers.^[71] The CA19-9 antibody used recognizes a distinct carbohydrate motif (GlcNAc-Gal, α 1,4 fucose, and α 2,3 sialic acid).^[72] Another antigen, F77 for prostate cancer, has also been previously described in the literature.^[73] The corresponding antibody for F77 recognizes the blood group H antigen-related Lewis Y glycan structures with α 1,2 fucose. It is established that most antibodies for carbohydrate detection are required to recognize between one and four structural epitopes (i.e., portion of the glycan that forms the binding region).^[38] Using such antibodies are quite useful for tissue IHC-based staining methods, however, these methods cannot distinguish between the types of glycan classes (i.e., glycolipids, *O*-glycans, and *N*-glycans).^[74] Alternatively, lectins or carbohydrate-binding proteins (CBPs) for many decades have evaluated glycoproteins and their structural features.^[74] In a similar way to antibodies for carbohydrate antigens, lectins recognize between two and four structural epitopes. However, lectins possess poor affinity-binding constants in the low micromolar range, which limits the tissue histochemistry applications mentioned previously.^[75] Lectin histochemistry applications have been successfully established to analyze FFPE tissue.^[76] Again, it has been described as difficult to distinguish between the presenting conjugate since the recognizable glycan motif is often the same between *N*- and *O*-glycans. Hence, MALDI-MSI is an important tool that provides not only spatial information, but also some specific *N*-glycan structural features. However, there is potential for the development of workflows to incorporate these antibody

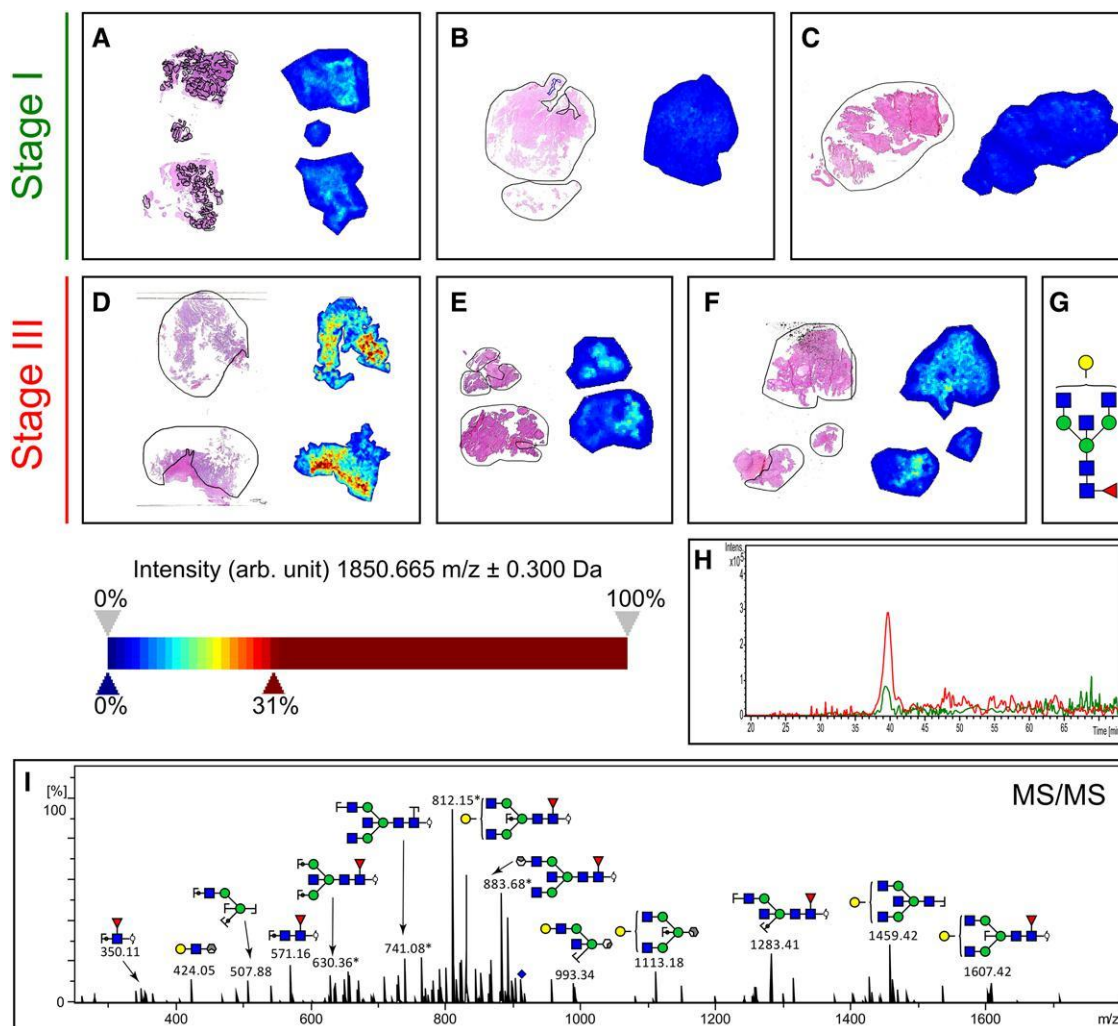


Figure 4. N -glycan MALDI-MSI of stage I ($n = 3$) and stage III ($n = 3$) serous ovarian cancer patients. Formalin-fixed paraffin-embedded tissue sections were treated with citric acid antigen retrieval prior to printing of dialyzed PNGase F with $250 \mu\text{m}$ spacing. DHB matrix was sprayed onto the sections and MS spectra were acquired by oversampling at $100 \mu\text{m}$ intervals using a MALDI-TOF/TOF-MS instrument. Monoisotopic glycan masses were measured in the positive ion reflectron mode as $(M + \text{Na})$ adducts for MALDI-MSI whereas PGC-LC-ESI-MS/MS revealed doubly negatively charged monoisotopic masses $([M - 2\text{H}]^{2-})$. Panels A-F show ion intensity maps of m/z 16663.581 from the stage I (green) and stage III (red) patients. The N -glycan, $(\text{Hex})_1(\text{HexNAc})_3(\text{Deoxyhexose})_1 + (\text{Man})_3(\text{GlcNAc})_2$, in panel (G) is the confirmed structure based on PGC chromatography (panel H) and MS/MS fragmentation (panel I).

or lectin histochemistry applications, as well as MALDI-MSI, to rapidly visualize the spatial localization of specific glycan motifs.

7.2. Molecular Biology

A combination of MS with molecular biology has recently provided further insight into aberrant N -glycosylation patterns. Many of these studies have utilized glyco-gene editing in mammalian cell lines combined with high-throughput MS approaches. Our most recent MS data has demonstrated that complex neutral and fucosylated N -glycans are highly intense in tissue from late-stage patients relative to early-stage (data not shown). These complex N -glycans are derived from the core N -glycan structure, utilizing glycosyltransferases to add

monosaccharide subunits such as N -acetylglucosamine, galactose, fucose, and sialic acid.^[77] Additionally, these complex N -glycans are often observed in nontumor (i.e., cancer-associated stroma) regions. For example, bisecting structures primarily expressed in tumor regions of tissue derived from late-stage patients and also various OC cell lines.^[43,62,69] This observation is consistent with glyco-gene studies on GnT-III activity, which is the glycosyltransferase responsible for attaching a GlcNAc monosaccharide in the β 1,4 linkage at the β -mannose of the mannosyl core. Bisecting structures have been found to suppress the further processing of N -glycans catalyzed by GnT-V, which is the glycotransferase responsible for β 1,6 branching. OC tissues have been found to have much higher levels of GnT-III compared to normal ovarian and fallopian tube tissues while other cancers have been found to have lower levels of GnT-III

than their respective normal tissues.^[20] With all of this information considered, bisecting *N*-glycan structures could potentially be highly specific and sensitive OC biomarkers. This is yet to be determined as further investigation and validation is required.

7.3. Glycoproteomics

Glycoproteomics focuses on the analysis of glycosylated proteins (i.e., glycoproteins) from cells, tissue, or bodily fluid using MS techniques.^[78] Despite recent advances with respect to sample preparation and next-generation MS platforms, glycoproteomic analysis is quite difficult due to both instrument and method limitations.^[79] However, this type of analysis provides both glycan composition and modification site information, which is ultimately a key to understanding the role of specific glycosylations in disease.

In addition to combining MS with other established techniques, there are several other recent advancements that exist for clinical-based approaches. There has been a shift toward utilizing high-throughput platforms to analyze ‘omics’ data from large patient cohorts.^[80] Utilizing these cohorts is an important process in first identifying novel biomarkers, and second validating these potential biomarkers on the long road to the clinic. Another recent advancement into glycoconjugate research has emerged from investigating circulating exosomes from pancreatic cancer.^[81] Proteoglycan glypican 1 (GPC1) was identified from circulating pancreatic cancer exosomes and contributed to early detection of this cancer. Therefore, this is a potential area for growth in OC research and the journey to better understand OC progression. Tumor-associated glycan antigens have also emerged as a potential application for early-stage detection of cancer. For example, specific auto-antibodies against aberrantly glycosylated MUC1 correlate with the detection of colorectal cancer, predicting this cancer with 95% specificity.^[82] However, other markers are still required in combination with this identified marker due to low sensitivity issues, therefore suggesting an array of antibodies may be required to detect cancer in its early stages. This approach has opened new avenues for investigating cancer-associated *N*-glycans and glycopeptides through microarray studies with the potential to transfer into clinical applications.^[83]

8. Conclusions and Future Directions

The glycomics field has immensely evolved over the past decade. Both technological and methodical advancements have emerged, with more recently MALDI-MSI being used as a platform to measure the spatial distribution of *N*-glycans on OC tissue sections. OC has shown to exhibit aberrant *N*-glycosylation patterns through the analysis of serum, plasma, cell line, and tissue samples. The recent advances in MALDI-MSI provides a rapid and robust platform to spatially study tissue sections, however, the current workflow fails to spatially identify isomeric structures of the same composition, although derivatization methods have recently emerged to distinguish between α 2–3 and α 2–6 sialic acid linkages by MALDI. MALDI-MSI method development is still in

its infancy with multiple facets requiring attention, such as *N*-glycan detection in the higher mass range, the identification of isomeric structures, analysis of *O*-linked glycan structures, and increased MALDI resolution and sensitivity. With caveats in the field set to be addressed over the next decade, there is a potential to discover novel biomarkers for OC early-detection, prediction, and monitoring of treatment response, as well as detection of OC recurrence.

Acknowledgements

M.T.B. and M.R.C. contributed equally to this work.

Conflict of Interest

The authors declare no conflict of interest.

Keywords

N-glycan, MALDI, mass spectrometry imaging, ovarian cancer, FPPE, tissue

Received: June 13, 2018
Revised: September 30, 2018
Published online:

- 1 Australian Institute of Health and Welfare, *Asia Pac. J. Clin. Oncol.* **2018**, *14*, 5.
- 2 Y. Zhu, R. Wu, N. Sangha, C. Yoo, K. R. Cho, K. A. Shedden, H. Katabuchi, D. M. Lubman, *Proteomics* **2006**, *6*, 5846.
- 3 I. Meinhold-Heerlein, C. Fotopoulou, P. Harter, C. Kurzeder, A. Mustea, P. Wimberger, S. Hauptmann, J. Sehoul, *Arch. Gynecol. Obstet.* **2016**, *293*, 695.
- 4 T. H. Bourne, S. Campbell, K. M. Reynolds, M. I. Whitehead, J. Hampson, P. Royston, T. J. Crayford, W. P. Collins, *BMJ* **1993**, *306*, 1025.
- 5 K. J. Carlson, S. J. Skates, D. E. Singer, *Ann. Intern. Med.* **1994**, *121*, 124.
- 6 R. Sankaranarayanan, J. Ferlay, *Best Pract. Res. Clin. Obstet. Gynaecol.* **2006**, *20*, 207.
- 7 a) J. H. Goldie, A. J. Coldman, *Cancer Treat. Rep.* **1979**, *63*, 1727; b) L. Iyer, M. J. Ratain, *Eur. J. Cancer* **1998**, *34*, 1493.
- 8 J. R. van Nagell Jr., J. T. Hoff, *Int. J. Womens Health* **2013**, *6*, 25.
- 9 S. I. Jung, *Ultrasonography* **2015**, *34*, 173.
- 10 E. L. Moss, J. Hollingworth, T. M. Reynolds, *J. Clin. Pathol.* **2005**, *58*, 308.
- 11 P. T. Lavin, R. C. Knapp, G. Malkasian, C. W. Whitney, J. C. Berek, R. Bast Jr., *Obstet. Gynecol.* **1987**, *69*, 223.
- 12 I. J. Jacobs, U. Menon, A. Ryan, A. Gentry-Maharaj, M. Burnell, J. K. Kalsi, N. N. Amso, S. Apostolidou, E. Benjamin, D. Cruickshank, D. Crump, S. K. Davies, A. Dawnay, S. Dobbs, G. Fletcher, J. Ford, Godfrey, R. Gunu, M. Habib, R. Hallett, J. Herod, H. Jenkins, C. Karpinskyj, S. Leeson, S. J. Lewis, W. R. Liston, A. Lopes, T. Mould, J. Murdoch, D. Oram, D. J. Rabideau, K. Reynolds, I. Scott, M. W. Seif, Sharma, N. Singh, J. Taylor, F. Warburton, M. Widschwendter, K. Williamson, R. Woolas, L. Fallowfield, A. J. McGuire, S. Campbell, M. Parmar, S. J. Skates, *Lancet* **2016**, *387*, 945.
- 13 M. J. Duffy, J. M. Bonfrer, J. Kulpa, G. J. Rustin, G. Soletormos, G. C. Torre, M. K. Tuxen, M. Zwirner, *Int. J. Gynecol. Cancer* **2005**, *15*, 679.

- 14 M. Friedlander, *Pathology* **2009**, *41*, 15.
- 15 R. C. Bast Jr., D. Badgwell, Z. Lu, R. Marquez, D. Rosen, J. Liu, K. A. Baggerly, E. N. Atkinson, S. Skates, Z. Zhang, A. Lokshin, U. Menon, Jacobs, K. Lu, *Int. J. Gynecol. Cancer* **2005**, *15*, 274.
- 16 a) E. Bandiera, L. Zanotti, A. S. Fabricio, E. Bucca, E. Squarcina, C. Romani, R. Tassi, E. Bignotti, P. Todeschini, G. Tognon, C. Romagnolo, Gion, E. Sartori, T. Maggino, S. Pecorelli, A. Ravaggi, *Clin. Chem. Lab. Med.* **2013**, *51*, 1815; b) D. Sasaroli, G. Coukos, N. Scholler, *Biomark Med* **2009**, *3*, 275.
- 17 R. G. Moore, D. S. McMeekin, A. K. Brown, P. DiSilvestro, M. C. Miller, J. Allard, W. Gajewski, R. Kurman, R. C. Bast Jr., S. J. Skates, *Gynecol. Oncol.* **2009**, *112*, 40.
- 18 R. L. Coleman, T. J. Herzog, D. W. Chan, D. G. Munroe, T. C. Pappas, Smith, Z. Zhang, J. Wolf, *Am J Obstet Gynecol* **2016**, *215*, 82 e1.
- 19 S. J. North, P. G. Hitchen, S. M. Haslam, A. Dell, *Curr. Opin. Struct. Biol.* **2009**, *19*, 498.
- 20 H. Guo, K. L. Abbott, *Adv Cancer Res* **2015**, *126*, 281.
- 21 R. Saldova, W. B. Struwe, K. Wynne, G. Elia, M. J. Duffy, P. M. Rudd, *Int. J. Mol. Sci.* **2013**, *14*, 15636.
- 22 P. Stanley, N. Taniguchi, M. Aebi, in *Essentials of Glycobiology*, (Eds A. Varki, R. D. Cummings, J. D. Esko, P. Stanley, G. W. Hart, M. Aebi, A. Darvill, T. Kinoshita, N. H. Packer, J. H. Prestegard, R. L. Schnaar, H. Seeberger), Cold Spring Harbor Laboratory Press, Cold Spring Harbor, NY **2015**, 99.
- 23 B. Mulloy, A. Dell, P. Stanley, J. H. Prestegard, in *Essentials of Glycobiology*, (Eds: A. Varki, R. D. Cummings, J. D. Esko, P. Stanley, G. W. Hart, M. Aebi, A. G. Darvill, T. Kinoshita, N. H. Packer, J. H. Prestegard, R. L. Schnaar, P. H. Seeberger), Cold Spring Harbor Laboratory Press, Cold Spring Harbor, NY **2015**, 639.
- 24 W. Morelle, V. Faid, F. Chirat, J. C. Michalski, *Methods Mol Biol* **2009**, *534*, 5.
- 25 M. D. Battistel, H. F. Azurmendi, B. Yu, D. I. Freedberg, *Prog. Nucl. Magn. Reson. Spectrosc.* **2014**, *79*, 48.
- 26 G. Lu, C. L. Crihfield, S. Gattu, L. M. Veltri, L. A. Holland, *Chem. Rev.* **2018**, *118*, 7867.
- 27 G. Zauner, A. M. Deelder, M. Wührer, *Electrophoresis* **2011**, *32*, 3456.
- 28 T. E. Bapiro, F. M. Richards, D. I. Jodrell, *Anal. Chem.* **2016**, *88*, 6190.
- 29 L. Novakova, D. Solichova, P. Solich, *J. Sep. Sci.* **2006**, *29*, 2433.
- 30 B. Godin, R. Agneessens, P. A. Gerin, J. Delcarte, *Talanta* **2011**, *85*, 2014.
- 31 Z. Szabo, J. R. Thayer, Y. Agroskin, S. Lin, Y. Liu, K. Srinivasan, J. Saba, Viner, A. Huhmer, J. Rohrer, D. Reusch, R. Harfouche, S. H. Khan, Pohl, *Anal. Bioanal. Chem.* **2017**, *409*, 3089.
- 32 A. Zamfir, J. Peter-Katalinic, *Electrophoresis* **2004**, *25*, 1949.
- 33 L. R. Ruhaak, R. Hennig, C. Huhn, M. Borowiak, R. J. Dolhain, A. M. Deelder, E. Rapp, M. Wührer, *J. Proteome Res.* **2010**, *9*, 6655.
- 34 D. Reusch, M. Habberger, B. Maier, M. Maier, R. Kloseck, B. Zimmermann, M. Hook, Z. Szabo, S. Tep, J. Wegstein, N. Alt, P. Bulau, M. Wührer, *mAbs* **2015**, *7*, 167.
- 35 Y. Mechref, *Electrophoresis* **2011**, *32*, 3467.
- 36 M. Wührer, A. van Remoortere, C. I. Balog, A. M. Deelder, C. H. Hokke, *Anal. Biochem.* **2010**, *406*, 132.
- 37 a) E. Falkowska, K. M. Le, A. Ramos, K. J. Doores, J. H. Lee, C. Blattner, Ramirez, R. Derking, M. J. van Gils, C. H. Liang, R. McBride, B. von Bredow, S. S. Shivatare, C. Y. Wu, P. Y. Chan-Hui, Y. Liu, T. Feizi, M. B. Zwick, W. C. Koff, M. S. Seaman, K. Swiderek, J. P. Moore, D. Evans, C. Paulson, C. H. Wong, A. B. Ward, I. A. Wilson, R. W. Sanders, Poinard, D. R. Burton, *Immunity* **2014**, *40*, 657; b) J. M. Binley, T. Wrin, B. Korber, M. B. Zwick, M. Wang, C. Chappey, G. Stiegler, R. Kunert, S. Zolla-Pazner, H. Katinger, C. J. Petropoulos, D. R. Burton, *Virology* **2004**, *78*, 13232; c) L. M. Walker, M. Huber, K. J. Doores, E. Falkowska, R. Pejchal, J. P. Julien, S. K. Wang, A. Ramos, P. Y. Chan-Hui, M. Moyle, J. L. Mitcham, P. W. Hammond, O. A. Olsen, P. Phung, Fling, C. H. Wong, S. Phogat, T. Wrin, M. D. Simek, G. P. I. Protocol, W. C. Koff, I. A. Wilson, D. R. Burton, P. Poinard, *Nature* **2011**, *477*, 466.
- 38 E. Sterner, N. Flanagan, J. C. Gildersleeve, *ACS Chem. Biol.* **2016**, *11*, 1773.
- 39 F. Jacob, D. R. Goldstein, N. V. Bovin, T. Pochechueva, M. Spengler, Caduff, D. Fink, M. I. Vuskovic, M. E. Hufleit, V. Heinzelmann-Schwarz, *Int. J. Cancer* **2012**, *130*, 138.
- 40 S. Purohit, T. Li, W. Guan, X. Song, J. Song, Y. Tian, L. Li, A. Sharma, Dun, D. Mysona, S. Ghamande, B. Rungruang, R. D. Cummings, G. Wang, J. X. She, *Nat. Commun.* **2018**, *9*, 258.
- 41 M. Wilm, *Mol. Cell. Proteomics* **2011**, *10*, M111 009407.
- 42 A. M. Haag, *Adv Exp Med Biol* **2016**, *919*, 157.
- 43 M. Anugraham, F. Jacob, S. Nixdorf, A. V. Everest-Dass, V. Heinzelmann-Schwarz, N. H. Packer, *Mol. Cell. Proteomics* **2014**, *13*, 2213.
- 44 M. Karas, F. Hillenkamp, *Anal. Chem.* **1988**, *60*, 2299.
- 45 a) C. Menzel, K. Dreisewerd, S. Berkenkamp, F. Hillenkamp, *J. Am. Soc. Mass Spectrom.* **2002**, *13*, 975; b) T. W. Jaskolla, M. Karas, *J. Am. Soc. Mass Spectrom.* **2011**, *22*, 976.
- 46 a) D. J. Harvey, *Mass Spectrom Rev* **2006**, *25*, 595; b) D. J. Harvey, *Mass Spectrom Rev* **2008**, *27*, 125; c) D. J. Harvey, *Mass Spectrom Rev* **2009**, *28*, 273; d) D. J. Harvey, *Mass Spectrom Rev* **2011**, *30*, 1; e) D. J. Harvey, *Mass Spectrom Rev* **2012**, *31*, 183; f) D. J. Harvey, *Mass Spectrom Rev* **2015**, *34*, 268; g) D. J. Harvey, *Mass Spectrom Rev* **2017**, *36*, 255; h) D. J. Harvey, *Mass Spectrom Rev* **2018**, *37*, 353.
- 47 J. Zaia, *Chem. Biol.* **2008**, *15*, 881.
- 48 a) K. R. Reiding, D. Blank, D. M. Kuijper, A. M. Deelder, M. Wührer, *Anal Chem* **2014**, *86*, 5784; b) M. R. Bladergroen, K. R. Reiding, A. Hipgrave Ederveen, G. C. Vreeker, F. Clerc, S. Holst, A. Bondt, M. Wührer, Y. E. van der Burgt, *J. Proteome Res.* **2015**, *14*, 4080.
- 49 E. Machado, S. Kandzia, R. Carilho, P. Altevogt, H. S. Conradt, J. Costa, *Glycobiology* **2011**, *21*, 376.
- 50 S. Domcke, R. Sinha, D. A. Levine, C. Sander, N. Schultz, *Nat. Commun.* **2013**, *4*, 2126.
- 51 R. Saldova, L. Royle, C. M. Radcliffe, U. M. Abd Hamid, R. Evans, N. Arnold, R. E. Banks, R. Hutson, D. J. Harvey, R. Antrobus, M. Petrescu, R. A. Dwek, P. M. Rudd, *Glycobiology* **2007**, *17*, 1344.
- 52 G. S. Leiserowitz, C. Lebrilla, S. Miyamoto, H. J. An, H. Duong, Kirmiz, B. Li, H. Liu, K. S. Lam, *Int J Gynecol Cancer* **2008**, *18*, 470.
- 53 R. Saldova, H. Piccard, M. Perez-Garay, D. J. Harvey, W. B. Struwe, C. Galligan, N. Berghmans, S. F. Madden, R. Peracaula, G. Opde-nacker, P. M. Rudd, *PLoS One* **2013**, *8*, e71159.
- 54 S. Hua, C. C. Williams, L. M. Dimapasoc, G. S. Ro, S. Ozcan, S. Miyamoto, C. B. Lebrilla, H. J. An, G. S. Leiserowitz, *J. Chromatogr. A* **2013**, *1279*, 58.
- 55 K. Biskup, E. I. Braicu, J. Sehouli, C. Fotopoulou, R. Tauber, M. Berger, Blanchard, *J. Proteome Res.* **2013**, *12*, 4056.
- 56 K. Biskup, E. I. Braicu, J. Sehouli, R. Tauber, V. Blanchard, *Dis Markers* **2014**, *2014*, 238197.
- 57 J. H. Kim, C. W. Park, D. Um, K. H. Baek, Y. Jo, H. An, Y. Kim, T. J. Kim, *Dis Markers* **2014**, *2014*, 634289.
- 58 X. Zhang, Y. Wang, Y. Qian, X. Wu, Z. Zhang, X. Liu, R. Zhao, L. Zhou, Y. Ruan, J. Xu, H. Liu, S. Ren, C. Xu, J. Gu, *PLoS One* **2014**, *9*, e87978.
- 59 K. Kim, L. R. Ruhaak, U. T. Nguyen, S. L. Taylor, L. Dimapasoc, C. Williams, C. Stroble, S. Ozcan, S. Miyamoto, C. B. Lebrilla, G. S. Leiserowitz, *Cancer Epidemiol Biomarkers Prev* **2014**, *23*, 611.
- 60 E. S. Hecht, E. H. Scholl, S. H. Walker, A. D. Taylor, W. A. Cliby, A. A. Motsinger-Reif, D. C. Muddiman, *J. Proteome Res.* **2015**, *14*, 4394.
- 61 K. Biskup, E. I. Braicu, J. Sehouli, R. Tauber, V. Blanchard, *J. Proteomics* **2017**, *157*, 33.
- 62 H. Allam, K. Aoki, B. B. Benigno, J. F. McDonald, S. G. Mackintosh, Tiemeyer, K. L. Abbott, *J. Proteome Res.* **2015**, *14*, 434.

- 63 M. Anugraham, F. Jacob, A. V. Everest-Dass, A. Schoetzau, S. Nixdorf, N. F. Hacker, D. Fink, V. Heinzelmann-Schwarz, N. H. Packer, *Mol Oncol* **2017**, *11*, 1595.
- 64 H. Chen, Z. Deng, C. Huang, H. Wu, X. Zhao, Y. Li, *Tumour Biol* **2017**, *39*, 1010428317716249.
- 65 R. L. Caldwell, R. M. Caprioli, *Mol. Cell. Proteomics* **2005**, *4*, 394.
- 66 J. O. Gustafsson, M. K. Oehler, A. Ruskiewicz, S. R. McColl, P. Hoffmann, *Int. J. Mol. Sci.* **2011**, *12*, 773.
- 67 P. M. Angel, R. M. Caprioli, *Biochemistry* **2013**, *52*, 3818.
- 68 R. Casadonte, R. M. Caprioli, *Nat. Protoc.* **2011**, *6*, 1695.
- 69 A. V. Everest-Dass, M. T. Briggs, G. Kaur, M. K. Oehler, P. Hoffmann, N. H. Packer, *Mol. Cell. Proteomics* **2016**, *15*, 3003.
- 70 A. V. Everest-Dass, J. L. Abrahams, D. Kolarich, N. H. Packer, M. P. Campbell, *J. Am. Soc. Mass Spectrom.* **2013**, *24*, 895.
- 71 U. K. Ballehaninna, R. S. Chamberlain, *Indian J Surg Oncol* **2011**, *2*, 88.
- 72 S. Singh, K. Pal, J. Yadav, H. Tang, K. Partyka, D. Kletter, P. Hsueh, E. Ensink, B. Kc, G. Hostetter, H. E. Xu, M. Bern, D. F. Smith, A. S. Mehta, R. Brand, K. Melcher, B. B. Haab, *J. Proteome Res.* **2015**, *14*, 2594.
- 73 X. Chen, Y. Nagai, Z. Zhu, H. Ruan, D. M. Peehl, M. I. Greene, H. Zhang, *Oncotarget* **2018**, *9*, 3631.
- 74 R. D. Cummings, M. E. Etzler, in *Essentials of Glycobiology*, (Eds: nd, A. Varki, R. D. Cummings, J. D. Esko, H. H. Freeze, P. Stanley, C. R. Bertozzi, G. W. Hart, M. E. Etzler), Cold Spring Harbor Laboratory Press, Cold Spring Harbor, NY **2009**.
- 75 H. Ghazarian, B. Itoni, S. B. Oppenheimer, *Acta Histochem.* **2011**, *113*, 236.
- 76 S. A. Brooks, D. M. Hall, *Methods Mol Biol* **2012**, *878*, 31.
- 77 L. L. Lairson, B. Henrissat, G. J. Davies, S. G. Withers, *Annu. Rev. Biochem.* **2008**, *77*, 521.
- 78 S. Pan, R. Chen, R. Aebersold, T. A. Brentnall, *Mol. Cell. Proteomics* **2011**, *10*, R110 003251.
- 79 D. C. Dallas, W. F. Martin, S. Hua, J. B. German, *Brief Bioinform* **2013**, *14*, 361.
- 80 T. W. Powers, B. A. Neely, Y. Shao, H. Tang, D. A. Troyer, A. S. Mehta, B. B. Haab, R. R. Drake, *PLoS One* **2014**, *9*, e106255.
- 81 S. A. Melo, L. B. Luecke, C. Kahlert, A. F. Fernandez, S. T. Gammon, J. Kaye, V. S. LeBleu, E. A. Mittendorf, J. Weitz, N. Rahbari, C. Reissfelder, C. Pilarsky, M. F. Fraga, D. Piwnica-Worms, R. Kalluri, *Nature* **2015**, *523*, 177.
- 82 J. W. Pedersen, A. Gentry-Maharaj, A. Nostdal, E. O. Fourkala, A. Dawnay, M. Burnell, A. Zaikin, J. Burchell, J. T. Papadimitriou, H. Clausen, I. Jacobs, U. Menon, H. H. Wandall, *Int. J. Cancer* **2014**, *134*, 2180.
- 83 C. D. Rillahan, J. C. Paulson, *Annu. Rev. Biochem.* **2011**, *80*, 797.

This page is intentionally left blank

1.3 | Aims

This PhD project aimed to further develop our established *N*-glycan MALDI mass spectrometry imaging workflow for other FFPE tissues, such as knee osteoarthritis, where there is difficulty with adherence to slides. Modifying this method also allowed us to investigate the *N*-glycosylation patterns of cartilage and bone marrow, which previously had not been characterised, in order to obtain a better understanding of disease progression.

Furthermore, this PhD project aimed to investigate the ovarian cancer *N*-glycome through spatially mapping FFPE tissue sections from both early- and late-stage patients. Using MALDI-MSI, it was possible to compare intrapatient regions, such as tumour, stroma, adipose and necrotic regions, from late-stage ovarian cancer tissue sections, and interpatient regions, such as tumour regions, from early- and late-stage ovarian cancer tissue sections.

To summarise, this thesis aimed to:

- 1 | Develop *N*-glycan MALDI mass spectrometry imaging for FFPE knee osteoarthritis tissue.
- 2 | Investigate the intrapatient variation of late-stage ovarian cancer tissues using *N*-glycan MALDI mass spectrometry imaging.
- 3 | Investigate the interpatient variation of early- and late-stage ovarian cancer tissues using *N*-glycan MALDI mass spectrometry imaging.

Long-term, this PhD project aims to discover potential diagnostic or prognostic markers which will improve stratification strategies and effective regimens for ovarian cancer patients.

This page is intentionally left blank

Chapter 2 | Materials and Methods



2.1 | Summary

Our group was the first group to combine complimentary mass spectrometry (MS) techniques to both spatially map and comprehensively characterise the *N*-glycome. We assigned *N*-glycan structures, confirmed by PGC-LC-ESI-MS/MS, to tissue-specific regions of FFPE murine kidney that were visualised by MALDI-MSI. For example, the oligomannose *N*-glycan $(\text{Hex})_6 + (\text{Man})_3(\text{GlcNAc})_2$ was observed in the medulla region while the fucosylated complex *N*-glycan $(\text{Hex})_2(\text{HexNAc})_3(\text{Deoxyhexose})_3 + (\text{Man})_3(\text{GlcNAc})_2$ was observed in the cortex region. More recently, this workflow was applied to FFPE tissue sections from late-stage ovarian cancer patients and then published as a protocol paper in *Rapid Communications in Mass Spectrometry*. This chapter presents this protocol paper and provides a step-by-step guide to its readers on how to establish our *N*-glycan MALDI-MSI workflow in their laboratory.

This page is intentionally left blank

2.2 | Statement of Authorship

Title of Paper	<i>N</i> -glycan matrix-assisted laser desorption/ionization mass spectrometry imaging protocol for formalin-fixed paraffin-embedded tissues
Publication Status	<input checked="" type="checkbox"/> Published <input type="checkbox"/> Accepted for Publication <input type="checkbox"/> Submitted for Publication <input type="checkbox"/> Unpublished and Unsubmitted work written in manuscript style
Publication Details	<u>Matthew T Briggs</u> , Yin Ying Ho, Gurjeet Kaur, Martin K Oehler, Arun V Everest-Dass, Nicolle H Packer, Peter Hoffmann: <i>N-glycan matrix-assisted laser desorption/ionization mass spectrometry imaging protocol for formalin-fixed paraffin-embedded tissues</i> . Rapid Communications in Mass Spectrometry 03/2017;, DOI:10.1002/rcm.7845

Principal Author

Name of Principal Author (Candidate)	Matthew T. Briggs
Contribution to the Paper	Conceived the project Data collection and analysis Prepared figures and wrote the main manuscript text
Overall percentage (%)	80%
Certification:	This paper reports on original research I conducted during the period of my Higher Degree by Research candidature and is not subject to any obligations or contractual agreements with a third party that would constrain its inclusion in this thesis. I am the primary author of this paper.
Signature	<div style="border-bottom: 1px solid black; width: 100%;"></div> <div style="display: flex; justify-content: space-between; border-top: 1px solid black; padding-top: 5px;"> Date 05/07/18 </div>

Co-Author Contributions

By signing the Statement of Authorship, each author certifies that:

- i. the candidate's stated contribution to the publication is accurate (as detailed above);
- ii. permission is granted for the candidate to include the publication in the thesis; and
- iii. the sum of all co-author contributions is equal to 100% less the candidate's stated contribution.

Name of Co-Author	Yin Ying Ho		
Contribution to the Paper	Conceived the project Wrote sections of the main manuscript text		
Signature		Date	12/12/17

Name of Co-Author	Gurjeet Kaur		
Contribution to the Paper	Annotated the H&E stained FFPE sections		
Signature		Date	13/12/17

Name of Co-Author	Martin K. Oehler		
Contribution to the Paper	Provided the ovarian tissue samples		
Signature		Date	12/12/17

Name of Co-Author	Arun V. Everest-Dass		
Contribution to the Paper	Conceived the project Data collection and analysis Prepared figures		
Signature		Date	12/12/17

Name of Co-Author	Nicolle H. Packer		
Contribution to the Paper	Conceived the project Designed the experiments and supervised the research		
Signature		Date	18/04/18

Name of Co-Author	Peter Hoffmann		
Contribution to the Paper	Conceived the project Designed the experiments and supervised the research		
Signature		Date	20/12/17

This page is intentionally left blank

N-Glycan matrix-assisted laser desorption/ionization mass spectrometry imaging protocol for formalin-fixed paraffin-embedded tissues

Matthew T. Briggs^{1,2}, Yin Ying Ho¹, Gurjeet Kaur³, Martin K. Oehler^{4,5}, Arun V. Everest-Dass^{6,7}, Nicolle H. Packer^{6,7}  and Peter Hoffmann^{1,2*} 

¹Adelaide Proteomics Centre, School of Biological Sciences, University of Adelaide, Adelaide, Australia, 5005

²Institute for Photonics and Advanced Sensing (IPAS), University of Adelaide, Adelaide, Australia, 5005

³Institute for Research in Molecular Medicine (INFORMM), Universiti Sains Malaysia, Pulau Pinang, Malaysia

⁴Department of Gynaecological Oncology, Royal Adelaide Hospital, Adelaide, South Australia, 5005, Australia

⁵Robinson Institute, University of Adelaide, Adelaide, Australia, 5005

⁶ARC Centre for Nanoscale BioPhotonics (CNBP), University of Adelaide, Adelaide, Australia, 5005

⁷Biomolecular Frontiers Research Centre, Macquarie University, Sydney, Australia, 2109

RATIONALE: Matrix-assisted laser desorption/ionization mass spectrometry imaging (MALDI-MSI) of the proteome of a tissue has been an established technique for the past decade. In the last few years, MALDI-MSI of the *N*-glycome has emerged as a novel MALDI-MSI technique. To assess the accuracy and clinical significance of the *N*-linked glycan spatial distribution, we have developed a method that utilises MALDI-MSI followed by liquid chromatography coupled to tandem mass spectrometry (LC/MS/MS) in order to assign glycan structures to the differentiating MALDI-MSI glycan masses released from the tissue glycoproteins.

METHODS AND RESULTS: Our workflow presents a comprehensive list of instructions on how to (i) apply MALDI-MSI to spatially map the *N*-glycome across formalin-fixed paraffin-embedded (FFPE) clinical samples, (ii) structurally characterise *N*-glycans extracted from consecutive FFPE tissue sections by LC/MS/MS, and (iii) match relevant *N*-glycan masses from MALDI-MSI with confirmed *N*-glycan structures determined by LC/MS/MS.

CONCLUSIONS: Our protocol provides groups that are new to this technique with instructions how to establish *N*-glycan MALDI-MSI in their laboratory. Furthermore, the method assigns *N*-glycan structural detail to the masses obtained in the MALDI-MS image. Copyright © 2017 John Wiley & Sons, Ltd.

Cells form tissues via a variety of highly specific and distinctive cell adhesion mechanisms typically involving adhesion receptors, cell-extracellular matrix (ECM) proteins and cytoplasmic peripheral membrane proteins. Cell adhesion receptors comprise transmembrane proteins which are glycosylated, specifically *N*-linked glycosylated. *N*-Glycosylation is the principal chemical modification that involves a series of catalytic processes where carbohydrates (i.e. glycans) are attached to proteins. The biosynthesis of glycoproteins is not guided by a template as is DNA, RNA and protein synthesis, and as such is a factor contributing to the enormous complexity of the *N*-glycoproteome. It is referred to as *N*-linked glycosylation because the addition of *N*-linked glycans occurs on the asparagine residue in the tripeptide sequence of Asn-X-Serine/Threonine (Ser/Thr) (where X is any amino acid except Pro),^[1] and, in a small number of cases, *N*-linked glycans have also been identified

on peptides with Asn-X-Cysteine (Cys) sequons.^[2–5] The biosynthesis of *N*-linked glycans begins in the rough ER with a dolichol phosphate-activated sugar as precursor and, in a sequential manner, a structure containing two *N*-acetylglucosamine (GlcNAc), nine mannose (Man) and three glucose (Glc) (Glc₃Man₉GlcNAc₂) is synthesised and subsequently transferred to a growing polypeptide chain in both prokaryotes and eukaryotes. From the ER into the Golgi apparatus and then to the cytoplasm, the *N*-linked glycans in vertebrates undergo processes such as trimming of the terminal monosaccharide residues and re-glycosylation with fucose (Fuc), sialic acid (SA), *N*-acetylglucosamine (GlcNAc) and galactose (Gal). The unique and specific structures of *N*-linked glycans play important roles in regulating signal transduction and cell functions such as growth, migration, differentiation and tumour progression.^[6,7] They have been increasingly considered as cancer biomarkers for early detection and disease prognosis since the altered glycan structures produced have been found to adversely affect cell adhesion, migration and tumour invasion.^[7–9] For example, in colorectal carcinoma an α -2,6-sialylated galactose epitope on carcinoembryonic antigen (CEA) is abundant compared with normal faecal antigen-2, a normal counterpart of

* Correspondence to: P. Hoffmann, Adelaide Proteomics Centre, School of Biological Sciences, University of Adelaide, Adelaide, Australia, 5005.

CEA.^[10,11] An increase in α -2,6-sialylation in colorectal carcinoma is usually a consequence of increase in α -2,6-sialyltransferase activity.^[12] In other malignancies such as ovarian cancer, *N*-linked glycans are of particular interest because structural alterations have been observed in the tumour microenvironment that promote tumour invasion and metastasis. Two sialylated isomeric structures of glycans, where the terminal galactose residues of core fucosylated biantennary *N*-glycans with either a α -2,6 or α -2,3 sialic acid (*N*-acetylneuraminic acid, Neu5Ac) linked to either arm, were identified to be quantitatively different between cancerous and benign ovarian cell lines.^[13] Interestingly, the α -2,6-linked sialic acids were exclusive to the ovarian cancer cell glycoproteins.^[13] This α -2,6-sialylated structure of *N*-glycans specific to ovarian cancer could be used to delineate cancerous from benign cells as a potential specific biomarker for ovarian cancer cells in tissue.

Structural analysis of *N*-glycans released from glycoproteins is a well-established method, routinely used to identify and distinguish glycan isomers. Enzymatic release of the *N*-glycans from the protein is achieved using a commercially available enzyme PNGase F.^[14] This enzyme selectively cleaves the reducing end of GlcNAc, high mannose, hybrid and complex asparagine-linked oligosaccharides when attached to an asparagine residue on a polypeptide that is at least three amino acids long.^[15,16] PNGase F will also cleave asparagine-linked oligosaccharides when there is an α -1,6-fucose attached on the GlcNAc residue directly linked to the asparagine residue. However, PNGaseF cannot cleave asparagine-linked oligosaccharides containing an α -1,3-fucose substituent attached to the GlcNAc residue that is directly linked to the asparagine residue^[17] which is found in glycoproteins from plants and insects.^[18]

Formalin-fixed paraffin-embedded (FFPE) tissue samples have been shown to be suitable for studying the spatial distribution of proteins in a variety of diseases. It has been shown that other molecules, such as *N*-glycans, can be extracted from these archived tissues without expiration date. Matrix-assisted laser desorption/ionization mass spectrometry imaging (MALDI-MSI) thus has the ability to measure the *in situ* spatial distribution of analytes, such as *N*-glycans. However, limited methods exist for *N*-glycan MALDI-MSI on FFPE tissues. MALDI-MSI data is also limited as there is not enough detail to elucidate structural isomers. Therefore, LC/MS/MS is incorporated in our method to characterise the *N*-glycan isomers observed in the MALDI-MSI data.

Liquid chromatography coupled to tandem mass spectrometry (LC/MS/MS) has evolved to be a powerful tool in characterising glycan structures. In this methodology, glycans are released from the glycoproteins and separated by chromatography using porous graphitised carbon (PGC) that offers extra retention of hydrophilic analytes such as glycans compared with reversed-phase chromatography. Glycans with sialic acid have substantially stronger retention on PGC than neutral *N*-linked glycans. *N*-Linked glycans are synthesised as mixtures of isobaric isomers and determination of the exact structure of the *N*-glycans is crucial in characterising the unique function of glycans. This structural elucidation of glycans requires the determination of monosaccharide sequence, linkage type between monosaccharide residues and their anomeric configuration.

The use of high-performance liquid chromatography (HPLC) and MS is increasingly popular in obtaining structural information from underivatised released glycan samples.^[14,19–21] Both electrospray ionization mass spectrometry (ESI-MS) and MALDI-MS are commonly used to characterise the glycans enzymatically cleaved from glycoprotein samples. MALDI-MS of permethylated glycans is also used for detecting glycans in the higher mass range and has higher tolerance to contaminants.^[22,23]

Permethylation is a chemical reaction replacing hydrogens on hydroxyl groups, amine groups and carboxyl groups with methyl groups. This process has shown to enhance ionisation efficiency by up to 20-fold.^[24,25] With tandem mass spectrometry, not only can the cleavage of glycosidic bonds be observed, but the cross-ring cleavages at the monosaccharide linkages can also be assigned, which is extremely useful for the structural characterisation of oligosaccharides.^[26] LC/MALDI-MS is possible whereby the glycan sample is separated by HPLC and then spotted directly onto the MALDI target plate. In LC/MS/MS, glycan samples can be directly loaded onto the PGC column and eluted for identification and detailed structural characterisation. The reducing end of cleaved glycans, i.e. the GlcNAc residue of released *N*-glycans, is readily reduced with sodium borohydride under alkaline conditions to remove separation of the reducing end alpha and beta structural glycan isomers on PGC-HPLC that complicate analysis. Reducing the *N*-glycans after release from the proteins also prevents degradative peeling reactions and provides a way to 'tag' the reducing end of oligosaccharides simultaneously.

Combining MALDI-MSI and subsequent LC/MS/MS using PGC chromatography has been successfully applied not only for the identifications of glycans from FFPE tissue of murine kidney, osteoarthritis and ovarian cancer tissue, but also the location and distribution of these glycans on tissue sections.^[27–30] It was found that high mannose glycans were significantly abundant in the tumour region whereas complex bi-antennary and tri-antennary were predominantly in the stromal region of ovarian cancer. This technique has clearly demonstrated the potential of obtaining glycan spatial information and structural identity from FFPE tissue samples in biomarker discovery experiments.

Here, we provide a detailed protocol for MALDI-MSI followed by LC/MS/MS structural determination of *N*-glycan masses released from glycoproteins in FFPE tissue sections, based on optimised methods from our proof-of-principle papers.^[19,27] The protocols can also be applied in the reverse direction where the LC/MS/MS analysis of the released glycans from microdissected regions of the FFPE tissue sections can provide the differentiating structure-specific glycan masses on which targeted MALDI-MSI experiments can be based. The advantages of these protocols are easy sample handling, excellent reproducibility, the ability to demonstrate glycan molecular spatial distributions *in situ*, assignment of glycan structure(s) to mass and compatibility with high-throughput image analysis. It is expected that these approaches can rapidly be used to validate, and eventually replace, the traditional human-skills-based assessment of haematoxylin and eosin (H&E)-stained FFPE pathology slides.

EXPERIMENTAL

Chemicals, consumables and equipment

See Table 1 for a comprehensive list of chemicals, consumables and equipment used in this protocol.

1. PROTOCOL-SPECIFIC SOLUTIONS

1.1. Tissue collection

The tissue is fixed in 4% (v/v) neutral-buffered formalin (Sigma-Aldrich) at room temperature, processed with an automatic processor and embedded in paraffin wax. Fixation in formalin usually takes between 12 and 24 h depending on the tissue size. Formalin penetrates tissue at a rate of approximately 1 mm/h.^[31] FFPE tissue can be stored at room temperature.

1.2. Xylene and ethanol solutions

Set up four glass Coplin jars (EMS), two with 100% (v/v) xylene (Merck, Australia) and two with 100% (v/v) ethanol (EtOH, Merck, Australia). Prepare these solutions fresh before the start of the experiment and discard them in waste at the end so that there is no contamination.

1.3. 10 mM Ammonium bicarbonate solution

Weigh out 0.3953 g of ammonium bicarbonate (NH₄CO₃, Merck, UK) to make 100 mM in a 50-mL Falcon tube (Corning). To make 10 mM ammonium bicarbonate, take 50 mL of this 100 mM solution and add 450 mL of water.

1.4. 10 mM Citric acid monohydrate solution

Weigh out 1.05 g of citric acid (Sigma-Aldrich, Japan) into a 500-mL measuring cylinder and add 480 mL water. Add a magnetic stirrer and stir while adding 12 mL of 1 M sodium hydroxide (NaOH, Merck, Germany). Then, measure the pH and add enough 1 M NaOH to reach pH 6.0. Make up the volume to 500 mL with water to make the 10 mM solution.

1.5. Calibration solution

Dilute the three *N*-glycan standards (see Table 2) to 1 pmol/μL and mix together in a 0.5-mL microcentrifuge tube. Store the aliquots in a freezer at -80°C.

1.6. Matrix solution

To prepare 20 mg/mL of 2,5-dihydroxybenzoic acid (DHB, Sigma-Aldrich, USA) in 1 mM sodium chloride (NaCl, Merck, Germany) and 0.1% (v/v) trifluoroacetic acid (TFA, Merck, Germany) matrix solution, first make 100 mM NaCl and 10% (v/v) TFA in 1.5-mL microcentrifuge tubes. Then, weigh out 100 mg of DHB to make 5 mL of matrix solution in a 15-mL Falcon tube and add water. Sonicate the solution for 30 min. Following sonication, add 1:100 dilution of 100 mM NaCl and 10% (v/v) TFA solutions made previously.

Figure 1 shows a workflow of *N*-glycan MALDI-MSI on FFPE tissues. Our group uses the Chemical Inkjet Printer (ChIP-1000, Shimadzu) and the HTX TM-Sprayer (HTX

Technologies) to apply PNGase F and DHB matrix, respectively. If alternative instruments are used, such as the ImagePrep (Bruker Daltonics) and SunCollect (SunChrom, Friedrichsdorf, Germany), the conditions need to be further tested and optimised. If a commercially available PNGase F is used, the ChIP-1000 is preferred as it requires lower loading volumes of the enzyme, and this is more cost-effective.

2. FFPE TISSUE SECTIONING

2.1. Fill the water bath (Leica HistoBath HI1210, Leica Instruments) with water and set the temperature to 39°C.

- Do not set the temperature of the water too high or the paraffin will melt, thus making it more difficult to mount the tissue sections.

2.2. Place the FFPE block onto the Microtome (Microm HM325, Zeiss) and adjust the angle of the holder appropriately. The microtome blade should be positioned parallel with the FFPE block.

2.3. Clean a microtome blade (35 × 80 mm, Feather Safety Razor Co.) with methanol and insert it into the holder.

2.4. Adjust the tissue thickness to between 4 and 10 μm and start sectioning.

- Tissue thickness is dependent on the FFPE sample and the experiment. Our group has selected an optimised thickness of 6 μm.

2.5. Mount the tissue sections in the water bath onto indium tin oxide (ITO)-coated conductive slides (Bruker Daltonics) or PEN membrane slides (MicroDissect) by guiding the slides underneath the tissue sections and lifting upwards.

- Make sure to mount the tissue sections in one smooth motion in order to prevent any folds or air bubbles forming.

2.6. Tap the slides gently in a vertical, upright position onto lint-free wipes.

2.7. Place the slides into a container inside a 37°C room for 1 h.

2.8. Store the slides at 4°C until use.

3. FFPE TISSUE SAMPLE PREPARATION

3.1. Lay the ITO-coated conductive slides, with the tissue facing up, on a heating block at 60°C for 1 h.

- Heating melts the paraffin, thereby improving tissue adherence to the slides.

Table 1. List of chemicals, consumables, calibrants and equipment required for the workflow that is outlined in this publication

Chemicals and consumables	Company	Product code
2,5-Dihydroxybenzoic acid (DHB)	Sigma-Aldrich (St. Louis, MO, USA)	Cat. No. 149357 – 10 g
Ammonium bicarbonate (NH ₄ HCO ₃)	Merck (Poole, UK)	Cat. No. 103025E – 1 kg
Ammonium acetate (NH ₄ CH ₃ CO ₂)	Merck (Darmstadt, Germany)	Cat. No. 1.01116.0500
Cation exchange resin (AG 50 W X8)	Bio-Rad (Hercules, CA, USA)	Cat. No. 142-1431
Citric acid monohydrate	Sigma-Aldrich (Tokyo, Japan)	Cat. No. C0706 – 500 g
Ethanol (EtOH)	Merck (Frenchs Forest, NSW, Australia)	Cat. No. 4.10230.2511
Eosin Y	ProSciTech (Kirwan, QLD, Australia)	Cat. No. C0971
Formalin solution, neutral buffered (10%)	Sigma-Aldrich (Darmstadt, Germany)	Cat. No. HT501128-4L
Glacial acetic acid	Merck (Germany)	Cat. No. 1.0063.2511
32% Hydrochloric acid (HCl)	Merck (Germany)	Cat. No. 1.00319.2511
Isopropanol	Merck (Germany)	Cat. No. 1.01040.2500
Mayer's haematoxylin	ProSciTech (Australia)	Cat. No. AMH-500
Methanol (MeOH)	Merck (Germany)	Cat. No. 1.06018.2500
Peptide-N-glycosidase F (PNGase F, glycerol-free, 75, 000 units)	New England Biolabs (Hitchin, UK)	Cat. No. P0705L
Peptide-N-glycosidase F (PNGase F)	Roche (Mannheim, Germany)	Cat. No. 11365185001
Potassium hydroxide (KOH)	Sigma-Aldrich (USA)	Cat. No. 484016 – 1 kg
Sodium borohydride (NaBH ₄)	Sigma-Aldrich (USA)	Cat. No. 1001430785
Sodium chloride (NaCl)	Merck (Germany)	Cat. No. 1.06404.0500 – 500 g
Sodium hydroxide (NaOH)	Merck (Germany)	Cat. No. 1.06498.0500
Trifluoroacetic acid (TFA)	Merck (Germany)	Cat. No. 1.08262.0100
Water (H ₂ O, ultrapure, ≥18.2 MΩ from Barnstead purifier)	Barnstead International (Dubuque, IA, USA)	Cat. No. D11951
Water-soluble Tipp-Ex	BIC (Eschborn, Germany)	Cat. No. 8806821
Xylene	Merck (Australia)	Cat. No. 1.08681.2500
Equipment	Company	
CanoScan 5600 F	Canon (Taipei, Taiwan)	
Chemical inkjet printer (ChIP-1000)	Shimadzu (Kyoto, Japan)	
Falcon tubes (15 mL)	Corning (Nueva Leon, Mexico)	
Falcon tubes (50 mL)	Corning (Mexico)	
Fume hood	Air Science (Fort Myers, FL, USA)	
Glass Coplin staining jars	EMS (Hatfield, PA, USA)	
Glass rectangular staining dishes	EMS (USA)	
HTX TM-Sprayer	HTX Technologies, LLC (Chapel Hill, NC, USA)	
Indium tin oxide (ITO)-coated conductive slides	Bruker Daltonics (Bremen, Germany)	
Kimwipes	Kimtech (Milsons Point, Australia)	
Leica AS LCM microscope	Leica Instruments (Wetzlar, Germany)	
Leica HistoBath HI1210	Leica Instruments (Germany)	
Mass spectrometer (e.g. ultrafleXtreme)	Bruker Daltonics (Germany)	
Mass spectrometric data acquisition software (e.g. flexControl and flexImaging)	Bruker Daltonics (Germany)	
Mass spectrometric data analysis software (e.g. flexImaging or SCiLS Lab)	Bruker Daltonics (Germany)	
Microcentrifuge tubes (safe-lock tubes, 0.5 mL)	Eppendorf (Macquarie Park, NSW, Australia)	
Microcentrifuge tubes (safe-lock tubes, 1.5 mL)	Eppendorf (Australia)	
Microm HM325 microtome	Zeiss (Oberkochen, Germany)	
MTP slide adaptor II	Bruker Daltonics (Germany)	
NanoZoomer automated microscope	Hamamatsu (Beijing, China)	
Nitrocellulose dialysis membrane (0.025 μm)	Millipore (Bayswater, VIC, Australia)	

(Continues)

Table 1. (Continued)

Equipment	Company
OSV Pack Assay (50)	Shimadzu (Japan)
PEN membrane slides	MicroDissect (Herborn, Germany)
Personal protective wear (e.g. gloves)	MicroFlex (Malaysia)
Piezo assay	Shimadzu (Japan)
SpeedVac concentrator	Savant SVC 100 (Thermo Scientific, Waltham, MA, USA)
Stainless steel cryotome blades (35 × 80 mm)	Feather Safety Razor Co. (Osaka, Japan)
Temperature-controlled water bath	Scientific Equipment Manufacturers (Thebarton, SA, Australia)
UFLC XR (LC pump)	Shimadzu (Japan)
ZipTip C18	Millipore (Australia)

3.2. Set a water bath to 70°C.

3.3. Wash the slides with 100% xylene twice for 5 min to remove the paraffin. Place the slides vertically in the Coplin jar (see section 1.2. for instructions).

3.4. Wash the slides with 100% EtOH twice for 2 min to remove the xylene and allow the slides to dry.

3.5. Wash the slides with 10 mM NH₄HCO₃ twice for 5 min to rehydrate the tissue (see section 1.3. for instructions).

3.6. Place one of the slides in a 50-mL Falcon tube with 10 mM citric acid monohydrate at pH 6.0 (see section 1.4. for instructions).

3.7. Place the 50-mL Falcon tube in the water bath heated to 70°C for 3 h.

3.8. Remove the slide from the Falcon tube and leave in a MTP AnchorChip box (Bruker Daltonics) to cool to room temperature.

3.9. Wash the slides with 10 mM NH₄HCO₃ twice for 1 min to get the tissue back to pH 8.0 (see section 1.3. for instructions).

3.10. Dry the slide at room temperature in a MTP AnchorChip box (Bruker Daltonics).

4. ENZYME DIALYSIS

The enzyme is dialysed prior to its application due to the salt content, which can affect MALDI-MS ionisation.

4.1. During step 3.7. fill a 1-L beaker with water (H₂O, ultrapure, ≥18.2 Ω from Barnstead).

4.2. Float a nitrocellulose membrane (0.025 μm pore size, Millipore) on top of the water.

4.3. Load 40 μL of Peptide-N-glycosidase F (PNGase F, New England Biolabs) on top of the nitrocellulose membrane (0.025 μm pore size, Millipore) and dialyse for 2 h.

- Make sure to use a glycerol-free PNGase F as there are no cleaning steps prior to the MALDI-MSI acquisition. Be careful when selecting PNGase F as different suppliers provide PNGase F with different activities.

4.4. Remove the PNGase F by pipetting, estimating the volume removed, and pipette into a microfuge tube.

4.5. Add 25 mM NH₄HCO₃ to obtain a total volume of 200 μL.

4.6. Store the dialysed PNGase F at 4°C until use (no longer than a day).

5. ENZYME APPLICATION

5.1. Turn on the chemical inkjet printer (ChIP-1000, Shimadzu) and vacuum pump.

- Make sure that the vacuum pump is connected to the ChIP-1000.

Table 2. *N*-glycan standard mixture (GLY3; Prozyme, Hayward, CA, USA) used for calibration of the MALDI-TOF/TOF MS instrument

<i>N</i> -Glycan composition	[M]	[M + Na ⁺] ⁺
Man ₅ GlcNAc ₂	1234.4333	1257.4225
Man ₃ GlcNAc ₅	1519.5659	1542.5551
Man ₃ Gal ₄ GlcNAc ₆	2370.8565	2393.8457
Concentration: 1 pmol/μL		

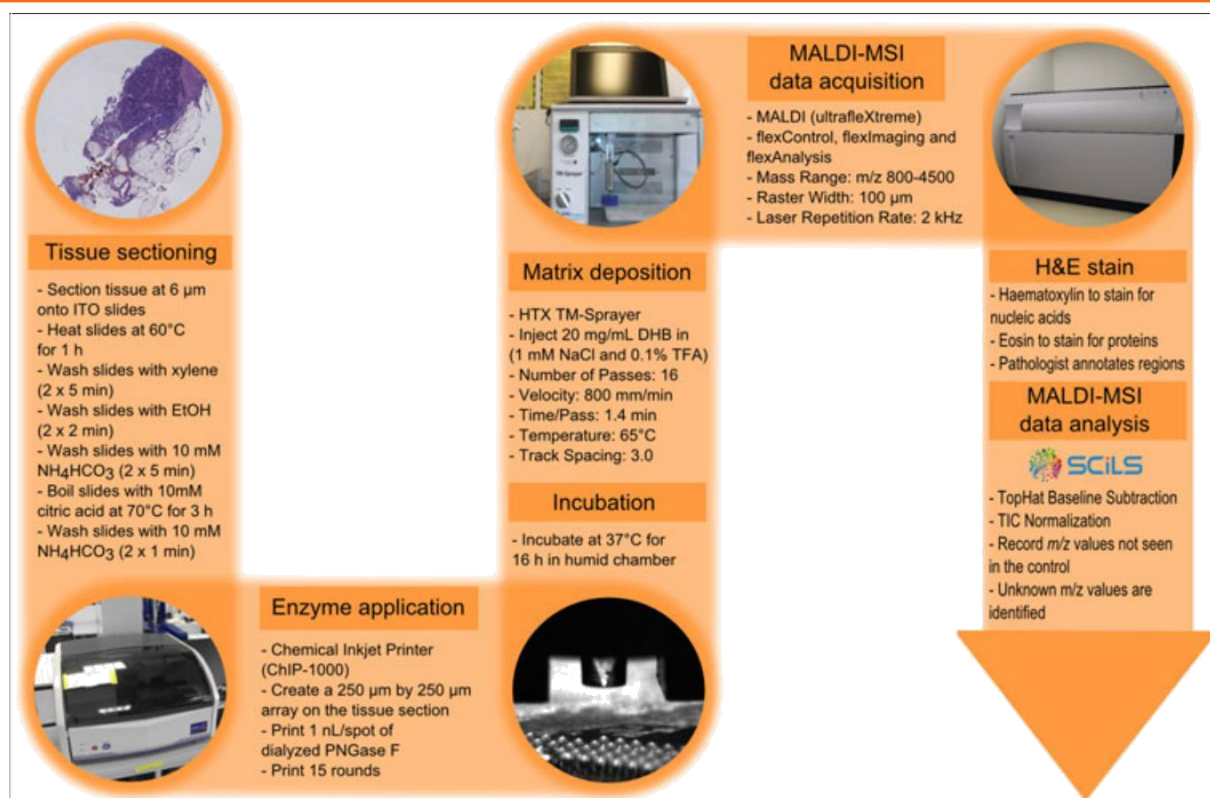


Figure 1. A workflow on how to spatially map the N-glycome by MALDI-MSI across FFPE clinical samples. First, the FFPE tissue is sectioned onto indium tin oxide (ITO)-coated slides, treated with citric acid antigen retrieval (CAAR) and digested with PNGase F to release N-glycans from glycoproteins. The PNGase F is printed using a chemical inkjet printer (ChIP-1000) to print an array across the tissue section. Secondly, dihydroxybenzoic acid (DHB) is sprayed across the tissue section using a HTX TM-Sprayer. Thirdly, mass spectra are acquired using MALDI-MS in a two-dimensional grid across the tissue section. Lastly, the data is analysed using MALDI-MSI software (SCiLS Lab, Bremen, Germany) by overlaying the image with the corresponding histological stain.

5.2. Load the slide onto the MTP slide adaptor II (Bruker Daltonics) and slide it into the left-hand slot of the stage with the tissue facing up.

5.3. Double click on the ChIP-1000 software icon found on the desktop computer connected to the ChIP-1000 by a USB cable.

5.4. Enter the UserID and Password to access the software.

5.5. Next, select the Sample icon which is located below the word Operate.

5.6. Select the Sample 1 tick box and click on Image Acquisition.

- A light will appear from the back of the instrument which is the scanner turning on and scanning the slide. Ignore all error messages, except in the case where there is no light.

5.7. Then, select the Create Area button, and click and drag to create a print area for the scanned tissue section.

5.8. Once you have created the region, an Area Setting box will appear on the screen. Enter 250 μm into the boxes labelled print pitch x and print pitch y.

- This will adjust the numbers in the boxes labelled print points of x and print points of y which tells you how many droplets are printed in the x and y axes. The maximum number of droplets for a selected area is 2000, but the instrument will still print more than this.

5.9. Select the OK button and the Stop Creating Area button.

5.10. Select Request and click on a blank box to create a process name.

5.11. Click on the box under the Job tab and select print.

5.12. Double click on the box under the heading parameter and enter in the relevant details.

- Solution: Process Name

Quantity of Solution: 15,000–30,000 pL is recommended for PNGase F printing.

Method of print (droplet interval): 0 ms per 0 drops.

5.13. Once finished, you will have to enter the **UserID** and **Password**.

5.14. Click and drag the process name that you just created onto the region of interest.

- The green region box will change to a blue grid once you have completed this step.

5.15. Now, close the **Request** box and click **Save** on the box labelled **Image Name 1**.

5.16. Enter the **Project**, **Experiment** and **Sample** details, and enter the **UserID** and **Password** after each detail is entered.

5.17. Select **Ok** and close the box.

5.18. Select **Do Process** located on the box labelled **Sample**.

- Make sure that the details of the method are correct in the next box that appears.

5.19. Select **Ok**, **Ok** and then **Skip** until you reach the window that is shown in Fig. 2.

5.20. Clean the piezoelectric printing head using MeOH (Merck, Germany) by loading 200 μ L of MeOH into the reservoir and pressing **Start** under the heading **Load Solution**.

- The loading time is usually set between 100 and 1000 ms to clean the piezoelectric printing head.

5.21. Once the reservoir is empty, twirl a lint-free wipe at the corner and clean the tip of the piezoelectric printing head.

- Make sure to watch the computer screen to see that all the MeOH is removed (there is a camera on the piezoelectric printing head).

5.22. Repeat steps 5.20. and 5.21., but with water (≥ 18.2 M Ω from Barnstead purifier) or 25 mM NH_4HCO_3 for PNGase F printing.

5.23. Next, optimize the printing conditions by clicking the **Start** button located under the heading **Test Printing** and adjust the **Dwell Voltage (V)** and **Dwell Time (μ s)**.

- There is a camera that points at the piezoelectric printing head. The camera takes multiple snapshots of test printing, thereby capturing the stability of the droplets. Optimise the

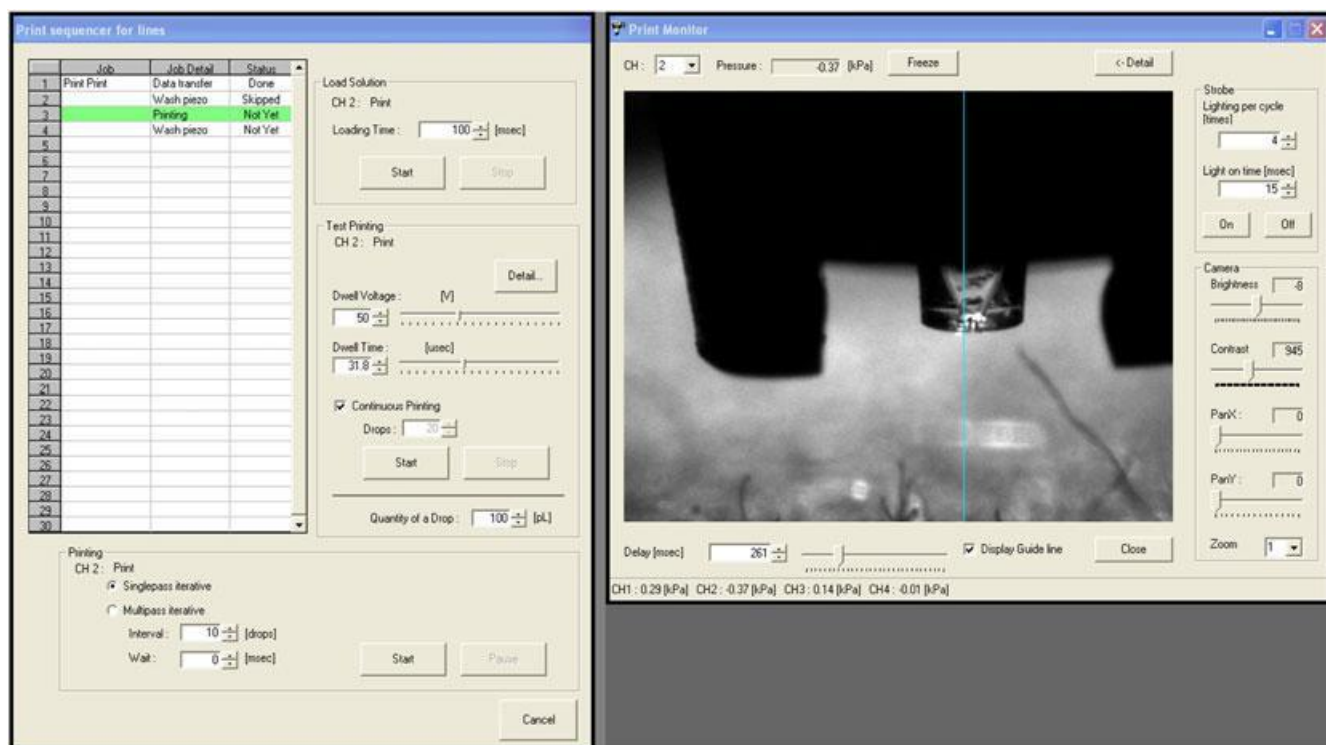


Figure 2. The Print sequencer for lines and Print Monitor interface for the Chemical Inkjet Printer (ChIP-1000). Enter the information detailed in the screenshot above and optimise the printing conditions by modifying the Dwell Voltage and Dwell Time under the Test Printing tab. View the test printing in the Print Monitor window and use the Display Guide Line to determine if the droplets are stable. Optimizing the camera Brightness and Contrast can help visualize the droplets better. Note: The ChIP-1000 is no longer commercially available.

printing conditions so that there is minimal movement and deviation of these droplets over time. Also, the Dwell Voltage and Dwell Time will have to be adjusted for every experiment.

5.24. Once the printing conditions have been optimised, add 200 μL of the dialysed PNGase F into the reservoir located above the piezoelectric printing head and click the **Start** button under the heading **Printing**.

5.25. Take the slide out of the MTP II adaptor and place it into a humid chamber (e.g. a plastic box containing wet lint-free wipes) and place it in a 37°C room for 16 h.

- Our group uses a small box that raises the slide at one end while wet lint-free wipes sit at the other end so that the slide does not get wet.

5.26. Clean the reservoir as outlined in steps 5.20. and 5.21.

5.27. On the next day, take the humid chamber out of the 37° C room and spot 1 μL of GLY3 (see Table 2) onto the control tissue region.

5.28. Mark the edges of the slides with water-based white-out to create teach marks, required later for data acquisition.

5.29. Scan the slides at 2400 dpi using a CanoScan 5600 F (Canon) scanner.

6. MATRIX DEPOSITION

DHB was optimized as a matrix for this MALDI-MSI protocol, but other matrices can be optimised in positive or negative mode to obtain comparable results.^[27–30]

6.1. Place the ITO-coated slide on the HTX TM-Sprayer (HTX Technologies) stage.

- Apply sticky tape on the edges of the slide so that the slide remains in position.

6.2. Turn on the TM-Sprayer and the nitrogen gas to 4 psi pressure.

- Make sure that the nitrogen gas is attached to the TM-sprayer.

6.3. Turn on the LC Pump (Shimadzu) and set it to a flow rate of 0.05 $\mu\text{L}/\text{min}$.

6.4. Double click on the HTX TM-Sprayer icon located on the desktop of the laptop.

6.5. Set up the TM-sprayer method by clicking on the **Spray Pattern Design** tab and enter the details shown in Fig. 3.

6.6. Click and drag to select a region of interest to be sprayed (i.e. the red grid shown in Fig. 3).

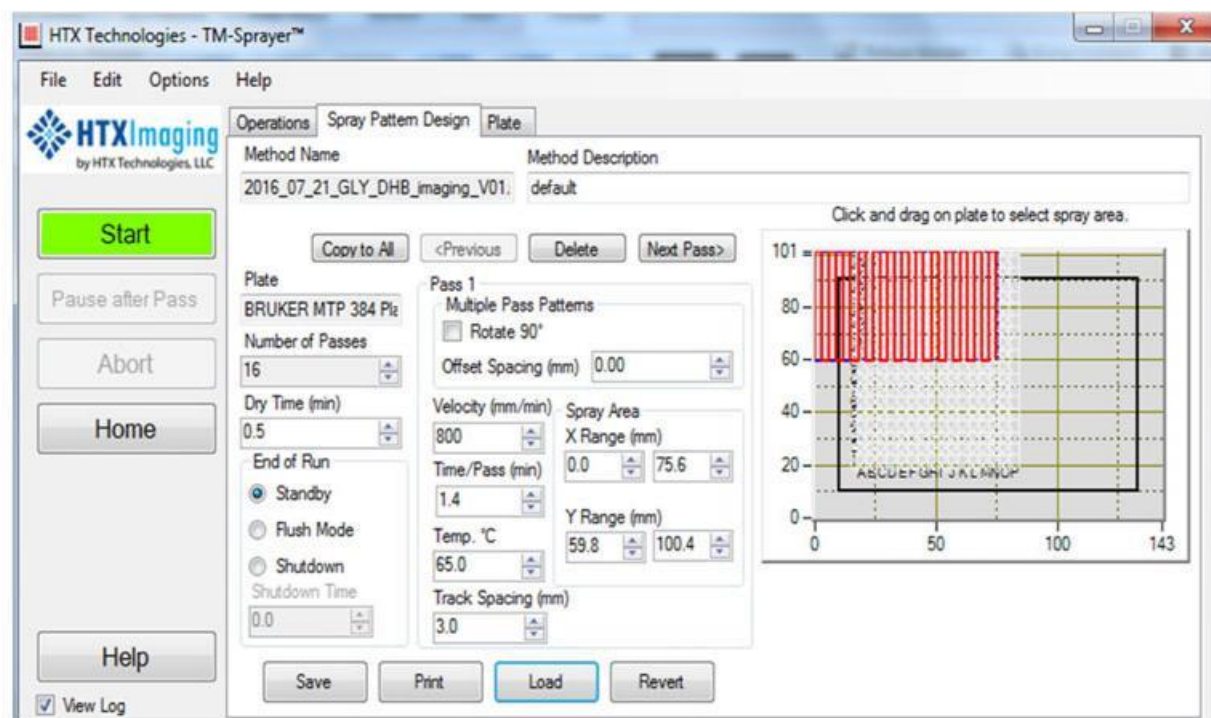


Figure 3. The Spray Pattern Design interface for the HTX TM-Sprayer. Enter the method-specific settings detailed in the screenshot above. Then, click and drag a red grid on the overview of the stage to create a region of interest for spraying.

6.7. Click **Save** to save the method with the appropriate details, and then press **Start** to load the method.

6.8. Inject 5 mL of 20 mg/mL DHB in (1 mM NaCl and 0.1% TFA) into the 5-mL sample loop using a syringe.

- Make sure that the toggle is switched to **LOAD** and not **SPRAY**.

6.9. Switch the toggle from **LOAD** to **SPRAY** and wait until the matrix moves through the sample loop and reaches the nozzle.

6.10. Now click the **Start** button on the laptop to start the run.

6.11. Once the run is complete, take the slide off the TM-Sprayer stage, insert it into a MTP slide adaptor II (Bruker Daltonics) and insert it into the MALDI-TOF/TOF mass spectrometer (ultrafleXtreme, Bruker Daltonics).

7. MALDI-MSI DATA ACQUISITION

7.1. Open the flexControl software (Bruker Daltonics) by double clicking on the icon located on the computer desktop.

7.2. Load a reflectron positive mode method in flexControl.

7.3. Optimise this loaded method for the instrument by adjusting the following settings:

- Laser power (instrument specific)
- Laser offset (instrument specific)
- Laser repetition rate (typically between 1 and 2 kHz)
- Detector gain (instrument specific)
- *m/z* measurement range (at least *m/z* 800–4500)
- Matrix suppression (700 Da, usually 100 Da below *m/z* range minimum)
- Acquisition rate (at least 1 GS/s for reflectron MS)

7.4. Open flexImaging (Bruker Daltonics) and select **create a new sequence** in the window that appears.

7.5. Enter the following details:

- Sequence name
- Data directory
- Sample preparation type (100 μ m raster width for this workflow)
- AutoXecute method (edit through flexControl)

7.6. Load the scanned image (from step 5.29) to teach the instrument where the tissue is located.

7.7. Assign the three teach marks applied earlier and then select **move sample carrier** from the edit drop down menu. Move the sample carrier to the edges of the assigned teach marks to confirm that the instrument teaching is accurate.

7.8. Move the sample carrier onto a region of tissue that has been digested with PNGase F and optimise the loaded method as detailed in step 7.3.

- An optimum laser power has been achieved when a high intensity spectrum can be acquired with 1000 accumulated shots. The intensity will be variable and can exceed 10^4 for some spectra.

7.9. Test the selected laser power on several randomly selected spots including the external calibrant.

7.10. Using the optimised method, move the sample carrier to the external calibrant.

7.11. Acquire spectra, ensuring that the peaks in the isotopic profile can be resolved to baseline.

7.12. Calibrate the instrument using the standard glycan calibration list and save the flexControl method.

7.13. Ensure that the flexControl autoXecute method contains the appropriate parameters.

- General (flexControl method only selected)
- Laser (set optimum laser power and turn fuzzy control off)
- Evaluation (should contain no background list)
- Accumulation (fuzzy control off, 1000 shots acquired in 1000 shot steps, dynamic termination off)
- Movement (random walk off)
- Processing (flexAnalysis method required – see below)
- MS/MS (no method)

7.14. Set up the flexAnalysis method by defining the additional settings in flexAnalysis Editing Processing Parameters and Edit Parameters windows.

- Smoothing (Gaussian, 2 cycles with width of 0.02 *m/z* units)
- Baseline subtraction (TopHat)
- Peak detection (monoisotopic, e.g. SNAP)

7.15. Start the imaging sequence from flexImaging by clicking on the icon shaped like a traffic light that is green (see Fig. 4).

7.16. Once the run is complete, remove the slide.

8. H&E STAINING

8.1. Rinse the slide with 70% EtOH in a glass Coplin staining jar (EMS) until the removal of the matrix.

8.2. Dip the slide into deionized water in a glass Coplin staining jar.

8.3. Immerse the slide in haematoxylin solution (ProSciTech) for 2 min in a glass Coplin staining jar.

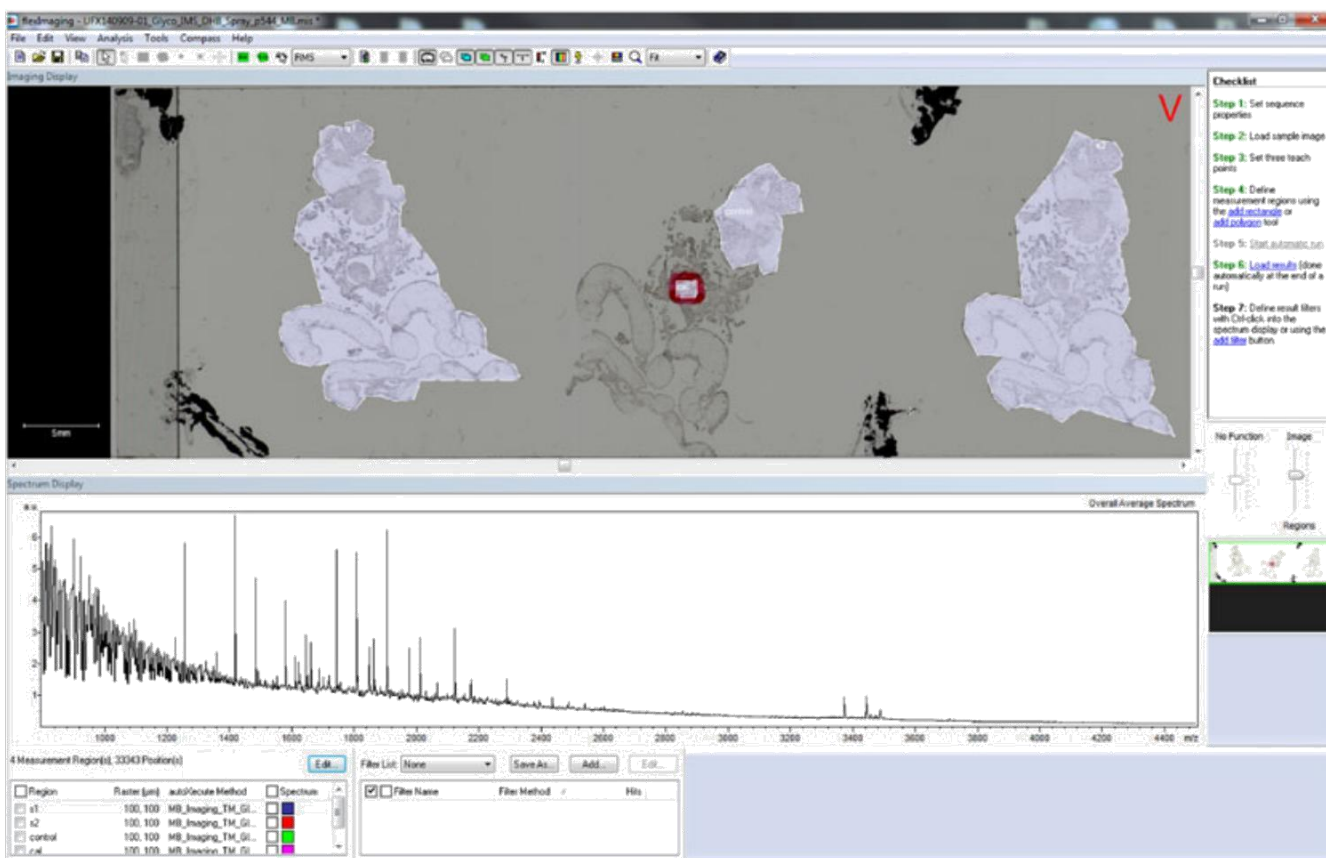


Figure 4. The Sequence interface for the flexImaging software (Bruker Daltonics). Regions of interest are created in the Image Display window by clicking on the blue polygon tool, and then by clicking and creating the region of interest on the scanned tissue section. Once the regions are created, save the sequence and acquire the data by clicking on the green traffic light icon. To visualise m/z values after data acquisition, click on the Spectrum Display window and select the m/z value of interest by holding Ctrl and right clicking.

8.4. Wash the slide with tap water for 2–5 min in a glass Coplin staining jar.

8.5. Immerse the slide in eosin solution (ProSciTech) 1 g/L in water for 1 min in a glass Coplin staining jar.

8.6. Rinse the slide with 70% (v/v) EtOH for 30 s in a glass Coplin staining jar.

8.7. Rinse the slide with 90% (v/v) EtOH for 30 s in a glass Coplin staining jar.

8.8. Rinse the slide with 100% (v/v) EtOH for 30 s in a glass Coplin staining jar.

8.9. Rinse the slide with 100% (v/v) isopropanol for 30 s in a glass Coplin staining jar.

8.10. Rinse the slide twice with 100% (v/v) xylene for 1 min in a glass Coplin staining jar.

8.11. Apply mounting medium onto a cover slide and cover the tissue section with the cover slide by gently press it on.

8.12. Let the cover slide dry overnight at room temperature.

8.13. Scan the tissue section using a NanoZoomer automated slide scanner (Hamamatsu).

8.14. Send the scanned tissue section to a pathologist to annotate the tissue regions of interest (e.g. cancer vs non-cancer).

9. MALDI-MSI DATA ANALYSIS

9.1. Double-click on the desktop icon of SCiLS Lab and select New (from flexImaging sequence).

9.2. Select the instrument type as Time-of-flight (TOF).

9.3. In the Add and arrange data sets window, click on + located in the lower left corner.

- 9.4. Next, select the flexImaging file (name.mis) for importing.
- 9.5. Then, select Import raw, fallback to reduced spectra (.dat) in the Select Preference window.
- 9.6. Click on the next button in both the Add and the arrange data sets and Mass range settings window.
- 9.7. Select TopHat as the Baseline removal algorithm and 200 Narrow as the Peak width, and then click the next button.
- 9.8. In the Import summary window, select the Import button and save as a SCiLS file (name.sl).
- 9.9. Open the Imported Dataset and the summed spectrum will appear.
- 9.10. Click on the Normalization tab located on the right and select Total Ion Count.
- 9.11. Next, click on File and select File Properties.
- 9.12. Change the Interval width to between ± 0.1 – 0.5 m/z units depending on the resolution.
- 9.13. Close the File Properties window and scroll using the mouse to zoom in on the summed spectrum.
- 9.14. Click on monoisotopic peaks in the summed spectrum by holding the Shift button and left click.
- 9.15. Manually scan through the summed spectrum recording m/z values that are only observed in the experimental tissue section and not the control tissue section.
- Figure 6 represents an example of an m/z value that is not observed in the control region (Fig. 6(A)), but is in the PNGase F treated region (Fig. 6(B)). This m/z value (2012.775) was observed in the stroma/adipose regions and not in the tumour regions, based on the pathologist's annotations in Fig. 5.
- 9.16. To find out if this m/z value is a true *N*-glycan, open a web browser and access ExPASy GlycoMod by entering this link into the browser.^[32]
- 9.17. Enter this m/z value into the box labelled Enter a list of experimental masses.
- 9.18. Enter the other parameters as listed below:
- Mass tolerance: ± 0.5 m/z units
 - Positive: Na^+
 - *N*-linked oligosaccharides: Free/PNGase released oligosaccharides

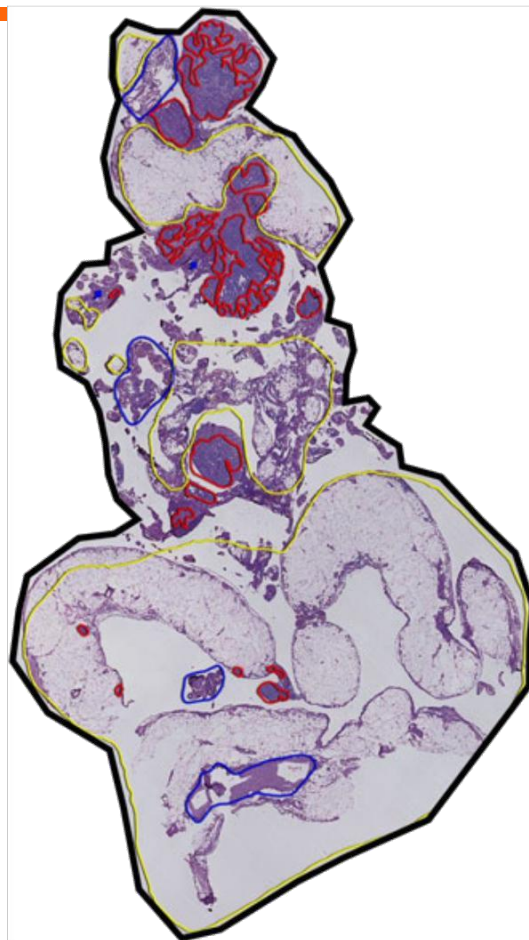


Figure 5. Haematoxylin and eosin (H&E) staining of a formalin-fixed paraffin-embedded stage III ovarian cancer tissue section with tissue-type annotations by a pathologist. The tumour region is coloured in red, the stroma region is coloured in blue and the adipose region is coloured in yellow.

- 9.19. Scroll down and at the bottom of the page, click the Start GlycoMod button.
- 9.20. Click on the UniCarbKB link next to the generated structures to identify the *N*-glycans previously observed in the literature.
- UniCarbKB^[33] is a database of known *N*-glycan structures reported in previous publications. There are often multiple *N*-glycan isomers of the same m/z value and this makes it difficult to annotate the spectrum with the correct structural isomer. Figure 5(B) shows a few examples of different *N*-glycan isomers for the same m/z value, but confirmation by LC/MS/MS is required as in situ MALDI-MS/MS is not detailed enough. The product ion spectrum from LC/MS/MS can confirm if the *N*-glycan structure is bisecting or tri-antennary.

Our group has previously identified and confirmed 18 *N*-glycans from FFPE murine kidney^[19] and 20 *N*-glycans from FFPE human ovarian tumour.^[27] Several *N*-glycan families have been observed, including paucimannose, high mannose,

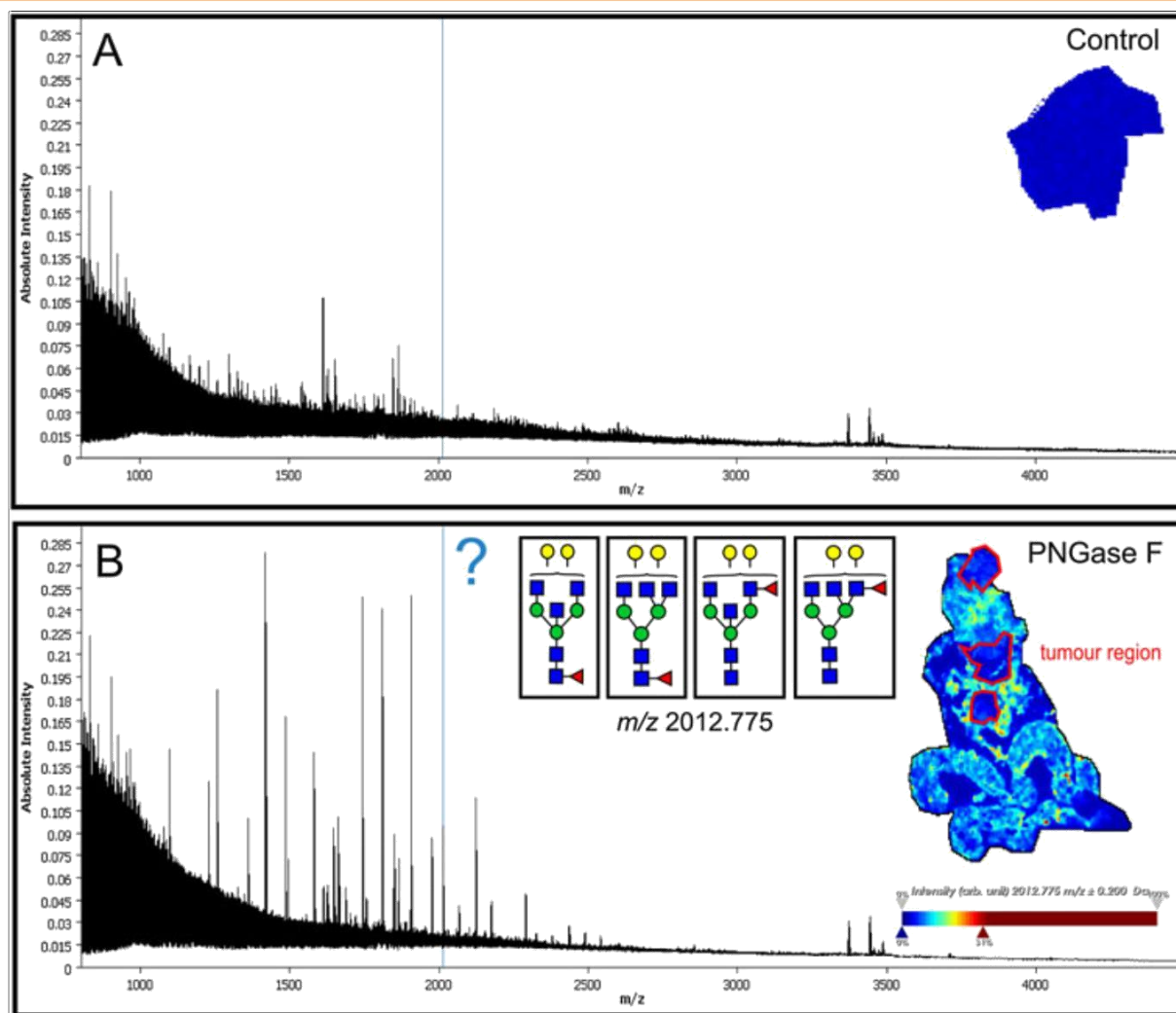


Figure 6. MALDI-MSI of a formalin-fixed paraffin-embedded stage III ovarian cancer tissue section. (A) The summed spectrum and the ion intensity map of m/z 2012.775 from the non-treated (control) region and (B) the summed MS spectrum and ion intensity map of m/z 2012.775 from the PNGase F-treated region. The m/z 2012.775 ion was observed in the stroma and adipose regions, based on the pathologist's annotation of the H&E-stained section in Fig. 5. Potential *N*-glycan structural isomers that correspond to m/z 2012.775 (of monosaccharide composition HexNAc5Hex5dHex1) are shown, but LC/MS/MS analysis of this *N*-glycan mass is required as in situ MALDI-MS/MS does not provide enough detail to elucidate the correct structural isomer. Fucose (red triangle); mannose (green circle); galactose (yellow circle); *N*-acetylglucosamine (blue square).

hybrid, complex, bisected, fucosylated and sialylated. Sialylated *N*-glycans have been identified as sodium adducts in positive mode; for example, a singly sialylated species is detected with two sodium ions while a doubly sialylated species is detected with three sodium ions. Tri-antennary and tetra-antennary *N*-glycans have rarely been observed in our MALDI-MSI datasets, but they are routinely identified by LC/MS from the same sample. Further investigation is required to elucidate why these structures are not observed in MALDI-MSI.

10. LC/MS/MS DATA ACQUISITION

Since in situ MALDI-MS/MS does not provide enough detail to elucidate the correct *N*-glycan isomer, LC/MS/MS is required. A consecutive tissue section is sectioned from the same FFPE block used in the MALDI-MSI experiment and

PNGase F is applied in-solution to release *N*-glycans from all the glycoproteins. This part of the protocol has been adapted from Gustafsson et al.^[19] and Jensen et al.^[14] (see Fig. 7).

10.1. Incubate the tissue section on the PEN membrane slide on a heating block at 60°C for 5 min.

10.2. Remove paraffin from the tissue section by placing the slide in a glass Coplin staining jar containing 100% (v/v) xylene and allow the tissue to stand in solution for 90 s.

10.3. Wash the tissue section by removing the slide from the staining jar and place it in a rectangular staining dish (EMS, USA) containing 100% (v/v) ethanol. Allow the tissue to stay in solution for 60 s.

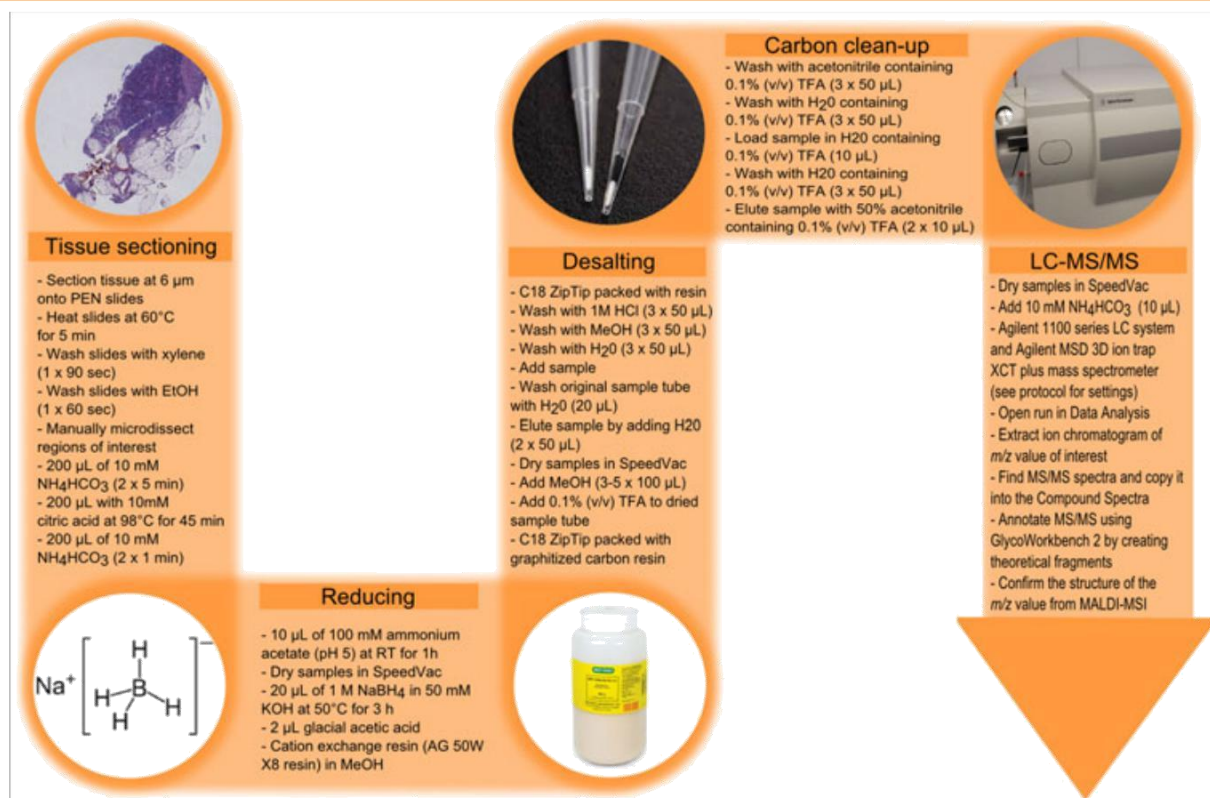


Figure 7. A workflow on how to structurally characterize the *N*-glycome by LC/MS/MS of microdissected regions of FFPE clinical samples. First, the FFPE tissue is sectioned onto PEN slides, treated with citric acid antigen retrieval (CAAR) and digested with PNGase F in-solution to release *N*-glycans from glycoproteins. Secondly, the released *N*-glycans are dried and reduced using sodium borohydride (NaBH_4). Thirdly, the released *N*-glycans are desalted using cation-exchange resin packed into a C18 ZipTip and then cleaned using graphitised carbon packed into a C18 ZipTip. Lastly, the released *N*-glycans are separated using a porous graphitised carbon (PGC) column and tandem mass spectrometry data is acquired using a three-dimensional ion trap.

10.4. Isolate the tissue sections by manual microdissection and transfer the sections into separate microcentrifuge tubes.

- The microdissection size will vary depending on the region of interest from the tissue section.

10.5. Incubate tissue sections in 200 μL of 10 mM NH_4HCO_3 buffer and incubate for 5 min at room temperature. Remove and discard liquid.

10.6. Repeat step 10.5. once.

10.7. Add 200 μL of 10 mM citric acid at pH 6 to tissue sections and heat at 98°C for 45 min.

10.8. Wash tissue sections twice in 10 mM NH_4HCO_3 buffer.

10.9. Add 2 μL of glycerol-free PNGase F (0.5 U/ μL , Roche) and 40 μL of 25 mM NH_4HCO_3 buffer to tissue sections.

- If a different commercially available PNGase F is used, make sure to prepare the enzyme in a buffer that is compatible with mass spectrometry and pH-specific for the PNGase F of choice.

10.10. Incubate for 16 h at 37°C.

10.11. Centrifuge the reaction tube at 14,000 g for 10 min and collect supernatant in individual centrifuge tubes.

10.12. Dry samples to completeness in a SpeedVac concentrator (Savant SVC 100) without heating.

10.13. Wash the tubes twice in 20 μL of water, and pool the washes with the sample.

10.14. Add 10 μL of 100 mM ammonium acetate (pH 5) to the samples and incubate at room temperature for 1 h.

10.15. Dry samples to completeness in a SpeedVac concentrator without heating.

10.16. Add 20 μL of 1 M NaBH_4 in 50 mM KOH to the dried *N*-glycans and incubate for 3 h at 50°C.

10.17. Collect the sample at the bottom of the tube by centrifugation at 2000 g for 30 s.

10.18. Neutralise the reaction by adding 2 μL of glacial acetic acid and mix the samples vigorously.

- Some effervescence might be seen upon the addition of acid.

10.19. Collect the sample at the bottom of the tube by centrifugation at 2000 g for 30 s.

10.20. Prepare a cation-exchange column (one per sample), and transfer a small fraction of cation-exchange resin (AG 50 W X8 resin in methanol) onto a ZipTip C18 tip.

10.21. Put the columns into microcentrifuge tubes and centrifuge at 2000 g for 30 s.

- Add more resin to get approximately 25 μL packed volume.

10.22. Wash the columns with 50 μL of 1 M HCl followed by three times with 50 μL of methanol by centrifugation at 2000 g for 30 s.

10.23. Transfer the columns into new microcentrifuge tubes and wash them three times with 50 μL of water.

10.24. Place the columns in final sample-collection microcentrifuge tubes.

10.25. Apply the glycan samples to the columns and centrifuge at 2000 g for 30 s or until only ~ 5 μL remains on top of the column.

10.26. Wash the original sample tube with 20 μL of water. Add this to the column and centrifuge as before.

10.27. Elute glycans by adding 50 μL of water and centrifuge as before. Combine the eluents.

10.28. Remove the columns from the tubes and dry the eluted glycans in the SpeedVac concentrator.

10.29. Add 100 μL of methanol to the samples. Vortex to mix the samples and dry the samples in the SpeedVac concentrator.

10.30. Repeat step 10.29. three to five times.

10.31. Add 10 μL of 0.1% (v/v) TFA to tube and mix well by vortexing. Samples are now ready for carbon clean-up procedure.

10.32. Prepare the column material by transferring 50 mg of carbon material into a fresh microcentrifuge and then add 1 mL of methanol.

- The slurry should have an approximate concentration of 50 mg/mL.

10.33. Load approximately 50 μL (≈ 2.5 mg) of the slurry onto a ZipTip C18 tip.

10.34. Place the tips into microcentrifuge tubes, spin down to pack column in the tips.

10.35. Wash the column with 50 μL of acetonitrile containing 0.1% (v/v) TFA by centrifugation at 2000 g for 30 s. Repeat this step with three washes.

10.36. Wash the tips three times with 50 μL of 0.1% (v/v) TFA.

10.37. Load the sample dissolved in 10 μL of 0.1% (v/v) TFA onto the top of the column and centrifuge at 2000 g for 30 s.

10.38. Wash column three times with 50 μL of 0.1% (v/v) TFA.

10.39. Discard the wash.

10.40. Transfer the columns to new microcentrifuge tube. Elute bound glycans twice with 10 μL of 50% (v/v) acetonitrile containing 0.1% (v/v) TFA.

10.41. Dry the eluted sample in the SpeedVac concentrator without heating.

10.42. The reduced *N*-linked glycans are dissolved in 10 μL of 10 mM NH_4HCO_3 and analysed by PGC-LC/MS/MS (for details, see Table 3).

11. LC/MS/MS DATA ANALYSIS

11.1. Open Data Analysis (Bruker Daltonics) by double-clicking on the desktop icon.

11.2. Click on **File** and select **Open** to open the LC/MS file (name.D).

11.3. Click on the file located under **Analysis List** and press delete on the keyboard.

11.4. Create an **Extracted Ion Chromatogram (EIC)** by clicking on the **Edit Chromatograms** icon and selecting EIC as the type.

Table 3. Details of the mass spectrometric analyses

Agilent 1100 Series LC system

Column: Hypercarb KAPPA capillary column, (0.18 × 100) mm, 5 μm particle size (Thermo Scientific, Waltham, MA, USA)

Mobile phase: A: 10 mM NH₄HCO₃
B: 45% (v/v) acetonitrile in buffer A

Gradient: 100% A for 8 min
0–35% B for 45 min
35–100% B for 20 min
100% B for 5 min
100–0% for 1 min
100% A for 4 min

Flow rate: 2 μL/min

Column temperature: Ambient

Agilent MSD three-dimensional ion trap XCT plus mass spectrometer

Polarity: Negative

MS full scan mass range: *m/z* 100–2000

Top 2 most intense precursor ions

11.5. In the Masses box, enter the *m/z* value of interest.

- Make sure to convert *m/z* values from MALDI-MS values into LC/MS values. For example, *m/z* [2012.775]¹⁺ from the MALDI-MSI dataset is non-reduced and sodiated while

the same *N*-glycan of *m/z* [994.9]² from the LC/MS dataset is reduced and non-sodiated. Therefore, *m/z* 994.9 would be entered into the Masses box to create an EIC of that *m/z* value.

- In Fig. 8(A), the component producing the ion at *m/z* [994.9]² elutes at 40.8 min as shown by the EIC. Although the composition of the glycan mass corresponds to (Gal)₂GlcNAc₃(Fuc)₁ + (Man)₃GlcNAc₂, several isomeric structures are biologically possible as shown in Fig. 6(B). Through detailed negative mode product ion analysis, the glycan structure corresponding to *m/z* [994.9]² can be elucidated.

11.6. Keep the Width at ±0.5 *m/z* units and click on the Add button.

11.7. Then click the Ok button to close the window.

11.8. Click on the Select Range/View Spectra icon and scan across the peaks in the chromatogram to find MS/MS spectra for the *m/z* value.

- If there are multiple peaks in the chromatogram, there are multiple *N*-glycan isomers of the same *m/z* value.

11.9. Copy the MS/MS spectra into the Compound Spectra by right clicking on the MS/MS and left clicking on Copy to Compound Spectra.

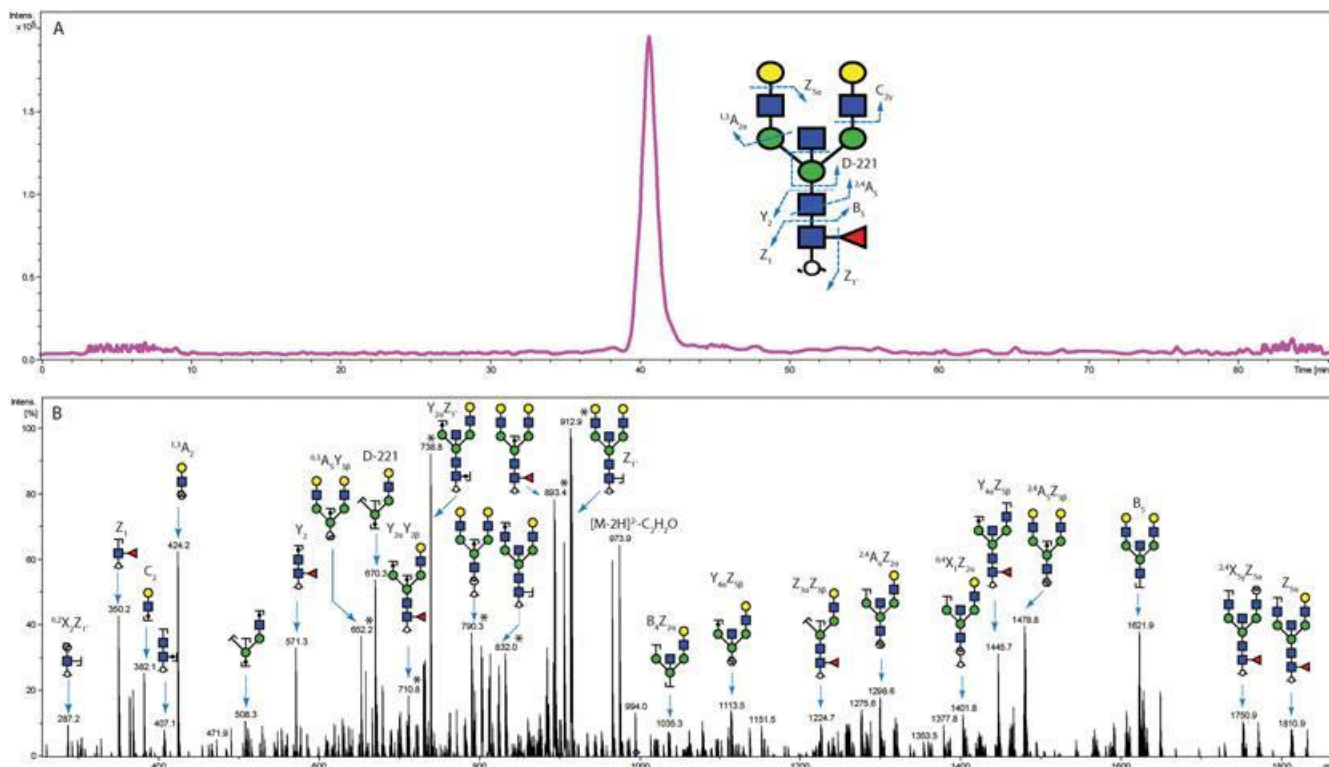


Figure 8. (A) Extracted ion chromatogram of *m/z* 994.9²⁻ corresponding to the glycan composition Gal₂GlcNAc₃Fuc₁ + Man₃GlcNAc₂ eluting at 40.8 min. (B) MS/MS product ion spectra derived from the doubly charged negative ion of *m/z* [994.9]²⁻. The product ions are labeled according to the scheme of Domon and Costello.^[35] Identified structures with key fragmentation are shown. Monosaccharide symbols are as defined by Essentials of Glycobiology. Asterisk denotes doubly charged ions.

11.10. Once the MS/MS spectra of interest have been copied over to the Compound Spectra, the product ions can be annotated using GlycoWorkbench 2 to identify the *N*-glycan isomers present.

11.11. Download GlycoWorkbench 2^[34]

11.12. Once downloaded, double-click on the GlycoWorkbench 2 desktop icon.

11.13. Click on the Structure tab and select a paucimannose *N*-glycan core structure.

11.14. Create multiple isomeric structures observed in the UniCarbKB database^[33] by clicking on the monosaccharide units of interest.

11.15. Once completed, left click and drag to select a single isomeric structure and right click.

11.16. Select Mass Options of Selected Structures and a window called Mass Options will appear.

11.17. Enter the information in Table 4 for LC/MS data and click the Ok button.

11.18. Left click and drag again to select a single isomeric structure, and then click on the Tools tab.

11.19. Move the cursor over Fragments and select Complete fragments for current structure.

11.20. In the Fragment options window, select the product ion types that you expect to observe and click the Ok button.

11.21. A product ion list will appear on the right with *m/z* values that correspond to the theoretical ions. Match these theoretical ions from the product ionlist to the ions in the compound spectra to characterize the glycan structure observed.

For example, in Fig. 8(B), the Z₁⁻ ion at *m/z* 350.2 and the Y₂ ion at *m/z* 571.3 from the product ion spectrum are evidence for the presence of the chitobiose core fucose. Another diagnostic ion

of significant importance is the so called D-ion.^[36] The D-ion arises from the loss of the chitobiose core (C ion cleavage between Manβ1–4GlcNAc), and the Z ion cleavage between Manα1–3Man forming the 3-antennae; thus, the D-ion mass corresponds to the composition of the six-arm antenna plus the two remaining branching core mannoses. Routinely, the D and [D–18] ions have been used to identify the composition of the *N*-glycan 6-antenna. If the *N*-glycan has a bisecting GlcNAc residue, the additional loss of this bisecting β1–4-linked GlcNAc gives rise to the D–221 ion. Figure 8(B) shows the product ion spectra contain the D–221 ion corresponding to *m/z* 670.3. The ion at *m/z* 508.3 further validates the bisecting structure as it is a consequence of the loss of the terminal Gal residue from the D–221 ion.

Our group has previously identified and confirmed 34 *N*-glycans (including structural and compositional isomers) from FFPE murine kidney^[19] and 56 *N*-glycans (including structural and compositional isomers) from FFPE human osteoarthritis cartilage.^[37] Several *N*-glycan families have been observed, including paucimannose, high mannose, hybrid, complex, bisected, fucosylated and sialylated.

12. CONCLUDING REMARKS

This protocol paper describes the capacity of MALDI-MSI to delineate tissue types simply by measuring the spatial distribution of the masses of glycans released from FFPE tissue glycoproteins. The approach stresses the importance of incorporating structural characterisation (LC/MS/MS) when spatially profiling (MALDI-MSI) *N*-glycans in order to confirm their composition and isomeric form. Without LC/MS/MS, the *N*-glycan masses and their corresponding monosaccharide compositions, but not their structures, can be assigned, therefore making it difficult to understand the biological significance of the mass distributions. Consequently, this protocol provides the detailed information required for other groups to adopt our group's complementary workflow to identify important glycomic changes in clinical tissues.

Acknowledgements

Martin K. Oehler and Peter Hoffmann acknowledge the support of the Australian Research Council (LP110100693), Bioplatforms Australia, and the Government of South Australia. Nicolle H. Packer and Arun V. Everest-Dass acknowledge the financial support of the ARC CoE in NanoScale BioPhotonics (ARC CE140100003).

REFERENCES

- [2] R. D. Marshall. The nature and metabolism of the carbohydrate-peptide linkages of glycoproteins. *Biochem. Soc. Symp.* 1974, 17.
- [3] T. Matsui, E. Takita, T. Sato, S. Kinjo, M. Aizawa, Y. Sugiura, T. Hamabata, K. Sawada, K. Kato. *N*-glycosylation at noncanonical Asn-X-Cys sequences in plant cells. *Glycobiology.* 2011, 21, 994.
- [4] J. P. Miletich, G. J. Broze Jr. Beta protein C is not glycosylated at asparagine 329. The rate of translation may influence the frequency of usage at asparagine-X-cysteine sites. *J. Biol. Chem.* 1990, 265, 11397.

Table 4. List of mass options for the select glycan structure such as derivatisation, reducing end, negative mode, and numbers of hydrogen and sodium ions

	LC/MS	MALDI-MS
Derivatization	Und	Und
Reducing end	redEnd	freeEnd
Negative mode	✓	N/A
# H ions	2	0
# Na ions	0	1

- [4] C. Sato, J. H. Kim, Y. Abe, K. Saito, S. Yokoyama, D. Kohda. Characterization of the N-oligosaccharides attached to the atypical Asn-X-Cys sequence of recombinant human epidermal growth factor receptor. *J. Biochem.* 2000, 127, 65.
- [5] S. Sun, H. Zhang. Identification and validation of atypical N-glycosylation sites. *Anal. Chem.* 2015, 87, 11948.
- [6] A. Helenius, M. Aebi. Intracellular functions of N-linked glycans. *Science* 2001, 291, 2364.
- [7] S. S. Pinho, C. A. Reis. Glycosylation in cancer: mechanisms and clinical implications. *Nat. Rev. Cancer* 2015, 15, 540.
- [8] F. M. Tuccillo, A. de Laurentiis, C. Palmieri, G. Fiume, P. Bonelli, A. Borrelli, P. Tassone, I. Scala, F. M. Buonaguro, I. Quinto, G. Scala. Aberrant glycosylation as biomarker for cancer: focus on CD43. *Biomed. Res. Int.* 2014, 2014, 742831.
- [9] F. M. Tuccillo, C. Palmieri, G. Fiume, A. de Laurentiis, M. Schiavone, C. Falcone, E. Iaccino, R. Galandrini, C. Capuano, A. Santoni, F. P. D'Armiento, C. Arra, A. Barbieri, F. Dal Piaz, D. Venzon, P. Bonelli, F. M. Buonaguro, I. Scala, M. Mallardo, I. Quinto, G. Scala. Cancer-associated CD43 glycoforms as target of immunotherapy. *Mol. Cancer Ther.* 2014, 13, 752.
- [10] K. Yamashita, K. Totani, M. Kuroki, Y. Matsuoka, I. Ueda, A. Kobata. Structural studies of the carbohydrate moieties of carcinoembryonic antigens. *Cancer Res.* 1987, 47, 3451.
- [11] K. Fukushima, T. Ohkura, M. Kanai, M. Kuroki, Y. Matsuoka, A. Kobata, K. Yamashita. Carbohydrate structures of a normal counterpart of the carcinoembryonic antigen produced by colon epithelial cells of normal adults. *Glycobiology* 1995, 5, 105.
- [12] F. Dall'Olio, N. Malagolini, G. di Stefano, F. Minni, D. Marrano, F. Serafini-Cessi. Increased CMP-NeuAc: Gal beta 1,4GlcNAc-R alpha 2,6 sialyltransferase activity in human colorectal cancer tissues. *Int. J. Cancer* 1989, 44, 434.
- [13] M. Anugraham, F. Jacob, S. Nixdorf, A. V. Everest-Dass, V. Heinzelmann-Schwarz, N. H. Packer. Specific glycosylation of membrane proteins in epithelial ovarian cancer cell lines: glycan structures reflect gene expression and DNA methylation status. *Mol. Cell. Proteomics* 2014, 13, 2213.
- [14] P. H. Jensen, N. G. Karlsson, D. Kolarich, N. H. Packer. Structural analysis of N- and O-glycans released from glycoproteins. *Nat. Protocols* 2012, 7, 1299.
- [15] J. Q. Fan, Y. C. Lee. Detailed studies on substrate structure requirements of glycoamidases A and F. *J. Biol. Chem.* 1997, 272, 27058.
- [16] F. Maley, R. B. Trimble, A. L. Tarentino, T. H. Plummer Jr. Characterization of glycoproteins and their associated oligosaccharides through the use of endoglycosidases. *Anal. Biochem.* 1989, 180, 195.
- [17] V. Tretter, F. Altmann, L. Marz. Peptide-N4-(N-acetyl-beta-glucosaminyl)asparagine amidase F cannot release glycans with fucose attached alpha-1-3 to the asparagine-linked N-acetylglucosamine residue. *Eur. J. Biochem.* 1991, 199, 647.
- [18] I. B. H. Wilson. Glycosylation of proteins in plants and invertebrates (vol 12, pg 569, 2002). *Curr. Opin. Struct. Biol.* 2003, 13, 141.
- [19] O. J. Gustafsson, M. T. Briggs, M. R. Condina, L. J. Winderbaum, M. Pelzing, S. R. McColl, A. V. Everest-Dass, N. H. Packer, P. Hoffmann. MALDI imaging mass spectrometry of N-linked glycans on formalin-fixed paraffin-embedded murine kidney. *Anal. Bioanal. Chem.* 2015, 407, 2127.
- [20] D. J. Harvey. Collision-induced fragmentation of underivatized N-linked carbohydrates ionized by electrospray. *J. Mass Spectrom.* 2000, 35, 1178.
- [21] W. Chai, V. Piskarev, A. M. Lawson. Branching pattern and sequence analysis of underivatized oligosaccharides by combined MS/MS of singly and doubly charged molecular ions in negative-ion electrospray mass spectrometry. *J. Am. Soc. Mass Spectrom.* 2002, 13, 670.
- [22] Z. Lin, D. M. Lubman, in *Mass Spectrometry Data Analysis in Proteomics*, (Ed: R. Matthiesen). Humana Press, Totowa, NJ, 2013, p. 289.
- [23] W. Morelle, J. C. Michalski. Analysis of protein glycosylation by mass spectrometry. *Nat. Protocols* 2007, 2, 1585.
- [24] D. J. Harvey. Matrix-assisted laser desorption/ionization mass spectrometry of carbohydrates. *Mass Spectrom. Rev.* 1999, 18, 349.
- [25] C. E. Costello, J. M. Contado-Miller, J. F. Cipollo. A glycomics platform for the analysis of permethylated oligosaccharide alditols. *J. Am. Soc. Mass Spectrom.* 2007, 18, 1799.
- [26] W. Morelle, M. C. Slomianny, H. Diemer, C. Schaeffer, A. van Dorsselaer, J. C. Michalski. Fragmentation characteristics of permethylated oligosaccharides using a matrix-assisted laser desorption/ionization two-stage time-of-flight (TOF/TOF) tandem mass spectrometer. *Rapid Commun. Mass Spectrom.* 2004, 18, 2637.
- [27] A. V. Everest-Dass, M. T. Briggs, G. Kaur, M. K. Oehler, P. Hoffmann, N. H. Packer. N-glycan MALDI imaging mass spectrometry on formalin-fixed paraffin-embedded tissue enables the delineation of ovarian cancer tissues. *Mol. Cell. Proteomics* 2016, 15, 3003.
- [28] S. Toghi Eshghi, S. Yang, X. Wang, P. Shah, X. Li, H. Zhang. Imaging of N-linked glycans from formalin-fixed paraffin-embedded tissue sections using MALDI mass spectrometry. *ACS Chem. Biol.* 2014, 9, 2149.
- [29] S. Holst, B. Heijs, N. de Haan, R. J. van Zeijl, I. H. Briaire-de Bruijn, G. W. van Pelt, A. S. Mehta, P. M. Angel, W. E. Mesker, R. A. Tollenaar, R. R. Drake, J. V. Bovee, L. A. McDonnell, M. Wuhrer. Linkage-specific *in situ* sialic acid derivatization for N-glycan mass spectrometry imaging of formalin-fixed paraffin-embedded tissues. *Anal. Chem.* 2016, 88, 5904.
- [30] T. W. Powers, B. A. Neely, Y. Shao, H. Tang, D. A. Troyer, A. S. Mehta, B. B. Haab, R. R. Drake. MALDI imaging mass spectrometry profiling of N-glycans in formalin-fixed paraffin embedded clinical tissue blocks and tissue microarrays. *PLoS One* 2014, 9, e106255.
- [31] W. J. Howat, B. A. Wilson. Tissue fixation and the effect of molecular fixatives on downstream staining procedures. *Methods* 2014, 70, 12.
- [32] Available: <http://web.expasy.org/glycomod/>.
- [33] Available: www.unicarbkb.org.
- [34] Available: <http://glycoworkbench.software.informer.com/2.0b/>.
- [35] B. Domon, C. E. Costello. Structure elucidation of glycosphingolipids and gangliosides using high-performance tandem mass spectrometry. *Biochemistry* 1988, 27, 1534.
- [36] D. J. Harvey, L. Royle, C. M. Radcliffe, P. M. Rudd, R. A. Dwek. Structural and quantitative analysis of N-linked glycans by matrix-assisted laser desorption ionization and negative ion nanospray mass spectrometry. *Anal. Biochem.* 2008, 376, 44.
- [37] M. T. Briggs, J. S. Kuliwaba, D. Muratovic, A. V. Everest-Dass, N. H. Packer, D. M. Findlay, P. Hoffmann. MALDI mass spectrometry imaging of N-glycans on tibial cartilage and subchondral bone proteins in knee osteoarthritis. *Proteomics* 2016, 16, 1736.

This page is intentionally left blank

Chapter 3 | Developing *N*-Glycan MALDI Mass Spectrometry Imaging for FFPE Knee Osteoarthritis Tissue



3.1 | *Summary*

Multiple *N*-glycan structures have been observed in the disease progression of osteoarthritis, although the *N*-glycome of bone marrow has not yet been characterised. Bone marrow lesions (BMLs) are typically visualised by magnetic resonance imaging (MRI) which provides diagnostic and prognostic information, however, this strategy does not provide a molecular understanding. Therefore, we modified our combined MALDI-MSI and PGC-LC-ESI-MS/MS workflow (see the original workflow outlined in *Chapter 2*) to identify and characterise *N*-glycan structures of interest on FFPE tibial cartilage and subchondral bone from knee osteoarthritis patients of different BML stages.

This page is intentionally left blank

3.2 | Statement of Authorship

Title of Paper	MALDI mass spectrometry imaging of <i>N</i> -glycans on tibial cartilage and subchondral bone proteins in knee osteoarthritis
Publication Status	<input checked="" type="checkbox"/> Published <input type="checkbox"/> Accepted for Publication <input type="checkbox"/> Submitted for Publication <input type="checkbox"/> Unpublished and Unsubmitted work written in manuscript style
Publication Details	<u>Matthew T. Briggs</u> , Julia S. Kuliwaba, Dzenita Muratovic, Arun V Everest-Dass, Nicolle H. Packer, David M. Findlay, Peter Hoffmann: <i>MALDI mass spectrometry imaging of N- glycans on tibial cartilage and subchondral bone proteins in knee osteoarthritis</i> . Proteomics 03/2016; 16(11):n/a-n/a., DOI:10.1002/pmic.201500461

Principal Author

Name of Principal Author (Candidate)	Matthew T. Briggs		
Contribution to the Paper	Conceived the project Data collection and analysis Prepared figures and wrote the main manuscript text		
Overall percentage (%)	80%		
Certification:	This paper reports on original research I conducted during the period of my Higher Degree by Research candidature and is not subject to any obligations or contractual agreements with a third party that would constrain its inclusion in this thesis. I am the primary author of this paper.		
Signature		Date	05/07/18

Co-Author Contributions

By signing the Statement of Authorship, each author certifies that:

- i. the candidate's stated contribution to the publication is accurate (as detailed above);
- ii. permission is granted for the candidate to include the publication in the thesis; and
- iii. the sum of all co-author contributions is equal to 100% less the candidate's stated contribution.

Name of Co-Author	Julia S. Kuliwaba		
Contribution to the Paper	Conceived the project Wrote sections of the main manuscript text		
Signature		Date	12/12/17

Name of Co-Author	Dzenita Muratovic		
Contribution to the Paper	Conceived the project Data collection and analysis		
Signature		Date	12/12/17

Name of Co-Author	Arun V. Everest-Dass		
Contribution to the Paper	Conceived the project Data collection and analysis		
Signature		Date	12/12/17

Name of Co-Author	David M. Findlay		
Contribution to the Paper	Conceived the project Designed the experiments and supervised the research		
Signature		Date	12/12/17

Name of Co-Author	Nicolle H. Packer		
Contribution to the Paper	Conceived the project Designed the experiments and supervised the research		
Signature		Date	18/04/18

Name of Co-Author	Peter Hoffmann		
Contribution to the Paper	Conceived the project Designed the experiments and supervised the research		
Signature		Date	20/12/17

This page is intentionally left blank

TECHNICAL BRIEF

MALDI mass spectrometry imaging of *N*-glycans on tibial cartilage and subchondral bone proteins in knee osteoarthritis

Matthew T. Briggs^{1,2}, Julia S. Kuliwaba^{3,4}, Dzenita Muratovic^{3,4}, Arun V. Everest-Dass^{5,6},
Nicolle H. Packer^{5,6}, David M. Findlay³ and Peter Hoffmann^{1,2}

1 Adelaide Proteomics Centre, School of Biological Sciences, University of Adelaide, Adelaide, South Australia, Australia

2 Institute of Photonics and Advanced Sensing (IPAS), University of Adelaide, Adelaide, South Australia, Australia

3 Discipline of Orthopaedics and Trauma, School of Medicine, University of Adelaide, Adelaide, South Australia, Australia

4 Bone and Joint Research Laboratory, SA Pathology, Adelaide, South Australia, Australia

5 Biomolecular Frontiers Research Centre, Faculty of Science, Macquarie University, Sydney, New South Wales, Australia

6 Centre of Excellence for Nanoscale BioPhotonics (CNBP), Macquarie University, Sydney, New South Wales, Australia

Magnetic resonance imaging (MRI) is a non-invasive technique routinely used to investigate pathological changes in knee osteoarthritis (OA) patients. MRI uniquely reveals zones of the most severe change in the subchondral bone (SCB) in OA, called bone marrow lesions (BMLs). BMLs have diagnostic and prognostic significance in OA, but MRI does not provide a molecular understanding of BMLs. Multiple *N*-glycan structures have been observed to play a pivotal role in the OA disease process. We applied matrix-assisted laser desorption/ionization (MALDI) mass spectrometry imaging (MSI) of *N*-glycans to formalin-fixed paraffin-embedded (FFPE) SCB tissue sections from patients with knee OA, and liquid chromatography-electrospray ionization-tandem mass spectrometry (LC-ESI-MS/MS) was conducted on consecutive sections to structurally characterize and correlate with the *N*-glycans seen by MALDI-MSI. The application of this novel MALDI-MSI protocol has enabled the first steps to spatially investigate the *N*-glycome in the SCB of knee OA patients.

Received: November 18, 2015

Revised: February 15, 2016

Accepted: March 11, 2016

Keywords:

Bone marrow lesion / Glycans / Glycoproteomics / Maldi imaging / Mass spectrometry / Osteoarthritis

Additional supporting information may be found in the online version of this article at the publisher's web-site

Correspondence: Professor Peter Hoffmann, Adelaide Proteomics Centre, School of Molecular and Biomedical Science, University of Adelaide, Adelaide, South Australia **E-mail:** peter.hoffmann@adelaide.edu.au

Fax: +61 (08) 0 8313 4362

Abbreviations: **BML**, bone marrow lesion; **CAAR**, citric acid antigen retrieval; **ECM**, extracellular matrix; **FFPE**, formalin-fixed paraffin-embedded; **ITO**, indium tin oxide; **MRI**, magnetic resonance imaging; **OA**, osteoarthritis; **PDFS**, proton density-weighted

Human osteoarthritis (OA) is an increasingly prevalent age-related joint disease with a high burden of personal and economic cost. The disease is characterized by articular cartilage degeneration, with the addition of both generalized and focal changes of the subchondral bone [1, 2]. Bone marrow lesions (BMLs) are features that have been identified in both early asymptomatic and severe late-stage OA patients and their presence associates with loss of overlying cartilage [3, 4]. Classically, BMLs are identified using magnetic resonance

Colour Online: See the article online to view Figs. 1 and 2 in colour.

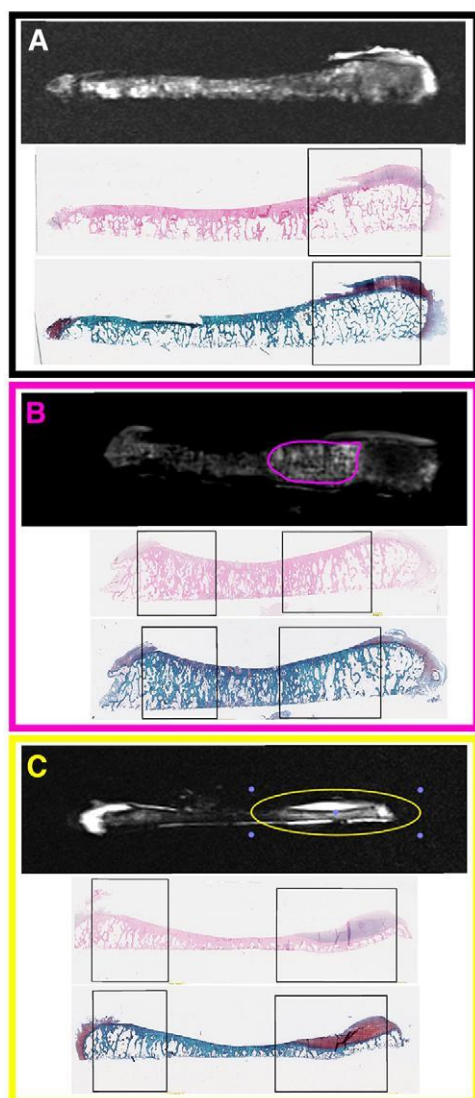


Figure 1. Knee osteoarthritis (OA) patients (A) without bone marrow lesions (No BML), (B) with BML stage 1 (BML 1), and (C) with BML stage 2 (BML 2). Each panel includes (from top to bottom) a PDFS-weighted MRI of the tibial plateau (BML stage 1 and 2 are annotated in pink and green, respectively), a haematoxylin and eosin (H&E) stain, and a Safranin-O/Fast Green stain of consecutive FFPE tissue sections. Regions of interest are annotated in black.

imaging (MRI) by either fat-suppressed and/or proton dense T2 weighted scans. The difference between T1 and T2 weighted scans is that BML areas appear hypointense (i.e. low signal) for T1 and hyperintense (i.e. high signal) for T2 [5, 6]. Therefore, T2 weighted scans depict BMLs to their full extent, while T1 weighted scans usually assess cartilage. A combination of these sequences provides diagnostic and prognostic information regarding OA disease progression [7, 8]. However, MRI does not provide a molecular understanding of BML formation and OA disease progression.

Adjacent to BMLs in the SCB is overlying cartilage composed of extracellular matrix (ECM) glycoproteins [9, 10]. Besides proteoglycans, there are glycosylated cell surface proteins, such as CD44 and integrins, which play an important role in mediating chondrocyte and ECM interactions [11, 12]. Glycans attached to these cartilage ECM glycoproteins are classified into mainly two groups: (i) *N*-linked glycans that are attached to asparagine residues and (ii) *O*-linked glycans that are attached to serine/threonine residues [13]. *N*-glycans are the most common glycan, with well-established methods for analysis from tissue [14, 15]. Multiple *N*-glycan structures have been observed to play a pivotal role in OA disease progression. Recently, using HPLC-MS, it has been shown that high-mannose type *N*-glycans are significantly decreased on proteins from both murine and human OA cartilage tissue [16]. In 2013, glycophenotyping of OA cartilage was carried out using several techniques, such as RT-PCR, MS and immunohistochemistry. Liquid chromatography-electrospray ionization-tandem mass spectrometry (LC-ESI-MS/MS) separation and structural identification of the released glycans confirmed 21 *N*-glycans on the human OA chondrocyte proteins isolated from femoral condyle articular cartilage [17]. The *N*-glycome of bone marrow from OA patients has not yet been characterized.

MALDI mass spectrometry imaging (MALDI-MSI) has previously been applied to the proteomic analysis of fresh frozen human OA knee cartilage and synovial tissue. Deep and superficial knee cartilage from human healthy and OA patients were sectioned and analysed by MALDI-MSI of the tryptic peptides [18]. Fibronectin and cartilage oligomeric matrix protein (COMP) were 2 glycoproteins identified in the OA patients, but not in the healthy controls. Moreover, the glycoprotein fibronectin was identified in the synovial membranes from OA patients, but not in healthy controls. In summary, glycoproteins have been observed to play an important role in OA changes of human knee cartilage and synovial tissue.

The measurement of *N*-glycans by MALDI-MSI on fresh frozen mouse brain tissue and various formalin-fixed paraffin-embedded (FFPE) tissues has been established previously [19, 20], with regions of interest, such as tumour and non-tumour, differentiated based on the pattern of *N*-glycans released. The limitation of MALDI analysis is that *N*-glycan masses can identify the glycan compositions but cannot identify the sequence and branching of the glycan structures. This has recently been overcome with a new workflow combining *N*-glycan analysis by MALDI-MSI and LC-ESI-MS/MS [21].

Here we investigate the *N*-glycome of FFPE cartilage and bone marrow tissue. Human knee SCB, from OA patients with BMLs (stage 1 and 2) or without BMLs were analysed to investigate *N*-glycosylation patterns.

Tibial plateaus were obtained from three patients (one male aged 52 years, two females aged 68 and 74 years) undergoing knee arthroplasty surgery for radiographic and severe symptomatic OA. Tibial plateau specimens were scanned *ex vivo*, using an MR scanner with an 8-channel wrist coil (3T MRI Siemens TRIO), at two specific sequences; fat

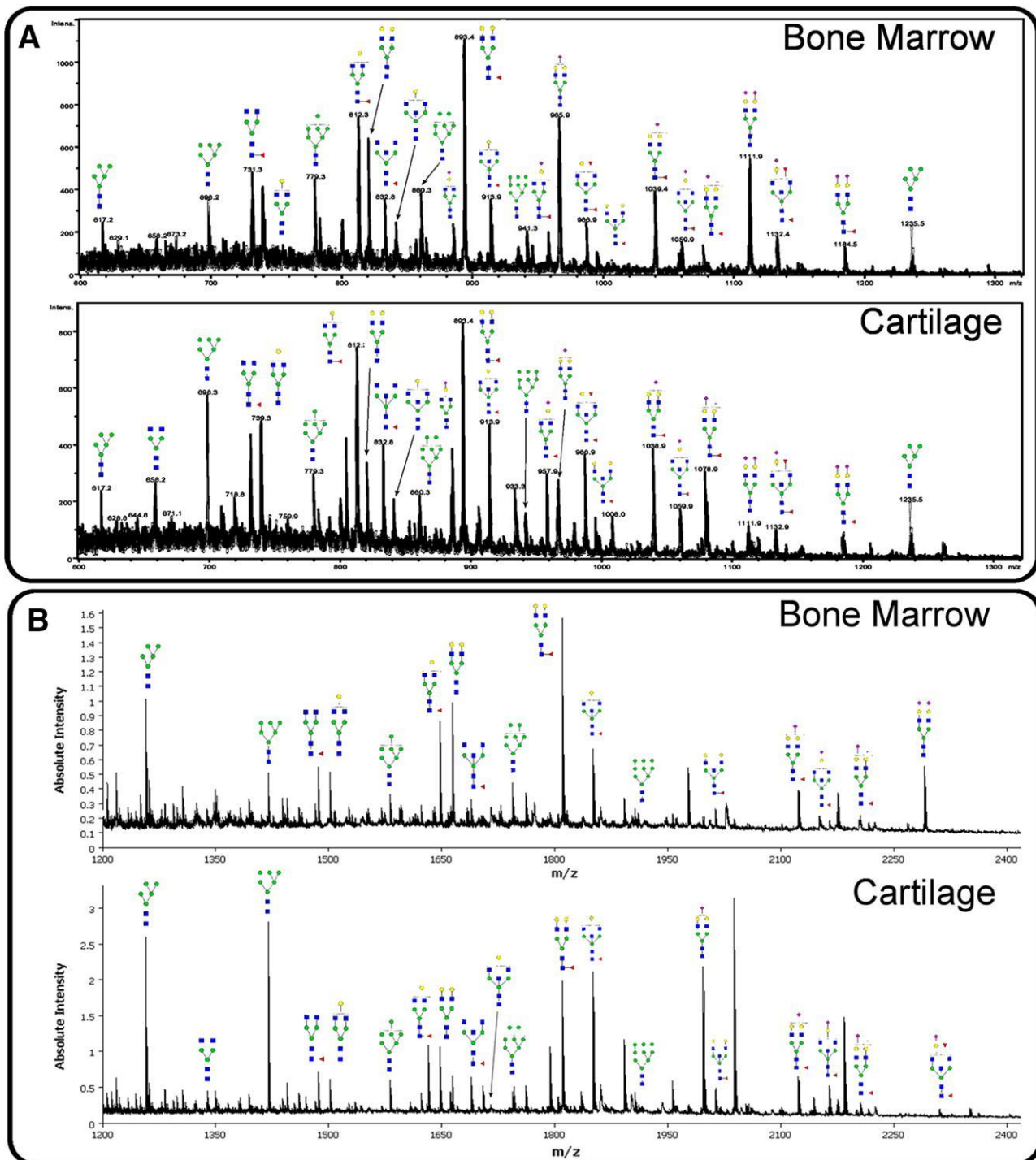


Figure 2. (A) LC-ESI-MS profiles of bone marrow and cartilage regions, and (B) MALDI-MS profiles of bone marrow and cartilage regions, annotated with confirmed *N*-glycan structures from LC-ESI-MS/MS. (A) *N*-glycans were released in-solution from formalin-fixed paraffin-embedded (FFPE) tissue sections using PNGase F prior to LC-ESI-MS/MS. (B) *N*-glycans were released in situ from FFPE tissue sections using PNGase F and analysed by MALDI-TOF/TOF-MS. Regions were selected based on histology in SCiLS lab software (V2015a, Bruker Daltonics, Bremen, Germany).

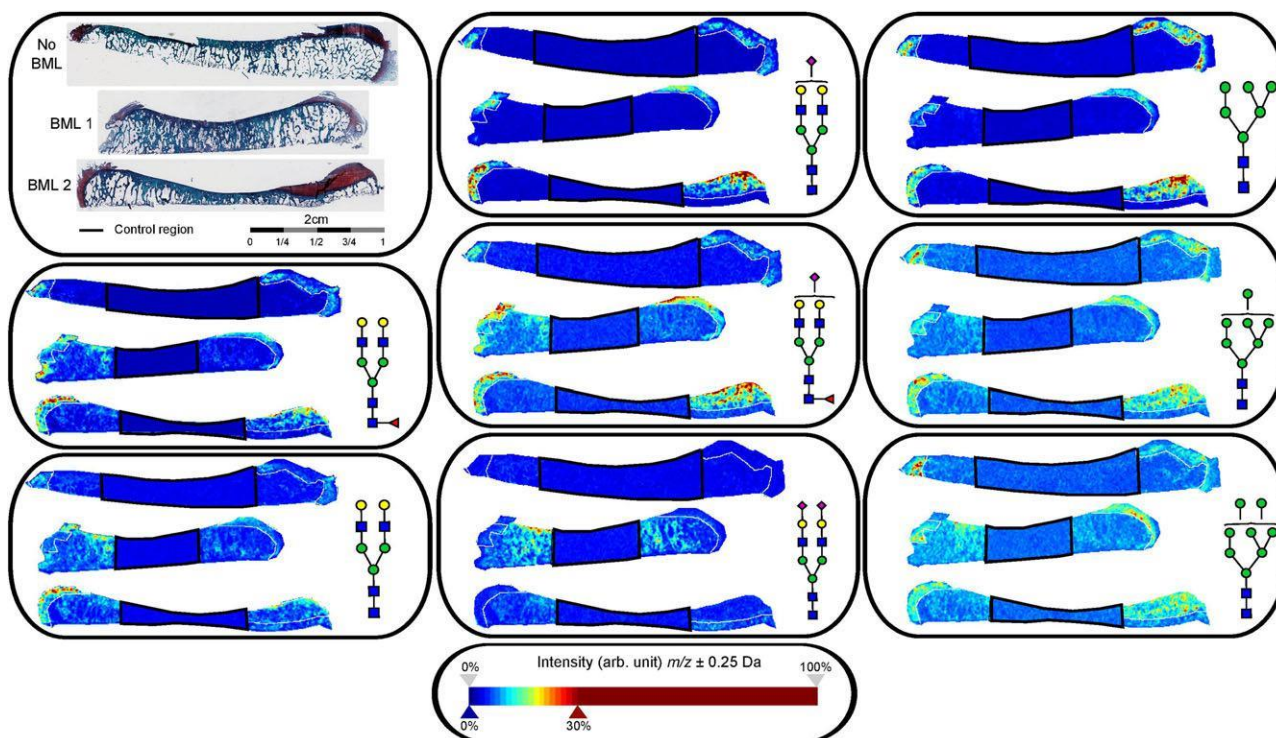


Figure 3. Safranin-O stained images and ion intensity maps of complex/hybrid, sialylated and high-mannose *N*-glycans observed in patients without bone marrow lesions (No BML), with BML stage 1 (BML 1) and with BML stage 2 (BML 2). *N*-glycans were released in situ on FFPE tissue sections using PNGase F and analysed by MALDI-TOF/TOF-MS. *m/z* values were selected and visualized in SCiLS lab software (V2015a, Bruker Daltonics, Bremen, Germany). Ion intensity maps were co-registered with safranin-O stained images to identify the distribution of the selected *N*-glycans. There was no distinct pattern between the same families (i.e. complex/hybrid, sialylated and high-mannose) of *N*-glycans. Control and calibrant regions (i.e. regions not treated with PNGase F) are annotated in black.

suppressed (FS) fast spin-echo proton density-weighted (PDFS) and T1 weighted spin echo in sagittal and coronal plane. Sagittal slice thickness was 1.6 mm with distance factor of 25%. Coronal slice thickness was 3.0 mm with 10% distance factor. Ex vivo MR imaging was confirmed to correspond to pre-operative imaging, by comparing pre- and post-operative MR data. BMLs were defined as changes of the MRI signal intensity in the bone marrow, located beneath cartilage and visible at least on two consecutive slices. BMLs detected on the PDFS sequence only (no signal on T1) are classified as BML stage 1 and correspond to mild-to-moderate osteochondral OA pathology; BMLs detected on both PDFS and T1 sequences are classified as BML stage 2 and represent severe OA osteochondral pathology [22]. Using precise mapping of BMLs (OsiriX software, Pixmeo-SARL, Switzerland), a sagittal slice of cartilage-subchondral bone (width 5 mm x depth 5 to 12 mm) containing the BML area (Fig. 1) was dissected using a low speed diamond wheel saw (Model 660, South Bay Technology, Inc.). Sagittal blocks of tissue were fixed in 4% (w/v) paraformaldehyde and slowly decalcified in 15% (w/v) ethylenediaminetetra acetic acid (EDTA). Following complete decalcification as determined by X-ray, samples were processed, embedded in paraffin and cut on a rotary

microtome (Leica RM 2235 Nussloch, Germany) into 5mm thick sections.

FFPE human OA tissue sections on indium tin oxide (ITO) or polyethylene naphthalate (PEN) slides were rehydrated using a modified procedure of citric acid antigen retrieval (CAAR) at 70°C for 3 h instead of 98°C for 30 min and printing 15 nL of PNGase F instead of 30 nL [21]. Mass spectra were acquired using an ultrafleXtreme MALDI-TOF/TOF mass spectrometer or LC-iontrap ESI-MS/MS analysis as described previously [21, 23].

BMLs were identified using PDFS and T1 weighted scans in MRI of the tibial plateaus. As depicted in Fig. 1 Panel A, there was no BML detected in this patient, while in Fig. 1 Panels B and C, BML stage 1 and 2, respectively, were detected. These BMLs are annotated in pink and green, as indicated on the MRI. Below each MRI, staining of FFPE tissue sections are shown. Haematoxylin and eosin (H&E) staining provides histological information and Safranin-O highlights the cartilage in red. Following acquisition of the MRI, the image was overlaid with the stained FFPE tissue sections and regions of interest were annotated in black. Although the identification of these BMLs using MRI is useful, it does not provide molecular information. Therefore, we performed MALDI-MSI of

the released *N*-glycans to investigate the molecular mechanisms behind BMLs.

For the CAAR [21, 24], we reduced the temperature and incubated longer to maintain adherence to the ITO slide. MALDI-MSI experiments were conducted in parallel with LC-ESI-MS/MS structural characterization. Consecutive tissue sections were manually micro-dissected, and the *N*-glycans were released and structurally characterized by LC-ESI-MS/MS. Figure 2 represents the summed LC-ESI-MS and MALDI-MS profiles of both bone marrow and cartilage. In Fig. 2 Panel A (LC-ESI-MS profiles), 52 individual *N*-glycan structures (including structural and compositional isomers) were identified from bone marrow proteins compared to 56 individual *N*-glycan masses (including structural and compositional isomers) identified from cartilage proteins, based on LC-ESI-MS/MS data (Supporting Information Table 1). The detailed structures were manually assigned from the MS/MS fragmentation data as illustrated in Supporting Information Fig. 1. A comparison of the LC-ESI-MS mass profiles revealed differences in intensity of particular *m/z* values. For example, *m/z* 1111.4 was observed as a lower intensity peak in the cartilage relative to the bone marrow.

Ion intensity maps were then generated by MALDI-MSI for *N*-glycan structures from the complex/hybrid, sialylated and high-mannose families that had been determined by LC-ESI-MS/MS analysis (refer to Fig. 2 Panel A for the summed LC-ESI-MS profiles). Figure 3 shows Safranin-O stained images and ion intensity maps for the same three patients described in Fig. 1. The region annotated in black represents the control (i.e. non-treated) and calibrant regions while the region annotated in white is cartilage. There were no differences observed between the complex/hybrid *N*-glycan masses in both the cartilage and bone marrow (even between fucosylated and non-fucosylated *N*-glycans). The log ion intensity map for (NeuAc)₁(Hex)₂(HexNAc)₂ + (Man)₃(GlcNAc)₂ was observed as a doubly sodiated species only in the cartilage whereas the core fucosylated version of this *N*-glycan was observed in both the cartilage and bone marrow. In addition, (NeuAc)₂(Hex)₂(HexNAc)₂ + (Man)₃(GlcNAc)₂ was observed as a triply sodiated species only in the bone marrow of the patient with BML stage 1, but not in patients with no BML or BML stage 2 as classified by MRI. This particular *N*-glycan was observed in LC-ESI-MS/MS profiles of both the cartilage and bone marrow, but exhibited decreased intensity in cartilage. This suggests that this *N*-glycan is too low in abundance in the cartilage for MALDI-MSI detection. High mannose *N*-glycans such as (Man)₃ + (Man)₃(GlcNAc)₂, (Man)₄ + (Man)₃(GlcNAc)₂ and (Man)₅ + (Man)₃(GlcNAc)₂ were compared between the three knee OA patients. The ion intensity map for (Man)₃ + (Man)₃(GlcNAc)₂ showed that this *N*-glycan was only observed in the cartilage region, whereas (Man)₄ + (Man)₃(GlcNAc)₂ and (Man)₅ + (Man)₃(GlcNAc)₂ were highlighted in both the cartilage and bone marrow.

Regions of interest (i.e. bone marrow and cartilage) were also selected based on histology and summed spectra were extracted from the MALDI-MSI dataset. Figure 2 panel B

represents summed spectra from these regions and show a lower sensitivity of detection compared to LC-ESI-MS/MS. A comparison of those structures found by MALDI-MSI and LC-ESI-MS/MS are shown in Supporting Information Table 1. The detected *m/z* from LC-ESI-MS corresponded to doubly charged [M–2H]²⁺ masses and the *m/z* from MALDI-MSI corresponded to the sodiated mass ([M+Na⁺]⁺). A total of 17 individual *N*-glycan masses were identified from bone marrow compared to 20 individual *N*-glycan masses from cartilage. As previously seen in the ion intensity maps, (NeuAc)₁(Hex)₂(HexNAc)₂ + (Man)₃(GlcNAc)₂ was only detected in the cartilage while (NeuAc)₂(Hex)₂(HexNAc)₂ + (Man)₃(GlcNAc)₂ was only detected in the bone marrow. There was a major difference between the intensity of the *N*-glycan *m/z* values observed with (Man)₃ + (Man)₃(GlcNAc)₂ being prominent in the cartilage relative to the bone marrow.

In summary, we have established a MALDI-MSI and LC-ESI-MS/MS workflow for FFPE tibial cartilage and SCB of knee OA patients. For the first time, the *N*-glycome of different regions of the same OA sample have been investigated, with individual *N*-glycan structural and compositional isomers in bone marrow and cartilage (a total of 52 and 56 respectively) being identified by LC-ESI-MS/MS. Using targeted masses in the MALDI-MSI experiments, the disialylated biantennary complex glycan, (NeuAc)₂(Hex)₂(HexNAc)₂ + (Man)₃(GlcNAc)₂ was identified to be prominent in the bone marrow for the BML stage 1 patient relative to all other patient samples. However, larger patient studies will be required in order to understand the biological relevance of this observation. Overall, further development of this novel MALDI-MSI protocol has enabled the first steps to investigate the spatial distribution of the *N*-glycome of knee OA patients.

PH gratefully acknowledges the financial support of the Australian Research Council (ARC LP110100693), Bioplatforms Australia, and the Government of South Australia. NHP and AVE-D acknowledges the financial support of the ARC CoE in NanoScale BioPhotonics (ARC CE140100003).

The authors have declared no conflict of interest.

References

- [1] Fautrel, B., Bourgeois, P., [Rheumatic disorders. Overview]. *Drugs* 2000, 59 Spec No 1, 1–9.
- [2] Beaupre, G. S., Stevens, S. S., Carter, D. R., Mechanobiology in the development, maintenance, and degeneration of articular cartilage. *J. Rehabil. Res. Dev.* 2000, 37, 145–151.
- [3] Roemer, F. W., Guermazi, A., Javadi, M. K., Lynch, J. A. et al., Change in MRI-detected subchondral bone marrow lesions is associated with cartilage loss: the MOST Study. A longitudinal multicentre study of knee osteoarthritis. *Ann. Rheum. Dis.* 2009, 68, 1461–1465.
- [4] Wluka, A. E., Hanna, F., Davies-Tuck, M., Wang, Y. et al., Bone marrow lesions predict increase in knee cartilage defects and loss of cartilage volume in middle-aged women without knee pain over 2 years. *Ann. Rheum. Dis.* 2009, 68, 850–855.

- [5] Loeuille, D., Chary-Valckenaere, I., MRI in OA: from cartilage to bone marrow lesion. *Osteoporos. Int.* 2012, 23 Suppl 8, S867–S869.
- [6] Dore, D., Martens, A., Quinn, S., Ding, C. et al., Bone marrow lesions predict site-specific cartilage defect development and volume loss: a prospective study in older adults. *Arthritis Res. Ther.* 2010, 12, R222.
- [7] Driban, J. B., Tassinari, A., Lo, G. H., Price, L. L. et al., Bone marrow lesions are associated with altered trabecular morphology. *Osteoarthritis Cartilage* 2012, 20, 1519–1526.
- [8] Hayashi, D., Guermazi, A., Kwok, C. K., Hannon, M. J. et al., Semiquantitative assessment of subchondral bone marrow edema-like lesions and subchondral cysts of the knee at 3T MRI: a comparison between intermediate-weighted fat-suppressed spin echo and Dual Echo Steady State sequences. *BMC Musculoskelet. Disord.* 2011, 12, 198.
- [9] Toegel, S., Pabst, M., Wu, S. Q., Grass, J. et al., Phenotype-related differential alpha-2,6- or alpha-2,3-sialylation of glycoprotein N-glycans in human chondrocytes. *Osteoarthritis Cartilage* 2010, 18, 240–248.
- [10] Ishihara, T., Kakiya, K., Takahashi, K., Miwa, H. et al., Discovery of novel differentiation markers in the early stage of chondrogenesis by glycoform-focused reverse proteomics and genomics. *Biochim. Biophys. Acta* 2014, 1840, 645–655.
- [11] Knudson, C. B., Knudson, W., Cartilage proteoglycans. *Semin. Cell Dev. Biol.* 2001, 12, 69–78.
- [12] Nicoll, S. B., Barak, O., Csoka, A. B., Bhatnagar, R. S., Stern, R., Hyaluronidases and CD44 undergo differential modulation during chondrogenesis. *Biochem. Biophys. Res. Commun.* 2002, 292, 819–825.
- [13] Kobata, A., Structures and functions of the sugar chains of glycoproteins. *Eur. J. Biochem.* 1992, 209, 483–501.
- [14] Tian, Y., Gurley, K., Meany, D. L., Kemp, C. J., Zhang, H., N-linked glycoproteomic analysis of formalin-fixed and paraffin-embedded tissues. *J. Proteome Res.* 2009, 8, 1657–1662.
- [15] Hu, Y., Zhou, S., Khalil, S. I., Renteria, C. L., Mechref, Y., Glycomic profiling of tissue sections by LC-MS. *Anal. Chem.* 2013, 85, 4074–4079.1741
- [16] Urita, A., Matsushashi, T., Onodera, T., Nakagawa, H. et al., Alterations of high-mannose type N-glycosylation in human and mouse osteoarthritis cartilage. *Arthritis Rheum.* 2011, 63, 3428–3438.
- [17] Toegel, S., Bieder, D., Andre, S., Altmann, F. et al., Glycoproteotyping of osteoarthritic cartilage and chondrocytes by RT-qPCR, mass spectrometry, histochemistry with plant/human lectins and lectin localization with a glycoprotein. *Arthritis Res. Ther.* 2013, 15, R147.
- [18] Cillero-Pastor, B., Eijkel, G. B., Kiss, A., Blanco, F. J., Heeren, R. M., Matrix-assisted laser desorption/ionization-mass spectrometry: a new methodology to study human osteoarthritic cartilage. *Arthritis Rheum.* 2013, 65, 710–720.
- [19] Powers, T. W., Jones, E. E., Betesh, L. R., Romano, P. R. et al., Matrix assisted laser desorption/ionization mass spectrometry workflow for spatial profiling analysis of N-linked glycan expression in tissues. *Anal. Chem.* 2013, 85, 9799–9806.
- [20] Powers, T. W., Neely, B. A., Shao, Y., Tang, H. et al., MALDI imaging mass spectrometry profiling of N-glycans in formalin-fixed paraffin embedded clinical tissue blocks and tissue microarrays. *PLoS one* 2014, 9, e106255.
- [21] Gustafsson, O. J., Briggs, M. T., Condina, M. R., Winderbaum, L. J. et al., MALDI imaging mass spectrometry of N-linked glycans on formalin-fixed paraffin-embedded murine kidney. *Anal. Bioanal. Chem.* 2015, 407, 2127–2139.
- [22] Muratovic, D., Cicuttini, F. M., Wluka, A. E., Wang, Y., Findlay, D. M. et al., Bone marrow lesions detected by different magnetic resonance sequences as potential biomarkers for knee osteoarthritis: comprehensive tissue level analysis. *Osteoarthritis Cartilage* 2015, 23, A303–A305.
- [23] Jensen, P. H., Karlsson, N. G., Kolarich, D., Packer, N. H., Structural analysis of N- and O-glycans released from glycoproteins. *Nat. Protoc.* 2012, 7, 1299–1310.
- [24] Gustafsson, J. O., Oehler, M. K., McColl, S. R., Hoffmann, P., Citric acid antigen retrieval (CAAR) for tryptic peptide imaging directly on archived formalin-fixed paraffin-embedded tissue. *J. Proteome Res.* 2010, 9, 4315–4328.

3.3 | Supplementary Information

Table 1: Proposed *N*-glycan structures detected and characterized by negative ion mode LC-ESI-ion trap MS/MS. Provided in this table are the detected *m/z* of the *N*-glycan structures found in formalin-fixed paraffin-embedded bone marrow and cartilage tissue sections. The detected *m/z* from LC-ESI-MS correspond to doubly charged $[M-2H]^{2-}$ masses and the *m/z* from MALDI-MSI correspond to the sodiated mass $([M+Na])^+$. *denotes the presence of additional sodium adducts observed in sialylated structures.

	Glycan composition	Glycan structure	Detected <i>m/z</i> in LC-ESI		Detected <i>m/z</i> MALDI imaging	
			Bone Marrow	Cartilage	Bone Marrow	Cartilage
1	(Hex) ₂ + (Man) ₃ (GlcNAc) ₂		617.2	617.2	1257.4	1257.4
2	(HexNAc) ₂ + (Man) ₃ (GlcNAc) ₂		ND	658.2	ND	1339.5
3	(Hex) ₃ + (Man) ₃ (GlcNAc) ₂		698.3	698.3	1419.5	1419.5
4	(HexNAc) ₂ (Deoxyhexose) ₁ + (Man) ₃ (GlcNAc) ₂		731.3	731.3	1485.5	1485.5
5	(Hex) ₁ (HexNAc) ₂ + (Man) ₃ (GlcNAc) ₂		739.3	739.3	1501.5	1501.5
6	(Hex) ₄ + (Man) ₃ (GlcNAc) ₂		779.3	779.3	1581.5	1581.5
7	(Hex) ₁ (HexNAc) ₂ (Deoxyhexose) ₁ + (Man) ₃ (GlcNAc) ₂		812.3	812.3	1647.6	1647.6
8	(Hex) ₂ (HexNAc) ₂ + (Man) ₃ (GlcNAc) ₂		820.3	820.3	1663.6	1663.6
9	(HexNAc) ₃ (Deoxyhexose) ₁ + (Man) ₃ (GlcNAc) ₂		832.8	832.8	1688.6	1688.6
10	(Hex) ₁ (HexNAc) ₃ + (Man) ₃ (GlcNAc) ₂		840.8	840.8	ND	1704.6
11	(Hex) ₅ + (Man) ₃ (GlcNAc) ₂		860.3	860.3	1743.6	1743.6
12	(Hex) ₁ (HexNAc) ₂ (NeuAc) ₁ + (Man) ₃ (GlcNAc) ₂		884.8	884.8	ND	ND
13	(Hex) ₂ (HexNAc) ₂ (Deoxyhexose) ₁ + (Man) ₃ (GlcNAc) ₂		893.4	893.4	1809.6	1809.6
14	(Hex) ₁ (HexNAc) ₃ (Deoxyhexose) ₁ + (Man) ₃ (GlcNAc) ₂		913.9	913.9	1850.7	1850.7
15	(Hex) ₆ + (Man) ₃ (GlcNAc) ₂		941.3	941.3	1905.6	1905.6
16	(Hex) ₁ (HexNAc) ₂ (Deoxyhexose) ₁ (NeuAc) ₁ + (Man) ₃ (GlcNAc) ₂		957.9	957.9	ND	ND
17	(Hex) ₂ (HexNAc) ₂ (NeuAc) ₁ + (Man) ₃ (GlcNAc) ₂		965.9	965.9	ND	ND
18	(Hex) ₁ (HexNAc) ₃ (Deoxyhexose) ₂ + (Man) ₃ (GlcNAc) ₂		986.9	986.9	ND	1997.1
19	(Hex) ₂ (HexNAc) ₃ (Deoxyhexose) ₁ + (Man) ₃ (GlcNAc) ₂		994.9	994.9	2012.7	2012.7
20 *	(Hex) ₂ (HexNAc) ₂ (Deoxyhexose) ₁ (NeuAc) ₁ + (Man) ₃ (GlcNAc) ₂		1038.9	1038.9	2123.1	2123.1
21 *	(Hex) ₁ (HexNAc) ₃ (Deoxyhexose) ₁ (NeuAc) ₁ + (Man) ₃ (GlcNAc) ₂		1059.3	1059.3	2163.0	2163.0
22	(Hex) ₂ (HexNAc) ₂ (Sulphate) ₁ (NeuAc) ₁ + (Man) ₃ (GlcNAc) ₂		1078.9	1078.9	ND	ND

23 *	(Hex) ₂ (HexNAc) ₂ (NeuAc) ₂ + (Man) ₃ (GlcNAc) ₂		1111.9	1111.9	2290.1	ND
24	(Hex) ₂ (HexNAc) ₂ (Deoxyhexose) ₁ (Acetate) ₁ (NeuAc) ₂ + (Man) ₃ (GlcNAc) ₂		1132.4	1132.4	ND	ND
25	(Hex) ₂ (HexNAc) ₂ (Deoxyhexose) ₁ (NeuAc) ₂ + (Man) ₃ (GlcNAc) ₂		1184.5	1184.5	ND	ND

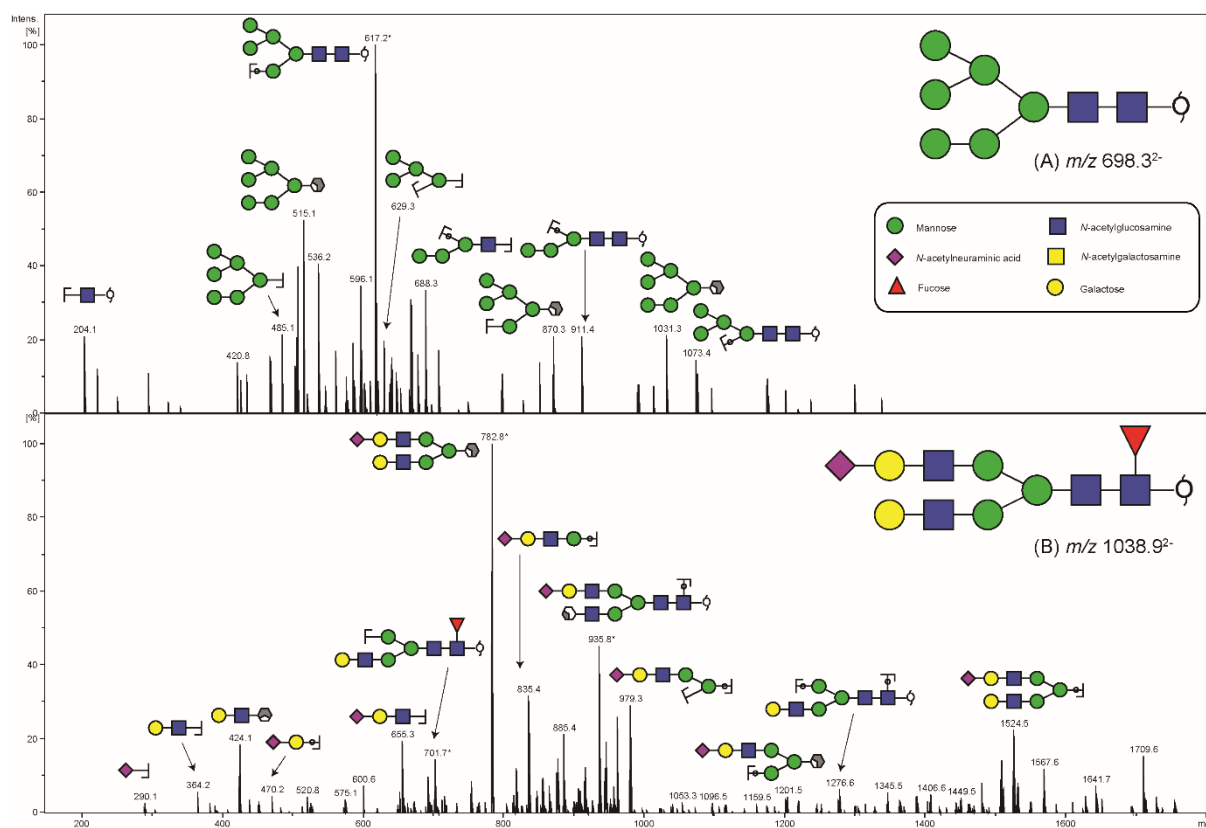


Figure S1: Tandem mass spectrometry fragmentation spectra derived from the doubly charged negative ion isomers of (A) m/z 698.32⁻ and (B) m/z 1038.92⁻, respectively. The identified structures with their key fragments are shown. Monosaccharide symbols are as defined by the Consortium for Functional Glycomics. *denotes doubly charged annotated masses.

Chapter 4 | Investigating the Inpatient Variation of Late-Stage Ovarian Cancer Tissues using *N*-Glycan MALDI Mass Spectrometry Imaging



4.1 | Summary

Matrix-assisted laser desorption/ionisation (MALDI) mass spectrometry imaging (MSI) has been used for the past two decades to spatially map biomolecules, such as proteins, lipids and metabolites, on formalin fixed paraffin embedded (FFPE) tissue sections which can correlate molecular information with histopathological changes found in patient-derived tissues. This chapter asked the question as to whether *N*-glycans, which are known to be aberrant in ovarian cancer, can be used to differentiate tissue-specific regions from FFPE tissue sections of late-stage ovarian cancer patients.

To summarise, this study showed that tissue regions (i.e. tumour, stroma, adipose and necrotic regions), isolated from FFPE tissue sections of late-stage serous ovarian cancers, can be clearly discriminated by the masses of the released *N*-glycans. Combined with liquid chromatography electrospray ionisation tandem mass spectrometry (LC-ESI-MS/MS), it was possible to characterise these masses that were visualised by high resolution MALDI-MSI, therefore providing strong evidence that these masses are true *N*-glycan structures.

The results from this study further indicate that the location and classification of various ovarian cancers and their subtypes could be made possible by high resolution MALDI-MSI combined with structural characterisation by LC-ESI-MS/MS analysis. It is envisioned that MALDI-MS, which already has instruments in pathology laboratories used for bacterial biotyping, will identify tissue-specific *N*-glycans which may improve ovarian cancer diagnosis and further lead to tissue-targeted therapeutic strategies to improve survival rates for patients.

4.2 | Statement of Authorship

Title of Paper	<i>N</i> -glycan MALDI Imaging Mass Spectrometry on Formalin-Fixed Paraffin-Embedded Tissue Enables the Delineation of Ovarian Cancer Tissues
Publication Status	<input checked="" type="checkbox"/> Published <input type="checkbox"/> Accepted for Publication <input type="checkbox"/> Submitted for Publication <input type="checkbox"/> Unpublished and Unsubmitted work written in manuscript style
Publication Details	Arun V. Everest-Dass, <u>Matthew T. Briggs</u> , Gurjeet Kaur, Martin K. Oehler, Peter Hoffmann, Nicolle H Packer: <i>N -Glycan MALDI Imaging Mass Spectrometry on Formalin-Fixed Paraffin-Embedded Tissue Enables the Delineation of Ovarian Cancer Tissues</i> . Molecular & Cellular Proteomics 07/2016; 15(9):mcp.M116.059816., DOI:10.1074/mcp.M116.059816

Principal Author

Name of Principal Author (Candidate)	Matthew T. Briggs		
Contribution to the Paper	Conceived the project Data collection and analysis Prepared figures and wrote the main manuscript text		
Overall percentage (%)	40%		
Certification:	This paper reports on original research I conducted during the period of my Higher Degree by Research candidature and is not subject to any obligations or contractual agreements with a third party that would constrain its inclusion in this thesis. I am the primary author of this paper.		
Signature		Date	05/07/18

Co-Author Contributions

By signing the Statement of Authorship, each author certifies that:

- i. the candidate's stated contribution to the publication is accurate (as detailed above);
- ii. permission is granted for the candidate to include the publication in the thesis; and
- iii. the sum of all co-author contributions is equal to 100% less the candidate's stated contribution.

Name of Co-Author	Arun V. Everest-Dass		
Contribution to the Paper	Conceived the project Data collection and analysis Prepared figures and wrote the main manuscript text Equally contributed to this work		
Signature		Date	12/12/17

Name of Co-Author	Gurjeet Kaur		
Contribution to the Paper	Annotated the H&E stained FFPE sections		
Signature		Date	13/12/17

Name of Co-Author	Martin K. Oehler		
Contribution to the Paper	Provided the ovarian tissue samples		
Signature		Date	12/12/17

Name of Co-Author	Nicolle H. Packer		
Contribution to the Paper	Conceived the project Designed the experiments and supervised the research		
Signature		Date	18/04/18

Name of Co-Author	Peter Hoffmann		
Contribution to the Paper	Conceived the project Designed the experiments and supervised the research		
Signature		Date	20/12/17

N-glycan MALDI Imaging Mass Spectrometry on Formalin-Fixed Paraffin-Embedded Tissue Enables the Delineation of Ovarian Cancer Tissues*†‡

Arun V. Everest-Dass‡‡^a, Matthew T. Briggs††^a, Gurjeet Kaur**, Martin K. Oehler‡‡§§, Peter Hoffmann††‡‡^b, and Nicolle H. Packer‡‡§^b

Ovarian cancer is a fatal gynaecological malignancy in adult women with a five-year overall survival rate of only 30%. Glycomic and glycoproteomic profiling studies have reported extensive protein glycosylation pattern alterations in ovarian cancer. Therefore, spatio-temporal investigation of these glycosylation changes may unearth tissue-specific changes that occur in the development and progression of ovarian cancer. A novel method for investigating tissue-specific N-linked glycans is using matrix-assisted laser desorption/ionization (MALDI) mass spectrometry imaging (MSI) on formalin-fixed paraffin-embedded (FFPE) tissue sections that can spatially profile N-glycan compositions released from proteins in tissue-specific regions. In this study, tissue regions of interest (e.g. tumor, stroma, adipose tissue and necrotic areas) were isolated from FFPE tissue sections of advanced serous ovarian cancers (n 3). PGC-LC-ESI-MS/MS and MALDI-MSI were used as complementary techniques to firstly generate structural information on the tissue-specific glycans in order to then obtain high resolution images

of the glycan structure distribution in ovarian cancer tissue. The N-linked glycan repertoires carried by the proteins in these tissue regions were structurally characterized for the first time in FFPE ovarian cancer tissue regions, using enzymatic peptide-N-glycosidase F (PNGase F) release of N-glycans. The released glycans were analyzed by porous graphitized carbon liquid chromatography (PGC-LC) and collision induced electrospray negative mode MS fragmentation analysis. The N-glycan profiles identified by this analysis were then used to determine the location and distribution of each N-glycan on FFPE ovarian cancer sections that were treated with PNGase F using high resolution MALDI-MSI. A tissue-specific distribution of N-glycan structures identified particular regions of the ovarian cancer sections. For example, high mannose glycans were predominantly expressed in the tumor tissue region whereas complex/hybrid N-glycans were significantly abundant in the intervening stroma. Therefore, tumor and non-tumor tissue regions were clearly demarcated solely on their N-glycan structure distributions. *Molecular & Cellular Proteomics* 15: 10.1074/mcp.M116.059816, 3003–3016, 2016.

From the ‡Faculty of Science, Biomolecular Frontiers Research Centre, Macquarie University, Sydney, NSW, 2109, Australia; §ARC Centre for Nanoscale BioPhotonics, Macquarie University, Sydney, NSW, 2109, Australia; †Adelaide Proteomics Centre, School of Biological Sciences, University of Adelaide, Adelaide, South Australia, 5005, Australia; Institute for Photonics & Advanced Sensing (IPAS), University of Adelaide, Adelaide, South Australia, 5005, Australia; **Institute for Research in Molecular Medicine (INFORMM), Universiti Sains Malaysia, Pulau Pinang, Malaysia; ‡‡Department of Gynaecological Oncology, Royal Adelaide Hospital, Adelaide, South Australia, 5005, Australia; §§Discipline of Obstetrics and Gynaecology, Robinson Institute, University of Adelaide, Adelaide, South Australia; †††Centre for Molecular Pathology, University of Adelaide, Adelaide, South Australia, 5005, Australia

Received March 20, 2016, and in revised form, July 7, 2016

Published, MCP Papers in Press, July 13, 2016, DOI

10.1074/mcp.M116.059816

Author contributions: NHP, PH, MTB and AVE-D conceived the project. NHP and PH, designed the experiments and supervised the research. MKO provided the ovarian tissue samples and GK annotated the H&E stained FFPE sections. MTB and AVE-D were primarily responsible for data collection and analysis. MTB and AVE-D prepared figures and wrote the main manuscript text. All authors contributed to the data analysis, discussions and manuscript preparation.

Ovarian cancer is the fifth most fatal malignancy in adult women with an estimated 21,290 new cases diagnosed and 14,180 deaths recorded in the United States during 2015 (1). There are several reasons for the poor prognosis of ovarian cancer and its diagnosis at advanced stage—lack of diagnostic markers for the early detection (2, 3), rapid metastasis of the disease (4), and limited or modest understanding of the etiology, origin and the diverse clinical and pathological behavior of the tumors (5). Moreover, epithelial ovarian cancer comprises of several distinct sub-types based on their histopathological features into serous, endometrioid, clear-cell, mucinous, and undifferentiated subtypes (6, 7).

Protein glycosylation is an important post-translational modification which has relevance in many biological processes such as cell signaling, immune responses, extracellular interaction and cell adhesion (8, 9). Aberrant protein glycosylation such as the expression of truncated glycans as well

as neo-expression of glycans are hallmarks of various cancers (10–12). These glycomic changes facilitate the discrimination between healthy and cancerous cells or potentially reflect tumor microheterogeneity caused by the variation between cancer subtypes (13, 14). Increased branching of *N*-glycans is a commonly observed glycosylation change in cancer, which has been shown to alter the overall structure and function of the glycoprotein (15–17). For example, the synthesis of increased branching antennas on the glycans creates available sites for the addition of sialic acids (Neu5Ac) by sialyltransferases, leading to increased sialylation being reported in many cancers (18–21). Similarly, changes in the expression of long chains of lactosamine (polyLacNAc) have also been reported to be associated with cancer (15). Likewise, terminal modifications of glycans on the cancer cell surface, such as fucosylation, give rise to the presence of Lewis and sialyl Lewis antigens that have been implicated in tumor progression and metastasis (22–26). These aberrant glycosylations play a significant role in malignant transformation and therefore afford a valuable opportunity to exploit cancer-specific protein glycosylation markers for prognosis and diagnosis (16).

Mass spectrometry (MS)-based glycomic methodologies are now regularly used for the reliable profiling of glycans from clinical samples (17–22). In fact, MS identification and measurement of glycans are being pursued as a structurally-informative approach as opposed to the clinically-established immunological assays (23–25) or arrays (26). Several quantitative glycomic profiling studies have identified *N*-glycan changes that were statistically elevated in ovarian cancer patients' plasma (17, 27–29). A significant increase in branching and sialylation patterns as well as increased expression of α 2–6 sialylation in ovarian cancer plasma as compared with healthy controls have been reported (28). Saladova *et al.*, reported specific *N*-glycosylation changes on serum glycoproteins from ovarian cancer patients, including a decrease in galactosylation of IgG and an increase in sialyl Lewis X (SLe(x)) on haptoglobin beta-chain, alpha1-acid glycoprotein and alpha1-antichymotrypsin (30). We have also observed membrane glycosylation changes between non-cancerous ovarian surface epithelial (HOSE 6.3 and HOSE 17.1) and serous ovarian cancer cell lines (SKOV 3, IGROV1, A2780, and OVCAR3) (31). The “bisecting *N*-acetylglucosamine” type *N*-glycans, increased levels of α 2–6 sialylated *N*-glycans and “N,N-diacetyl-lactosamine” type *N*-glycans were predominantly observed in serous ovarian cancer cell lines while absent in the noncancerous ovarian cells. Most of these studies yielded clinically relevant information on the differential expression of glycans, but the major focus of their analysis was on plasma-based tests to differentiate between healthy and diseased patients rather on the spatial tissue location of the expressed glycans.

To address this challenge, we have employed glycomic profiling strategy to first identify the detailed *N*-glycan struc-

tural changes that occur on different regions of FFPE ovarian tissues clinically diagnosed as serous ovarian cancer. Routine mass spectrometric glycoanalysis is well-established and reliable, but the analysis of whole tissues destroys any information relating to the spatial distribution of the analytes. Matrix-assisted laser desorption/ionization (MALDI) mass spectrometry imaging (MSI) is an emerging technique that seeks to utilize the analytical advantages of mass spectrometry while preserving the spatial information of the biological molecule of interest inherent in the sample. The unambiguous correlation between histopathology and MALDI-MSI allows the mass measurement of sugars, proteins, peptides, lipids, and metabolites directly from tissue regions. The distribution and intensity of the detected biomolecules can then be visualized as an image. Furthermore, conventional histological staining can be compared on the same tissue section. Overlaying the MS images and optical microscope morphological images then can differentiate the specific molecules in each minute tissue section and can relate molecular distribution to the biological functions and morphological changes of an organ/organelle.

MALDI-MSI can be used for both targeted and untargeted molecular mass analysis. A typical example of a targeted analysis is the measurement of a single metabolite mass distribution in tissue, whereas untargeted analysis could include the mass distribution of biomolecules such as protein, lipid or carbohydrates in a tissue. Some MALDI-MSI applications include gaining a fundamental understanding of the expression of biomolecules in a disease state, investigating and characterizing the biomolecules spatially across tissue sections, and developing new ways of imaging *in situ*. There have been a few MALDI-MSI based analyses on the spatial localization of *N*-glycans on tissue (32–35). Recently glycan MALDI-MSI was used to image released glycan masses from Tissue MicroArrays (TMAs) of liver cancer in which many small tumor tissue samples from different patients were assembled on a single slide, and provided proof of concept that released glycans could be imaged on FFPE liver cancer tissue sections (33).

Specifically, in this study we (1) identify the structural glycan features that are characteristic of serous ovarian cancer specimens by detailed PGC-LC-ESI-MS/MS, (2) use this information to identify a panel of tissue-specific glycan markers in

¹ The abbreviations used are: MALDI, matrix-assisted laser desorption/ionization; MSI, mass spectrometry imaging; FFPE, formalin-fixed paraffin-embedded; CID, collision-induced dissociation; ESI, electrospray ionization; LC, liquid chromatography; MS/MS, tandem mass spectrometry; GnT-V, *N*-acetylglucosaminyltransferase V; NeuAc, *N*-acetylneuraminic acid; NeuGc, *N*-glycolylneuraminic acid; Man, mannose; PGC, porous graphitized carbon; PNGase F, peptide-*N*-Glycosidase F; Le^a, Lewis a antigen; Gal, galactose; Fuc, fucose; GlcNAc, *N*-acetylglucosamine; ITO, Indium tin oxide; TFA, Trifluoroacetic acid; DHB, 2,5-Dihydroxybenzoic acid; EtOH, Ethanol; H&E, haematoxylin and eosin.

order to discriminate between tumor and nontumor tissue by high resolution MALDI-MSI, and (3) perform a rigorous evaluation of the tissue diagnostic glycan structures using independent statistical procedures. It is envisioned that the identification of the differential localization of glycan structures may improve ovarian cancer diagnosis and further lead to novel therapeutic strategies to improve survival rates for this malignancy.

MATERIALS AND METHODS

Reagents—Glycerol free PNGase F (P0705L, 75,000 NEB units) was purchased from New England Biolabs (Ipswich, MA). DHB matrix were purchased from Sigma-Aldrich (Steinheim, Germany) and Bruker Daltonics (Bremen, Germany). Formalin was from Sigma-Aldrich. Trifluoroacetic acid (TFA), ethanol and NaCl were from Merck (Darmstadt, Germany). Nitrocellulose membranes (0.025 μm VSWP) for dialysis were purchased from Millipore (Cork, Ireland). Xylene was purchased from Chem-Supply (Gillman, South Australia). Indium tin oxide (ITO) slides were purchased from Bruker Daltonics, whereas PEN membrane slides were from MicroDissect (Herborn, Germany). GLY3 standards ($\text{Man}_5\text{GlcNAc}_2$, $\text{Man}_3\text{GlcNAc}_5$, $\text{Man}_3\text{Gal}_4\text{GlcNAc}_6$) were purchased from Prozyme (Hayward, CA). Unless otherwise stated, all H_2O used was ultrapure (*i.e.* $\geq 18.2 \Omega$ and ≤ 5 ppb TOC).

Tissue Sectioning—Tissue sectioning was performed as previously described with some minor modifications (36). Ovarian tumors tissue was taken from FIGO stage III ovarian cancer patients as part of experiments with full ethics approval and in accordance with the policies of the University of Adelaide Ethics Committee. Formalin was diluted 1:9.25 in 1 PBS and tissues were immersed in this solution overnight at 4°C. Tissue was then removed from the formalin, rinsed with de-ionized H_2O and stored in 70% EtOH before processing with a Leica TP 1020 processor (Leica Biosystems, North Ryde, Australia). Protocol: 70% EtOH for 5 min, 80% EtOH for 2 h, 95% EtOH for 2 h, 3 x 100% EtOH for 2 h each, 2 x xylene for 2 h each and 2 x paraffin for 2 h each. A Leica EG 1140H embedder (Leica Biosystems) was used to create paraffin embedded tissue blocks. FFPE blocks were sectioned (6 μm thick) on a Microm HM325 microtome (Zeiss, Goettingen, Germany) and water bath mounted (39°C) onto ITO slides (Bruker Daltonics) or PEN membrane slides (MicroDissect). Slides were left to dry at 37°C for one hour prior to storage at 4°C.

PGC-LC-ESI-Ion Trap MS and MS/MS Analysis of N-glycans Released from FFPE Tissue Sections—

In-solution PNGase F Digestion—Tissue sections on PEN membrane slides ($n = 3$) were used and processed as described previously (34), with modifications. Briefly, following a 5 min 60°C heating block incubation, 90 s xylene wash and 60 s EtOH wash, the whole FFPE tissue section was scraped off slide by a scalpel and deposited into micro-vials. The tissue sections were incubated (2 x 5 min) in 10 mM NH_4HCO_3 . Solution was removed and replaced with 10 mM citric acid (pH 6) and heated at 98°C for 45 min. The samples were washed twice with 10 mM NH_4HCO_3 . Glycerol free PNGase F (2 μl , non-dialyzed) was added to the FFPE tissue in a 40 μl total reaction volume (with 25 mM NH_4HCO_3). The tissue digests were left overnight at 37°C.

N-linked Glycan Release—The released N-linked glycans were reduced and desalted according to previously described methods (34). After acidification with 100 mM NH_4COOH pH 5 (10 μl) for 60 min at room temperature, the samples were dried in a vacuum centrifuge and were reduced with 20 μl of 1 M NaBH_4 in 50 mM KOH at 50°C for 3 h. The reduction was quenched with 1 μl glacial acetic acid and the N-linked glycan alditols were desalted as described below.

Glycan Purification—The released N-glycans were desalted using cation exchange columns comprising 30 μl AG50W-X8 cation-exchange resin (BioRad, Hercules, CA) packed on top of a C18 StageTip Frit. Residual borate was removed by the addition of methanol (x3) and drying under vacuum. The glycans were further purified by tips using porous graphitized carbon slurry manually packed onto C18 StageTip Frits as previously described.

PGC-LC-ESI-Ion Trap MS and MS/MS—The N-glycans were resuspended in 10 μl of milli-Q water and subjected to PGC-LC-ESI MS/MS separation and analysis using an Agilent 1100 capillary LC (Agilent Technologies, Santa Clara, CA) and analyzed using an Agilent MSD, three-dimensional ion-trap XCT mass spectrometer coupled to the LC. Separation was performed on a Hypercarb Porous Graphitized Carbon column (PGC, 3 μm particle size, 100 x 0.18 mm, Hypercarb, Thermo Scientific). N-linked glycan alditols were separated across an 85 min gradient with a constant flow rate of 2 $\mu\text{l}/\text{min}$ using a linear gradient up to 45% (v/v) CH_3CN in 10 mM NH_4HCO_3 . ESI-MS was performed in negative ion mode with two scan events; MS full scan with mass range 100–2000 m/z and data dependent MS/MS scan after collision-induced dissociation (CID) of the top two most intense precursor ions.

MALDI-MSI Analysis of N-glycans Released In Situ From FFPE Tissue Sections—

Tissue Section Antigen Retrieval—Tissue sections were re-hydrated using a standard procedure for citric acid antigen retrieval (CAAR) (34). Briefly, the tissue sections were heated at 60°C for 1 h over a heatblock; washed in 100% xylene (2 x 5 min) and 100% ethanol (2 x 2 min). Sections were washed in 10 mM NH_4HCO_3 (2.5 min) followed by a 10 min incubation in boiling 10 mM citric acid (pH 6.0) and then by heating at 98°C for 30 min on a heating block. Finally, tissue sections were immersed twice in 10 mM NH_4HCO_3 (1 min) and dried at room temperature in a humid chamber.

In Situ PNGase F Digestion and Matrix Deposition—Neat PNGase F enzyme (40 μl) spotted onto a nitrocellulose membrane and drop dialyzed against water for 2 h at room temperature. NH_4HCO_3 (25 mM, pH 8.2) was added to the dialyzed PNGase F to a total volume of 200 μl and the PNGase F was printed onto retrieved tissue sections (15 nL at 250 μm spacing) using a ChIP-1000 (Shimadzu, Japan). Buffer control arrays (25 mM NH_4HCO_3) were printed using the same conditions on adjacent sections. Tissue sections were incubated overnight at 37°C in a humid chamber and GLY3 standard was manually spotted (0.5 μl) on an adjacent section. DHB (20 mg/ml) in 0.1% (v/v) TFA and 1 mM NaCl was sprayed onto prepared tissues using a TM-sprayer. Instrument specific settings: 16 passes, 0.05 ml/min flow rate, 4 psi N_2 pressure, 65°C capillary temperature, 800 mm/min.

MALDI-TOF/TOF Mass Spectrometry and Histological Staining—MS data was acquired using an ultrafleXtreme MALDI-TOF/TOF mass spectrometer (Bruker Daltonics) controlled by flexControl (v3.4, Bruker Daltonics) and flexImaging (v4.0, Bruker Daltonics). Instrument-specific settings were as follows: 800 – 4500 m/z range, 700 Da matrix suppression, 2 kHz laser repetition rate and 2.5 GS/s. Method-specific settings were as follows: 75% laser power and 2698 V detector gain. A total of 1000 shots were acquired at each position with no walk. Data was acquired by oversampling from an arbitrary array with center to center acquisition distance of 100 μm overlaid onto the 250 μm PNGase F array. The MALDI-TOF/TOF instrument was externally calibrated using the included GLY3 standard spots prior to MALDI imaging.

Following analysis, DHB matrix was eluted using 70% EtOH and tissue sections were hematoxylin and eosin (H&E) stained as described previously (34).

Data Analysis—MALDI-MSI data was analyzed by SCiLS Lab (version 2014a, SCiLS, Bruker Daltonics). Raw data was loaded and

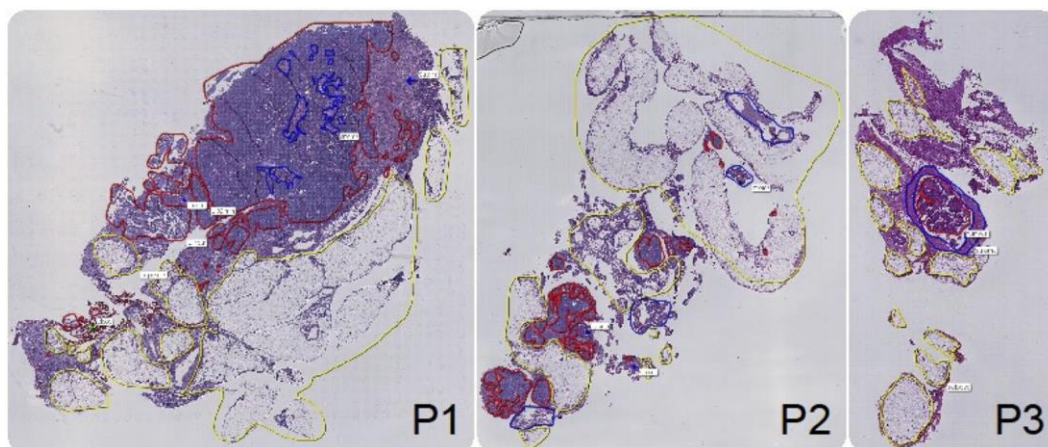


FIG. 1. Hematoxylin and eosin (H&E) stains of tissue sections from each patient (P1, P2 and P3) that were used for MALDI mass spectrometry imaging (MSI) analysis. Tissue-types were annotated by a pathologist post-MALDI-MSI based on the histology with tumor (red), stroma (blue), adipose (yellow), and necrotic (green) regions identified.

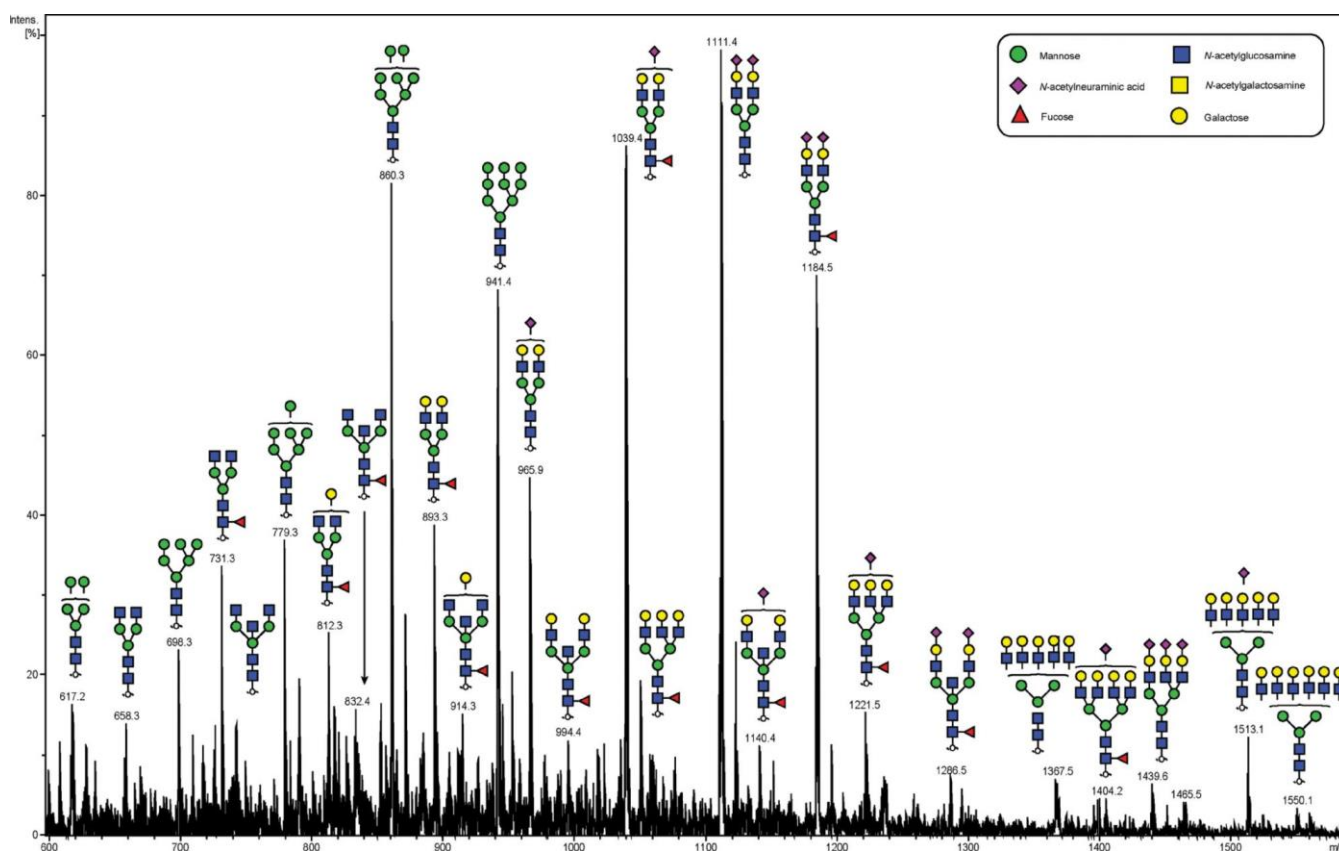


FIG. 2. Negative ion mode summed MS spectrum of patient P1 ovarian tissue annotated with proposed structures for *N*-glycans identified by PGC-LC-ESI MS/MS. *N*-glycans released in-solution from formalin-fixed paraffin-embedded ovarian cancer tissue (P1) using PNGaseF were reduced, de-salted and purified on a carbon column prior to porous graphitic column chromatography coupled online to an ESI-IT-MS system. The proposed glycan structures were deduced from their doubly charged negative ion monoisotopic masses $[M-2H]^{-2}$.

reduced to 50,000 points per spectrum. Data was preprocessed by baseline subtraction and normalization to total ion current (TIC). Peaks were picked, aligned and the preprocessed data was used to generate log ion intensity maps. These log ion intensity maps were weakly denoised with automatic hotspot removal. Data analysis of the LC-ESI-MS/MS data was carried out in ESI-Compass 1.3 (Bruker Daltonics, Bremen, Germany).

RESULTS

In this study, we employed the *N*-linked glycan mass spectrometry imaging technique that we have previously established (34). Briefly, the method combines released *N*-glycan MALDI-MSI of FFPE tissue with parallel detailed *N*-glycan structural characterization by negative ion PGC-LC-ESI-

TABLE 1

N-glycan structures assigned by PGC-LC-ESI-ion trap MS/MS. *N*-glycan structures found in formalin-fixed paraffin-embedded ovarian cancer tissue (P1 and P2) by PGC-LC-ESI-MS/MS (singly negatively charged monoisotopic masses ($M-H^{-1}$ were calculated from their observed doubly negatively charged monoisotopic masses ($M-2H^{-2}$), matching composition and proposed structure. Y = Yes, N = No; observed in the patient samples

No.	RT(mins)	[M-2H] ²⁻	[M-H] ⁻¹	P1	P2	P3	Composition	Structure
1	45.1		911.3	Y	Y	Y	(Man) ₃ (GlcNAc) ₂	
2	34.2	617.3	1235.6	Y	Y	Y	(Man) ₂ + (Man) ₃ (GlcNAc) ₂	
3	37.5	658.3	1317.6	Y	N	N	(GlcNAc) ₂ + (Man) ₃ (GlcNAc) ₂	
4a	34.5	698.3	1397.6	Y	Y	Y	(Man) ₃ + (Man) ₃ (GlcNAc) ₂	
4b	38.4							
5	44	731.4	1463.8	Y	Y	Y	(GlcNAc) ₂ (Fuc) ₁ + (Man) ₃ (GlcNAc) ₂	
6	41.2	739.3	1479.6	Y	Y	Y	(Gal) ₁ (GlcNAc) ₂ + (Man) ₃ (GlcNAc) ₂	
7a	33.7	779.3	1559.6	Y	Y	Y	(Man) ₄ + (Man) ₃ (GlcNAc) ₂	
7b	36.8							
7c	38.7							
8	41.3	799.7	1600.5	N	Y	Y	(Gal) ₁ (Man) ₂ (GlcNAc) ₁ + (Man) ₃ (GlcNAc) ₂	
9	44.2	812.3	1625.6	Y	Y	Y	(Gal) ₁ (GlcNAc) ₂ (Fuc) ₁ + (Man) ₃ (GlcNAc) ₂	
10	43.1	820.3	1641.6	Y	Y	Y	(Gal) ₂ (GlcNAc) ₂ + (Man) ₃ (GlcNAc) ₂	
11	35.9	832.8	1666.6	Y	Y	Y	(GlcNAc) ₃ (Fuc) ₁ + (Man) ₃ (GlcNAc) ₂	
12a	33.5	860.3	1721.6	Y	Y	Y	(Man) ₅ + (Man) ₃ (GlcNAc) ₂	
12b	37.2							
13	47.7	893.3	1787.6	Y	Y	Y	(Gal) ₂ (GlcNAc) ₂ (Fuc) ₁ + (Man) ₃ (GlcNAc) ₂	

MS/MS (36). The *N*-glycan analysis was applied to FFPE sections of the ovarian tissue from three FIGO stage III ovarian cancer patients labeled P1, P2 and P3. Fig. 1 shows hematoxylin and eosin (H&E) stains for tissue sections from patients P1, P2, and P3.

We initially characterized the *N*-glycans of whole tissue sections in detail using negative ion mode PGC-LC-ESI-MS/MS to construct a repository which could be used for assigning a glycan structure to the corresponding glycan masses from spatially localized MALDI-MSI data. *N*-glycan structures were manually assigned *via* the following steps: (1) The monosaccharide composition was deduced based on the mass of the released *N*-glycan masses (using GlycoMod <http://web.expasy.org/glycomod/>) (36) whereas structures, where shown, were deduced by interpretation of the MS² fragments and biological pathway constraints, (2) mass-

matching of theoretical fragment mass ions produced by tandem MS for each structure, (3) use of diagnostic fragment ions in negative ion mode that have been previously reported for the identification of specific glycan structural features (19, 37, 38), and (4) known expression of glycans based on biological pathway constraints. A representative summed negative ion mode MS profile of patient P1 with assigned glycan structures is shown in Fig. 2.

In total, 40 individual *N*-glycan masses (including structural and compositional isomers) were detected across the whole FFPE sections from in-solution enzyme release of the *N*-glycans from a whole FFPE ovarian tissue section (see Table I). These *N*-glycan classes included high mannose, core fucosylated, hybrid and complex (neutral and sialylated). Sialylated *N*-glycans were further classified based on the number of sialic acid residues, in which mono-, di- and tri-sialylated

TABLE 1—continued

14	38	913.8	1828.6	Y	Y	Y	(Gal) ₂ (GlcNAc) ₃ (Fuc) ₁ + (Man) ₃ (GlcNAc) ₂	
15	37.5	941.3	1883.6	Y	N	Y	(Man) ₆ + (Man) ₃ (GlcNAc) ₂	
16	42.1	945.4	1891.8	N	Y	Y	(Gal) ₁ (Man) ₂ (GlcNAc) ₁ (NeuAc) ₁ + (Man) ₃ (GlcNAc) ₂	
17a	43.9	965.9	1932.8	Y	Y	Y	(Gal) ₂ (GlcNAc) ₂ (NeuAc) ₁ + (Man) ₃ (GlcNAc) ₂	
17b	51.2							
18	39.4	994.9	1990.8	Y	Y	Y	(Gal) ₂ (GlcNAc) ₃ (Fuc) ₁ + (Man) ₃ (GlcNAc) ₂	
19	39.6	1022.4	2045.8	Y	Y	Y	(Glc) ₁ (Man) ₆ + (Man) ₃ (GlcNAc) ₂	
20a	48	1038.9	2078.8	Y	Y	Y	(Gal) ₂ (GlcNAc) ₂ (Fuc) ₁ (NeuAc) ₁ + (Man) ₃ (GlcNAc) ₂	
20b	55.3							
21	47.3	1075.9	2152.8	Y	Y	Y	(Gal) ₃ (GlcNAc) ₃ (Fuc) ₁ + (Man) ₃ (GlcNAc) ₂	
22	41.1	1140.5	2282	Y	Y	Y	(Gal) ₂ (GlcNAc) ₃ (Fuc) ₁ (NeuAc) ₁ + (Man) ₃ (GlcNAc) ₂	
23	34.2	1062.3	2125.6	N	Y	Y	(Glc) ₁ (Man) ₇ (Phos) ₁ + (Man) ₃ (GlcNAc) ₂	
24a	44.4	1111.4	2223.8	Y	Y	Y	(Gal) ₂ (GlcNAc) ₂ (NeuAc) ₂ + (Man) ₃ (GlcNAc) ₂	
24b	48.2							
24c	51.5							
25a	52.5	1184.4	2369.8	Y	Y	Y	Gal) ₂ (GlcNAc) ₂ (Fuc) ₁ (NeuAc) ₂ + (Man) ₃ (GlcNAc) ₂	
25b	55							
25c	60.3							
26	55.3	1221.4	2443.8	Y	Y	N	(Gal) ₃ (GlcNAc) ₃ (Fuc) ₁ (NeuAc) ₁ + (Man) ₃ (GlcNAc) ₂	
27	41.8	1285.9	2572.8	N	N	N	(Gal) ₂ (GlcNAc) ₃ (Fuc) ₁ (NeuAc) ₂ + (Man) ₃ (GlcNAc) ₂	
28	52.5	1368.3	2737.6	N	N	N	(Gal) ₅ (GlcNAc) ₅ (Fuc) ₁ + (Man) ₃ (GlcNAc) ₂	
29	51.4	1404.2	2809.4	N	N	N	(Gal) ₄ (GlcNAc) ₄ (Fuc) ₁ (NeuAc) ₁ + (Man) ₃ (GlcNAc) ₂	
30	49.7	1439.7	2880.4	N	N	N	(Gal) ₃ (GlcNAc) ₃ (NeuAc) ₃ + (Man) ₃ (GlcNAc) ₂	

N-glycans were all observed to be present, Specifically the three most abundant glycan structures were comprised of sialylated *N*-glycans characterized by LC-ESI-MS/MS analy-

sis, Structural isomers corresponding to differences in sialic acid linkages were also observed for some of the *N*-glycan masses. (1111.4² and 1184.4²). Isomers with α 2–3 or α

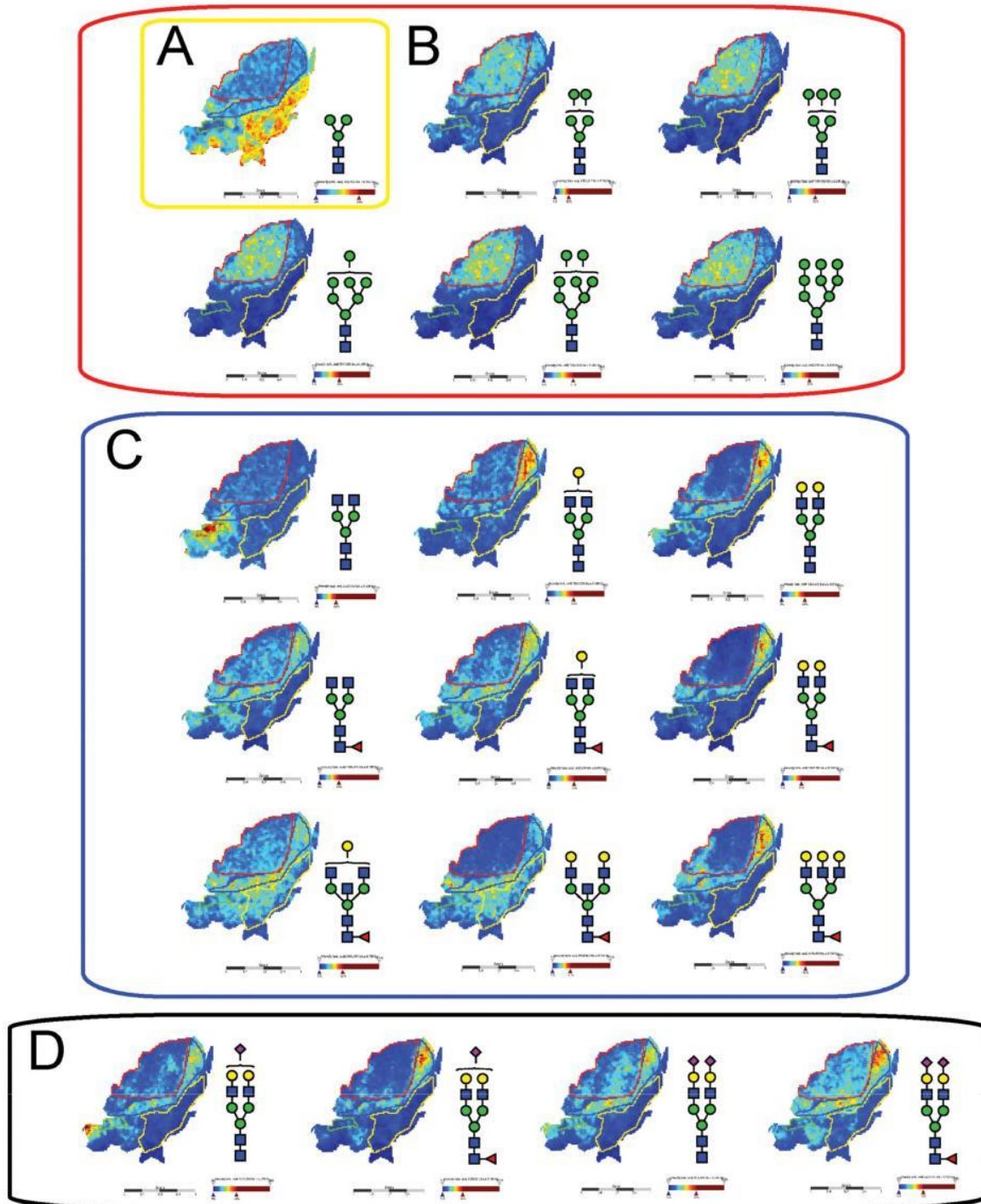


FIG. 3. MALDI mass spectrometric imaging of *N*-linked glycans released from patient P1 ovarian cancer tissue sections. Formalin-fixed paraffin-embedded ovarian cancer tissue sections were treated with antigen retrieval prior to printing of 15 nL/spot dialyzed PNGase F or buffer control arrays with 250 μm spacing. DHB (20 mg/ml) was sprayed onto the sections and MS spectra were acquired by oversampling at 100 μm intervals using a MALDI-TOF/TOF MS instrument. Monoisotopic glycan masses were measured in the positive ion reflectron mode as (M Na) adducts. Panel A shows the log ion intensity map for the m/z 933.3 of a pauci mannose structure was observed to be localized and relatively highly expressed in the adipose tissue region of the FFPE tissue. The agalactosylated bisecting structure of m/z 1339.4 was observed only in the necrotic tissue of the sample P1. Five high mannose structures (m/z 1257.4, 1419.4, 1581.5, 1743.4, and 1905.6) were observed predominantly in the tumor region as shown in panel B. The hybrid/complex *N*-glycan structures were indicative of the stroma region as shown in panel C (m/z 1501.5, 1663.5, 1485.4, 1809.6, 1647.6, 1850.6, 2012.7, and 2174.7) and the sialylated structures are represented in panel D shows log ion intensities of the sialylated glycans of m/z 1954.6, 2245.7, 2100.7, and 2391.8.

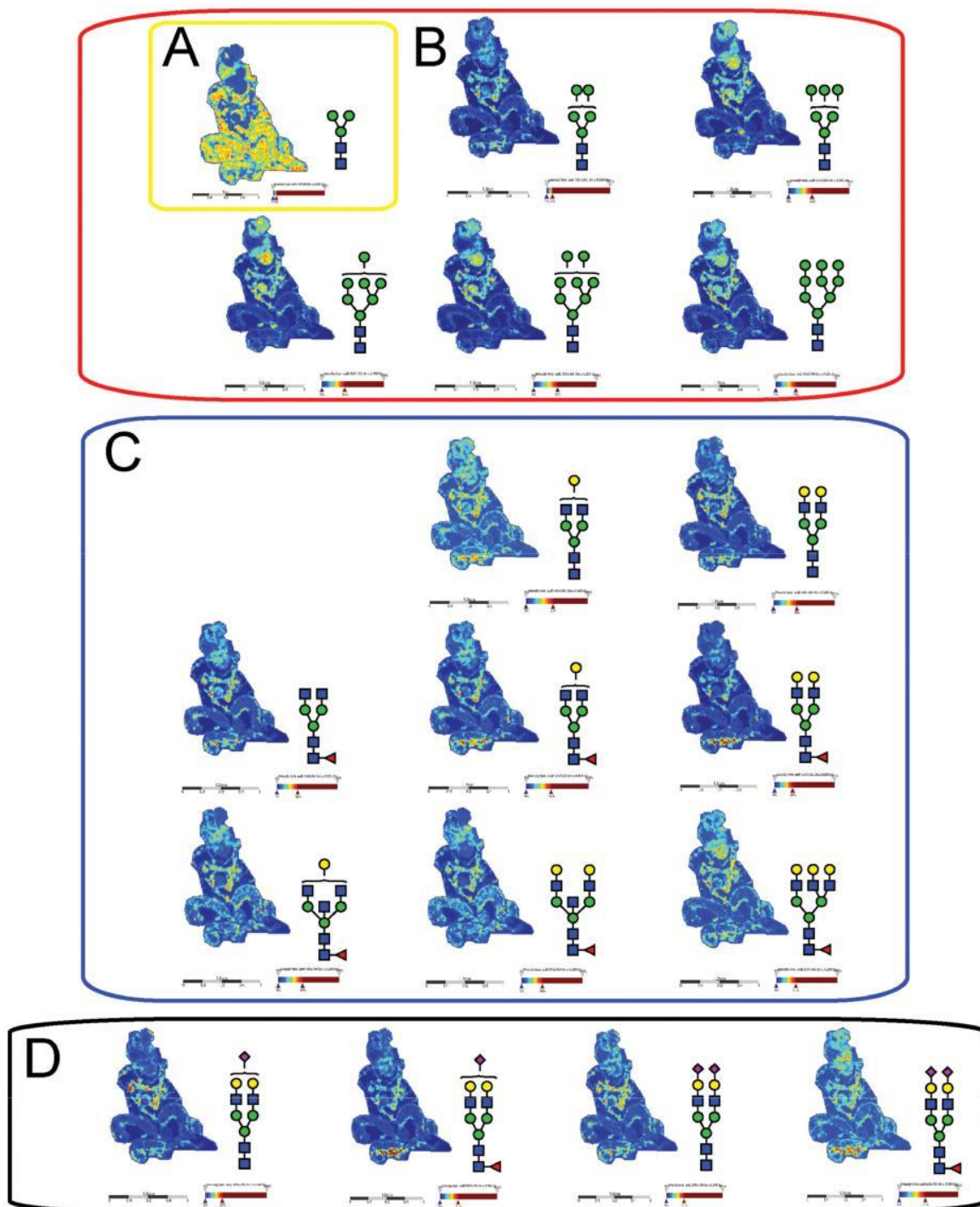


FIG. 4. MALDI mass spectrometry imaging of *N*-linked glycans released from patient P2 ovarian cancer tissue sections. Formalin-fixed paraffin-embedded ovarian cancer tissue sections were treated with antigen retrieval prior to printing of 15 nL/spot dialyzed PNGase F or buffer control arrays with 250 μm spacing. DHB (20 mg/ml) was sprayed onto the sections and MS spectra were acquired by oversampling at 100 μm intervals using a MALDI-TOF/TOF MS instrument. Monoisotopic glycan masses were measured in the positive ion reflectron mode as (M Na) adducts. Panel A, shows the log ion intensity map for the m/z 933.3 of a pauci-mannose structure was observed to be localized and relatively highly expressed in the adipose tissue region of the FFPE tissue. Five high-mannose structures (m/z 1257.4, 1419.4, 1581.5, 1743.4, and 1905.6) were observed predominantly in the tumor region as shown in panel B. The hybrid/complex *N*-glycan structures were indicative of the stroma region as shown in panel C (m/z 1501.5, 1663.5, 1485.4, 1809.6, 1647.6, 1850.6, 2012.7, and 2174.7) and the sialylated structures are represented in panel D shows log ion intensities of the sialylated glycans of m/z 1954.6, 2245.7, 2100.7, and 2391.8.

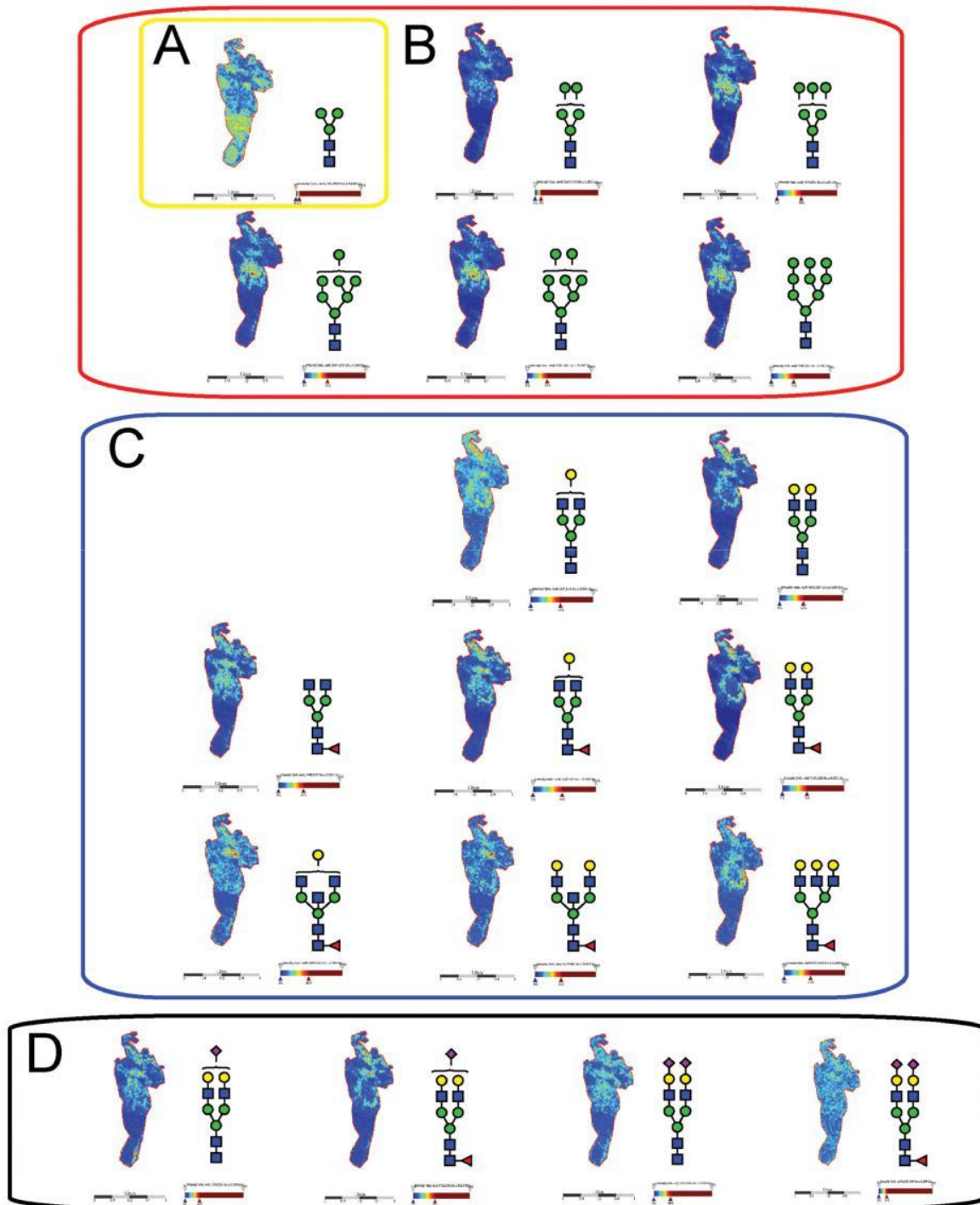


FIG. 5. MALDI mass spectrometry imaging of *N*-linked glycans released from patient P3 ovarian cancer tissue sections. Formalin-fixed paraffin-embedded ovarian cancer tissue sections were treated with antigen retrieval prior to printing of 15 nL/spot dialyzed PNGase F or buffer control arrays with 250 μm spacing. DHB (20 mg/ml) was sprayed onto the sections and MS spectra were acquired by oversampling at 100 μm intervals using a MALDI-TOF/TOF MS instrument. Monoisotopic glycan masses were measured in the positive ion reflectron mode as (M Na) adducts. Panel A shows the log ion intensity map for the m/z 933.3 of a pauci mannose structure was observed to be localized and relatively highly expressed in the adipose tissue region of the FFPE tissue. Five high mannose structures (m/z 1257.4, 1419.4, 1581.5, 1743.4, and 1905.6) were observed predominantly in the tumor region as shown in panel B. The hybrid/complex *N*-glycan structures were indicative of the stroma region as shown in panel C (m/z 1501.5, 1663.5, 1485.4, 1809.6, 1647.6, 1850.6, 2012.7, and 2174.7) and the sialylated structures are represented in panel D shows log ion intensities of the sialylated glycans of m/z 1954.6, 2245.7, 2100.7, and 2391.8.

2– 6 sialic acids were differentiated based on the chromatographic behavior and retention times of previous studies (31, 38, 39). Detailed structural characterization of the N-glycans was carried out by tandem MS fragmentation analysis. Examples of the collision-induced dissociation (CID) fragmentation of N-glycans in negative mode analysis characterized in this study is described using two examples in supplemental Fig. S2 for glycan masses of (1) m/z 693.3² and (2) m/z 832.8².

For MALDI imaging analysis, duplicate FFPE ovarian tumor sections of each patient (P1, P2 and P3) were then prepared for N-glycan MALDI-MSI by antigen retrieval and PNGase F printing onto the tissue sections followed by overnight incubation at 37°C and spray deposition of DHB.

Intensity ion maps for the three FFPE samples (P1, P2, P3) of the glycan masses detected (Table 1) in the LC-ESI-MS analysis were constructed. Representative ion intensity maps of the positive ion monoisotopic masses of the tissue sections are shown in Figs. 3, 4 and 5. The spatial distribution and localization of these structures were observed to be class dependent. For example, the adipose tissue region corresponded to the location of the pauci-mannose glycan (Man)₃(GlcNAc)₂ of mass m/z 933.3 in all patient samples (Fig. 3A, 4A, 5A). Similarly, all high mannose glycans were significantly abundant in the tumor region across the three samples (Fig. 3B, 4B, and 5B) corresponding to glycan masses of m/z 1257.4, 1419.4, 1581.5, 1743.4, and 1905.6. Although complex bi-antennary and tri-antennary antennary structures were abundantly observed in the stromal region (masses m/z 1501.5, 1663.5, 1485.4, 1809.6, 1647.6, 1850.6, 2012.7, and 2174.7 (Fig. 3C, 4C, and 5C), mono and di-sialylated structures (m/z 1954.6, 2245.7, 2100.7, and 2391.8) were observed as sodiated adducts as shown in Fig. 3D, 4D, and 5D, predominantly in the stromal region, although traces of these species were also observed in the tumor regions.

The *In situ* PNGase-F released N-glycans were easily able to discriminate these four tissue-types by single unique glycan masses; for example, four distinct N-glycan masses that are representative of different glycan classes discriminated the four different tissues within the FFPE section as shown in Fig. 6. The log ion intensity map for the m/z 1339.4 corresponding to the agalactosylated bi-antennary glycan (GlcNAc)₂(Man)₃(GlcNAc)₂ was observed to be localized and relatively highly abundant only in the necrotic region of the FFPE tissue section (Fig. 6C). On the other hand, the mass m/z 2175.5 corresponding to a complex fucosylated tri-antennary structure ((Gal)₃(GlcNAc)₃(Fuc)₁(Man)₃(GlcNAc)₂) was observed predominantly in the stroma region. The adipose tissue region was demarcated solely by the mass of the pauci-mannose glycan (Man)₃(GlcNAc)₂ of mass m/z 933.3 (Fig. 6A). Importantly, the high mannose mass of m/z 1743.5 ((Man)₅(Man)₃(GlcNAc)₂) was indicative of the tumor region (Fig. 6B).

Statistical analysis by receiver operating curve (ROC) analysis and determination of the area under the ROC curve (AUC), was carried out to determine the specificity and sensitivity of using these N-glycans as potential discriminators of different tissue types. The AUC value from the ROC test is indicative of the diagnostic value of a specific indicator; specifically by a plot of sensitivity (*i.e.* the true-positive rate) versus specificity (*i.e.* the false-positive rate).

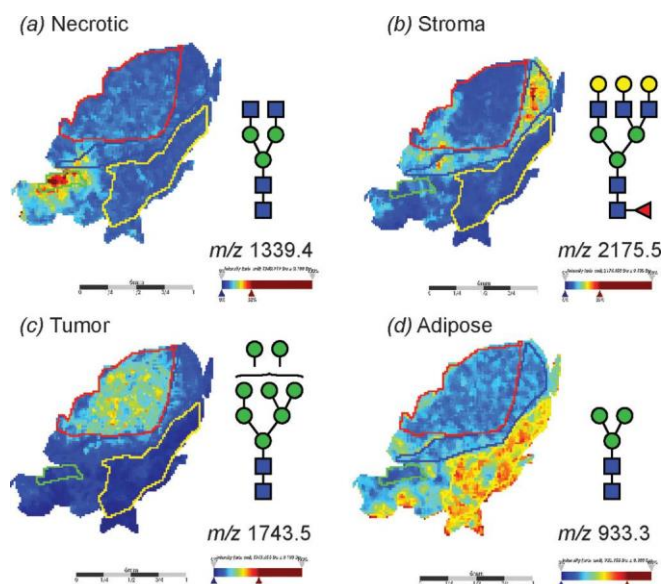


FIG. 6. MALDI imaging MS of N-linked glycans released from ovarian cancer sections. Formalin-fixed ovarian cancer sections were treated with antigen retrieval prior to printing of 30 nL/spot dialyzed PNGase F or buffer control arrays with 250 μ m spacing. DHB (20 mg/ml) was sprayed onto the sections and MS spectra were acquired by oversampling at 100 μ m intervals using a MALDI-TOF/TOF MS instrument. Monoisotopic glycan masses were measured in the positive ion reflectron mode as (M Na) adducts. Panel A shows the log ion intensity map for the m/z 1339.4 that corresponds to a (GlcNAc)₂(Man)₃(GlcNAc)₂ that was observed to be localized and relatively highly expressed in the necrotic tissue region of the FFPE tissue. Similarly, B m/z 2175.5 (Gal)₃(GlcNAc)₃(Fuc)₁(Man)₃(GlcNAc)₂ corresponding to a complex tri-antennary structure was observed predominantly in the stroma region. The high mannose mass of C m/z 1743.5 (Man)₅(Man)₃(GlcNAc)₂ was indicative of the tumor region. The adipose tissue region corresponded to the pauci-mannose glycan D (Man)₃(GlcNAc)₂ of mass m/z 933.3.

The four glycan masses used to discriminate the different tissue regions observed in Fig. 6 (masses m/z 1339.4, 2175.5, 1743.5, and 933.3) showed high AUC values between 0.84 to 0.99 (Fig. 7), confirming their potential power as discriminators between tumor, stromal, adipose, and necrotic tissue regions.

A data-driven approach was also implemented to discover whether glycan structural data alone can be used to define tissue morphology. To achieve this, the MALDI imaging data spectra were loaded into SCiLS Lab 2D software (version 2014a, SCiLS GmbH), which provides computational methods to analyze MALDI imaging datasets. A key feature of this software is spatial segmentation which allows whole spectra with similar features (*i.e.* peaks) to be clustered and thereby define regions in the tissue containing similar features.

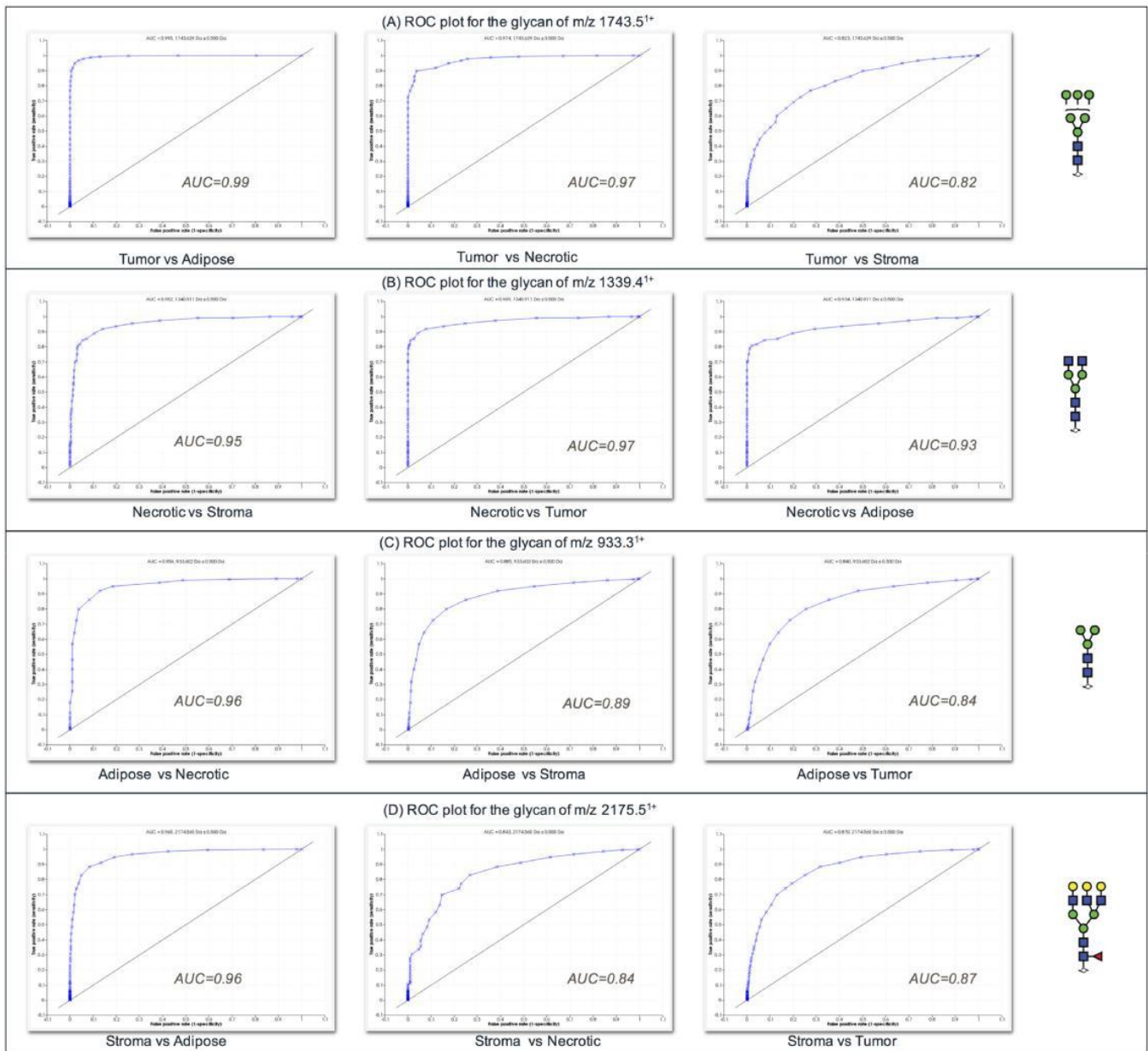


FIG. 7. Receiver operating characteristics (ROC) plots of glycan m/z from Fig. 6 used to discriminate tissue regions from sample P1. A, ROC plot for the glycan m/z 1743.5 B, ROC plot for the glycan m/z 1339.4 C, ROC plot for the glycan m/z 933.3 D, ROC plot for the glycan m/z 2175.5.

The segmentation map for the entire data set of patient P1 as shown in Fig. 8 discriminates between tumors (dark blue), stromal (light blue) and adipose (orange) of the sections at the segmentation levels selected (see insert). The segmentation map illustrates the potential that glycans possess in distinctly segmenting a histologically complex tissue section, and also highlights the heterogeneity of cancer tissue samples.

This striking tissue segmentation map demonstrates the potential to use individual *N*-glycan masses to identify specific tissue regions, however the summed mass spectra from the different tissue regions could also be used as a mass-spectral pattern to identify and discriminate unique tissue

regions as shown in supplemental Fig. S3. Using a series of massses with distinctive relative intensities as observed in the summed mass spectra in supplemental Fig. S3, could increase the sensitivity and facilitate high throughput analysis through complex pattern matching algorithms.

DISCUSSION

MALDI-MSI of *N*-glycans is a relatively new technique that has immense potential in several clinical applications including identification and validation of biomarkers in cancer tissues. Glycosylation changes are a hallmark of disease states and identification of the aberrant glycan changes directly

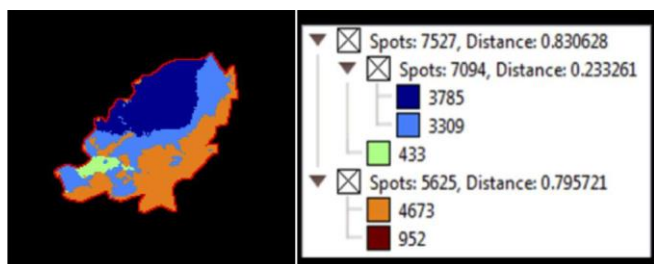


FIG. 8. MALDI imaging MS of *N*-linked glycans released from formalin-fixed ovarian cancer sections. Formalin-fixed ovarian cancer sections were treated with antigen retrieval prior to printing of (30 nL/position) dialyzed PNGase F or buffer control arrays with 250 μ m spacing. DHB (20 mg/ml) was sprayed onto the sections and MS spectra were acquired by oversampling at 100 μ m intervals using a MALDI-TOF/TOF MS instrument. Data was loaded raw into SCiLS, pre-processed for baseline subtraction and normalization to total ion current (TIC) prior to segmentation analysis (maximum processing mode, interval width of 0.5 Da, strong smoothing). The segmentation map for the entire data set of patient P1 discriminates between tumor (dark blue), stroma (light blue), adipose (orange) necrotic (green) and tissue border (brown) of the sections at the segmentation levels selected (see insert). The dendrogram (Fig. insert) shows the number of spectra clustered together for each region.

relates to molecular changes in the glycosylation machinery. Cancer cells frequently display glycans at different levels or with fundamentally different structures than those observed from normal cells (10). There are several advantages offered by the analysis of these post-translationally added glycans, because aberrant glycosylation affects several glycoproteins simultaneously and is therefore an amplified effect that may be easily distinguished compared with other biomolecules. This is clearly demonstrated in this study, where the observation of significant abundances of the entire class of high-mannose *N*-glycans is apparent specifically in the tumor tissue of all three patients. This high abundance localization of the early products of the *N*-glycan biosynthetic pathway specifically in the tumor may reflect the incomplete time for processing of the structures in the rapidly dividing cancer cell environment.

MALDI-MS is known to result in a loss of sialylation of glycan species. This limitation for the measurement of sialylated *N*-glycans by MALDI-MSI is confirmed by this study where the sialylated species were observed in negative ion mode by ESI and CID fragmentation whereas MALDI-MSI in the positive ion mode had few sialylated species detected. The masses of the low abundance sialylated species that were detected in the MALDI-MSI analysis corresponded to multiply sodiated adducts. The prominence of sialylated glycans in these samples and their isomeric differentiation observed by PGC-LC-ESI-MS illustrates the need in the future development of this technique for the use of derivatization techniques for MALDI-MSI analysis of these labile glycans (40) or by optimization of MALDI-MSI analysis in the negative ion mode that protects the sialylation. Very recently Holst *et al.*, have demonstrated a promising linkage-specific *in situ*

sialic acid derivatization for *N*-Glycan mass spectrometry imaging of formalin-fixed paraffin-embedded tissues (41).

Through the combination of detailed structural characterization by negative mode PGC-LC-ESI-MS/MS analysis and positive mode high resolution MALDI-MSI, we were able to differentiate tumor from non-tumor tissue regions in three ovarian cancer FFPE tissue sections by using only 4 masses corresponding to four specific *N*-glycan structures that are representative of different *N*-glycan classes. Distinct *N*-glycans were identified that were consistently able to differentiate between the tissues across biological samples. Surprisingly, specific single glycan masses were able to discriminate between necrotic, tumor, adipose and stromal tissue regions. The *N*-glycan based tissue differentiation observed in this study offers a unique advantage in analysis of ovarian cancer. The results from this study indicate that the location, diversification or classification of the various ovarian cancers and their subtypes could be made possible by high resolution MALDI-MSI aided by structural characterization of the implicated glycan structures by PGC-LC-ESI-MS/MS analysis.

The increase in high mannose structures have been previously reported in breast cancer progression in mouse models, colorectal cancer cell lines and hepatocellular carcinoma, among others (42–44). The increased expression of high-mannose glycans could suggest a premature termination of the glycosylation pathway during glycan synthesis. Although we observed some sialylation in the tumor region, it was considerably lower than that of the underlying stroma. It would be of interest to compare the sialylation of ovarian tumor region with its health counterpart.

The need to constantly improve and advance MALDI-MSI is also evident from this study. The PGC-LC-ESI-MS analysis revealed several *N*-glycans, specifically the sialylated and highly branched structures, which were not detected using the MALDI-MSI technique. There is also a need to further optimize and improve the sensitivity of detection for *N*-glycan MALDI-MSI and extend the detection into the *O*-glycan space. Although several challenges and limitations are evident, the combination of structural detail from PGC-LC-ESI-MS/MS and spatial localization from MALDI-MSI is a unique tool, is able to be performed with current technologies and offers far more information for distinguishing and classifying tissue compared with the more conventional histopathology staining methods.

* PH received financial support from the Australian Research Council (ARC LP110100693), Bioplatfroms Australia, and the Government of South Australia. NHP and AVE-D received financial support of the ARC CoE in NanoScale BioPhotonics (ARC CE140100003).

This article contains [supplemental material](#).

To whom correspondence should be addressed: Department of Chemistry and Biomolecular Sciences, Macquarie University, Sydney, NS 2109 Australia. Tel.: 61-02-98508176; Fax: 61-02-98508313; E-mail: nicki.packer@mq.edu.au.

^{a,b} These authors contributed equally to this work.

REFERENCES

- Torre, L. A., Bray, F., Siegel, R. L., Ferlay, J., Lortet-Tieulent, J., and Jemal, A. (2015) Global cancer statistics, 2012. *Cancer J. Clin.* **65**, 87–108
- Suh, K. S., Park, S. W., Castro, A., Patel, H., Blake, P., Liang, M., and Goy, A. (2010) Ovarian cancer biomarkers for molecular biosensors and translational medicine. *Expert Rev. Mol. Diagn.* **10**, 1069–1083
- Erickson, B. K., Conner, M. G., and Landen, C. N., Jr. (2013) The role of the fallopian tube in the origin of ovarian cancer. *Am. J. Obstet. Gynecol.* **209**, 409–414
- Bhoola, S., and Hoskins, W. J. (2006) Diagnosis and management of epithelial ovarian cancer. *Obstet. Gynecol.* **107**, 1399–1410
- Nik, N. N., Vang, R., Shih, I. M., and Kurman, R. J. (2014) Origin and pathogenesis of pelvic (ovarian, tubal, and primary peritoneal) serous carcinoma. *Annu. Rev. Pathol.* **9**, 27–45
- Scully, R. E., Young, R. H., and Clement, P. B. (1998) Tumors of the ovary, maldeveloped gonads, fallopian tube, and broad ligament. *Atlas of tumor pathology*, Armed Forces Institute of Pathology, Washington, DC. **30**, 1523–1524
- Kurman, R. J., and Shih, I. M. (2010) The origin and pathogenesis of epithelial ovarian cancer: a proposed unifying theory. *Am. J. Surg. Pathol.* **34**, 433–443
- Varki, A. (1993) Biological roles of oligosaccharides: all of the theories are correct. *Glycobiology* **3**, 97–130
- Ohtsubo, K., and Marth, J. D. (2006) Glycosylation in cellular mechanisms of health and disease. *Cell* **126**, 855–867
- Dube, D. H., and Bertozzi, C. R. (2005) Glycans in cancer and inflammation—potential for therapeutics and diagnostics. *Nat. Rev. Drug Discov.* **4**, 477–488
- Reis, C. A., Osorio, H., Silva, L., Gomes, C., and David, L. (2010) Alterations in glycosylation as biomarkers for cancer detection. *J. Clin. Pathol.* **63**, 322–329
- Hakomori, S. (2002) Glycosylation defining cancer malignancy: new wine in an old bottle. *Proc. Natl. Acad. Sci. U.S.A.* **99**, 10231–10233
- West, M. B., Segu, Z. M., Feasley, C. L., Kang, P., Klouckova, I., Li, C., Novotny, M. V., West, C. M., Mechref, Y., and Hanigan, M. H. (2010) Analysis of site-specific glycosylation of renal and hepatic gamma-glutamyl transpeptidase from normal human tissue. *J. Biol. Chem.* **285**, 29511–29524
- Abbott, K. L., Lim, J. M., Wells, L., Benigno, B. B., McDonald, J. F., and Pierce, M. (2010) Identification of candidate biomarkers with cancer-specific glycosylation in the tissue and serum of endometrioid ovarian cancer patients by glycoproteomic analysis. *Proteomics* **10**, 470–481
- Gao, L., Shen, L., Yu, M., Ni, J., Dong, X., Zhou, Y., and Wu, S. (2014) Colon cancer cells treated with 5-fluorouracil exhibit changes in poly-lactosaminetype N-glycans. *Mol. Med Rep.* **9**, 1697–1702
- Drake, P. M., Cho, W., Li, B., Prakhobol, A., Johansen, E., Anderson, N. L., Regnier, F. E., Gibson, B. W., and Fisher, S. J. (2010) Sweetening the pot: adding glycosylation to the biomarker discovery equation. *Clin. Chem.* **56**, 223–236
- Alley, W. R., Jr, Vasseur, J. A., Goetz, J. A., Svoboda, M., Mann, B. F., Matei, D. E., Menning, N., Hussein, A., Mechref, Y., and Novotny, M. V. (2012) N-linked glycan structures and their expressions change in the blood sera of ovarian cancer patients. *J. Proteome Res.* **11**, 2282–2300
- Chu, C. S., Ninonuevo, M. R., Clowers, B. H., Perkins, P. D., An, H. J., Yin, H., Killeen, K., Miyamoto, S., Grimm, R., and Lebrilla, C. B. (2009) Profile of native N-linked glycan structures from human serum using high performance liquid chromatography on a microfluidic chip and time-of-flight mass spectrometry. *Proteomics* **9**, 1939–1951
- Harvey, D. J. (2009) Analysis of carbohydrates and glycoconjugates by matrix-assisted laser desorption/ionization mass spectrometry: An update for 2003–2004. *Mass Spectrom. Rev.* **28**, 273–361
- Mereiter, S., Balmana, M., Gomes, J., Magalhaes, A., and Reis, C. A. (2016) Glycomic Approaches for the Discovery of Targets in Gastrointestinal Cancer. *Front. Oncol.* **6**, 55
- He, Y., Xie, Q., Wang, Y., Liang, Y., Xu, X., Li, Y., Miao, J., Chen, Z., and Li, Y. (2016) Liquid chromatography mass spectrometry-based O-glycomics to evaluate glycosylation alterations in gastric cancer. *Proteomics Clin. Appl.* **10**, 206–215
- Hu, Y., Mayampurath, A., Khan, S., Cohen, J. K., Mechref, Y., and Volchenboum, S. L. (2015) N-linked glycan profiling in neuroblastoma cell lines. *J. Proteome Res.* **14**, 2074–2081
- Scholler, N., Crawford, M., Sato, A., Drescher, C. W., O'Briant, K. C., Kiviat, N., Anderson, G. L., and Urban, N. (2006) Bead-based ELISA for validation of ovarian cancer early detection markers. *Clin. Cancer Res.* **12**, 2117–2124
- Wu, J., Zhu, J., Yin, H., Buckanovich, R. J., and Lubman, D. M. (2014) Analysis of glycan variation on glycoproteins from serum by the reverse lectin-based ELISA assay. *J. Proteome Res.* **13**, 2197–2204
- Shirovani, K., Futakawa, S., Nara, K., Hoshi, K., Saito, T., Tohyama, Y., Kitazume, S., Yuasa, T., Miyajima, M., Arai, H., Kuno, A., Narimatsu, H., and Hashimoto, Y. (2011) High throughput ELISAs to measure a unique glycan on transferrin in cerebrospinal fluid: A possible extension toward Alzheimer's disease biomarker development. *Int. J. Alzheimer's Dis.* **2011**, 5
- Yue, T., Goldstein, I. J., Hollingsworth, M. A., Kaul, K., Brand, R. E., and Haab, B. B. (2009) The prevalence and nature of glycan alterations on specific proteins in pancreatic cancer patients revealed using antibody-lectin sandwich arrays. *Mol. Cell. Proteomics* **8**, 1697–1707
- Kim, J.-H., Park, C. W., Um, D., Baek, K. H., Jo, Y., An, H., Kim, Y., and Kim, T. J. (2014) Mass spectrometric screening of ovarian cancer with serum glycans. *Disease Markers* **2014**, 9
- Saldova, R., Royle, L., Radcliffe, C. M., Abd Hamid, U. M., Evans, R., Arnold, J. N., Banks, R. E., Hutson, R., Harvey, D. J., Antrobus, R., Petrescu, S. M., Dwek, R. A., and Rudd, P. M. (2007) Ovarian cancer is associated with changes in glycosylation in both acute-phase proteins and IgG. *Glycobiology* **17**, 1344–1356
- Biskup, K., Braicu, E. I., Sehouli, J., Fotopoulou, C., Tauber, R., Berger, M., and Blanchard, V. (2013) Serum glycome profiling: a biomarker for diagnosis of ovarian cancer. *J. Proteome Res.* **12**, 4056–4063
- Saldova, R., Piccard, H., Perez-Garay, M., Harvey, D. J., Struwe, W. B., Galligan, M. C., Berghmans, N., Madden, S. F., Peracaula, R., Opdenakker, G., and Rudd, P. M. (2013) Increase in sialylation and branching in the mouse serum N-glycome correlates with inflammation and ovarian tumour progression. *PLoS ONE* **8**, e71159
- Anugraham, M., Jacob, F., Nixdorf, S., Everest-Dass, A. V., Heinzelmann-Schwarz, V., and Packer, N. H. (2014) Specific glycosylation of membrane proteins in epithelial ovarian cancer cell lines: glycan structures reflect gene expression and DNA methylation status. *Mol. Cell. Proteomics* **13**, 2213–2232
- Briggs, M. T., Kuliwaba, J. S., Muratovic, D., Everest-Dass, A. V., Packer, N. H., Findlay, D. M., and Hoffmann, P. (2016) MALDI mass spectrometry imaging of N-glycans on tibial cartilage and subchondral bone proteins in knee osteoarthritis. *Proteomics* **10.1002/pmic.201500461**
- Powers, T. W., Holst, S., Wuhler, M., Mehta, A. S., and Drake, R. R. (2015) Two-dimensional N-glycan distribution mapping of hepatocellular carcinoma tissues by MALDI-imaging mass spectrometry. *Biomolecules* **5**, 2554–2572
- Gustafsson, O. J., Briggs, M. T., Condina, M. R., Winderbaum, L. J., Peizling, M., McColl, S. R., Everest-Dass, A. V., Packer, N. H., and Hoffmann, P. (2015) MALDI imaging mass spectrometry of N-linked glycans on formalin-fixed paraffin-embedded murine kidney. *Anal. Bioanal. Chem.* **407**, 2127–2139
- Toghi Eshghi, S., Yang, S., Wang, X., Shah, P., Li, X., and Zhang, H. (2014) Imaging of N-linked glycans from formalin-fixed paraffin-embedded tissue sections using MALDI mass spectrometry. *ACS Chem. Biol.* **9**, 2149–2156
- Cooper, C. A., Gasteiger, E., and Packer, N. H. (2001) GlycoMod—a software tool for determining glycosylation compositions from mass spectrometric data. *Proteomics* **1**, 340–349
- Everest-Dass, A. V., Kolarich, D., Campbell, M. P., and Packer, N. H. (2013) Tandem mass spectra of glycan substructures enable the multistage mass spectrometric identification of determinants on oligosaccharides. *Rapid Commun. Mass Spectrom.* **27**, 931–939
- Everest-Dass, A. V., Abrahams, J. L., Kolarich, D., Packer, N. H., and Campbell, M. P. (2013) Structural feature ions for distinguishing N- and O-linked glycan isomers by LC-ESI-IT MS/MS. *J. Am. Soc. Mass Spectrom.* **24**, 895–906
- Nakano, M., Saldanha, R., Gobel, A., Kavallaris, M., and Packer, N. H. (2011) Identification of glycan structure alterations on cell membrane proteins in desoxyepithelone B resistant leukemia cells. *Mol. Cell. Proteomics* **10**, M111 009001
- Reiding, K. R., Blank, D., Kuijper, D. M., Deelder, A. M., and Wuhler, M.

- (2014) High-throughput profiling of protein *N*-glycosylation by MALDI-TOF-MS employing linkage-specific sialic acid esterification. *Anal. Chem.* **86**, 5784–5793
41. Holst, S., Heijs, B., de Haan, N., van Zeijl, R. J., Briaire-de Bruijn, I. H., van Pelt, G. W., Mehta, A. S., Angel, P. M., Mesker, W. E., Tollenaar, R. A., Drake, R. R., Bovee, J. V., McDonnell, L. A., and Wuhler, M. (2016) Linkage-Specific in Situ Sialic Acid Derivatization for *N*-Glycan Mass Spectrometry Imaging of Formalin-Fixed Paraffin-Embedded Tissues. *Anal Chem* **88**(11), 5904–13
42. de Leoz, M. L., Young, L. J., An, H. J., Kronewitter, S. R., Kim, J., Miyamoto, S., Borowsky, A. D., Chew, H. K., and Lebrilla, C. B. (2011) High-mannose glycans are elevated during breast cancer progression. *Mol. Cell. Proteomics* **10**, M110 002717
43. Sethi, M. K., Thaysen-Andersen, M., Smith, J. T., Baker, M. S., Packer, N. H., Hancock, W. S., and Fanayan, S. (2014) Comparative *N*-glycan profiling of colorectal cancer cell lines reveals unique bisecting GlcNAc and alpha-2,3-linked sialic acid determinants are associated with membrane proteins of the more metastatic/aggressive cell lines. *J. Proteome Res.* **13**, 277–288
44. Amin, A., Bashir, A., Zaki, N., McCarthy, D., Ahmed, S., and Lotfy, M. (2015) Insights into glycan biosynthesis in chemically-induced hepatocellular carcinoma in rats: A glycomic analysis. *World J. Gastroenterol.* **21**, 6167–6179

4.3 | Supplementary Information

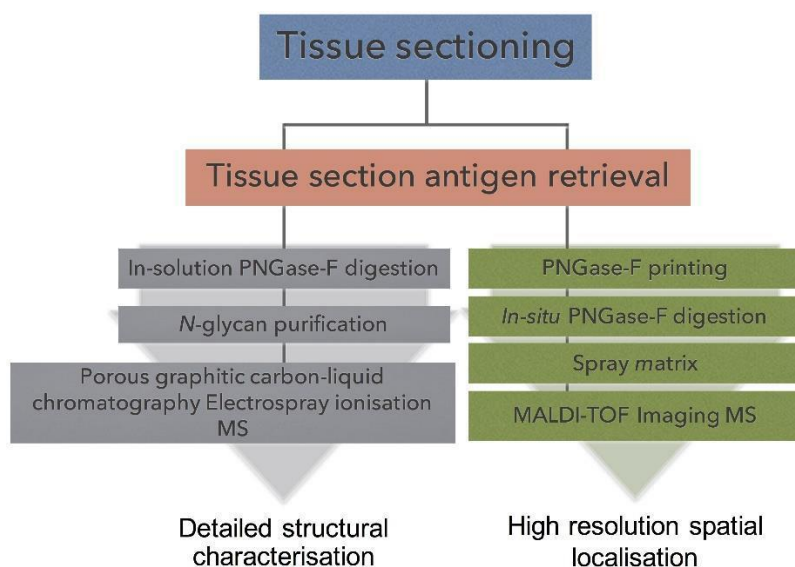


Figure S1: Combining *N*-glycan MALDI imaging and PGC-LC-ESI-MS/MS in FFPE-preserved tissue type tissue with glycomic characterization by MS/MS.

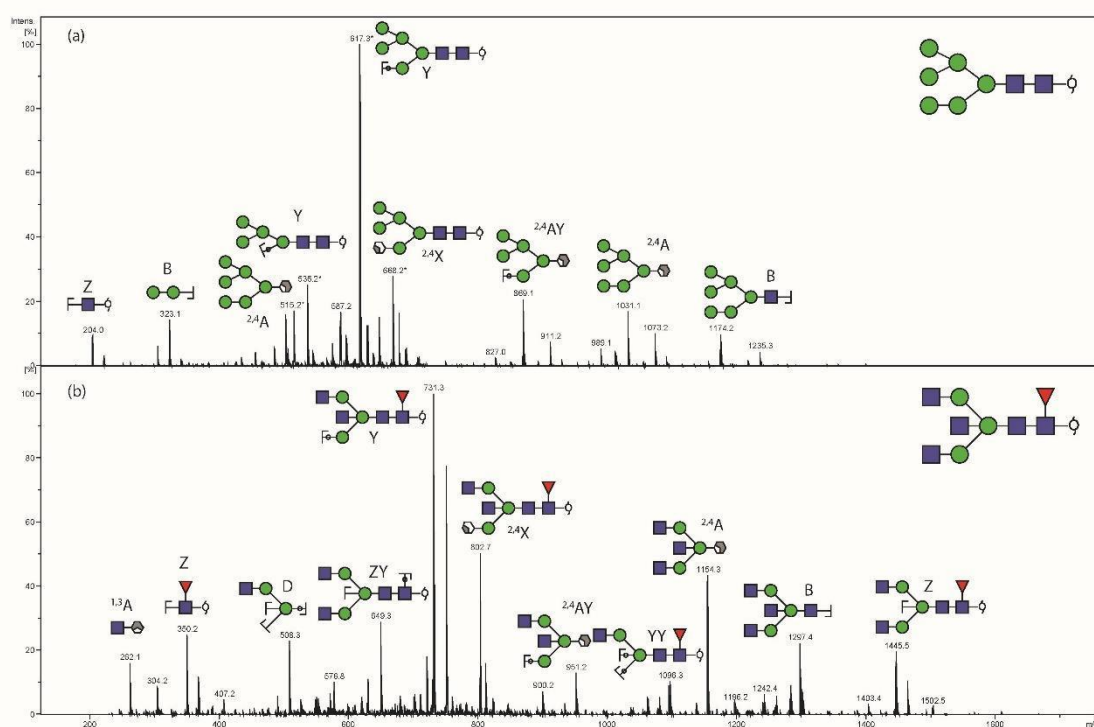


Figure S2: Negative ion mode fragmentation analysis of *N*-glycans of *m/z* 693.32 (a) and *m/z* 832.82 (b). The fragmentation analysis was carried out using structural feature ions observed in negative mode analysis of oligosaccharides and *N*-glycosylation biological pathway constraints. Figure S2a shows the tandem mass spectrum in negative ion mode of a high mannose structure ((Man)₃+(Man)₃(GlcNAc)₂) of *m/z* 698.2 (M-2H)⁻. Figure S2b shows the tandem mass spectra resulting from CID in the negative mode of a core-fucosylated bisecting biantennary agalactosylated glycan structure of *m/z* 832.82. (GlcNAc)₃ (Fuc)₁ + (Man)₃(GlcNAc)₂.

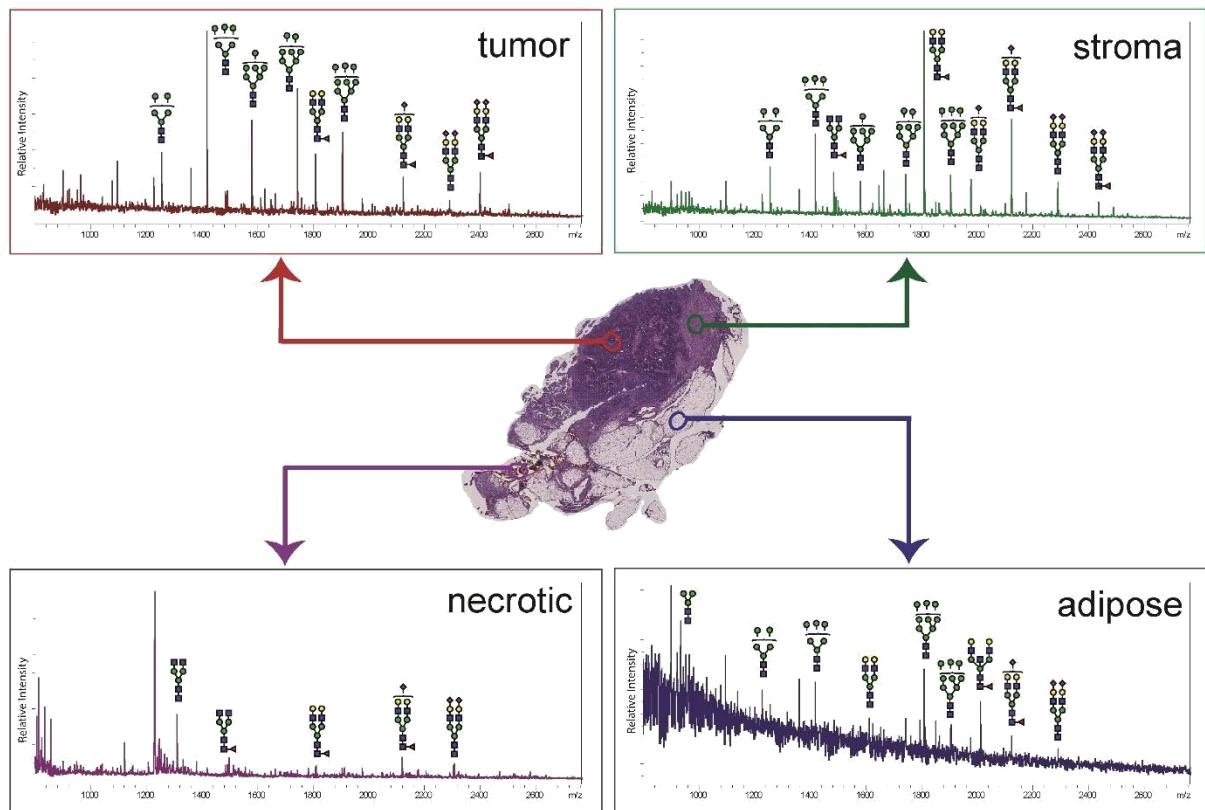


Figure S3: Positive ion mode summed MS spectrum of various tissue regions and annotated glycans with proposed structures identified by PGC-LC-ESI MS/MS. Formalin-fixed ovarian cancer sections (patient P1) were treated with antigen retrieval prior to printing of 30 nL/spot dialyzed PNGase F or buffer control arrays with 250 μm spacing. DHB (20 mg/mL) as matrix was sprayed onto the sections and MS spectra were acquired by oversampling at 100 μm intervals using a MALDI-TOF/TOF MS instrument.

Chapter 5 | Investigating the Interpatient Variation of Early- and Late-Stage Ovarian Cancer Tissues using *N*-Glycan MALDI Mass Spectrometry Imaging



5.1 | Summary

Studies on protein *N*-glycosylation have extensively reported aberrant patterns in the ovarian cancer tumour microenvironment. Therefore, obtaining spatial information is essential to uncover tumour-specific *N*-glycan alterations in ovarian cancer development and progression. Matrix-assisted laser desorption/ionization (MALDI) mass spectrometry imaging (MSI) was employed to investigate the spatial distribution of *N*-glycans on formalin-fixed paraffin-embedded (FFPE) ovarian cancer tissue sections from both early- and late-stage patients. Tumour-specific *N*-glycans were identified and structurally characterised by PGC-LC-ESI-MS/MS. A total of 14 *N*-glycans were visualised as ion intensity maps using MALDI-MSI while 42 *N*-glycans (including structural and compositional isomers) were identified and structurally characterised by PGC-LC-ESI-MS. The spatial distribution of oligomannose, complex neutral, bisecting and sialylated *N*-glycan families were only observed to be localised to the tumour regions of late-stage ovarian cancer patients relative to early-stage patients.

This page is intentionally left blank

5.2 | Statement of Authorship

Title of Paper	MALDI Mass Spectrometry Imaging of Early- and Late-Stage Serous Ovarian Cancer Tissue Reveals Stage-Specific <i>N</i> -Glycans
Publication Status	<input type="checkbox"/> Published <input type="checkbox"/> Accepted for Publication <input type="checkbox"/> Submitted for Publication <input checked="" type="checkbox"/> Unpublished and Unsubmitted work written in manuscript style
Publication Details	

Principal Author

Name of Principal Author (Candidate)	Matthew T. Briggs	
Contribution to the Paper	Conceived the project Data collection and analysis Prepared figures and wrote the main manuscript text	
Overall percentage (%)	80%	
Certification:	This paper reports on original research I conducted during the period of my Higher Degree by Research candidature and is not subject to any obligations or contractual agreements with a third party that would constrain its inclusion in this thesis. I am the primary author of this paper.	
Signature		Date 05/07/18

Co-Author Contributions

By signing the Statement of Authorship, each author certifies that:

- i. the candidate's stated contribution to the publication is accurate (as detailed above);
- ii. permission is granted for the candidate to include the publication in the thesis; and
- iii. the sum of all co-author contributions is equal to 100% less the candidate's stated contribution.

Name of Co-Author	Yin Ying Ho		
Contribution to the Paper	Conceived the project Method development Data collection and analysis		
Signature		Date	12/12/17

Name of Co-Author	Mark R. Condina		
Contribution to the Paper	Conceived the project Method development Wrote sections of the main manuscript text		
Signature		Date	13/12/17

Name of Co-Author	Gurjeet Kaur		
Contribution to the Paper	Annotated the H&E stained FFPE sections		
Signature		Date	13/12/17

Name of Co-Author	Martin K. Oehler		
Contribution to the Paper	Provided the ovarian tissue samples		
Signature		Date	12/12/17

Name of Co-Author	Arun V. Everest-Dass		
Contribution to the Paper	Conceived the project Data collection and analysis Prepared figures		
Signature		Date	12/12/17

Name of Co-Author	Nicolle H. Packer		
Contribution to the Paper	Conceived the project Designed the experiments and supervised the research		
Signature		Date	18/04/18

Name of Co-Author	Peter Hoffmann		
Contribution to the Paper	Conceived the project Designed the experiments and supervised the research		
Signature		Date	20/12/17

This page is intentionally left blank

MALDI Mass Spectrometry Imaging of Early- and Late-Stage Serous Ovarian Cancer Tissue Reveals Stage-Specific *N*-Glycans

Matthew T. Briggs^{1,2,3}, Yin Ying Ho¹, Mark R. Condina⁴, Arun V. Everest-Dass^{5,6}, Gurjeet Kaur⁷, Martin K. Oehler^{8,9}, Nicolle H. Packer^{5,6}, Peter Hoffmann⁴.

¹Adelaide Proteomics Centre, School of Biological Sciences, University of Adelaide, Australia, 5005

²ARC Centre for Nanoscale BioPhotonics (CNBP), University of Adelaide, Adelaide, Australia, 5005

³Institute for Photonics and Advanced Sensing (IPAS), University of Adelaide, Adelaide, Australia, 5005

⁴Future Industries Institute, Mawson Lakes Campus, University of South Australia, Mawson Lakes, 5095

⁵Institute for Glycomics, Gold Coast Campus, Griffith University, Gold Coast, Australia, 4215

⁶ARC Centre for Nanoscale BioPhotonics (CNBP), Macquarie University, Sydney, Australia, 2109

⁷Institute for Research in Molecular Medicine (INFORMM), Universiti Sains Malaysia, Pulau Pinang, Malaysia

⁸Department of Gynaecological Oncology, Royal Adelaide Hospital, Adelaide, South Australia, 5000

⁹Robinson Institute, University of Adelaide, Adelaide, Australia, 5005

Corresponding Author

Prof. Peter Hoffmann
The University of South Australia

Future Industries Institute, Building X – X1-10
Mawson Lakes Campus
Mawson Lakes Boulevard
Mawson Lakes, SA 5095

+61 8 830 25563

peter.hoffmann@unisa.edu.au

Running Title

Investigating the spatial *N*-glycome of early- and late-stage serous ovarian cancer patients.

Keywords

N-glycan, MALDI, mass spectrometry imaging, ovarian cancer, FFPE, tissue

Abbreviations

MALDI – Matrix-assisted laser desorption/ionization

MSI – Mass spectrometry imaging

LC – Liquid chromatography

ESI – Electrospray ionization

MS/MS – tandem mass spectrometry

PGC – Porous graphitized carbon

FF – Fresh Frozen

FFPE – Formalin-Fixed Paraffin-Embedded

LCM – Laser Capture Microdissection

TIC – Total ion count

Abstract

Epithelial ovarian cancer is one of the most fatal gynaecological malignancies in adult women. Studies on protein *N*-glycosylation have extensively reported aberrant patterns in the ovarian cancer tumour microenvironment. Therefore, obtaining spatial information is essential to uncover tumour-specific *N*-glycan alterations in ovarian cancer development and progression. Matrix-assisted laser desorption/ionization (MALDI) mass spectrometry imaging (MSI) was employed to investigate the spatial distribution of *N*-glycans on formalin-fixed paraffin-embedded (FFPE) ovarian cancer tissue sections from both early-stage ($n = 3$) and late-stage ($n = 3$) patients. Tumour-specific *N*-glycans were identified and structurally characterised by PGC-LC-ESI-MS/MS, and then assigned to images obtained from MALDI-MSI. A total of 14 *N*-glycans were visualised as ion intensity maps using MALDI-MSI while 42 *N*-glycans (including structural and compositional isomers) were identified and structurally characterised by LC-MS. The spatial distribution of oligomannose, complex neutral, bisecting and sialylated *N*-glycan families were only observed to be localised to the tumour regions of late-stage ovarian cancer patients relative to early-stage patients. Potential *N*-glycan diagnostic markers that emerged include the high mannose structure, $(\text{Hex})_6 + (\text{Man})_3(\text{GlcNAc})_2$, the bisecting structure, $(\text{Hex})_1 (\text{HexNAc})_3 (\text{Deoxyhexose})_1 + (\text{Man})_3(\text{GlcNAc})_2$, and the sialylated structure, $(\text{Hex})_2 (\text{HexNAc})_2 (\text{NeuAc})_1 + (\text{Man})_3(\text{GlcNAc})_2$. These observations require validation on large patient cohorts, by utilising tissue microarrays (TMAs) as well as evaluation of specific glyco-gene expression levels.

1. Introduction

Epithelial ovarian cancer (EOC) is the most fatal gynaecological malignancy in adult women with an estimated 1,580 new cases diagnosed and 1,047 deaths estimated in Australia during 2017 (Australian Institute of Health and Welfare, 2017). Ovarian cancer is asymptomatic, leading to late-stage diagnosis of patients with stage III or IV cancer based on the International Federation of Gynaecology and Obstetrics (FIGO) staging system (see *Table 1*).

Table 1: FIGO stages of epithelial ovarian cancer and the extent of tumour spread.

FIGO stage	Tumour spread
I	Confined to ovaries
II	Ovaries and pelvic extension
III	Ovaries, peritoneum outside the pelvis and/or retroperitoneal lymph nodes
IV	Distant metastasis excluding peritoneal metastasis

Surgery combined with chemotherapy is the standard treatment protocol for late-stage ovarian cancer. The effectiveness of this treatment strategy is poor, which leads to poor prognosis and a five-year overall survival rate of 30% (Zhu et al., 2006). Furthermore, the ability to diagnose ovarian cancer patients in the early-stages of the disease is also poor. Improvements in treatment and diagnosis may be possible by utilising clinical information such as grade, metastatic status and/or treatment response in conjunction with molecular level information, such as 'omics' data, from these patients.

It has been well documented that genomics can divide ovarian cancer into two distinct groups. Group I contains low-grade and 'borderline' serous tumours, endometrioid, mucinous and clear cell tumours, while group II contains high-grade serous and endometrioid tumours, and many low incidence tumours (Vang et al., 2009). Although there are benefits of this classification strategy, there are also disadvantages, such as gene transcription levels not mirroring levels of protein translation (Lu et al., 2007). In addition, genomics can only predict sites of post-translational modifications (PTMs), which do not necessarily correlate with genuine PTM sites (Kim et al., 2008). A holistic molecular understanding of globally regulated pathways in ovarian cancer therefore require the combination of genomic information with protein abundance and modification state.

Proteomics is well established has been widely applied to ovarian cancer tissue samples. For example, El Ayed, M. *et al* measured the spatial distribution of intact proteins and tryptic peptides across stage III and IV adenocarcinoma, borderline and benign tumour tissue sections (El Ayed et al., 2010). It was concluded that S100 proteins, cytoskeleton modifying proteins and even an oviduct-specific glycoprotein (OGP, Mucin-9), a marker of normal oviductal epithelium, were all observed to be spatially localised to tumour regions. Mucin-9 has previously been found to be a tubal differentiation marker, therefore indicating early events of ovarian carcinogenesis. Glycoproteomics is a rapidly emerging field where glycoproteins are extensively studied; however there are limitations with determining glycan structure. Therefore, to address this caveat, glycans are released from biological samples and analysed through the field of glycomics.

Glycomics is the comprehensive study of sugars present on complex molecules, such as proteins, lipids and proteoglycans, in an organism. The attachment of glycans to such molecules is a widely studied PTM that is relevant to several biological processes such as cell signalling, immune responses, extracellular interaction and cell adhesion (Ohtsubo and Marth, 2006). There are two main types of protein linked glycosylation; *N*- and *O*-linked, which are attached to asparagine and serine/threonine residues respectively (North et al., 2009). In the tumour microenvironment, there have been reports of aberrant *N*-linked glycosylation patterns associated with tumour growth, cancer development and metastasis (Carvalho et al., 2016; Dube and Bertozzi, 2005; Hakomori, 2002). These observations of aberrant glycosylation provide molecular-level glycomic profiles of different disease states relative to healthy samples (Abbott et al., 2010). The *N*-glycome can be studied by enzymatic release using PNGase F followed by reduction and clean-up, and then run on porous graphitised carbon (PGC) liquid chromatography (LC) electrospray ionization (ESI) tandem mass spectrometry (MS/MS), which is one of the most sensitive and comprehensive mass spectrometry techniques (Jensen et al., 2012).

Anugraham, M. *et al* used PGC-LC-ESI-MS/MS to structurally characterize *N*-glycans released from ovarian cancer (SKOV 3, IGROV1, A2780, OVCAR 3) and normal ovarian cell lines (HOSE 6.3 and HOSE 17.1) (Anugraham et al., 2014). It was discovered that bisecting structures were highly expressed in serous ovarian cancer cell lines relative to the normal ovarian cell lines. This observation was then correlated with gene expression profiles of the glycosyltransferase enzyme (*MGAT3*), which adds a GlcNAc residue in a β 1-4 linkage to the *N*-glycan core to create bisecting structures. Additionally, this study also concluded that *MGAT3* expression may be epigenetically regulated by DNA hypomethylation, leading to an increase of abundance in bisecting *N*-glycans. SKOV 3, and its highly metastatic derivative SKOV 3-ip, were also studied in 2014 (Zhang et al., 2014). A total of 17 *N*-glycans were identified and structurally characterised, with bisecting *N*-glycans featuring a significant decrease in the highly metastatic cell line SKOV 3-ip relative to SKOV 3 cell line. This observation was subsequently validated using real-time PCR, western blotting, transwell assay, lectin blotting and immunohistochemistry (IHC) analysis. The decrease of bisecting *N*-glycans from SKOV 3-ip cells requires investigation to further understand this observation. Although ovarian cancer cell lines provide a wealth of biological information, it has been documented that the most frequently used cell lines do not represent high-grade serous ovarian cancer, based on their genomes (Domcke et al., 2013).

Evaluation of tissue excised from ovarian cancer patients offers the ability to directly correlate glycan changes with classified low- and high-grade ovarian cancer. Excised samples can be preserved in two

conventional ways; as fresh frozen (FF) or formalin-fixed paraffin-embedded (FFPE). Fresh frozen tissue has been utilized in several studies; however, most studies have turned to formalin-fixation due to specific handling/storage requirements and expense associated with storage and transport of fresh frozen samples. There have been only a handful of publications that study the glycomes of ovarian cancer tissue. In 2015, Allam, H. *et al* isolated *N*-glycans from FF endometrioid, serous and healthy ovarian cancer tissue sections (Allam et al., 2015). It was discovered that bisecting *N*-glycan structures were elevated in the serous ovarian cancer tissue as well as the glycosyltransferase enzyme, *MGAT 3*. More recently, the glycomes from cancer tissue originating from the ovaries and peritoneum were compared using PGC-LC-ESI-MS/MS (Anugraham et al., 2017). This study reported high levels of α 2-6 sialylated and bisecting *N*-glycan structures from both cancers originating from the ovaries and peritoneum. However, there were several glycan structures specific to the cancer originating from the ovaries, such as LacdiNAc-type (GalNAc β 1-4GINAc) motifs that were correlated with gene expression of *B4GALNT3* and *B4GALNT4*. In 2017, Chen, H. *et al* used MALDI-MS to compare *N*-glycan profiles of different pathological grades of epithelial ovarian cancer tissue and healthy controls (Chen et al., 2017). A total of

80 *N*-glycan compositions were detected, with high mannose *N*-glycans highly expressed in cancer relative to healthy. Four oligomannose and three fucosylated neutral complex *N*-glycans were combined together and analysed by receiver operating characteristic (ROC) using binary logistic regression rule to generate good discrimination between cancer and healthy samples.

Overall, these three publications concluded that there are *N*-glycan families specific to ovarian cancer. However, there is no mention confirming that tumour regions were isolated from underlying stroma or adipose, for instance, by laser capture microdissection (LCM) (Hinneburg et al., 2017). The caveat with LCM is the removal of spatial information as it is difficult to isolate tissue-specific regions. This is a key concept as it would be ideal to correlate changes in *N*-glycosylation pathways with tissue morphology, and in particular, surgical annotations. This has recently been overcome with a novel workflow that combines mass spectrometry techniques, providing both spatial and structural information (Briggs et al., 2017).

Matrix-assisted laser desorption/ionization mass spectrometry imaging (MALDI-MSI) is a spatial technique applied to tissue sections to measure the distribution of analytes, such as proteins, peptides, lipids, drugs, metabolites and *N*-glycans. The recent complementation of *N*-glycan MALDI-MSI and PGC-LC-ESI-MS/MS as a workflow for comprehensive *N*-glycan analysis was first employed in 2015 as

a proof-of-principle (Gustafsson et al., 2015). This straightforward method utilised FFPE murine kidney, therefore identifying confirmed *N*-glycan structures that could distinguish between the cortex, medulla and pelvis. We have recently published a detailed protocol paper that provides readers with step-by-step instructions on combining MALDI-MSI with PGC-LC-ESI-MS/MS in order to obtain both spatial and structural information on protein linked *N*-glycans respectively (Briggs et al., 2017).

Powers, T. *et al* have utilised MALDI Fourier-transform ion cyclotron resonance (FTICR) for its mass accuracy and on-tissue collision-induced dissociation (CID) fragmentation to identify and characterise *N*-glycan structures from MALDI-MSI experiments (Powers et al., 2015; Powers et al., 2014). As an example, a singly core fucosylated *N*-glycan was analysed from FFPE hepatocellular cancer tissue using MALDI-FTICR and continuous accumulation of selection ions (CASI), coupled with CID, generated a fragmentation pattern capable of characterising its structure. In this analysis, only two fragment ions were generated, therefore providing incomplete structural information of the isolated *N*-glycan. Additionally, this approach does not provide comprehensive structural information on the possible related *N*-glycan isomers (i.e. *N*-glycoforms). In 2016, Holst, S. *et al* developed a novel method to address this issue by using a derivatization approach of the differently linked sialic acids for subsequent MALDI-MSI to identify linkage-specific sialylated species (i.e. α 2-3 and α 2-6 sialic acid) (Holst et al., 2016). However, only sialylated *N*-glycoforms could be identified as potential *N*-glycan candidates, while non-sialylated *N*-glycoforms could not be considered due to limitations with methodology.

We recently applied our released *N*-glycan MALDI-MSI and PGC-LC-ESI-MS/MS protocol to FFPE ovarian cancer patient tissues (Everest-Dass et al., 2016). Late-stage (or stage IIIC) patient FFPE sections were selected (n = 3) and analysed for the glycan distribution across the tissue sections. We identified 40 individual *N*-glycan structural and compositional isomers by PGC-LC-ESI-MS/MS and could discriminate between tumour, stroma, adipose and necrotic regions of the ovarian tissue sections based on specific *N*-glycan families. For example, oligomannose *N*-glycans were predominantly expressed in tumour regions while complex *N*-glycans were the abundant protein-linked structure in the adjacent stroma.

This study extends this work using MALDI-MSI with PGC-LC-ESI-MS/MS to investigate whether *N*-glycans released from proteins in ovarian cancer FFPE tissue sections could discriminate between early-stage (i.e. stage I) and late-stage (i.e. stage III) ovarian cancer. The combination of spatial and structural information of the *N*-glycans offers the potential to discover specific *N*-glycans that are

indicative of ovarian cancer progression and could lead to the development of targeted therapeutic strategies for ovarian cancer patients.

2. Materials and Methods:

2.1. Reagents

See Table 1 from our previous publication for a comprehensive list of chemicals, consumables and equipment used in this protocol (Briggs et al., 2017).

2.2. Tissue Sectioning

Tissue sectioning was performed as previously described (Briggs et al., 2017). Epithelial ovarian cancer tissue from FIGO stage IA/IC and IIIC were obtained from patients at surgery from 2009 to 2016 and staged by a pathologist according to the approved protocol from the Royal Adelaide Hospital (RAH) Human Ethics Committee (RAH protocol number: 140101). The tissues were fixed in 10% (w/v) formalin (F1635, Sigma Aldrich) for 48 hours at 4°C. Tissue was then removed from the formalin, rinsed with de-ionized H₂O and stored in 70% (v/v) EtOH before processing with a Leica TP 1020 processor (Leica Biosystems, North Ryde, Australia). Protocol: 70% (v/v) EtOH for 5 min, 80% (v/v) EtOH for 2 h, 95% (v/v) EtOH for 2 h, 3 x 100% (v/v) EtOH for 2 hours each, 2 x xylene for 2 h each and 2 x paraffin for 2 h each. A Leica EG 114OH embedder (Leica Biosystems) was used to create paraffin embedded tissue blocks. FFPE blocks were sectioned (6 µm thick) on a Microm HM325 microtome (Zeiss, Göttingen, Germany) and water bath mounted (39°C) onto ITO slides (Bruker Daltonics) or PEN membrane slides (MicroDissect). Slides were left to dry at 37°C for one hour prior to storage at 4°C.

2.3. N-glycan MALDI-MSI of FFPE Tissue Sections

2.3.1. Tissue Section Antigen Retrieval

Tissue sections were re-hydrated using a standard procedure for citric acid antigen retrieval (CAAR) (Briggs et al., 2017). Briefly, the tissue sections were heated at 60 °C for 1 h over on a heatblock; washed in 100% (v/v) xylene (2 x 5 min) and 100% (v/v) ethanol (2 x 2 min). Sections were washed in 10 mM NH₄HCO₃ (2 x 5 min) followed by a 10 min incubation in boiling 10 mM citric acid (pH 6.0) and then by heating at 98 °C for 30 min on a heating block. Finally, tissue sections were immersed twice in 10 mM NH₄HCO₃ (1 min) and dried at room temperature in a humid chamber.

2.3.2. *In Situ* PNGase F Digestion and Matrix Deposition

40 μL of glycerol-free PNGase F (75,000 units, New England Biolabs) was spotted onto a nitrocellulose membrane and drop dialyzed against water for 2 h at room temperature. NH_4HCO_3 (25 mM, pH \sim 8.2) was added to the dialyzed PNGase F to a total volume of 200 μL and the PNGase F was printed onto tissue sections (15 nL at 250 μm spacing) using a CHIP-1000 (Shimadzu, Japan). Buffer control arrays (25 mM NH_4HCO_3) were printed using the same conditions on adjacent sections. Tissue sections were incubated overnight for approximately 16 h at 37°C in a humid chamber and GLY3 standard was manually spotted (1 μL) on an adjacent section. ITO slides are marked at the edges with water-based white out and tissue sections are scanned at 2400 dpi on a CanoScan 5600 F (Canon) scanner for instrument teaching purposes. 2,5-DHB (20 mg/ml) in 0.1% (v/v) TFA and 1 mM NaCl was sprayed onto prepared tissues using a HTX TM-sprayer. Instrument specific settings: 16 passes, 0.05 ml/min flow rate, 4 psi N_2 pressure, 65 °C capillary temperature, 800 mm/min. The addition of NaCl to the 2,5-DHB mixture is necessary to detect sodiated *N*-glycan adducts in positive ion-MS.

2.3.3. MALDI-TOF/TOF Mass Spectrometry

MS data was acquired using an ultrafleXtreme MALDI-TOF/TOF mass spectrometer (Bruker Daltonics) controlled by flexControl (v3.4, Bruker Daltonics) and flexImaging (v4.0, Bruker Daltonics) in reflectron positive ion mode. Instrument-specific settings were as follows: 800– 4500 *m/z* range, 700 Da matrix suppression, 2 kHz laser repetition rate and 2.5 GS/s. Method-specific settings were as follows: 75% laser power and 2698 V detector gain. A total of 1000 shots were acquired at each position with no walk. Data was acquired by oversampling from an arbitrary array with centre to centre acquisition distance of 100 μm overlaid onto the 250 μm PNGase F array at the Smartbeam '4_large' setting. *N*-glycan delocalisation was assessed by acquiring spectra off-tissue. The MALDI-TOF/TOF instrument was externally calibrated using a quadratic fit prior to acquisition using the GLY3 standard spots prior to MALDI-MSI (see Table 2).

Table 2: *N*-glycan standard mixture (GLY3; Prozyme, Hayward, CA, USA) used for calibration of the MALDI-TOF/TOF MS instrument.

<i>N</i>-glycan composition	[M]	[M + Na⁺]⁺
Man5GlcNAc2	1234.4333	1257.4225
Man3GlcNAc5	1519.5659	1542.5551
Man3Gal4GlcNAc6	2370.8565	2393.8457
Concentration: 1 pmol/μL		

2.3.4. Histological Staining

Following MALDI imaging, 2,5-DHB matrix was eluted using 70% EtOH and tissue sections were haematoxylin and eosin (H&E) stained as described previously (Briggs et al., 2017). Tumour regions on tissue sections were annotated by pathologist Professor Gurjeet Kaur.

2.3.5. Data Analysis

Raw MALDI-MSI data was analysed by SCiLS Lab (version 2016b, SCiLS, Bruker Daltonics). Raw data was loaded and pre-processed by baseline subtraction (TopHat at default peak width) and normalization to total ion current (TIC). Peaks were picked, aligned and the pre-processed data was used to generate log ion intensity maps. These log ion intensity maps were weakly denoised with automatic hotspot removal.

2.4. PGC-LC-ESI-Ion Trap MS and MS/MS of *N*-glycans released from Laser Captured Microdissected FFPE Tissue Sections

2.4.1. In-solution PNGase F digestion

Tissue sections on PEN membrane slides ($n = 6$) were used and processed as described previously, with modifications (Briggs et al., 2017). Briefly, following a 5 min 60°C heating block incubation, 90 sec xylene wash and 60 sec EtOH wash, the tissue sections were stained with haematoxylin and a 604, 259 μm^2 tumour region was selected and isolated by LCM from each section (using a Leica AS LCM microscope), and deposited into a micro-vial. The tissue was incubated (2 x 5 min) in 10 mM NH_4HCO_3 . Solution was removed and replaced with 10 mM citric acid (pH 6) and heated at 98°C for 45 min. The tissue regions were washed twice with 10 mM NH_4HCO_3 . Glycerol free PNGase F (2 μL , non-dialysed) was added to the FFPE tissue in a 10 μL total reaction volume (with 25 mM NH_4HCO_3) for the tumour regions. The tissue digests were left overnight for approximately 16 h at 37°C.

2.4.2. *N*-linked glycan reduction

The released *N*-linked glycans were reduced and desalted according to previously described methods (Jensen et al., 2012). After acidification with 100 mM NH_4COOH pH 5 (10 μL) for 60 min at room temperature, the samples were dried in a vacuum centrifuge and were reduced with 20 μL of 1 M

NaBH₄ in 50 mM NaOH at 50°C for 3 h. The reduction was quenched with 2 µL glacial acetic acid and the *N*-linked glycan alditols were desalted as described below.

2.4.3. Glycan purification

The released *N*-glycans were desalted using cation exchange columns comprising 30 µL AG50W-X8 cation-exchange resin (BioRad, Hercules) pipetted on top of a C18 ZipTip (0.1-10 µL, Millipore). Residual borate was removed by the addition of methanol (x 3) and drying under vacuum. The glycans were further purified by tips using porous graphitised carbon slurry (GlycoClean H Cartridges, Prozyme) manually pipetted onto C18 ZipTip (0.1-10 µL, Millipore) as previously described (Jensen et al., 2012).

2.4.4. PGC-LC-ESI-Ion Trap MS and MS/MS

The reduced *N*-glycans were resuspended in 10 µL of ultra-pure water and subjected to PGC-LC-ESI-MS/MS based on previously published settings (Hinneburg et al., 2017). A 1100 capillary and nano-pump LC system (Agilent Technologies, CA) was used and coupled to an amaZon ETD Ion Trap MS (Bruker Daltonics, Bremen, Germany) via a CaptiveSpray nano ionisation source with nanoBooster (Bruker Daltonics) under the control of HyStar software (version 3.0.394.0, Bruker Daltonics) and TrapControl (version 7.2, Bruker Daltonics). 1 µL of reduced glycans was loaded onto a trapping column (Hypercarb, 30 x 0.32 mm, 5 µm particle size, Thermo Scientific) at a flow rate of 8 µl/min in 10 min using buffer A (ultra-pure water). Glycan separation was performed on a Hypercarb analytical column (100 x 0.075 mm, 3 µm particle size, Thermo Scientific) using water as buffer A and 60 % (v/v) ACN as buffer B, at 800 µL/min flow rate using a linear gradient of 3 to 15.8 % buffer B for 1 min, 15.8 to 40.3 % buffer B for 49 min before washing in 60 % buffer B for 10 and a 15 min column equilibration in 3 % buffer B. A total of 85 min chromatographic time was performed. The amaZon ETD ion trap MS was operated in negative mode with CaptiveSpray capillary voltage set to 1200 V in the mass range of *m/z* 300 to 1800. Scan mode of ultrascan with ICC target of 40,000 in 200 ms maximum accumulation time averaging 5 spectra and rolling average of 2 were set. Top three precursors were subjected to data-dependent acquisition where an ion threshold of 25,000 with -2 as preferred charge stage in the scanning range of *m/z* 100 to 2500. Exclusion was activated to exclude precursor after 1 spectrum and release after 0.2 min for CID fragmentation using enhanced smart fragmentation of 32 ms fragmentation time and 27% default collision energy at an amplitude of 70%. Raw data was analysed using Data Analysis (version 4.0, Bruker Daltonics) and GlycoWorkbench (version 2.1). *N*-glycans identified and confirmed by PGC-LC-ESI-MS/MS were matched to the corresponding *m/z* values from MALDI-MSI as detailed previously (Briggs et al., 2017).

3. Results

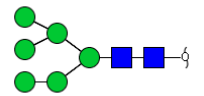
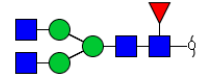
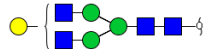
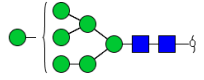
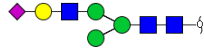
In this study, we performed *N*-glycan MALDI mass spectrometry imaging (MSI) on FFPE serous ovarian cancer tissue from early-stage ($n = 3$) and late-stage ($n = 3$) patients (see *Supplementary Table 1*), as previously described in our protocol paper (Briggs et al., 2017). Briefly, the FFPE tissue sections were prepared by citric acid antigen retrieval (CAAR) and printed with dialyzed glycerol-free PNGase F using a Chemical Inkjet Printer (ChIP-1000, Shimadzu, Japan), followed by an overnight incubation at 37°C and DHB matrix deposition using a HTX TM-Sprayer (Shimadzu, Japan). The PNGase F treated and non-treated (i.e. control) regions were then imaged using an UltrafleXtreme MALDI-TOF/TOF mass spectrometer (Bruker Daltonics) and the data was analysed by SCiLS Lab. In SCiLS Lab, the spectra from the early-stage patients were summed and compared to the late-stage patients. To identify putative *N*-glycan structures from PNGase F treated regions, we compared the summed spectra from treated and non-treated regions to generate unique m/z values. We identified 14 unique m/z values specific to PNGase F treated regions (see Figure 1). The remaining m/z values were assigned to DHB matrix clusters. However, to confirm that these 14 unique m/z values were *N*-glycan structures, we required further structural information.

Detailed structural information was obtained by PGC-LC-ESI-MS/MS analysis of *N*-glycans released from laser capture microdissected tumour regions, isolated from haematoxylin stained consecutive tissue sections of early-stage ($n = 3$) and late-stage ($n = 3$) serous ovarian cancer patients. Briefly, the tumour-specific regions were selected using annotated H&E stained images and images from MALDI-MSI. *N*-glycans were released from tumour regions from consecutive sections of the H&E and MSI sections by in-solution digest using PNGase F and then reduced, desalted, purified and separated over a porous graphitized carbon (PGC) column coupled to electrospray ionization (ESI) tandem mass spectrometry (MS/MS). The raw data was analysed using Data Analysis (version 4.0, Bruker Daltonics) to identify and characterise all *N*-glycan structures and their compositions. We used the following tools and methods to achieve comprehensive identification and characterisation of these structures: (1) GlycoMod (<http://web.expasy.org/glycomod/>), which calculates the theoretical monosaccharide composition based on the parent mass obtained from LC-MS, and then links to the UniCarbKB database (Campbell et al., 2011), which lists known *N*-glycan structures from the literature (Cooper et al., 2001), (2) negative mode diagnostic fragmentation ions which match previously reported *N*-glycan structures (Everest-Dass et al., 2013a; Everest-Dass et al., 2013b), and (3) the knowledge of *N*-glycosylation synthesis pathways.

A total of 42 *N*-glycan structures (including structural and compositional isomers) were identified and characterised from the laser microdissected tumour-specific regions using PGC-LC-ESI-MS/MS analysis (see *Table 2* for the full list). This approach allowed the assignment of actual glycan structures to the 14 unique *m/z* values obtained by MALDI-MSI, which categorised into oligomannose, complex neutral, bisecting and sialylated *N*-glycan families (see *Table 2* for the full list). Interestingly, hybrid *N*-glycan structures were only detected by PGC-LC-ESI-MS/MS analysis and were not part of the 14 unique *m/z* values generated from MALDI-MSI analysis.

The early- and late-stage serous ovarian cancer summed spectra (see *Supplementary Figure 1*) were annotated using the *N*-glycan structures identified and characterised by PGC-LC-ESI-MS/MS analysis (see *Figure 1*). Overall, oligomannose *N*-glycans (see *Figure 2* and *Supplementary Figures 2-5*) were observed to be more abundant in the summed MALDI-MSI spectra glycans released from the ovarian tissues of late-stage patients relative to early-stage patients. Several complex neutral *N*-glycan structures, such as *m/z* 1809.639 (Hex)₂(HexNAc)₂ (Deoxyhexose)₁ + (Man)₃(GlcNAc)₂, were observed only in the late-stage patients (see *Figure 3*). Specific bisecting (see *Figure 4*) and sialylated (see *Supplementary Figures 11 and 12*) *N*-glycan structures followed a similar trend with *m/z* 1850.665 (Hex)₁ (HexNAc)₃ (Deoxyhexose)₁ + (Man)₃(GlcNAc)₂ and *m/z* 1977.666 (Hex)₂ (HexNAc)₂ (NeuAc)₁ + (Man)₃(GlcNAc)₂ being detected at low intensity or absent from the early-stage sum spectrum.

Table 3: N-glycan structures identified and characterised by PGC-LC-ESI-MS/MS and MALDI-MSI. N-glycans were released from early-stage (n = 3) and late-stage (n = 3) ovarian cancer patients. Singly negatively charged monoisotopic masses [M-H]⁻ were calculated from their observed doubly negatively charged monoisotopic masses ([M-2H]²⁻), matching composition and proposed structure. Y = Yes, N = No, states the occurrence of the glycan in the patient cohort based on the chromatography, fragmentation, and the 14 unique m/z values from MALDI-MSI. *Doubly and triply sodiated N-glycans.

PGC-LC-ESI-MS/MS				Stage I			Stage III			MALDI-MSI	Composition	Structure
Number	RT (mins)	[M-2H] ²⁻	[M-H] ⁻	277	1575	1934	847	1943	1890	[M+Na] ¹⁺		
1a	38.5	698.3	1397.6	N	Y	Y	N	N	N	1419.5	(Hex) ₃ + (Man) ₃ (GlcNAc) ₂	
1b	40.1			Y	Y	Y	Y	Y	Y			
2	43.3	731.4	1463.8	N	Y	N	Y	Y	Y	1485.5	(HexNAc) ₂ (Deoxyhexose) ₁ + (Man) ₃ (GlcNAc) ₂	
3	40.4	739.3	1479.5	N	N	N	Y	N	N	N	(Hex) ₁ (HexNAc) ₂ + (Man) ₃ (GlcNAc) ₂	
4a	39.4	779.3	1559.6	Y	Y	Y	Y	Y	Y	1581.5	(Hex) ₄ + (Man) ₃ (GlcNAc) ₂	
4b	40.4			N	N	N	Y	Y	Y			
5a	39.3	783.2	1567.6	Y	Y	Y	Y	Y	Y	N	(Hex) ₁ (HexNAc) ₁ (NeuAc) ₁ + (Man) ₃ (GlcNAc) ₂	
5b	46.8			N	N	N	N	Y	Y			
5c	57.4			N	N	N	N	Y	Y			

6	41.5	799.7	1600.4	N	N	N	Y	Y	Y	N	(Hex) ₃ (HexNAc) ₁ + (Man) ₃ (GlcNAc) ₂	
7a	39.5	812.3	1625.6	N	N	N	Y	N	N	1647.6	(Hex) ₁ (HexNAc) ₂ (Deoxyhexose) ₁ + (Man) ₃ (GlcNAc) ₂	
7b	44.9			N	Y	N	Y	N	Y			
8	41.8	820.3	1641.6	N	N	N	Y	N	Y	1663.6	(Hex) ₂ (HexNAc) ₂ + (Man) ₃ (GlcNAc) ₂	
9	38.2	832.8	1666.6	Y	Y	Y	N	Y	Y	1688.6	(HexNAc) ₃ (Deoxyhexose) ₁ + (Man) ₃ (GlcNAc) ₂	
10	63.0	856.1	1713.6	N	N	N	N	Y	Y	N	(Hex) ₁ (HexNAc) ₁ (NeuAc) ₁ (Deoxyhexose) ₁ + (Man) ₃ (GlcNAc) ₂	
11	39.4	860.3	1721.6	Y	Y	Y	Y	Y	Y	1743.6	(Hex) ₅ + (Man) ₃ (GlcNAc) ₂	
12	46.4	893.3	1785.6	N	Y	N	Y	Y	Y	1809.6	(Hex) ₂ (HexNAc) ₂ (Deoxyhexose) ₁ + (Man) ₃ (GlcNAc) ₂	
13	38.8	913.8	1827.6	N	Y	N	Y	Y	Y	1850.6	(Hex) ₁ (HexNAc) ₃ (Deoxyhexose) ₁ + (Man) ₃ (GlcNAc) ₂	

14	39.9	941.3	1883.6	Y	Y	Y	Y	Y	Y	1905.6	(Hex) ₆ + (Man) ₃ (GlcNAc) ₂	
15a	59.3	945.4	1891.8	N	N	N	N	Y	N	N	(Hex) ₃ (HexNAc) ₁ (NeuAc) ₁ + (Man) ₃ (GlcNAc) ₂	
15b	60.0			N	N	N	N	Y	N			
16a	51.9	965.9	1932.8	Y	N	N	N	N	N	1977.6*	(Hex) ₂ (HexNAc) ₂ (NeuAc) ₁ + (Man) ₃ (GlcNAc) ₂	
16b	56.4			N	N	N	Y	N	N			
16c	59.9			N	N	Y	N	Y	Y			
17	39.6	994.9	1990.8	N	Y	N	Y	Y	Y	2012.7	(Hex) ₂ (HexNAc) ₃ (Deoxyhexose) ₁ + (Man) ₃ (GlcNAc) ₂	
18	41.3	1022.4	2045.8	N	Y	N	Y	Y	Y	N	(Hex) ₇ + (Man) ₃ (GlcNAc) ₂	
19a	60	1038.9	2078.8	N	N	N	Y	N	N	2123.7*	(Hex) ₂ (HexNAc) ₂ (Deoxyhexose) ₁ (NeuAc) ₁ + (Man) ₃ (GlcNAc) ₂	
19b	64.1			Y	N	N	N	Y	Y			
19c	68.3			N	N	N	Y	N	N			
19d	68.8			N	N	N	Y	N	N			
19e	73.1			N	N	N	N	Y	Y			
20a	54.1	1140.5	2282	N	N	N	Y	N	N	N	(Hex) ₂ (HexNAc) ₃ (Deoxyhexose) ₁ (NeuAc) ₁ + (Man) ₃ (GlcNAc) ₂	
20b	57.8			N	N	Y	N	Y	Y			

21	40.4	1062.3	2125.6	N	Y	N	N	N	N	(Hex) ₇ (Phos) ₁ + (Man) ₃ (GlcNAc) ₂	
22a	44.7	1111.4	2223.8	Y	N	N	Y	N	Y	(Hex) ₂ (HexNAc) ₂ (NeuAc) ₂ + (Man) ₃ (GlcNAc) ₂	
22b	45.9			N	N	N	Y	N	N		
22c	57.3			N	N	N	Y	N	Y		
22d	60.4			N	N	N	N	Y	N		
23	48.2	1184.4	2369.8	Y	N	N	Y	N	N	(Hex) ₂ (HexNAc) ₂ (Deoxyhexose) ₁ (NeuAc) ₂ + (Man) ₃ (GlcNAc) ₂	
24	59.5	1221.4	2443.8	N	N	N	Y	N	N	(Hex) ₃ (HexNAc) ₃ (Deoxyhexose) ₁ (NeuAc) ₁ + (Man) ₃ (GlcNAc) ₂	
25	46.1		1235.5	N	Y	Y	Y	Y	Y	(Hex) ₂ + (Man) ₃ (GlcNAc) ₂	
26	42.8	1285.9	2572.8	N	N	N	Y	N	N	(Hex) ₂ (HexNAc) ₃ (Deoxyhexose) ₁ (NeuAc) ₂ + (Man) ₃ (GlcNAc) ₂	

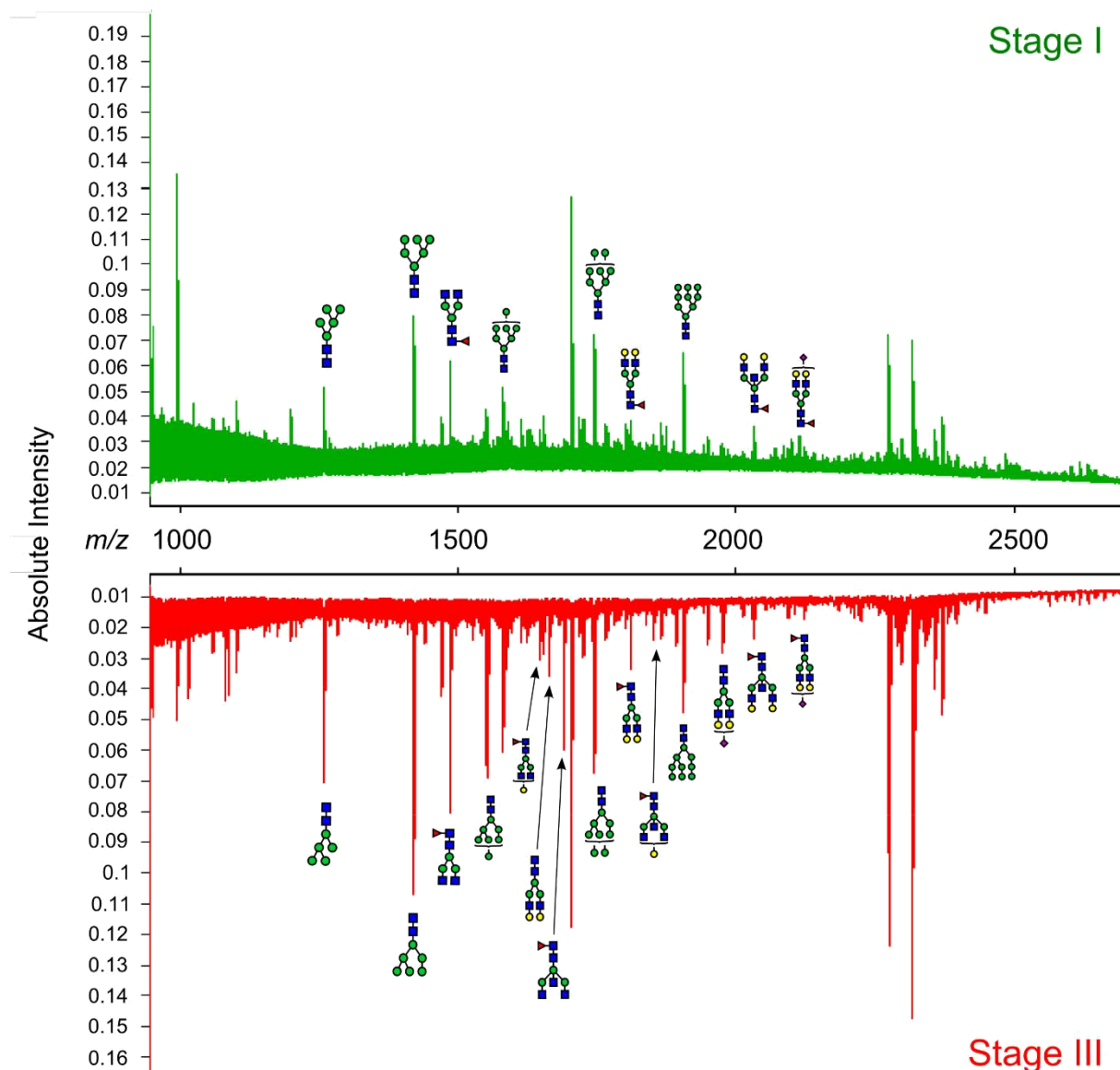


Figure 1: Representative *N*-glycan MALDI mass spectrometry imaging summed spectra (zoomed in *m/z* range) of combined stage I (n = 3) and stage III (n = 3) serous ovarian cancer patients. The raw data was loaded into SCiLS Lab (version 2016b, SCiLS, Bruker Daltonics) and pre-processed by TopHat baseline subtraction, normalization to total ion current (TIC), peak picking and alignment. This figure was manually annotated based on MS/MS fragmentation from PGC-LC-ESI-MS/MS data. The figure was formatted and created in Inkscape (version 2.0, www.inkscape.org).

Ion intensity maps for early-stage (n = 3) and late-stage (n = 3) FFPE serous ovarian cancer tissue sections were constructed from the 14 unique *m/z* values acquired in MALDI-MSI (see *Figures 2-5* and *Supplementary Figures 2-12*). The corresponding *N*-glycan masses were spatially localised by MALDI-MSI and structurally characterised by PGC-LC-ESI-MS/MS, as already described (see *Table 2*). *Figure 2* and *Supplementary Figures 2-5* show that all oligomannose *N*-glycans were predominantly observed in the tumour microenvironment of the late-stage patients. For example, *m/z* 1905.633 (Hex)₆ + (Man)₃(GlcNAc)₂, was observed to be abundant in tumour regions of late-stage patients (see *Figure 2*

Panels A-F). Figure 2 Panel G shows the N-glycan structure assigned to the ion intensity maps in Panels A-F based on the corresponding extracted ion chromatogram (Panel H) and fragmentation (Panel I).

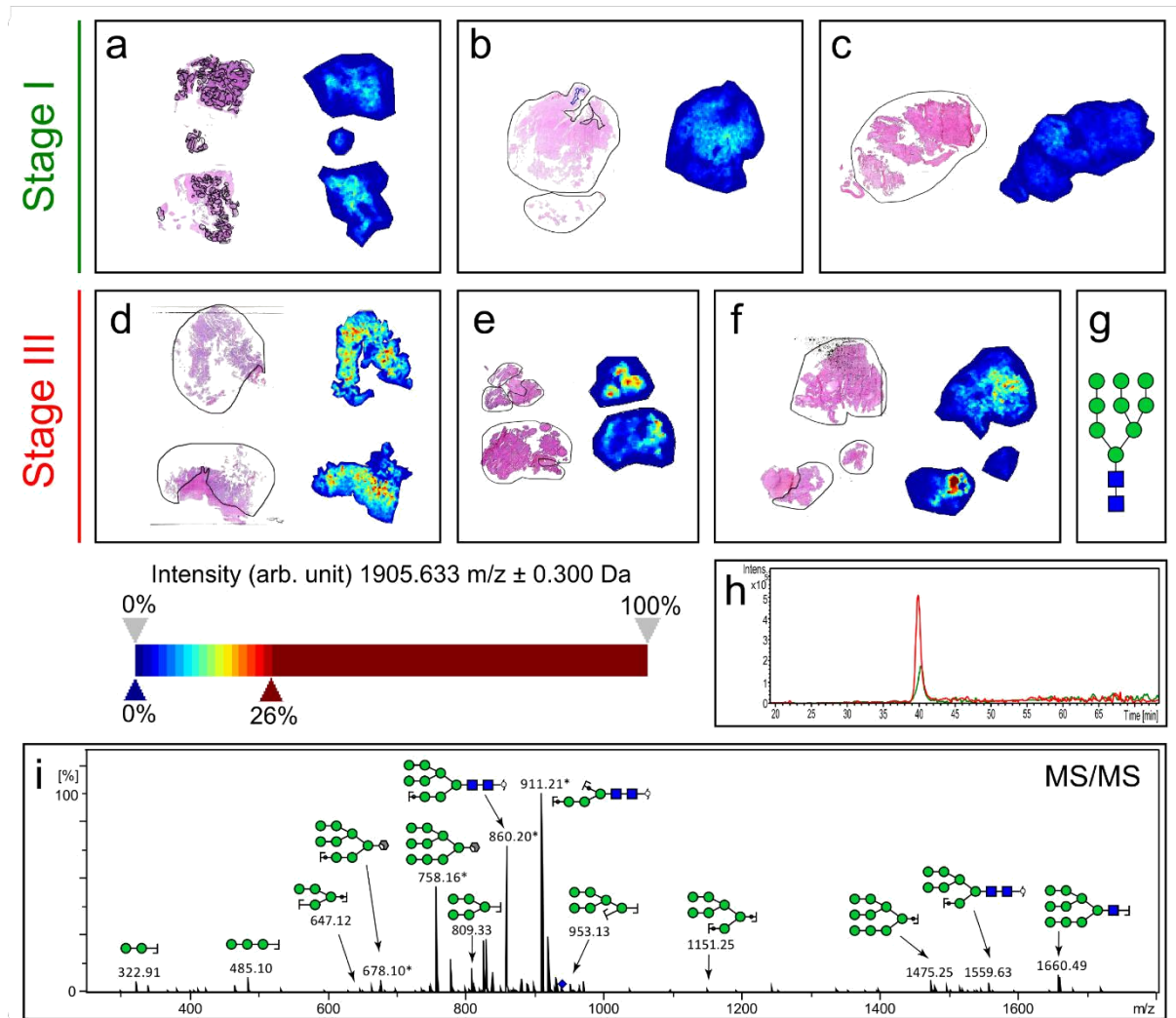


Figure 2: Single N-glycan mass MALDI mass spectrometry imaging (MSI) of stage I (n = 3) and stage III (n = 3) serous ovarian cancer patients. Formalin-fixed paraffin-embedded tissue sections were treated with citric acid antigen retrieval prior to printing of dialyzed PNGase F with 250 μm spacing. 2,5-DHB matrix was sprayed onto the sections and MS spectra were acquired by oversampling at 100 μm intervals using a MALDI-TOF/TOF MS instrument. Monoisotopic glycan masses were measured in the positive ion reflectron mode as $(M + \text{Na}) \pm 0.3$ Da adducts for MALDI-MSI whereas PGC-LC-ESI-MS/MS revealed doubly negative charged monoisotopic masses $([M-2\text{H}]^{2-})$. Panels A-F show annotated tumour regions (black – annotated by pathologist) of H&E stained tissue sections and ion intensity maps of m/z 1905.633 from stage I (green) and stage III (red) patients. The N-glycan, $(\text{Hex})_6 + (\text{Man})_3(\text{GlcNAc})_2$, corresponding to m/z 1905.633 in G is the confirmed structure based on the extracted ion chromatography of 941.3 (Panel H) and the MS/MS fragmentation (Panel I).

Furthermore, complex neutral N-glycans (see Figure 3 and Supplementary Figures 6-8) were more intense in the tumour microenvironment of the late-stage patients compared to early stage, as well as

being intense in the adjacent cancer-associated stroma regions. However, fucosylated, truncated biantennary neutral *N*-glycan, m/z 1485.533 (HexNAc)₂ (Deoxyhexose)₁ + (Man)₃(GlcNAc)₂ was not consistent with this observation as it was only observed in necrotic regions, which is consistent with the literature (see *Supplementary Figure 6*) (Everest-Dass et al., 2016). The larger m/z 1809.639 (Hex)₂ (HexNAc)₂ (Deoxyhexose)₁ + (Man)₃(GlcNAc)₂ was an example of a complex neutral *N*-glycan that is predominantly in the tumour microenvironment of late-stage patients (see *Figure 3 Panels A-F*). This *N*-glycan was structurally characterised by PGC-LC-ESI-MS/MS analysis, therefore confirming its structural and compositional features (*Panel I*).

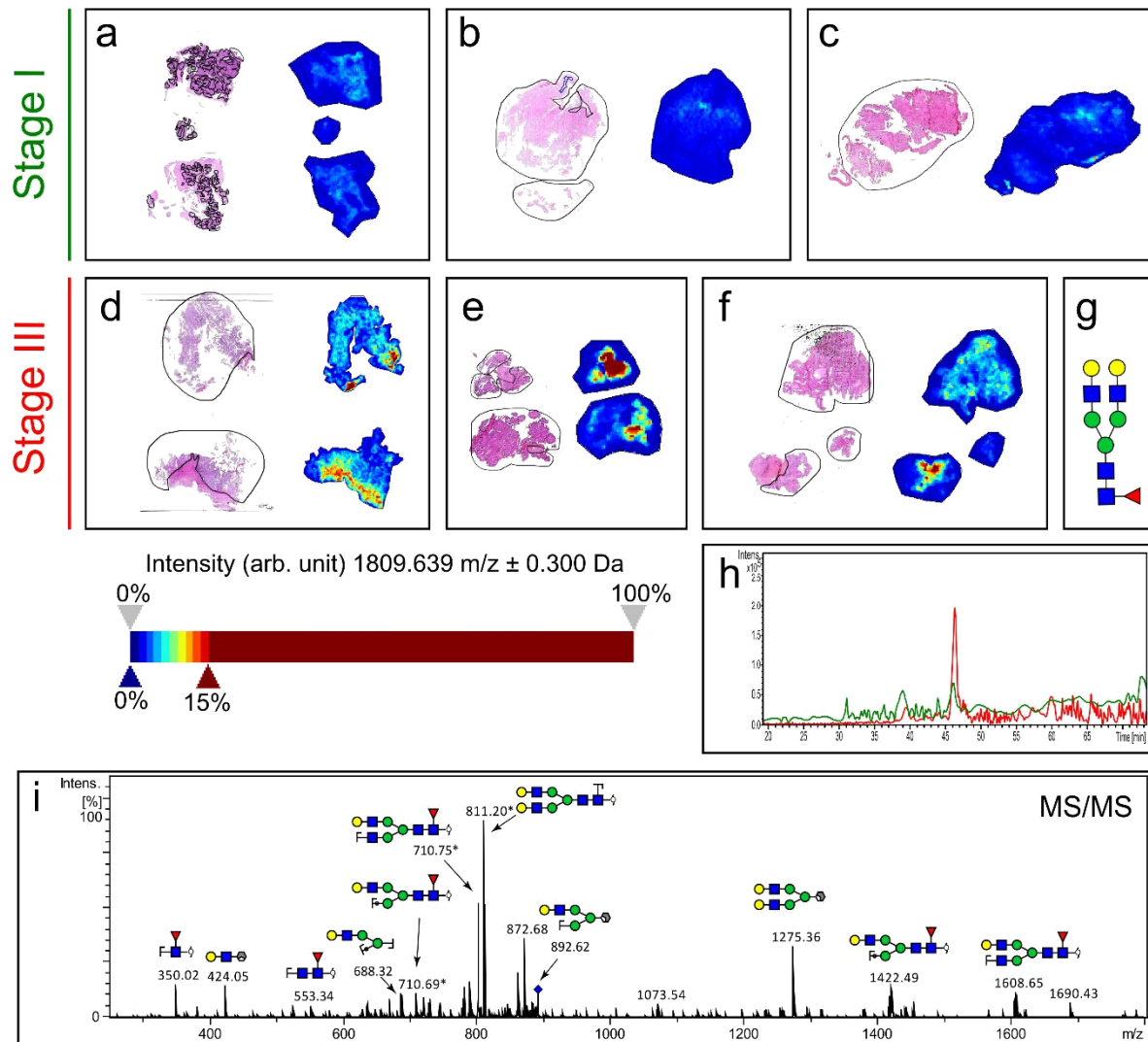


Figure 3: Single N-glycan mass MALDI mass spectrometry imaging (MSI) of stage I (n = 3) and stage III (n = 3) serous ovarian cancer patients. Formalin-fixed paraffin-embedded tissue sections were treated with citric acid antigen retrieval prior to printing of dialyzed PNGase F with 250 μm spacing. 2,5-DHB matrix was sprayed onto the sections and MS spectra were acquired by oversampling at 100 μm intervals using a MALDI-TOF/TOF MS instrument. Monoisotopic glycan masses were measured in the positive ion reflectron mode as $(M + \text{Na}) \pm 0.3$ Da adducts for MALDI-MSI whereas PGC-LC-ESI-MS/MS revealed doubly negatively charged monoisotopic masses $([M-2H]^{2-})$. Panels A-F show annotated tumour regions (black – annotated by pathologist) of H&E stained tissue sections and ion intensity maps of m/z 1809.639 from the stage I (green) and stage III (red) patients. The N-glycan, $(\text{Hex})_2(\text{HexNAc})_2(\text{Deoxyhexose})_1 + (\text{Man})_3(\text{GlcNAc})_2$, corresponding to m/z 1809.639 in G is the confirmed structure based on the extracted ion chromatography of 893.3 (Panel H) and fragmentation (Panel I).

Another tumour-specific N-glycan predominantly observed in late-stage patients, relative to early-stage, were galactosylated bisecting structures (see Figure 4 and Supplementary Figures 9-10). For example, m/z 1850.665 $(\text{Hex})_1(\text{HexNAc})_3(\text{Deoxyhexose})_1 + (\text{Man})_3(\text{GlcNAc})_2$ was observed mostly in the tumour microenvironment of late-stage patients (see Figure 4 Panels A-F). As detailed in Panel H, the

galactosylated bisecting structure eluted at around 40 minutes. This specific *N*-glycan was characterised by PGC-LC-ESI-MS/MS analysis (see *Figure 4 Panel I*) with the *m/z* 350 fragment ion being assigned as core fucosylation.

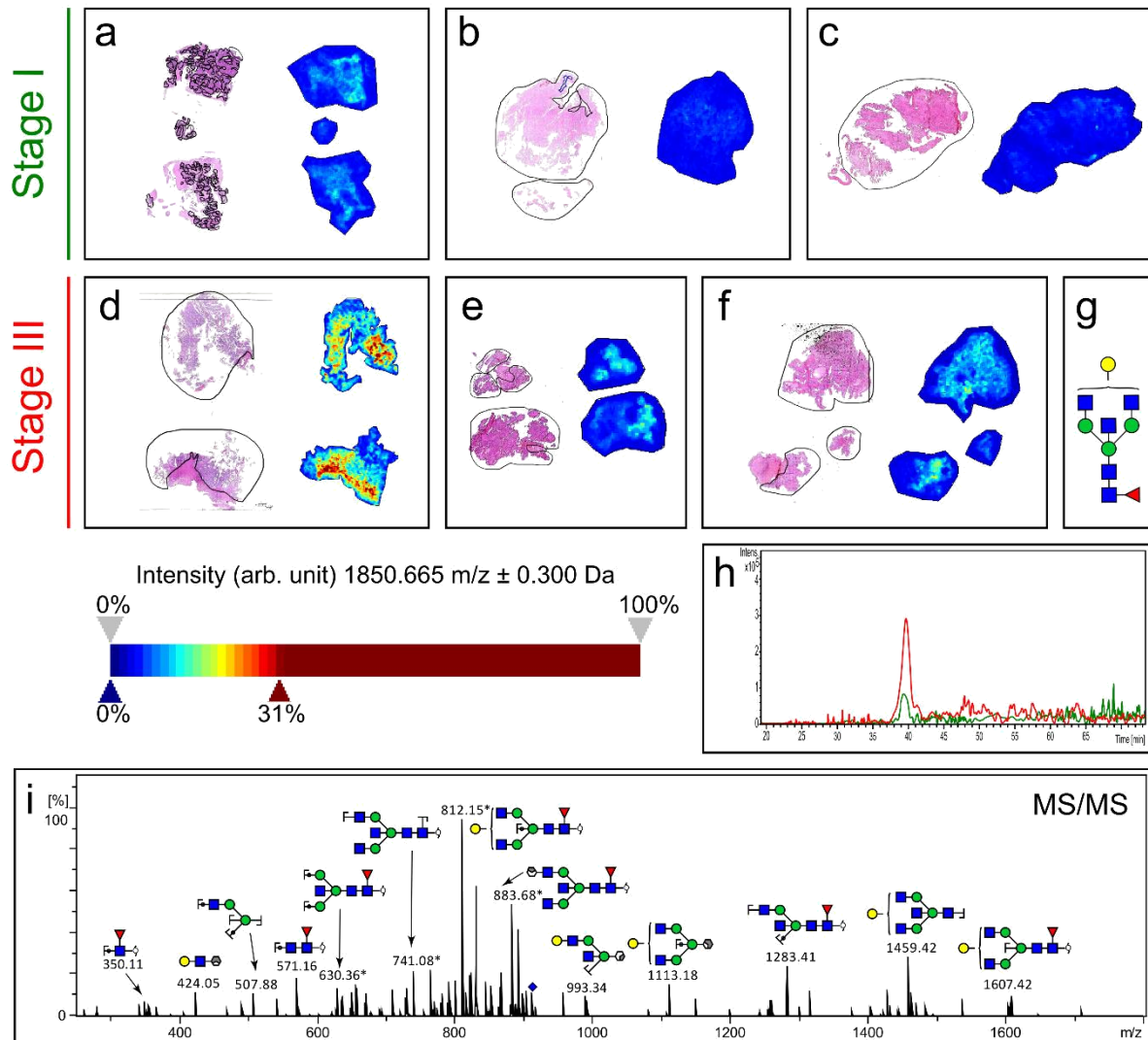


Figure 4: Single *N*-glycan mass MALDI mass spectrometry imaging (MSI) of stage I (n = 3) and stage III (n = 3) serous ovarian cancer patients. Formalin-fixed paraffin-embedded tissue sections were treated with citric acid antigen retrieval prior to printing of dialyzed PNGase F with 250 μm spacing. 2,5-DHB matrix was sprayed onto the sections and MS spectra were acquired by oversampling at 100 μm intervals using a MALDI-TOF/TOF MS instrument. Monoisotopic glycan masses were measured in the positive ion reflectron mode as $(M + \text{Na}) \pm 0.3$ Da adducts for MALDI-MSI whereas PGC-LC-ESI-MS/MS revealed doubly negatively charged monoisotopic masses $([M-2\text{H}]^{2-})$. Panels A-F show annotated tumour regions (black – annotated by pathologist) of H&E stained tissue sections and ion intensity maps of *m/z* 1850.665 from the stage I (green) and stage III (red) patients. The *N*-glycan, $(\text{Hex})_1(\text{HexNAc})_3(\text{Deoxyhexose})_1 + (\text{Man})_3(\text{GlcNAc})_2$, corresponding to *m/z* 1850.665 in G is the confirmed structure based on the extracted ion chromatography of 913.8 (Panel H) and fragmentation (Panel I).

In summary, several *N*-glycan structures were identified as potential markers for early-stage diagnosis of serous ovarian cancer, including the high mannose structure, (Hex)₆ + (Man)₃(GlcNAc)₂ (see *Figure 2*), the galactosylated bisecting structure, (Hex)₁ (HexNAc)₃ (Deoxyhexose)₁ + (Man)₃(GlcNAc)₂ (see *Figure 3*), and the sialylated structure, (Hex)₂ (HexNAc)₂ (NeuAc)₁ + (Man)₃(GlcNAc)₂ (see *Figure 4*).

4. Discussion

We applied our established *N*-glycan MALDI-MSI and PGC-LC-ESI-MS/MS workflow to FFPE serous ovarian cancer tissue sections and confirmed that there are notable aberrant *N*-glycans in the ovarian cancer tumour microenvironment between early- and late-stage patients. Sample numbers were low in this study due to difficulty with early-stage patient sample accessibility. These alterations have previously been observed as a result of changes to the *N*-glycosylation pathway in cancer as reflected by expression of different glycosyltransferase genes and glycan structures (Allam et al., 2015; Anugraham et al., 2014; Everest-Dass et al., 2016). Oligomannose *N*-glycans have consistently been found to be highly abundant on membrane glycoproteins from ovarian cancer cell lines (Anugraham et al., 2014) and from stage IIIc serous ovarian cancer (Everest-Dass et al., 2016). This was the first time that the spatial protein glycosylation of late-stage ovarian cancer patients has been compared to early-stage patients using this approach. This study has confirmed that oligomannose *N*-glycan structures are predominantly in the late-stage tumour microenvironment, based on combined MALDI-MSI and PGC-LC-ESI-MS/MS analysis (see *Figure 2* and *Supplementary Figures 2-5*). In the literature, murine and human pluripotent stem cells have presented increased oligomannose *N*-glycans, therefore indicating cancer stem cell populations could present a similar glycosylation pattern (An et al., 2012; Nairn et al., 2008). Additionally, Man9 structures have been found in mouse breast tumour models and human sera of patients with breast cancer (de Leoz et al., 2011).

Furthermore, complex neutral and fucosylated *N*-glycan structures were also observed to be localized to the late-stage tumour microenvironment; however they were more intense in the cancer-associated stroma regions than in the tumour, as previously detailed in the literature (Everest-Dass et al., 2016). Through MALDI-MSI analysis, (HexNAc)₂ (Deoxyhexose)₁ + (Man)₃(GlcNAc)₂ was determined to be spatially distributed across a mixture of early- and late-stage patients, which is not consistent with the other complex neutral and fucosylated *N*-glycan structures that are only seen in the late-stage patients (see *Supplementary Figure 6*). Upon further investigation, the pathologist noticed that this early-stage patient, shown in *Panel C* of *All Figures*, contains necrotic and tumour regions. Therefore, the observation of (HexNAc)₂ (Deoxyhexose)₁ + (Man)₃(GlcNAc)₂ in this patient is consistent with previous data that concludes this specific *N*-glycan structure is localised to necrotic regions (Everest-Dass et al., 2016). Other complex neutral *N*-glycan structures, (Hex)₂ (HexNAc)₂ (Deoxyhexose)₁ + (Man)₃(GlcNAc)₂ and (Hex)₂ (HexNAc)₂ + (Man)₃(GlcNAc)₂, were observed to be highly intense in both tumour and stroma regions of late stage tissues (see *Figure 3* and *Supplementary Figure 8* respectively). These structures were confirmed by PGC-LC-ESI-MS/MS fragmentation analysis, but, to

the contrary these complex neutral and fucosylated *N*-glycans were found in cell lines to be more intense in healthy cells compared to tumour cells (Anugraham et al., 2014). This may suggest that ovarian cancer cell lines do not present identical *N*-glycomes to ovarian cancer tissue. In serous and endometrioid ovarian cancer tissues, it has been discovered that core fucosylation is elevated (Abbott et al., 2008; Nairn et al., 2008; Takahashi et al., 2000). This observation is consistent with the results presented herein.

Bisecting *N*-glycan structures have been extensively observed in the tumour microenvironment of serous ovarian cancer from cell lines and tissue (Allam et al., 2015; Anugraham et al., 2014). This observation is consistent with the MALDI-MSI analysis reported here, where two galactosylated bisecting structures were detected predominantly in the tumour region of late-stage patients relative to early-stage patients (see *Figure 4* and *Supplementary Figures 10*). The galactosylated bisecting *N*-glycan structure, (Hex)₁ (HexNAc)₃ (Deoxyhexose)₁ + (Man)₃(GlcNAc)₂, was observed to be the most intense based on both MALDI-MSI analysis, and PGC-LC-ESI-MS/MS analysis (see *Figure 4*). However, the agalactosylated bisecting *N*-glycan structure, (HexNAc)₃ (Deoxyhexose)₁ + (Man)₃(GlcNAc)₂, was not consistent with the galactosylated structures (see *Supplementary Figure 9*). This observation is novel and requires further investigation into specific glycosyltransferase activities surrounding early- and late-stage patients. Recently, bisecting *N*-glycan structures have been found to be associated with ovarian cancer cell survival by correlation with *MGAT 3* expression (N-acetylglucosaminyltransferase III, GnT-III), which synthesises bisecting GlcNAc by adding GlcNAc in a β1-4 linkage to the core *N*-glycan (Kohler et al., 2016). However, in breast cancer tissue, the levels of the GnT-III enzyme are low compared to the ovarian cancer studies. For example, breast cancer tissues have lower levels of GnT-III relative to normal breast tissue (Potapenko et al., 2010) while ovarian cancer tissues have higher levels of GnT-III relative to normal ovarian and fallopian tube tissues (Abbott et al., 2008; Nairn et al., 2008). The expression of GnT-III in ovarian cancer cell lines is believed to be regulated by epigenetic hypomethylation (Anugraham et al., 2014). Additionally, GnT-III mRNA levels and enzymatic activity were seen to be increased in ovarian tumour tissues derived from mouse models and human samples of endometrioid ovarian carcinoma (Abbott et al., 2010).

Sialylated *N*-glycan structures have previously been found to be glyco-markers of tumorigenesis (Anugraham et al., 2017; Anugraham et al., 2014). (Hex)₂ (HexNAc)₂ (NeuAc)₁ + (Man)₃(GlcNAc)₂ was discovered in our study to be predominantly in late-stage ovarian cancer patients relative to the early-stage patients based on MALDI-MSI and PGC-LC-ESI-MS/MS analysis (see *Supplementary Figure 12*). However, PGC-LC-ESI-MS/MS chromatography and fragmentation was unable to elucidate different

isomeric sialylated structures, such as α -2,3 and α -2,6 sialic acid linkage, due to poor chromatographic resolution and poor fragmentation pattern. In the literature, it has been shown that the α -2,6 linkage of sialic acid is increased in ovarian cancer cell lines relative to normal cell lines while α -2,3 linkage is increased in normal cell lines relative to ovarian cancer cell lines (Anugraham et al., 2014). Therefore, further investigation into sialic acid linkage differences between stages is required with a larger patient cohort through the construction of a tissue micro-array (TMA). MALDI-MSI analysis of a TMA would also reduce experimental variability as multiple patients can be analysed in a single experiment as opposed to single sections that are often analysed across multiple experiments. Additionally, we did not expect to see many sialylated species since we heated the sample in the citric acid antigen retrieval (CAAR) and utilised reflectron mode in MALDI-MSI analysis that is known to desialylate glycan structures. To address this caveat in future, we can either optimize our method for linear and/or negative mode or use chemical modifications to derivatize the sialylated species such that they are not cleaved in the MALDI-MSI analysis. For example, Holst *et al.*, developed a novel derivatization method where *in situ* di-methylamidation is performed to identify linkage-specific sialylated *N*-glycans using MALDI-MSI (Holst et al., 2016). In that study of FFPE colon carcinoma tissue, sialylated *N*-glycans were discovered to be α 2-3 linkage in stroma, tumor, and necrotic regions, while sialylated *N*-glycans with α 2-6 linkage were observed in necrotic, collagen-rich, and red blood cell regions. However, the limitation with this novel derivatization method is that other *N*-glycan isomeric structures were not considered (i.e. high mannose, complex/hybrid).

5. Conclusion

In summary, this is the first study where late-stage and early-stage serous ovarian cancer patient tissues have been compared by MALDI-MSI to spatially map protein *N*-glycans using PGC-LC-ESI-MS/MS to structurally characterise the *N*-glycan masses. A total of 14 *N*-glycans were confirmed from MALDI-MSI across tumour and non-tumour regions, while 42 *N*-glycan structures (including structural and compositional isomers) were identified and characterised using PGC-LC-ESI-MS/MS. The spatial distribution and localisation of specific *N*-glycans were visualised in the tumour regions of late-stage serous ovarian cancer tissue sections relative to early-stage. *N*-glycans of interest that classified these late-stage patients by their abundance included the oligomannose structure, (Hex)₆ + (Man)₃(GlcNAc)₂, the bisecting structure (Hex)₁ (HexNAc)₃ (Deoxyhexose)₁ + (Man)₃(GlcNAc)₂, and the sialylated structure, (Hex)₂ (HexNAc)₂ (NeuAc)₁ + (Man)₃(GlcNAc)₂. However, further investigation is required to validate these observations in a larger patient cohort as well as to determine the function and significance of the changes in *N*-glycans attached to specific glycoproteins to understand ovarian cancer development and progression.

Acknowledgements

PH received financial support from the Australian Research Council (ARC LP110100693), Bioplatforms Australia, and the Government of South Australia. NHP and AVED received financial support of the ARC CoE in Nanoscale Biophotonics (ARC CE140100003).

Author Contributions

PH, NHP, MTB and YYH conceived the project. PH and NHP supervised the research. MKO provided the ovarian tissue samples and GK annotated the H&E stained FFPE sections. MTB, YYH, MRC and AVED were primarily responsible for data collection and analysis. MTB and AVED prepared figures and MTB wrote the main manuscript text. All authors contributed to the discussions and manuscript preparation.

References

- Abbott, K.L., Lim, J.M., Wells, L., Benigno, B.B., McDonald, J.F., Pierce, M., 2010. Identification of candidate biomarkers with cancer-specific glycosylation in the tissue and serum of endometrioid ovarian cancer patients by glycoproteomic analysis. *Proteomics* 10, 470-481.
- Abbott, K.L., Nairn, A.V., Hall, E.M., Horton, M.B., McDonald, J.F., Moremen, K.W., Dinulescu, D.M., Pierce, M., 2008. Focused glycomic analysis of the N-linked glycan biosynthetic pathway in ovarian cancer. *Proteomics* 8, 3210-3220.
- Allam, H., Aoki, K., Benigno, B.B., McDonald, J.F., Mackintosh, S.G., Tiemeyer, M., Abbott, K.L., 2015. Glycomic analysis of membrane glycoproteins with bisecting glycosylation from ovarian cancer tissues reveals novel structures and functions. *Journal of proteome research* 14, 434-446.
- An, H.J., Gip, P., Kim, J., Wu, S., Park, K.W., McVaugh, C.T., Schaffer, D.V., Bertozzi, C.R., Lebrilla, C.B., 2012. Extensive determination of glycan heterogeneity reveals an unusual abundance of high mannose glycans in enriched plasma membranes of human embryonic stem cells. *Molecular & cellular proteomics: MCP* 11, M111 010660.
- Anugraham, M., Jacob, F., Everest-Dass, A.V., Schoetzau, A., Nixdorf, S., Hacker, N.F., Fink, D., Heinzelmann-Schwarz, V., Packer, N.H., 2017. Tissue glycomics distinguish tumour sites in women with advanced serous adenocarcinoma. *Molecular oncology* 11, 1595-1615.
- Anugraham, M., Jacob, F., Nixdorf, S., Everest-Dass, A.V., Heinzelmann-Schwarz, V., Packer, N.H., 2014. Specific glycosylation of membrane proteins in epithelial ovarian cancer cell lines: glycan structures reflect gene expression and DNA methylation status. *Molecular & cellular proteomics: MCP* 13, 2213-2232.
- Australian Institute of Health and Welfare, 2017. Cancer in Australia: Actual incidence data from 1982 to 2013 and mortality data from 1982 to 2014 with projections to 2017. *Asia-Pacific journal of clinical oncology*.
- Briggs, M.T., Ho, Y.Y., Kaur, G., Oehler, M.K., Everest-Dass, A.V., Packer, N.H., Hoffmann, P., 2017. N-Glycan matrix-assisted laser desorption/ionization mass spectrometry imaging protocol for formalin-fixed paraffin-embedded tissues. *Rapid communications in mass spectrometry: RCM* 31, 825-841.
- Campbell, M.P., Hayes, C.A., Struwe, W.B., Wilkins, M.R., Aoki-Kinoshita, K.F., Harvey, D.J., Rudd, P.M., Kolarich, D., Lisacek, F., Karlsson, N.G., Packer, N.H., 2011. UniCarbKB: putting the pieces together for glycomics research. *Proteomics* 11, 4117-4121.
- Carvalho, S., Reis, C.A., Pinho, S.S., 2016. Cadherins Glycans in Cancer: Sweet Players in a Bitter Process. *Trends in cancer* 2, 519-531.
- Chen, H., Deng, Z., Huang, C., Wu, H., Zhao, X., Li, Y., 2017. Mass spectrometric profiling reveals association of N-glycan patterns with epithelial ovarian cancer progression. *Tumour biology: the journal of the International Society for Oncodevelopmental Biology and Medicine* 39, 1010428317716249.
- Cooper, C.A., Gasteiger, E., Packer, N.H., 2001. GlycoMod—a software tool for determining glycosylation compositions from mass spectrometric data. *Proteomics* 1, 340-349.

de Leoz, M.L., Young, L.J., An, H.J., Kronewitter, S.R., Kim, J., Miyamoto, S., Borowsky, A.D., Chew, H.K., Lebrilla, C.B., 2011. High-mannose glycans are elevated during breast cancer progression. *Molecular & cellular proteomics: MCP* 10, M110 002717.

Domcke, S., Sinha, R., Levine, D.A., Sander, C., Schultz, N., 2013. Evaluating cell lines as tumour models by comparison of genomic profiles. *Nature communications* 4, 2126.

Dube, D.H., Bertozzi, C.R., 2005. Glycans in cancer and inflammation--potential for therapeutics and diagnostics. *Nature reviews. Drug discovery* 4, 477-488.

El Ayed, M., Bonnel, D., Longuespee, R., Castelier, C., Franck, J., Vergara, D., Desmons, A., Tasiemski, A., Kenani, A., Vinatier, D., Day, R., Fournier, I., Salzet, M., 2010. MALDI imaging mass spectrometry in ovarian cancer for tracking, identifying, and validating biomarkers. *Medical science monitor: international medical journal of experimental and clinical research* 16, BR233-245.

Everest-Dass, A.V., Abrahams, J.L., Kolarich, D., Packer, N.H., Campbell, M.P., 2013a. Structural feature ions for distinguishing N- and O-linked glycan isomers by LC-ESI-IT MS/MS. *Journal of the American Society for Mass Spectrometry* 24, 895-906.

Everest-Dass, A.V., Briggs, M.T., Kaur, G., Oehler, M.K., Hoffmann, P., Packer, N.H., 2016. N-glycan MALDI Imaging Mass Spectrometry on Formalin-Fixed Paraffin-Embedded Tissue Enables the Delineation of Ovarian Cancer Tissues. *Molecular & cellular proteomics: MCP* 15, 3003-3016.

Everest-Dass, A.V., Kolarich, D., Campbell, M.P., Packer, N.H., 2013b. Tandem mass spectra of glycan substructures enable the multistage mass spectrometric identification of determinants on oligosaccharides. *Rapid communications in mass spectrometry: RCM* 27, 931-939.

Gustafsson, O.J., Briggs, M.T., Condina, M.R., Winderbaum, L.J., Pelzing, M., McColl, S.R., Everest-Dass, A.V., Packer, N.H., Hoffmann, P., 2015. MALDI imaging mass spectrometry of N-linked glycans on formalin-fixed paraffin-embedded murine kidney. *Analytical and bioanalytical chemistry* 407, 2127-2139.

Hakomori, S., 2002. Glycosylation defining cancer malignancy: new wine in an old bottle. *Proceedings of the National Academy of Sciences of the United States of America* 99, 10231-10233.

Hinneburg, H., Korac, P., Schirmeister, F., Gasparov, S., Seeberger, P.H., Zoldos, V., Kolarich, D., 2017. Unlocking Cancer Glycomes from Histopathological Formalin-fixed and Paraffin-embedded (FFPE) Tissue Microdissections. *Molecular & cellular proteomics: MCP* 16, 524-536.

Holst, S., Heijs, B., de Haan, N., van Zeijl, R.J., Briaire-de Bruijn, I.H., van Pelt, G.W., Mehta, A.S., Angel, P.M., Mesker, W.E., Tollenaar, R.A., Drake, R.R., Bovee, J.V., McDonnell, L.A., Wuhrer, M., 2016. Linkage-Specific in Situ Sialic Acid Derivatization for N-Glycan Mass Spectrometry Imaging of Formalin-Fixed Paraffin-Embedded Tissues. *Analytical chemistry* 88, 5904-5913.

Jensen, P.H., Karlsson, N.G., Kolarich, D., Packer, N.H., 2012. Structural analysis of N- and O-glycans released from glycoproteins. *Nature protocols* 7, 1299-1310.

Kim, H., Wu, R., Cho, K.R., Thomas, D.G., Gossner, G., Liu, J.R., Giordano, T.J., Shedden, K.A., Misek, D.E., Lubman, D.M., 2008. Comparative proteomic analysis of low stage and high stage endometrioid ovarian adenocarcinomas. *Proteomics. Clinical applications* 2, 571-584.

Kohler, R.S., Anugraham, M., Lopez, M.N., Xiao, C., Schoetzau, A., Hettich, T., Schlotterbeck, G., Fedier, A., Jacob, F., Heinzelmann-Schwarz, V., 2016. Epigenetic activation of MGAT3 and corresponding bisecting GlcNAc shortens the survival of cancer patients. *Oncotarget* 7, 51674-51686.

Lu, P., Vogel, C., Wang, R., Yao, X., Marcotte, E.M., 2007. Absolute protein expression profiling estimates the relative contributions of transcriptional and translational regulation. *Nature biotechnology* 25, 117-124.

Nairn, A.V., York, W.S., Harris, K., Hall, E.M., Pierce, J.M., Moremen, K.W., 2008. Regulation of glycan structures in animal tissues: transcript profiling of glycan-related genes. *The Journal of biological chemistry* 283, 17298-17313.

North, S.J., Hitchen, P.G., Haslam, S.M., Dell, A., 2009. Mass spectrometry in the analysis of N-linked and O-linked glycans. *Current opinion in structural biology* 19, 498-506.

Ohtsubo, K., Marth, J.D., 2006. Glycosylation in cellular mechanisms of health and disease. *Cell* 126, 855-867.

Potapenko, I.O., Haakensen, V.D., Luders, T., Helland, A., Bukholm, I., Sorlie, T., Kristensen, V.N., Lingjaerde, O.C., Borresen-Dale, A.L., 2010. Glycan gene expression signatures in normal and malignant breast tissue; possible role in diagnosis and progression. *Molecular oncology* 4, 98-118.

Powers, T.W., Holst, S., Wuhrer, M., Mehta, A.S., Drake, R.R., 2015. Two-Dimensional N-Glycan Distribution Mapping of Hepatocellular Carcinoma Tissues by MALDI-Imaging Mass Spectrometry. *Biomolecules* 5, 2554-2572.

Powers, T.W., Neely, B.A., Shao, Y., Tang, H., Troyer, D.A., Mehta, A.S., Haab, B.B., Drake, R.R., 2014. MALDI imaging mass spectrometry profiling of N-glycans in formalin-fixed paraffin embedded clinical tissue blocks and tissue microarrays. *PLoS one* 9, e106255.

Takahashi, T., Ikeda, Y., Miyoshi, E., Yaginuma, Y., Ishikawa, M., Taniguchi, N., 2000. alpha1,6fucosyltransferase is highly and specifically expressed in human ovarian serous adenocarcinomas. *International journal of cancer* 88, 914-919.

Vang, R., Shih le, M., Kurman, R.J., 2009. Ovarian low-grade and high-grade serous carcinoma: pathogenesis, clinicopathologic and molecular biologic features, and diagnostic problems. *Advances in anatomic pathology* 16, 267-282.

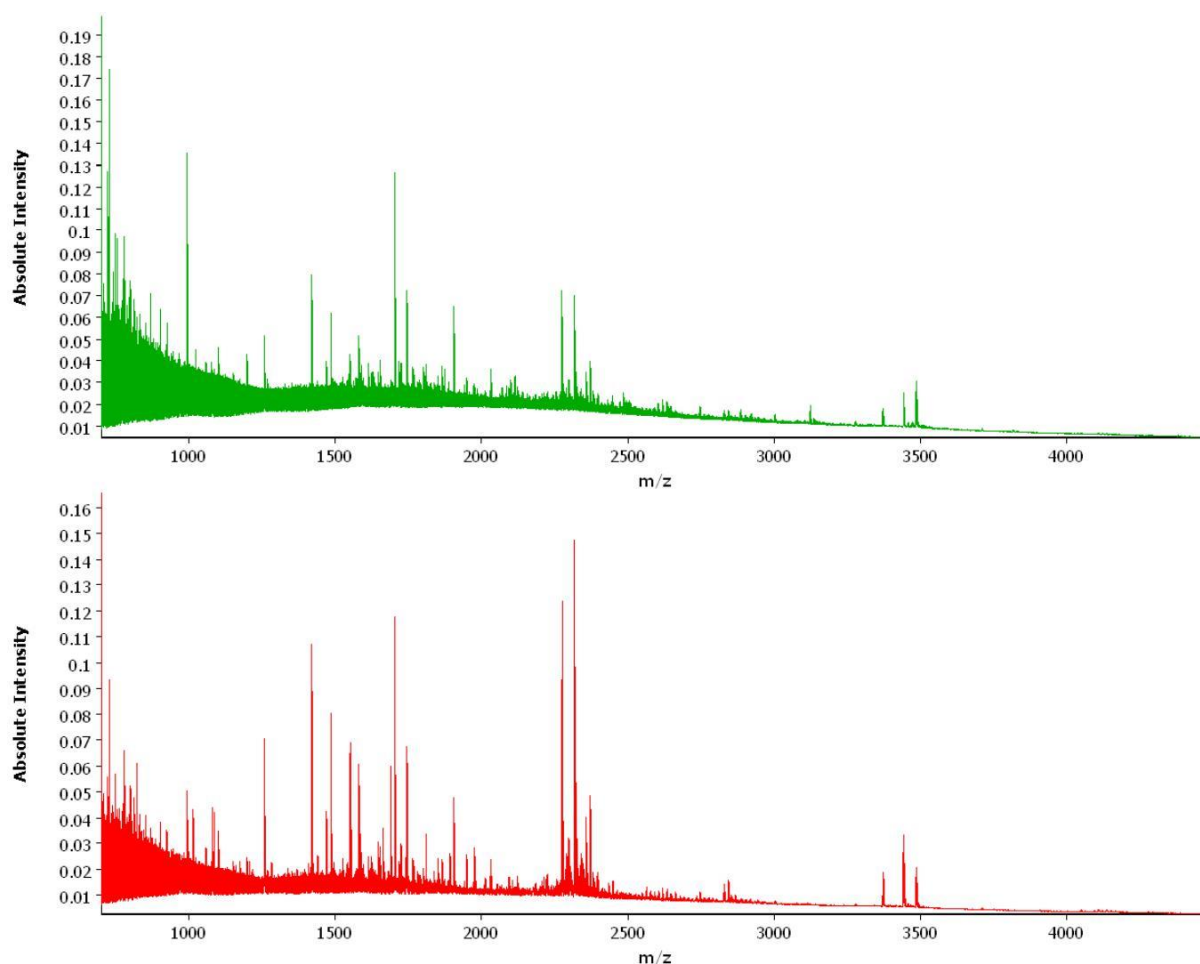
Zhang, X., Wang, Y., Qian, Y., Wu, X., Zhang, Z., Liu, X., Zhao, R., Zhou, L., Ruan, Y., Xu, J., Liu, H., Ren, S., Xu, C., Gu, J., 2014. Discovery of specific metastasis-related N-glycan alterations in epithelial ovarian cancer based on quantitative glycomics. *PLoS one* 9, e87978.

Zhu, Y., Wu, R., Sangha, N., Yoo, C., Cho, K.R., Shedden, K.A., Katabuchi, H., Lubman, D.M., 2006. Classifications of ovarian cancer tissues by proteomic patterns. *Proteomics* 6, 5846-5856.

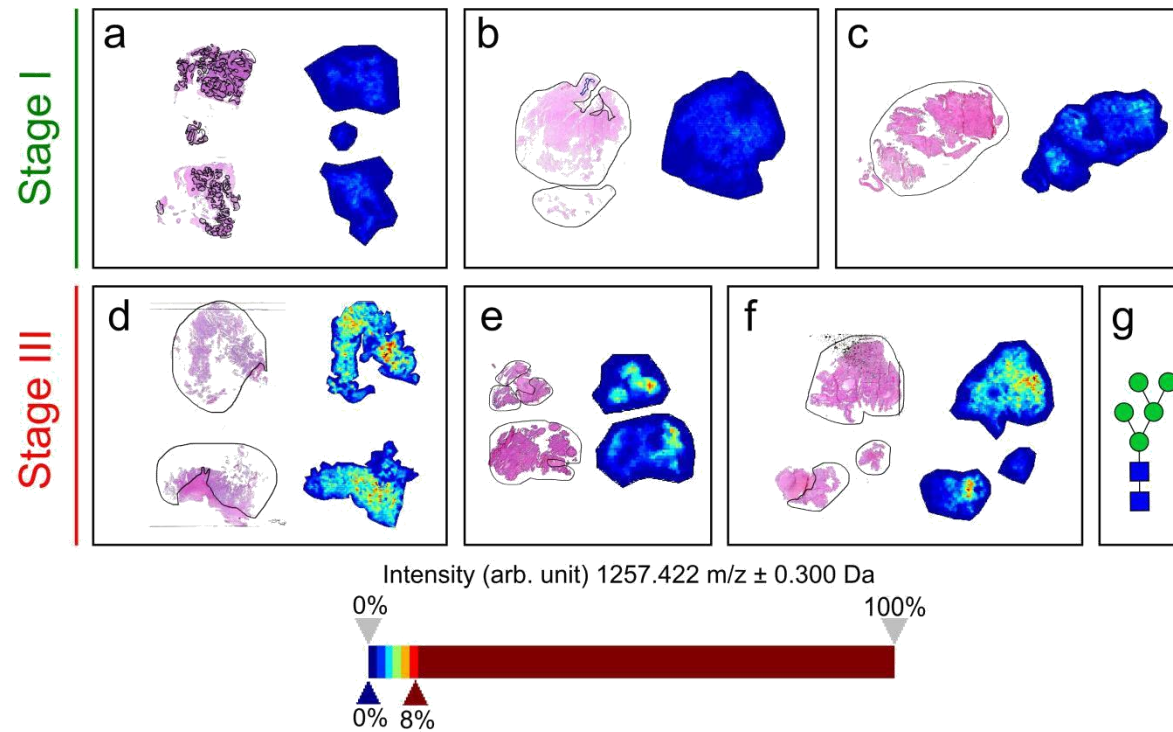
5.3 | Supplementary Information

Supplementary Table 1: FIGO stage I and stage III serous ovarian cancer patient information, including patient number, date collected, age, grade and diagnosis.

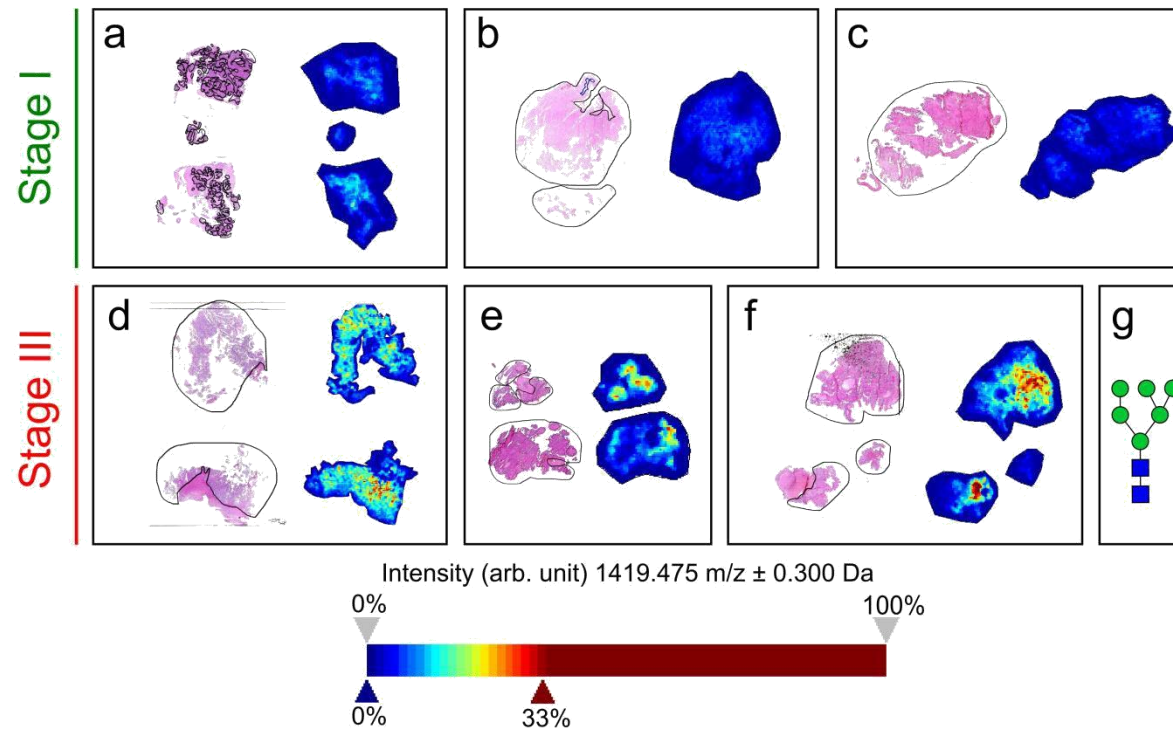
Patient Number	Date Collected	Age	Stage	Grade	Diagnosis
277	15/12/2009	58	IC	3	Serous Ovarian Cancer
1575	05/09/2014	46	IC	3	Serous Papillary Carcinoma
1934	11/04/2016	59	IA	3	High Grade Serous Carcinoma
847	18/05/2012	66	IIIC	3	Serous Papillary Carcinoma
1943	26/04/2016	47	IIIC	3	High Grade Serous Carcinoma
1890	05/02/2016	60	IIIC	3	High Grade Serous Carcinoma



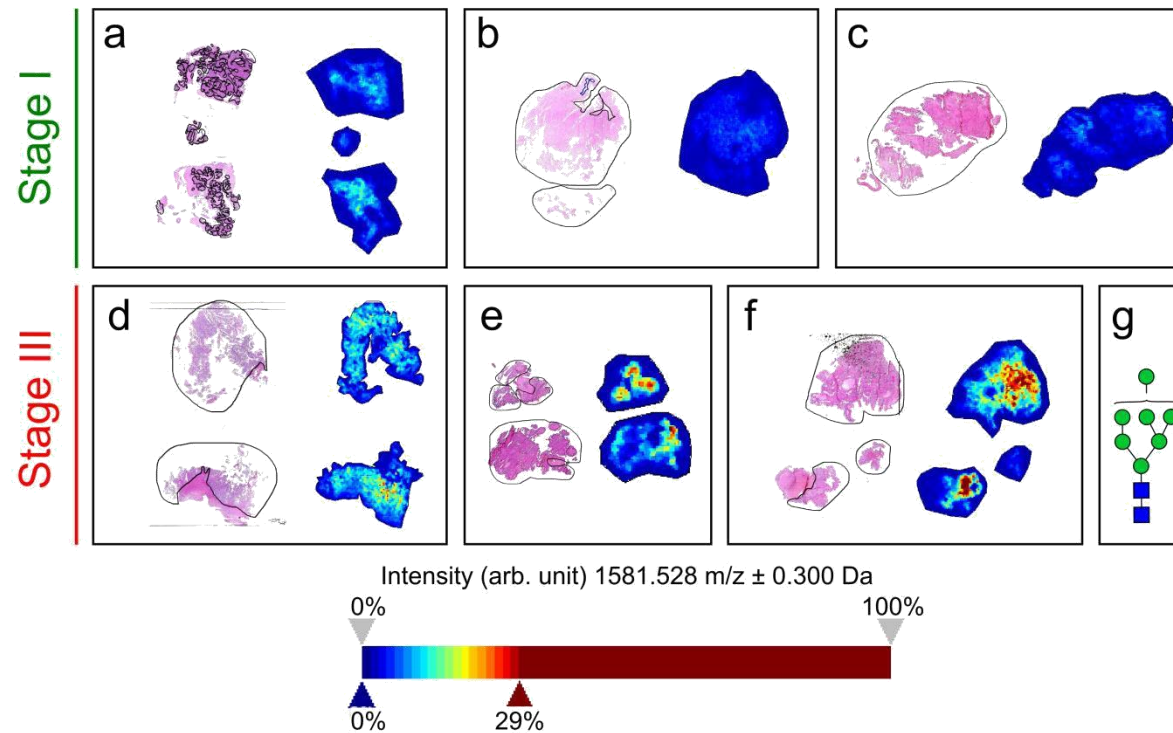
Supplementary Figure 1: Representative *N*-glycan MALDI mass spectrometry imaging sum spectra (800-4500 *m/z* range) of combined stage I (n = 3) and stage III (n = 3) serous ovarian cancer patients. The raw data was loaded into SCiLS Lab (version 2016b, SCiLS, Bruker Daltonics) and pre-processed by TopHat baseline subtraction, normalization to total ion current (TIC), peak picking and alignment. This figure was created in SCiLS Lab (version 2016b, SCiLS, Bruker Daltonics).



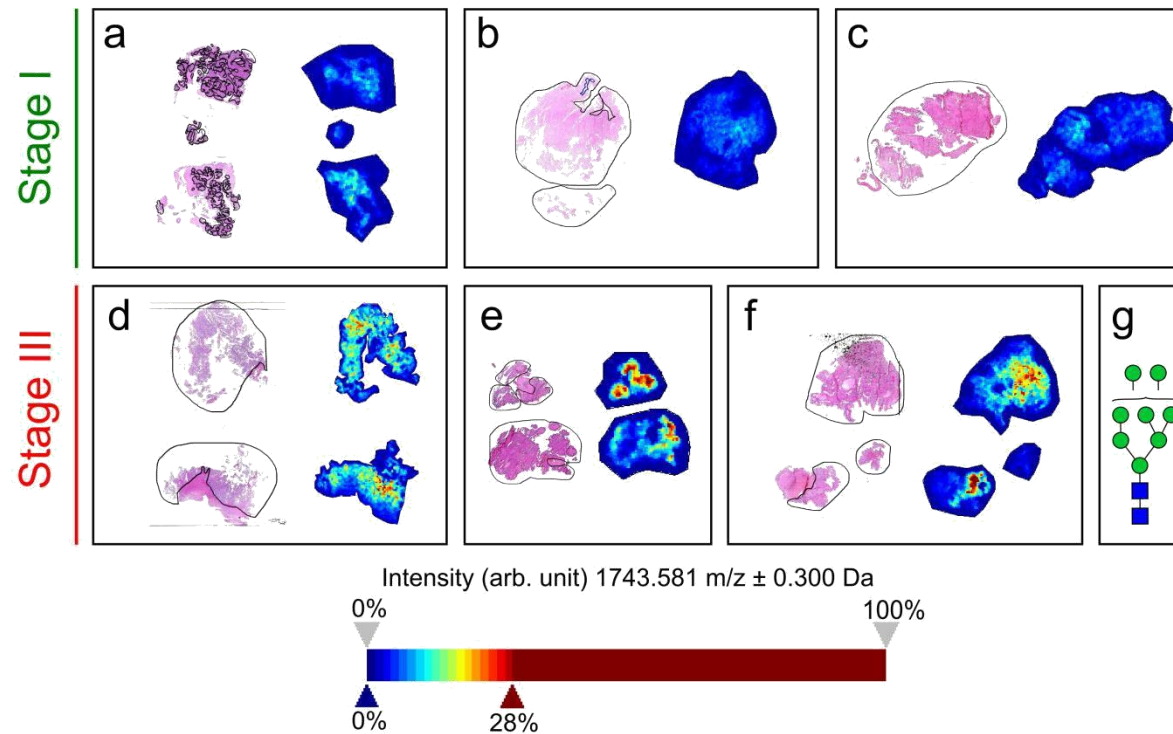
Supplementary Figure 2: N-glycan MALDI mass spectrometry imaging (MSI) of stage I (n = 3) and stage III (n = 3) serous ovarian cancer patients. Formalin-fixed paraffin-embedded tissue sections were treated with citric acid antigen retrieval prior to printing of dialyzed PNGase F with 250 μm spacing. 2,5-DHB matrix was sprayed onto the sections and MS spectra were acquired by oversampling at 100 μm intervals using a MALDI-TOF/TOF MS instrument. Monoisotopic glycan masses were measured in the positive ion reflectron mode as $(M + \text{Na}) \pm 0.3 \text{ Da}$ adducts for MALDI-MSI whereas PGC-LC-ESI-MS/MS revealed doubly negatively charged monoisotopic masses ($[M-2H]^{2-}$). Panels A-F show ion intensity maps of m/z 1257.422 from the stage I (green) and stage III (red) patients. The N-glycan, $(\text{Hex})_2 + (\text{Man})_3(\text{GlcNAc})_2$, in G is the confirmed structure based on PGC-LC-ESI-MS/MS analysis (data not shown).



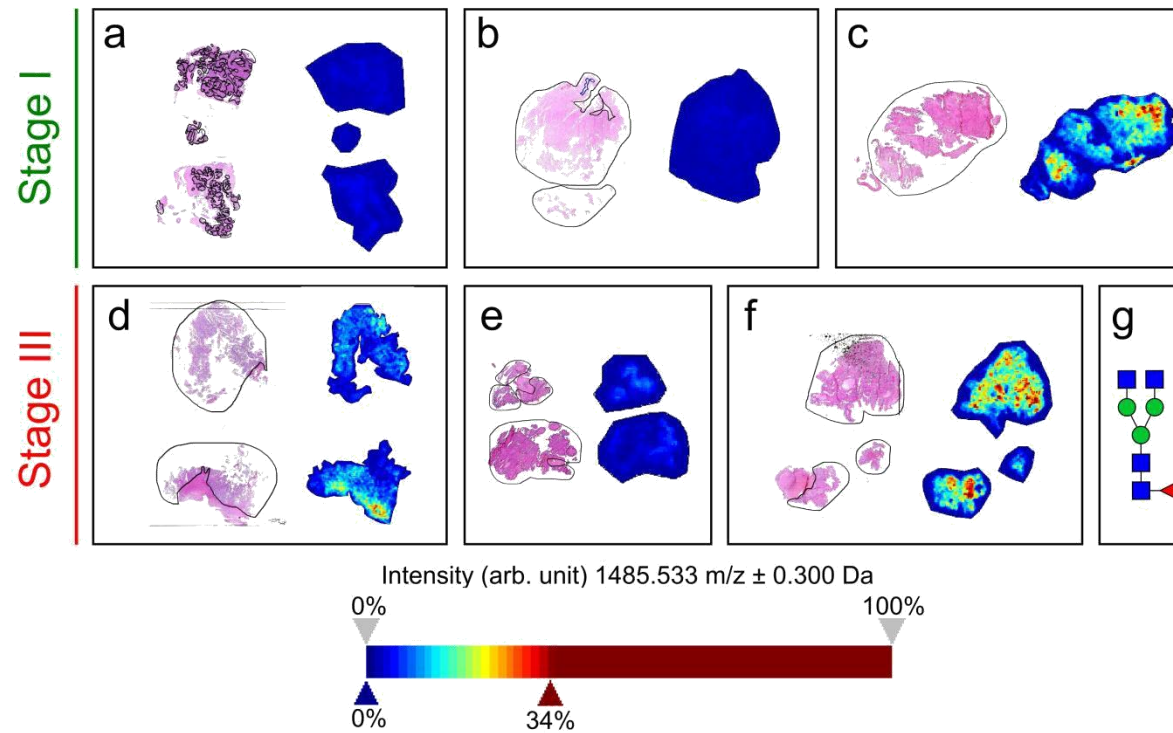
Supplementary Figure 3: N-glycan MALDI mass spectrometry imaging (MSI) of stage I (n = 3) and stage III (n = 3) serous ovarian cancer patients. Formalin-fixed paraffin-embedded tissue sections were treated with citric acid antigen retrieval prior to printing of dialyzed PNGase F with 250 μm spacing. 2,5-DHB matrix was sprayed onto the sections and MS spectra were acquired by oversampling at 100 μm intervals using a MALDI-TOF/TOF MS instrument. Monoisotopic glycan masses were measured in the positive ion reflectron mode as $(M + \text{Na}) \pm 0.3 \text{ Da}$ adducts for MALDI-MSI whereas PGC-LC-ESI-MS/MS revealed doubly negatively charged monoisotopic masses ($[M-2\text{H}]^{2-}$). Panels A-F show ion intensity maps of m/z 1419.475 from the stage I (green) and stage III (red) patients. The N-glycan, $(\text{Hex})_3 + (\text{Man})_3(\text{GlcNAc})_2$, in G is the confirmed structure based on PGC-LC-ESI-MS/MS analysis (data not shown).



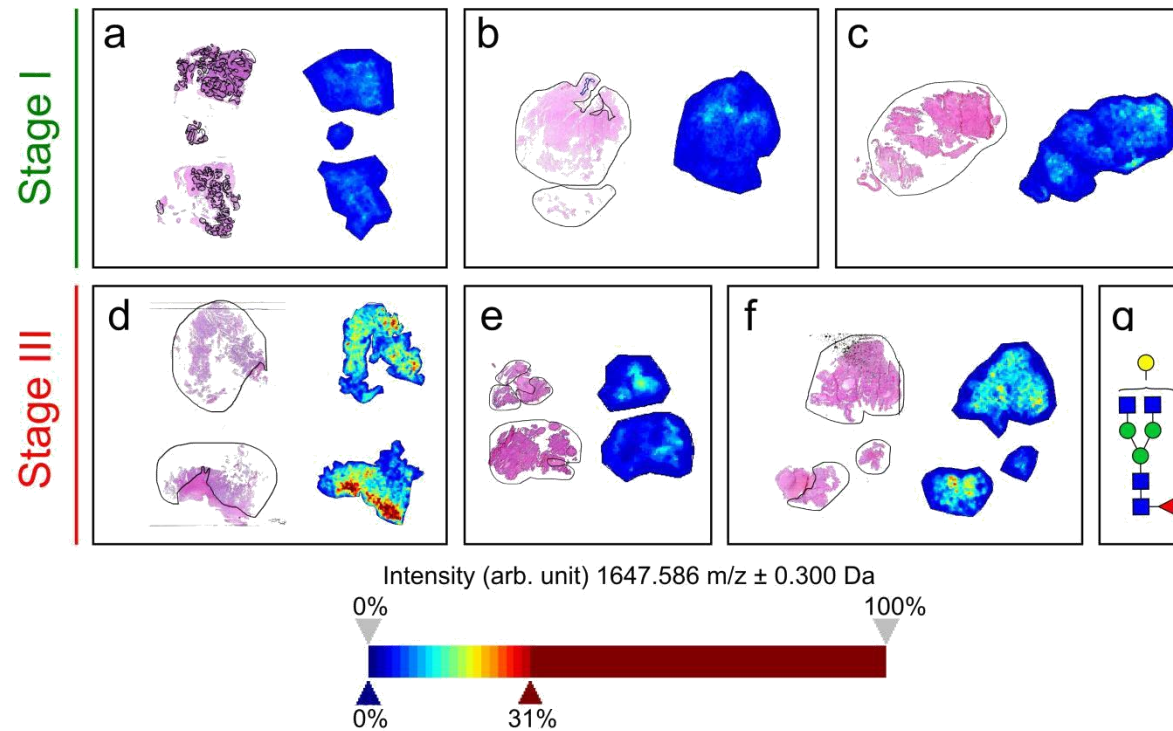
Supplementary Figure 4: N-glycan MALDI mass spectrometry imaging (MSI) of stage I (n = 3) and stage III (n = 3) serous ovarian cancer patients. Formalin-fixed paraffin-embedded tissue sections were treated with citric acid antigen retrieval prior to printing of dialyzed PNGase F with 250 μm spacing. 2,5-DHB matrix was sprayed onto the sections and MS spectra were acquired by oversampling at 100 μm intervals using a MALDI-TOF/TOF MS instrument. Monoisotopic glycan masses were measured in the positive ion reflectron mode as $(M + \text{Na}) \pm 0.3 \text{ Da}$ adducts for MALDI-MSI whereas PGC-LC-ESI-MS/MS revealed doubly negatively charged monoisotopic masses ($[M-2H]^{2-}$). Panels A-F show ion intensity maps of m/z 1581.528 from the stage I (green) and stage III (red) patients. The N-glycan, $(\text{Hex})_4 + (\text{Man})_3(\text{GlcNAc})_2$, in G is the confirmed structure based on PGC-LC-ESI-MS/MS analysis (data not shown).



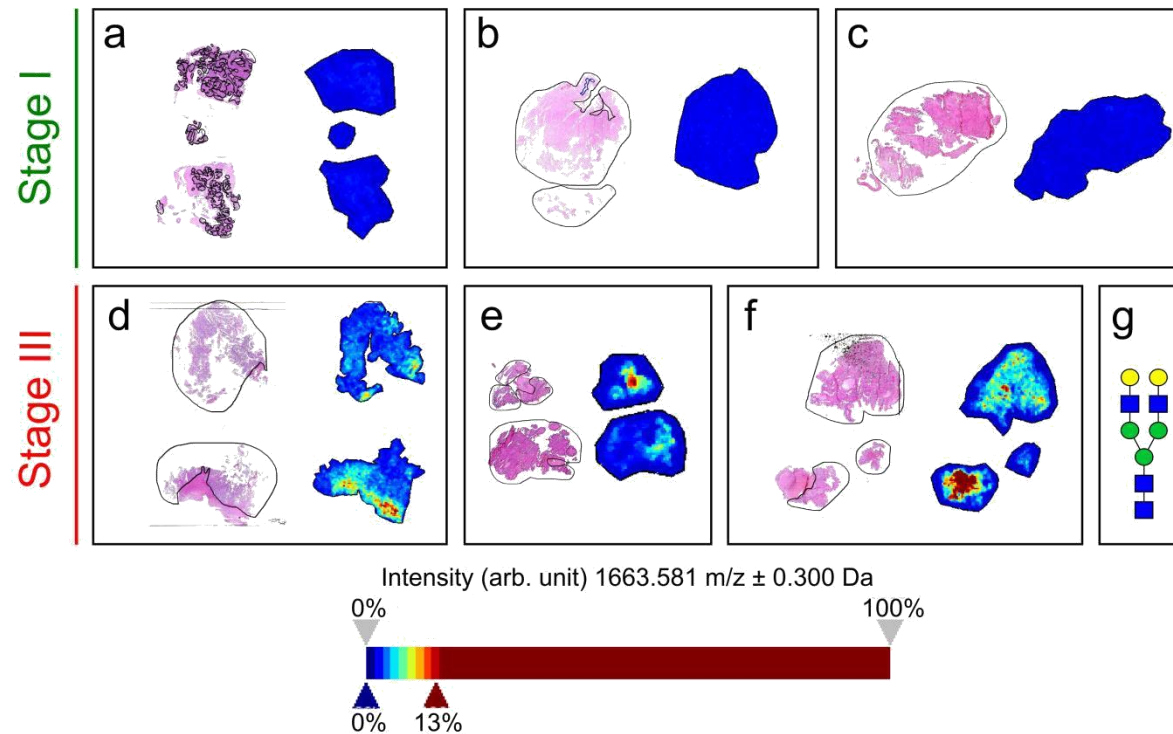
Supplementary Figure 5: N-glycan MALDI mass spectrometry imaging (MSI) of stage I (n = 3) and stage III (n = 3) serous ovarian cancer patients. Formalin-fixed paraffin-embedded tissue sections were treated with citric acid antigen retrieval prior to printing of dialyzed PNGase F with 250 μm spacing. 2,5-DHB matrix was sprayed onto the sections and MS spectra were acquired by oversampling at 100 μm intervals using a MALDI-TOF/TOF MS instrument. Monoisotopic glycan masses were measured in the positive ion reflectron mode as $(M + \text{Na}) \pm 0.3$ Da adducts for MALDI-MSI whereas PGC-LC-ESI-MS/MS revealed doubly negatively charged monoisotopic masses ($[M-2\text{H}]^{2-}$). Panels A-F show ion intensity maps of m/z 1743.581 from the stage I (green) and stage III (red) patients. The N-glycan, $(\text{Hex})_5 + (\text{Man})_3(\text{GlcNAc})_2$, in G is the confirmed structure based on PGC-LC-ESI-MS/MS analysis (data not shown).



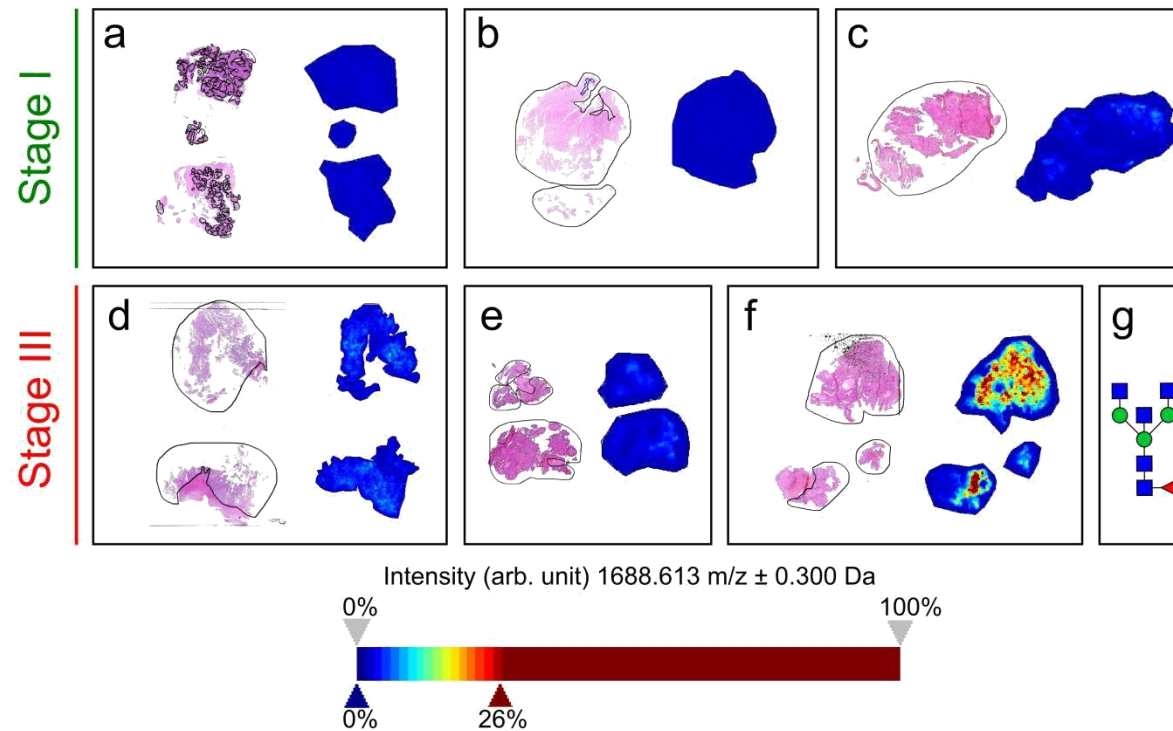
Supplementary Figure 6: N-glycan MALDI mass spectrometry imaging (MSI) of stage I (n = 3) and stage III (n = 3) serous ovarian cancer patients. Formalin-fixed paraffin-embedded tissue sections were treated with citric acid antigen retrieval prior to printing of dialyzed PNGase F with 250 μm spacing. 2,5-DHB matrix was sprayed onto the sections and MS spectra were acquired by oversampling at 100 μm intervals using a MALDI-TOF/TOF MS instrument. Monoisotopic glycan masses were measured in the positive ion reflectron mode as $(M + \text{Na}) \pm 0.3 \text{ Da}$ adducts for MALDI-MSI whereas PGC-LC-ESI-MS/MS revealed doubly negatively charged monoisotopic masses ($[M-2H]^{2-}$). Panels A-F show ion intensity maps of m/z 1485.533 from the stage I (green) and stage III (red) patients. The N-glycan, $(\text{HexNAc})_2 (\text{Deoxyhexose})_1 + (\text{Man})_3 (\text{GlcNAc})_2$, in G is the confirmed structure based on PGC-LC-ESI-MS/MS analysis (data not shown).



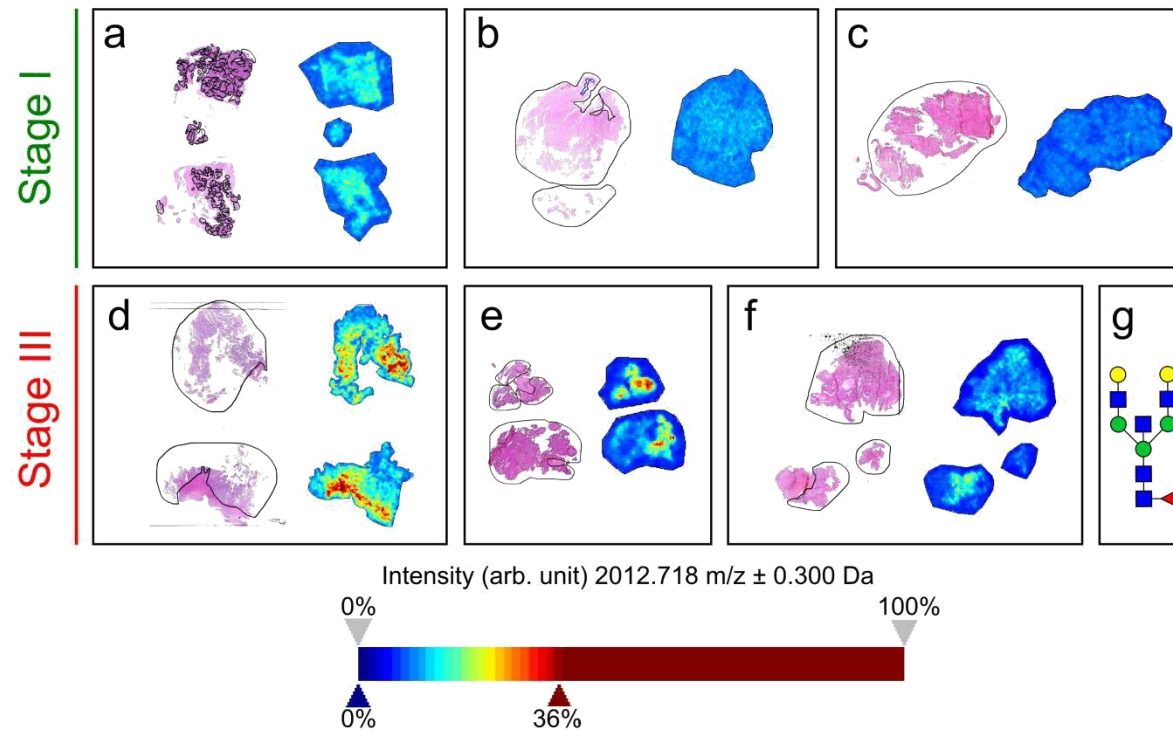
Supplementary Figure 7: N-glycan MALDI mass spectrometry imaging (MSI) of stage I (n = 3) and stage III (n = 3) serous ovarian cancer patients. Formalin-fixed paraffin-embedded tissue sections were treated with citric acid antigen retrieval prior to printing of dialyzed PNGase F with 250 μm spacing. 2,5-DHB matrix was sprayed onto the sections and MS spectra were acquired by oversampling at 100 μm intervals using a MALDI-TOF/TOF MS instrument. Monoisotopic glycan masses were measured in the positive ion reflectron mode as $(M + \text{Na}) \pm 0.3 \text{ Da}$ adducts for MALDI-MSI whereas PGC-LC-ESI-MS/MS revealed doubly negatively charged monoisotopic masses ($[M-2\text{H}]^{2-}$). Panels A-F show ion intensity maps of m/z 1647.586 from the stage I (green) and stage III (red) patients. The N-glycan, $(\text{Hex})_1 (\text{HexNAc})_2 (\text{Deoxyhexose})_1 + (\text{Man})_3(\text{GlcNAc})_2$, in G is the confirmed structure based on PGC-LC-ESI-MS/MS analysis (data not shown).



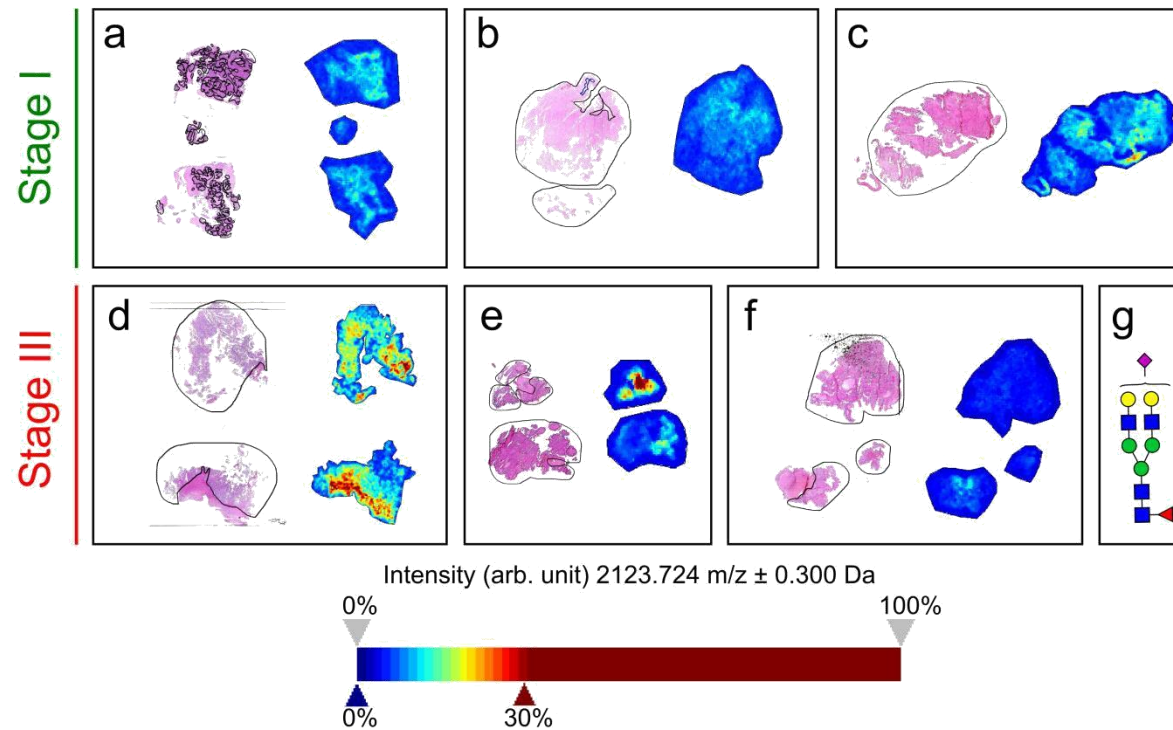
Supplementary Figure 8: N-glycan MALDI mass spectrometry imaging (MSI) of stage I (n = 3) and stage III (n = 3) serous ovarian cancer patients. Formalin-fixed paraffin-embedded tissue sections were treated with citric acid antigen retrieval prior to printing of dialyzed PNGase F with 250 μm spacing. 2,5-DHB matrix was sprayed onto the sections and MS spectra were acquired by oversampling at 100 μm intervals using a MALDI-TOF/TOF MS instrument. Monoisotopic glycan masses were measured in the positive ion reflectron mode as $(M + \text{Na}) \pm 0.3$ Da adducts for MALDI-MSI whereas PGC-LC-ESI-MS/MS revealed doubly negatively charged monoisotopic masses ($[M-2H]^{2-}$). Panels A-F show ion intensity maps of m/z 16663.581 from the stage I (green) and stage III (red) patients. The N-glycan, $(\text{Hex})_2 (\text{HexNAc})_2 + (\text{Man})_3 (\text{GlcNAc})_2$, in G is the confirmed structure based on PGC-LC-ESI-MS/MS analysis (data not shown).



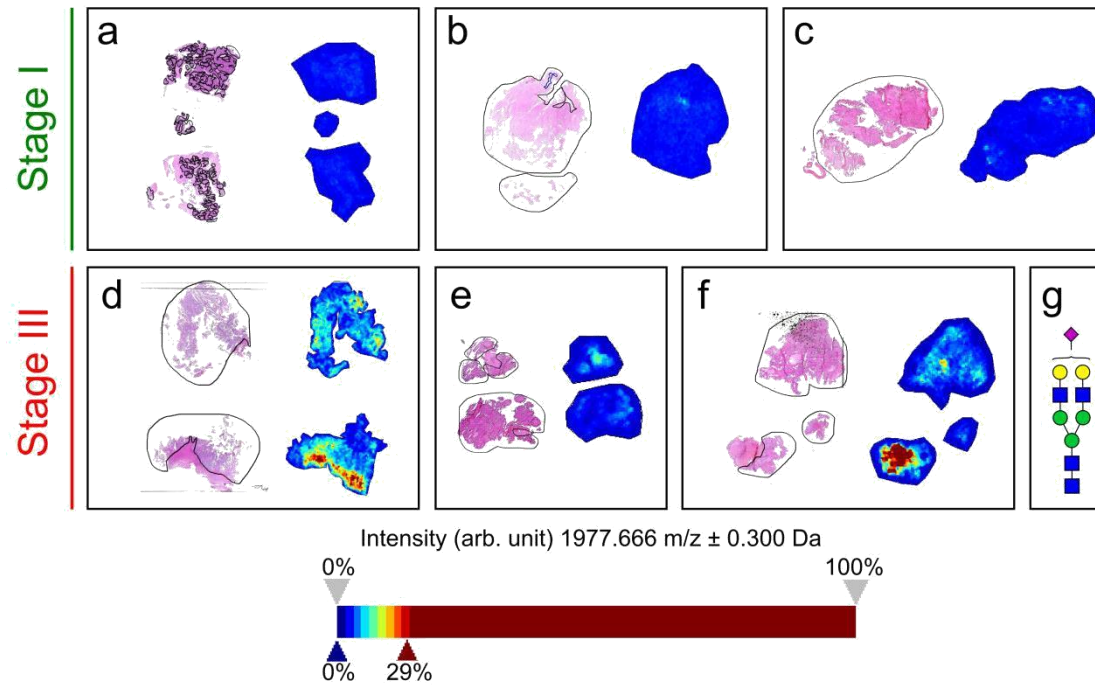
Supplementary Figure 9: N-glycan MALDI mass spectrometry imaging (MSI) of stage I (n = 3) and stage III (n = 3) serous ovarian cancer patients. Formalin-fixed paraffin-embedded tissue sections were treated with citric acid antigen retrieval prior to printing of dialyzed PNGase F with 250 μm spacing. 2,5-DHB matrix was sprayed onto the sections and MS spectra were acquired by oversampling at 100 μm intervals using a MALDI-TOF/TOF MS instrument. Monoisotopic glycan masses were measured in the positive ion reflectron mode as $(M + \text{Na}) \pm 0.3 \text{ Da}$ adducts for MALDI-MSI whereas PGC-LC-ESI-MS/MS revealed doubly negatively charged monoisotopic masses ($[M-2\text{H}]^{2-}$). Panels A-F show ion intensity maps of m/z 1688.613 from the stage I (green) and stage III (red) patients. The N-glycan, $(\text{HexNAc})_3 (\text{Deoxyhexose})_1 + (\text{Man})_3 (\text{GlcNAc})_2$, in G is the confirmed structure based on PGC-LC-ESI-MS/MS analysis (data not shown).



Supplementary Figure 10: N-glycan MALDI mass spectrometry imaging (MSI) of stage I (n = 3) and stage III (n = 3) serous ovarian cancer patients. Formalin-fixed paraffin-embedded tissue sections were treated with citric acid antigen retrieval prior to printing of dialyzed PNGase F with 250 μm spacing. 2,5-DHB matrix was sprayed onto the sections and MS spectra were acquired by oversampling at 100 μm intervals using a MALDI-TOF/TOF MS instrument. Monoisotopic glycan masses were measured in the positive ion reflectron mode as $(M + \text{Na}) \pm 0.3$ Da adducts for MALDI-MSI whereas PGC-LC-ESI-MS/MS revealed doubly negatively charged monoisotopic masses $([M-2\text{H}]^2)$. Panels A-F show ion intensity maps of m/z 2012.718 from the stage I (green) and stage III (red) patients. The N-glycan, $(\text{Hex})_2(\text{HexNAc})_3(\text{Deoxyhexose})_1 + (\text{Man})_3(\text{GlcNAc})_2$, in G is the confirmed structure based on PGC-LC-ESI-MS/MS analysis (data not shown).



Supplementary Figure 11: N-glycan MALDI mass spectrometry imaging (MSI) of stage I (n = 3) and stage III (n = 3) serous ovarian cancer patients. Formalin-fixed paraffin-embedded tissue sections were treated with citric acid antigen retrieval prior to printing of dialyzed PNGase F with 250 μm spacing. 2,5-DHB matrix was sprayed onto the sections and MS spectra were acquired by oversampling at 100 μm intervals using a MALDI-TOF/TOF MS instrument. Monoisotopic glycan masses were measured in the positive ion reflectron mode as $(M + \text{Na}) \pm 0.3 \text{ Da}$ adducts for MALDI-MSI whereas PGC-LC-ESI-MS/MS revealed doubly negatively charged monoisotopic masses $([M-2\text{H}]^{2-})$. Panels A-F show ion intensity maps of m/z 2123.724 from the stage I (green) and stage III (red) patients. The N-glycan, $(\text{Hex})_2 (\text{HexNAc})_2 (\text{Deoxyhexose})_1 (\text{NeuAc})_1 + (\text{Man})_3 (\text{GlcNAc})_2$, in G is the confirmed structure based on PGC-LC-ESI-MS/MS analysis (data not shown).



Supplementary Figure 12: N-glycan MALDI mass spectrometry imaging (MSI) of stage I (n = 3) and stage III (n = 3) serous ovarian cancer patients. Formalin-fixed paraffin-embedded tissue sections were treated with citric acid antigen retrieval prior to printing of dialyzed PNGase F with 250 μm spacing. 2,5-DHB matrix was sprayed onto the sections and MS spectra were acquired by oversampling at 100 μm intervals using a MALDI-TOF/TOF MS instrument. Monoisotopic glycan masses were measured in the positive ion reflectron mode as $(M + \text{Na}) \pm 0.3$ Da adducts for MALDI-MSI whereas PGC-LC-ESI-MS/MS revealed doubly negatively charged monoisotopic masses $([M-2H]^{2-})$. Panels A-F show annotated tumour regions (black) of H&E stained tissue sections and ion intensity maps of m/z 1977.666 from the stage I (green) and stage III (red) patients. The N-glycan, $(\text{Hex})_2 (\text{HexNAc})_2 (\text{NeuAc})_1 + (\text{Man})_3(\text{GlcNAc})_2$, in G is the confirmed structure based on the chromatography (Panel H) and fragmentation (Panel I).

Chapter 6 | Discussion

This discussion will touch on the topics of glycosyltransferases and their biological significance in epithelial ovarian cancer (EOC), avenues for further workflow development through the stabilisation of sialylated *N*-glycans or through combining *N*-glycan MALDI-MSI with tryptic peptide MALDI-MSI, or using complimentary techniques, such as lectin or antibody histochemistry applications, to then eventually translate analytical applications into clinical strategies for screening or monitoring EOC.

Glycosyltransferases in Epithelial Ovarian Cancer

EOC is the most fatal gynaecological malignancy in adult women [1]. Over 30 years ago, the first glycan changes were observed in tissue sections using periodic acid Schiff staining of mucin polysaccharides [2]. With advancements in mass spectrometry, there have been multiple cases of glycan changes documented across several types of samples, including the identification of specific glycoproteins and glycopeptides. Some of most recent unpublished data (see Chapter 5) has demonstrated that complex neutral and fucosylated *N*-glycans are highly intense in tissue from late-stage patients (n=3) relative to early-stage patients (n=3). These complex *N*-glycans are derived from the core *N*-glycan structure, utilising glycosyltransferases to add monosaccharide subunits such as N-acetylglucosamine, galactose, fucose, and sialic acid [3]. Additionally, these complex *N*-glycans have been observed in non-tumour (i.e. cancer-associated stroma) regions as well [4]. Bisecting structures have been shown to be primarily expressed in the tumour regions of tissue derived from late-stage patients (see Chapter 4) and various ovarian cancer cell lines [5]. This observation is consistent with genomic and transcriptomic studies on GnT-III activity, which is the glycosyltransferase responsible for attaching a GlcNAc monosaccharide in the β 1,4 formation at the β -mannose of the mannosyl core [6]. Bisecting structures have been found to suppress the further processing of *N*-glycans catalysed by GnT-V, which is the glycosyltransferase responsible for β 1,6 branching [7]. Ovarian cancer tissues have been found to have much higher levels of GnT-III compared to normal ovarian and fallopian tube tissues while other cancers have been found to have lower levels of GnT-III than their respective normal tissues [8].

There are six N-acetylglucosaminyltransferases (GnTs) responsible for *N*-glycan biosynthesis that are localised to the medial Golgi. GnT-V and GnT-III, as already mentioned, are two of the most extensively studied enzymes [9, 10]. GnT-V is involved in forming β 1,6 GlcNAc branches at the α 1,6 Man in the trimannosyl core [11]. In cancer, branching is often extended with N-acetyllactosamine (poly-LacNAc) or sialic acid monosaccharides. The expression of GnT-V in many cancers is regulated by oncogenic

pathways that include src, ras, raf, and HER-2/neu, therefore impacting tumourgenesis and invasiveness [12]. Although, it appears that GnT-V has minimal activity in ovarian cancer [13]. However, GnT-V activity is highly expressed at the mRNA level in mouse and human endometrioid ovarian cancer tissues [14]. Mass spectrometry analysis of *N*-glycans isolated from membrane glycoproteins of ovarian cancer cell lines demonstrated that there was an absence of β 1,6 GlcNAc branched structures [5]. This observation could indicate that GnT-V activity may be inhibited by high GnT-III expression levels in ovarian cancer.

Another glycosyltransferase family, GnT-IV, exists as two isoenzymes termed GnT-IVa and GnT-IVb that are responsible for the formation of the β 1,4 branch of the Man α 1,3 arm of the *N*-glycan core [15]. These two isoenzymes have different expression profiles in normal tissues. For example, GnT-IVa is more abundant in pancreatic and gastrointestinal tissues while GnT-IVb is generally expressed more in most tissues [16]. In ovarian cancer tissue derived from human endometrioid ovarian carcinoma, it was determined there was a 2.5-fold and 1.5-fold increase of mRNA levels for both GnT-IVa and GnT-IVb respectively, relative to non-malignant ovarian tissues [17]. Additionally, a DSL lectin, specific to GnT-IV branching, was discovered to show increased binding to glycoproteins in ovarian cancer tissues [17]. CA125, the most common clinical biomarker used for ovarian cancer monitoring, has also been shown to possess mono-, bi-, and tri-antennary *N*-glycan structures that are synthesised by GnT-IV [18]. However, the functional significance of these GnT-IV structures and their relation to specific glycoproteins have not yet been investigated in ovarian cancer.

These glycosyltransferases mentioned are responsible for determining specific *N*-glycan composition and structure. This was best demonstrated in a study of glyco-gene transcripts from murine organs which were compared to the most abundant *N*-glycans from each tissue [19]. It was concluded that most transcripts correlated with specific *N*-glycan structure abundance. Recently, the transcriptome profiles of glycosyltransferases have been utilised to predict the *N*-glycan compositions and structures present in particular samples, and *N*-glycosylation reaction network analysis strategies have been developed [20]. The Cancer Genome Atlas (TCGA) can provide a wealth of information regarding multiple types of cancer and *N*-glycan gene expression data [21]. Utilising this platform with transcriptomic data and *N*-glycan MALDI-MSI data will provide further insight into how *N*-glycans are regulated and function in different cancer types and potentially even in cancer progression.

N-glycan MALDI-MSI – The Past, Present and Future

N-glycan MALDI-MSI combined with LC-ESI-MS/MS is a relatively new platform to spatially identify and characterise tissue-specific N-glycans that can be matched with histological and clinical information [4, 22]. One of the first N-glycan MALDI-MSI methods to emerge was on FF murine brain tissue where Powers, T. *et al* spatially mapped the N-glycome [23]. The N-glycans were also extracted off-tissue, modified and processed for structural characterisation by HPLC-ESI-MS/MS. It was concluded that this novel approach could lead to disease-related targets for biomarkers and therapeutic applications. Subsequent N-glycan MALDI-MSI workflows were applied to FFPE tissue, such as glioblastoma tumor xenografts and normal brain sections [24]. A total of 42 N-glycans were found to be spatially distributed across the mouse brain coronal tissue sections. Oligomannose and non-fucosylated complex N-glycans were observed to be localized to the brainstem while fucosylated N-glycans were more abundant in the cortex. Our group was the first to combine MALDI-MSI with PGC-LC-ESI-MS/MS to both spatially map and comprehensively characterise the N-glycome [22]. Using this approach, we assigned N-glycan structures, confirmed by MS/MS, to tissue-specific regions of FFPE murine kidney. For example, the high mannose N-glycan (Hex)₆ + (Man)₃(GlcNAc)₂ was observed in the medulla region while the fucosylated complex N-glycan (Hex)₂(HexNAc)₃(Deoxyhexose)₃ + (Man)₃(GlcNAc)₂ was observed in the cortex region. Our group also modified our existing N-glycan MALDI-MSI workflow to spatially identify and characterise N-glycans from FFPE osteoarthritis tissue (See *Chapter 3*). We could successfully differentiate between cartilage and bone marrow based on the N-glycosylation patterns observed [25].

Throughout this thesis, it has been discussed already that these methods need to be further optimised. There have been suggestions for improvement in the areas of derivatization, optimisation of the citric acid antigen retrieval step and using negative ion mode in order to stabilise sialylated N-glycans during MALDI-MSI. Additionally, it has been mentioned that it would be beneficial to detect N-glycan isomers spatially using MALDI-MSI. In ovarian cancer, there have been several reports of level alterations in α 2,3 and α 2,6 sialic acid linkage of sialylated N-glycans [5, 17]. Other future prospects include the analysis of larger patient cohorts using tissue microarrays (TMAs), and ultimately, glycoproteomics analysis which would provide site-specific information on protein glycosylation.

Stabilising Sialylated *N*-glycans and Identifying Isomeric *N*-glycans

The detection of sialylated *N*-glycans by MALDI in reflectron mode is difficult due to their labile nature during the ionisation process. However, the Solarix series MALDI-FT-ICR instruments (Bruker Daltonics) use an alternative source configuration and cooling gas, which provides softer ionisation, therefore limiting sialic acid cleavage [26]. Using a standard MALDI instrument results in the increased abundance of non-sialylated complex *N*-glycans due to the destabilisation of sialic acids, which therefore does not reflect the abundance of sialylated *N*-glycans present biologically. Additionally, standard and non-standard MALDI instruments cannot distinguish between sialylated *N*-glycan linkages. Powers, T. *et al* was the first to develop an approach to investigate the spatial localisation of isomeric sialylated *N*-glycan structures from FFPE human hepatocellular carcinoma (HCC) tissue by applying their existing *N*-glycan MALDI-MSI method to single sections and a TMA [27]. A total of 30 *N*-glycans were detected and a novel off-tissue ethyl esterification method was developed to stabilise sialylated *N*-glycans for region-specific α 2,3 and α 2,6 linkage identification. This approach showed that α 2,6 sialylated *N*-glycans were higher in abundance of the HCC regions compared to α 2,3 sialylated *N*-glycans. Additionally, *N*-glycan MALDI-MSI and lectin histochemistry revealed that core fucosylated complex *N*-glycans are highly expressed in HCC regions relative to normal tissue. In 2016, another novel derivatization method was developed by the same group, where *in situ* dimethylamidation is performed to identify linkage-specific sialylated *N*-glycans using the existing MALDI-MSI workflow [28]. From FFPE colon carcinoma tissue, sialylated *N*-glycans were discovered to be α 2,3 linkage in stroma, tumor, and necrotic regions, while sialylated *N*-glycans with α 2,6 linkage were observed in necrotic, collagen-rich, and red blood cell regions. However, the limitation of these novel derivatization methods is that other *N*-glycan isomeric structures from different *N*-glycan families are not considered (i.e. high mannose, complex/hybrid). A recent advancement in mass spectrometry-based technology has emerged termed Ion Mobility (IM)-MS [29]. This platform (coupled by LC) has been utilised most recently to characterise *N*-glycan isomers using post-source gas-phase separation to separate the isomers based on a collision cross-section [30]. There have been a few studies published recently where IM-MS has been applied to FF tissue sections for imaging other analytes [31]. According to Drake *et al.*, there have been preliminary applications of IM-MS imaging to PNGase F digested FFPE tissue sections (data not shown).

Combined *N*-glycan and Tryptic Peptide MALDI-MSI

N-glycan MALDI-MSI allows the visualisation of tissue-specific *N*-glycan structures which can potentially lead to identifying corresponding glycoproteins and glycopeptides in subsequent experiments. The most conventional way to approach this would be by targeting tissue-specific regions with trypsin, followed by enrichment of glycopeptides. Although this is a direct way to study both the glycan and peptide sequences through high-resolution LC-ESI-MS/MS, large quantities of sample are required which is difficult to achieve if the regions of interest are small. A novel approach was recently developed to image *N*-glycans and tryptic peptides in the same experiment while sequencing the peptides for protein identification and correlating the *N*-glycans with regions that overlap. Heijs, B. *et al* established this alternative workflow in 2016 [32]. The *N*-glycans and tryptic peptides were both measured by MALDI-FTICR-MS, and then these analytes were extracted from consecutive tissue sections for structural characterisation by MALDI-TOF/TOF-MS/MS and Q-Exactive MS/MS respectively. A total of 509 unique proteins were identified from PNGase F and trypsin treated FFPE colorectal cancer, which corresponded to 1334 unique peptides. There were considerably more protein and peptide identifications relative to consecutive sections that were treated with trypsin alone, totalling 236 unique proteins and 948 unique peptides. Therefore, the evidence suggests that the sequential digestion workflow improved protein identification with the most likely explanation belonging to *N*-glycans preventing tryptic digestion at specific sites. The cleavage of *N*-glycans from asparagine residues results in deamidation, thereby converting these residues to aspartic acid which is easily detectable and identifiable during LC-ESI-MS/MS analysis [33]. However, this modification can also form without the proper sample preparation processes in place. It was determined that there were 20 deamidated peptides from the FFPE colorectal cancer tissue after combined glycan and peptide digestion, relative to the trypsin digestion sample alone which had no deamidated peptides detected. In 2017, this novel workflow was published as a protocol paper so other groups can adapt it [34]. It is hoped that the glycoproteins identified spatially can then be validated using standard techniques, such as immunohistochemistry, which involves the application of the relevant antibody reagents [35]. Fortunately, most of these glycoproteins are highly abundant which provides further opportunities to develop clinical biomarker assays.

Lectin and Anti-Carbohydrate Antibody Applications

Specific lectins and anti-carbohydrate antibodies are routinely used to evaluate the spatial localisation of *N*-glycans and other carbohydrates *in situ*. For example, the carbohydrate antigen CA19-9 is measured in the clinic to determine the prognosis of pancreatic and other gastrointestinal cancers [36, 37]. The CA19-9 antibody used recognises a distinct carbohydrate motif (GlcNAc-Gal, α 1,4 fucose, and α 2,3 sialic acid). Another antigen, F77 for prostate cancer, has also been previously described in the literature [38]. The corresponding antibody for F77 recognises the blood group H antigen-related Lewis Y glycan structures with α 1,2 fucose. It is established that most antibodies for carbohydrate detection are required to recognise between 1-4 structural epitopes [35]. Using such antibodies are quite useful for tissue immunohistochemistry-based staining methods, however, these methods cannot distinguish between the types of glycan classes (i.e. glycolipids, *O*-glycans, *N*-glycans). Alternatively, lectins or carbohydrate-binding proteins (CBPs) for many decades have evaluated glycoproteins and their structural features [39]. In a similar way to antibodies for carbohydrate antigens, lectins recognise between 2-4 structural epitopes. However, lectins possess poor affinity-binding constants in the low micromolar range, which limits the tissue histochemistry applications mentioned previously. Although, lectin histochemistry applications have been successfully established to analyse FFPE tissue [40]. Again, it has been described as difficult to distinguish between glycan classes since the recognisable glycan motif is often the same between *N*- and *O*-glycans. Hence, MALDI-MSI is an important tool that provides not only spatial information, but also specific *N*-glycan structural features. However, there is potential for the development of MALDI-MSI workflows to incorporate these antibody or lectin histochemistry applications to rapidly visualise the spatial localisation of specific glycan motifs.

Alternative Applications

Other future prospects following the conclusion of this project would include large patient studies using tissue microarrays (TMAs) of patients at different stages (i.e. early-stage vs. late-stage ovarian cancer). Powers, T. *et al* was the first to apply their *N*-glycan MALDI-MSI workflow to FFPE tissue sections of murine kidney, pancreatic and prostate cancers, and human hepatocellular carcinoma (HCC) in the form of a TMA [41]. A total of 21 known or previously identified *N*-glycans were observed to be distributed across the TMA, with the majority of *N*-glycans being highly abundant in HCC regions relative to non-tumour regions. The authors' concluded that this was the first study that applied *N*-glycan MALDI-MSI to a TMA, therefore developing a method for high-throughput analysis of clinical samples. However, the *N*-glycans were identified based on known *N*-glycosylation pathway constraints and on-tissue collision-induced fragmentation, which does not elucidate isomeric information.

There are also areas where the existing workflow can be modified or optimised to improve sensitivity and obtain more structural information *in situ*. For example, other glycosidic enzymes could be applied to tissue sections in combination with PNGase F to provide more comprehensive structural information. Glycosidic enzymes include galactosidase for the cleavage of galactose, fucosidase for the cleavage of fucose, and sialidase or neuraminidase for the cleavage of sialic acid [42]. The advantage with many of these glycosidic enzymes is the linkage specific information obtained, which provides structural, compositional and isomeric information not typically obtained by PNGase F digestion. For example, there is a glycosidic enzyme that only cleaves core fucosylated *N*-glycans which could be optimised for an existing *N*-glycan MALDI-MSI workflow.

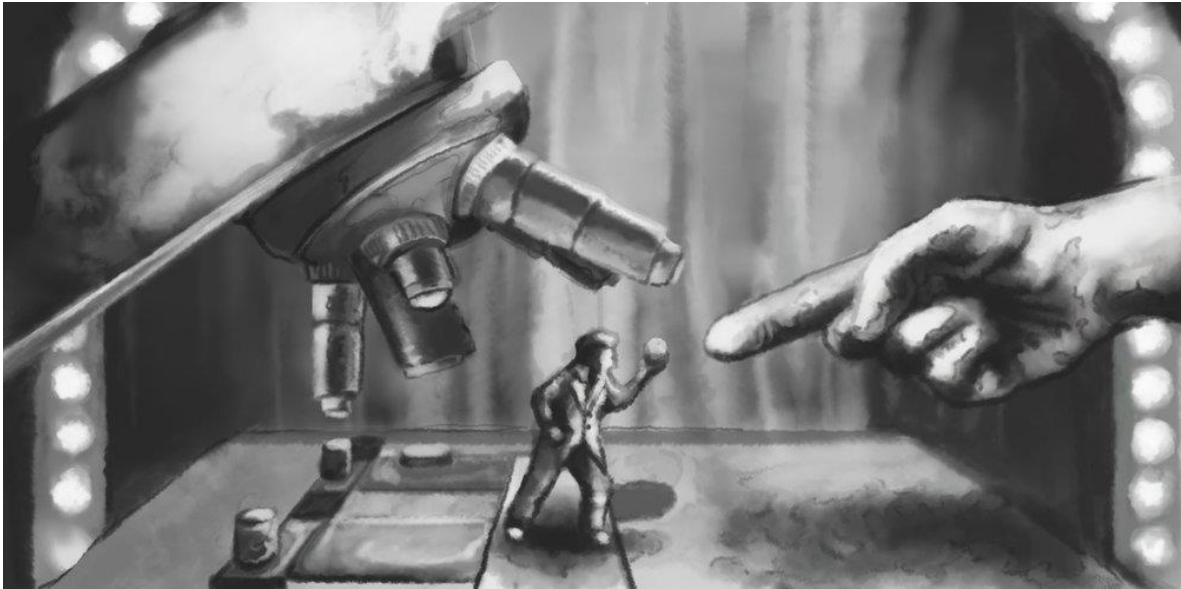
Clinical Applications of *N*-glycan MALDI-MSI

A new MALDI-MSI platform with potential clinical applications has emerged called the rapifleX MALDI TissueTyper TOF instrument (Bruker Daltonics). This advancement in instrumentation and technology has significantly decreased the acquisition and processing time by fivefold or even more, increased the resolution to 10-20 μm , and refined the laser spot sizes. With improved acquisition times, it may be feasible to analyse multiple patient biopsy samples and other pathological samples (e.g. serum) in a matter of minutes.

Identifying the location of *N*-glycan structures in tissue-specific regions, in particular within the tumour microenvironment, provides a potentially better understanding of biological mechanisms behind cancer progression. Additionally, this may also lead to the development of specific lectin-based assays that can be used to detect specific *N*-glycans directly (i.e. a lectin histochemistry tissue assay), as already discussed. Another possible approach not yet discussed could include the use of anti-carbohydrate epitope antibodies in fluorescent or light microscopy experiments to visualise tissue-specific biomarkers. Although these lectins and antibodies recognise *N*-glycan structural motifs, they also recognise similar features on glycosphingolipids or *O*-glycosylated proteins.

In summary, *N*-glycan MALDI-MSI has been developed immensely in recent times, with improvements in sensitivity and mass accuracy, structural and compositional analysis by complementary techniques (i.e. PGC-LC-ESI-MS/MS and lectin histochemistry staining), and identification of linkage-specific sialylated *N*-glycans by *in situ* derivatization methods. However, further work in the field is required to comprehensively answer clinical questions and discover disease-specific biomarkers or develop new diagnostic methods based on *N*-glycans.

Chapter 7 | Conclusion: Striking the Stage



N-glycan MALDI-MSI is a relatively new platform that has shown much promise in the area of cancer research; however, there are still strides to make in order for MALDI-MSI to be able to (1) screen and detect ovarian cancer in the early-stages, (2) monitor treatment effectiveness, (3) detect ovarian cancer recurrence and (4) stratify ovarian cancer patients. As detailed in the discussion, such improvements can be made through multiple strategies including the stabilisation of sialylated *N*-glycans while also spatially mapping α 2,3 and α 2,6 sialic acid linkages, combining *N*-glycan MALDI-MSI with tryptic peptide MALDI-MSI to obtain comprehensive biological information, and investigating larger patient cohorts through the means of tissue microarrays (TMAs). With these improvements implemented, it may be possible to work towards creating a library of biomolecules that can be routinely measured by clinicians to diagnose ovarian cancer in its early-stages or monitor regimens for patients.

The evidence obtained throughout this PhD project suggests that the *N*-glycome is aberrantly expressed in the tumour microenvironment of early- and late-stage ovarian cancer tissues. For example, mass spectrometry and molecular biology techniques have been revealed that there are increased levels of bisecting structures in late-stage ovarian cancer tissues relative to early-stage. This observation requires further investigation once the workflow has been further developed to be more sensitive and specific as outlined above.

This page is intentionally left blank

Chapter 8 | References

- [1] Ozols, R. F., Bookman, M. A., Connolly, D. C., Daly, M. B., *et al.*, Focus on epithelial ovarian cancer. *Cancer Cell* 2004, 5, 19-24.
- [2] Warnock, M. L., Stoloff, A., Thor, A., Differentiation of adenocarcinoma of the lung from mesothelioma. Periodic acid-Schiff, monoclonal antibodies B72.3, and Leu M1. *Am J Pathol* 1988, 133, 30-38.
- [3] Stanley, P., Schachter, H., Taniguchi, N., in: nd, Varki, A., Cummings, R. D., Esko, J. D., *et al.* (Eds.), *Essentials of Glycobiology*, Cold Spring Harbor (NY) 2009.
- [4] Everest-Dass, A. V., Briggs, M. T., Kaur, G., Oehler, M. K., *et al.*, N-glycan MALDI Imaging Mass Spectrometry on Formalin-Fixed Paraffin-Embedded Tissue Enables the Delineation of Ovarian Cancer Tissues. *Mol Cell Proteomics* 2016, 15, 3003-3016.
- [5] Anugraham, M., Jacob, F., Nixdorf, S., Everest-Dass, A. V., *et al.*, Specific glycosylation of membrane proteins in epithelial ovarian cancer cell lines: glycan structures reflect gene expression and DNA methylation status. *Mol Cell Proteomics* 2014, 13, 2213-2232.
- [6] Narasimhan, S., Lee, J. W., Cheung, R. K., Gelfand, E. W., Schachter, H., Beta-1,4-mannosylglycoprotein beta-1,4-N-acetylglucosaminyltransferase III activity in human B and T lymphocyte lines and in tonsillar B and T lymphocytes. *Biochem Cell Biol* 1988, 66, 889-900.
- [7] Kizuka, Y., Taniguchi, N., Enzymes for N-Glycan Branching and Their Genetic and Nongenetic Regulation in Cancer. *Biomolecules* 2016, 6.
- [8] Allam, H., Johnson, B. P., Zhang, M., Lu, Z., *et al.*, The glycosyltransferase GnT-III activates Notch signaling and drives stem cell expansion to promote the growth and invasion of ovarian cancer. *J Biol Chem* 2017, 292, 16351-16359.
- [9] Guo, H. B., Jiang, A. L., Ju, T. Z., Chen, H. L., Opposing changes in N-acetylglucosaminyltransferase-V and -III during the cell cycle and all-trans retinoic acid treatment of hepatocarcinoma cell line. *Biochim Biophys Acta* 2000, 1495, 297-307.
- [10] Taniguchi, N., Miyoshi, E., Ko, J. H., Ikeda, Y., Ihara, Y., Implication of N-acetylglucosaminyltransferases III and V in cancer: gene regulation and signaling mechanism. *Biochim Biophys Acta* 1999, 1455, 287-300.
- [11] Hamanoue, M., Ikeda, Y., Ogata, T., Takamatsu, K., Predominant expression of N-acetylglucosaminyltransferase V (GnT-V) in neural stem/progenitor cells. *Stem Cell Res* 2015, 14, 68-78.
- [12] Chen, L., Zhang, W., Fregien, N., Pierce, M., The her-2/neu oncogene stimulates the transcription of N-acetylglucosaminyltransferase V and expression of its cell surface oligosaccharide products. *Oncogene* 1998, 17, 2087-2093.
- [13] Guo, H., Abbott, K. L., Functional impact of tumor-specific N-linked glycan changes in breast and ovarian cancers. *Adv Cancer Res* 2015, 126, 281-303.
- [14] Abbott, K. L., Lim, J. M., Wells, L., Benigno, B. B., *et al.*, Identification of candidate biomarkers with cancer-specific glycosylation in the tissue and serum of endometrioid ovarian cancer patients by glycoproteomic analysis. *Proteomics* 2010, 10, 470-481.
- [15] Taniguchi, N., Kizuka, Y., Glycans and cancer: role of N-glycans in cancer biomarker, progression and metastasis, and therapeutics. *Adv Cancer Res* 2015, 126, 11-51.
- [16] Takamatsu, S., Antonopoulos, A., Ohtsubo, K., Ditto, D., *et al.*, Physiological and glycomic characterization of N-acetylglucosaminyltransferase-IVa and -IVb double deficient mice. *Glycobiology* 2010, 20, 485-497.
- [17] Abbott, K. L., Nairn, A. V., Hall, E. M., Horton, M. B., *et al.*, Focused glycomic analysis of the N-linked glycan biosynthetic pathway in ovarian cancer. *Proteomics* 2008, 8, 3210-3220.
- [18] Saldova, R., Struwe, W. B., Wynne, K., Elia, G., *et al.*, Exploring the glycosylation of serum CA125. *Int J Mol Sci* 2013, 14, 15636-15654.

- [19] Nairn, A. V., York, W. S., Harris, K., Hall, E. M., *et al.*, Regulation of glycan structures in animal tissues: transcript profiling of glycan-related genes. *J Biol Chem* 2008, *283*, 17298-17313.
- [20] Campbell, M. P., Aoki-Kinoshita, K. F., Lisacek, F., York, W. S., Packer, N. H., in: rd, Varki, A., Cummings, R. D., Esko, J. D., *et al.* (Eds.), *Essentials of Glycobiology*, Cold Spring Harbor (NY) 2015, pp. 667-679.
- [21] Ashkani, J., Naidoo, K. J., Glycosyltransferase Gene Expression Profiles Classify Cancer Types and Propose Prognostic Subtypes. *Sci Rep* 2016, *6*, 26451.
- [22] Gustafsson, O. J., Briggs, M. T., Condina, M. R., Winderbaum, L. J., *et al.*, MALDI imaging mass spectrometry of N-linked glycans on formalin-fixed paraffin-embedded murine kidney. *Anal Bioanal Chem* 2015, *407*, 2127-2139.
- [23] Powers, T. W., Jones, E. E., Betesh, L. R., Romano, P. R., *et al.*, Matrix assisted laser desorption ionization imaging mass spectrometry workflow for spatial profiling analysis of N-linked glycan expression in tissues. *Anal Chem* 2013, *85*, 9799-9806.
- [24] Toghi Eshghi, S., Yang, S., Wang, X., Shah, P., *et al.*, Imaging of N-linked glycans from formalin-fixed paraffin-embedded tissue sections using MALDI mass spectrometry. *ACS Chem Biol* 2014, *9*, 2149-2156.
- [25] Briggs, M. T., Kuliwaba, J. S., Muratovic, D., Everest-Dass, A. V., *et al.*, MALDI mass spectrometry imaging of N-glycans on tibial cartilage and subchondral bone proteins in knee osteoarthritis. *Proteomics* 2016, *16*, 1736-1741.
- [26] O'Connor, P. B., Costello, C. E., A high pressure matrix-assisted laser desorption/ionization Fourier transform mass spectrometry ion source for thermal stabilization of labile biomolecules. *Rapid Commun Mass Spectrom* 2001, *15*, 1862-1868.
- [27] Powers, T. W., Holst, S., Wuhrer, M., Mehta, A. S., Drake, R. R., Two-Dimensional N-Glycan Distribution Mapping of Hepatocellular Carcinoma Tissues by MALDI-Imaging Mass Spectrometry. *Biomolecules* 2015, *5*, 2554-2572.
- [28] Holst, S., Heijs, B., de Haan, N., van Zeijl, R. J., *et al.*, Linkage-Specific in Situ Sialic Acid Derivatization for N-Glycan Mass Spectrometry Imaging of Formalin-Fixed Paraffin-Embedded Tissues. *Anal Chem* 2016, *88*, 5904-5913.
- [29] Lanucara, F., Holman, S. W., Gray, C. J., Evers, C. E., The power of ion mobility-mass spectrometry for structural characterization and the study of conformational dynamics. *Nat Chem* 2014, *6*, 281-294.
- [30] Pagel, K., Harvey, D. J., Ion mobility-mass spectrometry of complex carbohydrates: collision cross sections of sodiated N-linked glycans. *Anal Chem* 2013, *85*, 5138-5145.
- [31] Stauber, J., MacAleese, L., Franck, J., Claude, E., *et al.*, On-tissue protein identification and imaging by MALDI-ion mobility mass spectrometry. *J Am Soc Mass Spectrom* 2010, *21*, 338-347.
- [32] Heijs, B., Holst, S., Briaire-de Bruijn, I. H., van Pelt, G. W., *et al.*, Multimodal Mass Spectrometry Imaging of N-Glycans and Proteins from the Same Tissue Section. *Anal Chem* 2016, *88*, 7745-7753.
- [33] Palmisano, G., Melo-Braga, M. N., Engholm-Keller, K., Parker, B. L., Larsen, M. R., Chemical deamidation: a common pitfall in large-scale N-linked glycoproteomic mass spectrometry-based analyses. *J Proteome Res* 2012, *11*, 1949-1957.
- [34] Angel, P. M., Mehta, A., Norris-Caneda, K., Drake, R. R., MALDI Imaging Mass Spectrometry of N-glycans and Tryptic Peptides from the Same Formalin-Fixed, Paraffin-Embedded Tissue Section. *Methods Mol Biol* 2017.
- [35] Sterner, E., Flanagan, N., Gildersleeve, J. C., Perspectives on Anti-Glycan Antibodies Gleaned from Development of a Community Resource Database. *ACS Chem Biol* 2016, *11*, 1773-1783.
- [36] Poruk, K. E., Gay, D. Z., Brown, K., Mulvihill, J. D., *et al.*, The clinical utility of CA 19-9 in pancreatic adenocarcinoma: diagnostic and prognostic updates. *Curr Mol Med* 2013, *13*, 340-351.
- [37] Wu, E., Zhou, S., Bhat, K., Ma, Q., CA 19-9 and pancreatic cancer. *Clin Adv Hematol Oncol* 2013, *11*, 53-55.
- [38] Gao, C., Liu, Y., Zhang, H., Zhang, Y., *et al.*, Carbohydrate sequence of the prostate cancer-associated antigen F77 assigned by a mucin O-glycome designer array. *J Biol Chem* 2014, *289*, 16462-16477.

- [39] Hyun, J. Y., Pai, J., Shin, I., The Glycan Microarray Story from Construction to Applications. *Acc Chem Res* 2017, 50, 1069-1078.
- [40] Zou, X., Yoshida, M., Nagai-Okatani, C., Iwaki, J., *et al.*, A standardized method for lectin microarray-based tissue glycome mapping. *Sci Rep* 2017, 7, 43560.
- [41] Powers, T. W., Neely, B. A., Shao, Y., Tang, H., *et al.*, MALDI imaging mass spectrometry profiling of N-glycans in formalin-fixed paraffin embedded clinical tissue blocks and tissue microarrays. *PLoS One* 2014, 9, e106255.
- [42] Freeze, H. H., Kranz, C., Endoglycosidase and glycoamidase release of N-linked glycans. *Curr Protoc Protein Sci* 2010, Chapter 12, Unit12 14.

This page is intentionally left blank

Chapter 9 | Appendices

9.1 | Statement of Authorship

Title of Paper	The Glycomic Quest for the Holy Grail: An Early Stage Biomarker for Ovarian Cancer.
Publication Status	<input checked="" type="checkbox"/> Published <input type="checkbox"/> Accepted for Publication <input type="checkbox"/> Submitted for Publication <input type="checkbox"/> Unpublished and Unsubmitted work written in manuscript style
Publication Details	M Briggs, A Everest-Dass, M Oehler, N Packer, P Hoffmann: <i>The Glycomic Quest for the Holy Grail: An Early Stage Biomarker for Ovarian Cancer.</i>

Principal Author

Name of Principal Author (Candidate)	Matthew T. Briggs	
Contribution to the Paper	Conceived the project Data collection and analysis Prepared figures and wrote the main manuscript text	
Overall percentage (%)	80%	
Certification:	This paper reports on original research I conducted during the period of my Higher Degree by Research candidature and is not subject to any obligations or contractual agreements with a third party that would constrain its inclusion in this thesis. I am the primary author of this paper.	
Signature	Date	05/07/18

Co-Author Contributions

By signing the Statement of Authorship, each author certifies that:

- i. the candidate's stated contribution to the publication is accurate (as detailed above);
- ii. permission is granted for the candidate to include the publication in the thesis; and
- iii. the sum of all co-author contributions is equal to 100% less the candidate's stated contribution.

Name of Co-Author	Arun V. Everest-Dass		
Contribution to the Paper	Conceived the project Data collection and analysis		
Signature		Date	12/12/17

Name of Co-Author	Martin K. Oehler		
Contribution to the Paper	Provided the ovarian tissue samples		
Signature		Date	12/12/17

Name of Co-Author	Nicolle H. Packer		
Contribution to the Paper	Conceived the project Designed the experiments and supervised the research		
Signature		Date	18/04/18

Name of Co-Author	Peter Hoffmann		
Contribution to the Paper	Conceived the project Designed the experiments and supervised the research		
Signature		Date	20/12/17

The Glycomic Quest for the Holy Grail: An Early Stage Biomarker for Ovarian Cancer

Matthew Briggs^{1,2*}, Arun Everest-Dass³, Martin Oehler⁴,
Nicolle Packer³ and Peter Hoffmann^{1,2}

¹Adelaide Proteomics Centre, School of Biological Sciences, University of Adelaide, SA 5005

²Institute for Photonics and Advanced Sensing, University of Adelaide, SA 5005

³Faculty of Science, Biomolecular Frontiers Research Centre, Macquarie University, Sydney, NSW 2019

⁴Department of Gynaecological Oncology, Royal Adelaide Hospital, SA 5000

*Corresponding author: matthew.briggs@student.adelaide.edu.au

Ovarian Cancer

Ovarian cancer is the most lethal gynaecological malignancy with an estimated 1,470 new cases diagnosed in 2014 and 1,640 expected by 2020 in Australia (1, 2). Due to the asymptomatic nature of the disease, most patients are diagnosed at late-stage (International Federation of Gynaecology and Obstetrics (FIGO) stages III and IV) (3). The standard treatment regimen for patients is surgery followed by chemotherapy. Since treatment for many patients is not effective, prognosis is poor, with a five-year overall survival rate of only 44% (4).

Genomics of Ovarian Cancer

The genomic status of the patients allows us to divide the disease into two distinct groups. Group I contains low-grade and 'borderline' serous tumours, endometrioid, mucinous and clear cell tumours. These tumours generally contain mutations in *PTEN*, *PI3K* catalytic subunit- α (*PI3KCA*), *KRAS*, *BRAF* and β -catenin (*CTNNB1*). Group II contains high-grade serous and endometrioid tumours, and many low incidence tumours. This group typically presents with mutations in *TP53* in 60–80% of cases. Genetic instability is observed more frequently with *BRCA1/BRCA2* mutations, suggesting a role for *TP53* in hereditary ovarian disease (5).

Although there are benefits in the use of this classification strategy (6), there are also disadvantages such as gene transcript levels not always mirroring levels of protein translation (7). In addition, genomics can only predict sites of post-translational modifications (PTMs), which do not necessarily correlate with genuine PTM sites (8). In 2015, a *Nature* paper was published on whole-genome sequencing of 92 chemo-resistant ovarian cancer patients (9). The results revealed the most common genetic mutations and highlighted the heterogeneity of the disease. A holistic molecular understanding of globally regulated pathways in ovarian cancer therefore requires the combination of genomic information with protein abundance and modification state. With these details elucidated it may be possible to identify tissue or tumour subtype-specific markers to stratify patient groups and also isolate novel treatment targets.

Proteomics of Ovarian Cancer

Proteomics, a term coined by Marc Wilkins in 1994, describes the quantitative analysis of proteomes through high sensitivity measurement of hundreds to thousands of proteins in a complex mixture (10). Proteomics has been successfully implemented in ovarian cancer. However, there are limitations that have significantly hampered proteomic analysis. For example, proteomics does not directly address the position and nature of PTMs, which has led to the growth of niche-fields such as phosphoproteomics and glycoproteomics (11). These fields use modification-specific methods (e.g. enrichment and improvements to ionisation efficiency in the mass spectrometer) to facilitate the determination of PTM location and, in the case of glycoproteomics, composition.

Glycoproteomics of Ovarian Cancer

Glycoproteomics is the branch of proteomics where glycosylated proteins (glycoproteins) are identified and characterised from cells, tissue, or bodily fluid (12). Glycosylation is the enzymatic process where sugars (glycans) are attached to proteins, lipids or other organic molecules. In the human body it is estimated that 50–60% of proteins are glycosylated (13). *N*-linked glycans (sugars attached to asparagine residues in proteins) are of particular interest in ovarian cancer because structural alterations have been observed in the tumour microenvironment that promote tumour invasion and metastasis.

A structural alteration of interest is formation of bisecting *N*-acetylglucosamine (GlcNAc) on several *N*-glycan complexes. Previous studies have found that the glycoprotein CA125, an ovarian tumour marker, contains monofucosylated, bisecting GlcNAc *N*-glycans (14). The most recent work confirmed the expression of bisecting GlcNAc, but also correlated this observation with the gene expression of a glycosyltransferase enzyme (MGAT3), which complexes the core of *N*-glycans in a β 1-4 linkage (15). Bisecting GlcNAc was not detected in the control tissue, while in ovarian cancer cells 13% of *N*-glycans contained this modification. MGAT3 is believed to be involved in *N*-glycosylation patterns on E-cadherin, which is involved in the regulation of epithelial-mesenchymal transitions (16).

Compositional analysis allows us to identify and quantify these *N*-glycans while correlating them with clinical outcomes. The most common technique used to structurally characterise *N*-glycans from biological samples is by means of peptide-*N*-glycosidase (PNGase F) release, followed by liquid chromatography (LC) coupled to electrospray ionization (ESI) tandem mass spectrometry (MS/MS) (17).

LC-MS/MS

A recent study from our collaborators structurally characterised *N*-glycans from non-cancerous ovarian surface epithelium and serous ovarian cancer cell lines (15). Characteristic features identified that were unique to ovarian cancer membrane proteins include bisecting GlcNAc, α 2-6 sialylated and LacdiNAc type *N*-glycans. The *N*-glycans identified from the LC-MS/MS data were further verified using qRT-PCR of their corresponding genes (*MGAT3*, *ST6GAL1* and *B4GALNT3*).

At Macquarie University, Professor Nicolle Packer and Dr Arun Dass already have an established LC-MS/MS method to structurally characterise *N*-glycans. The caveat is that LC-MS/MS sample preparation removes spatial information through tissue disruption. This is a

key concept here as it would be ideal to correlate changes in protein glycosylation with tissue morphology, and in particular, surgical pathology annotations. To address this analytical shortfall, our group at the Adelaide Proteomics Centre have developed a novel approach to retain spatial information of *N*-glycans using a technique known as matrix-assisted laser desorption/ionisation (MALDI) imaging mass spectrometry (IMS) (18 and article by Boughton and Roessner in this issue).

MALDI-IMS

In the past decade, the gold standard of MALDI-IMS has been to spatially analyse the proteome of native or formalin-fixed paraffin-embedded (FFPE) tissue samples. Preparation of these tissue sections for MALDI-IMS consists of chemical treatments tailored to suit detection of specific molecule classes. For example, FFPE tissue requires antigen retrieval and proteolytic digestion to access the proteome. After proteolytic digestion, a matrix is homogeneously deposited across the tissue sections to co-crystallise with the analyte. Following sample preparation, MALDI-TOF/TOF (time of flight) MS acquisitions are performed across the entire tissue section in a two-dimensional grid to produce spatially referenced mass

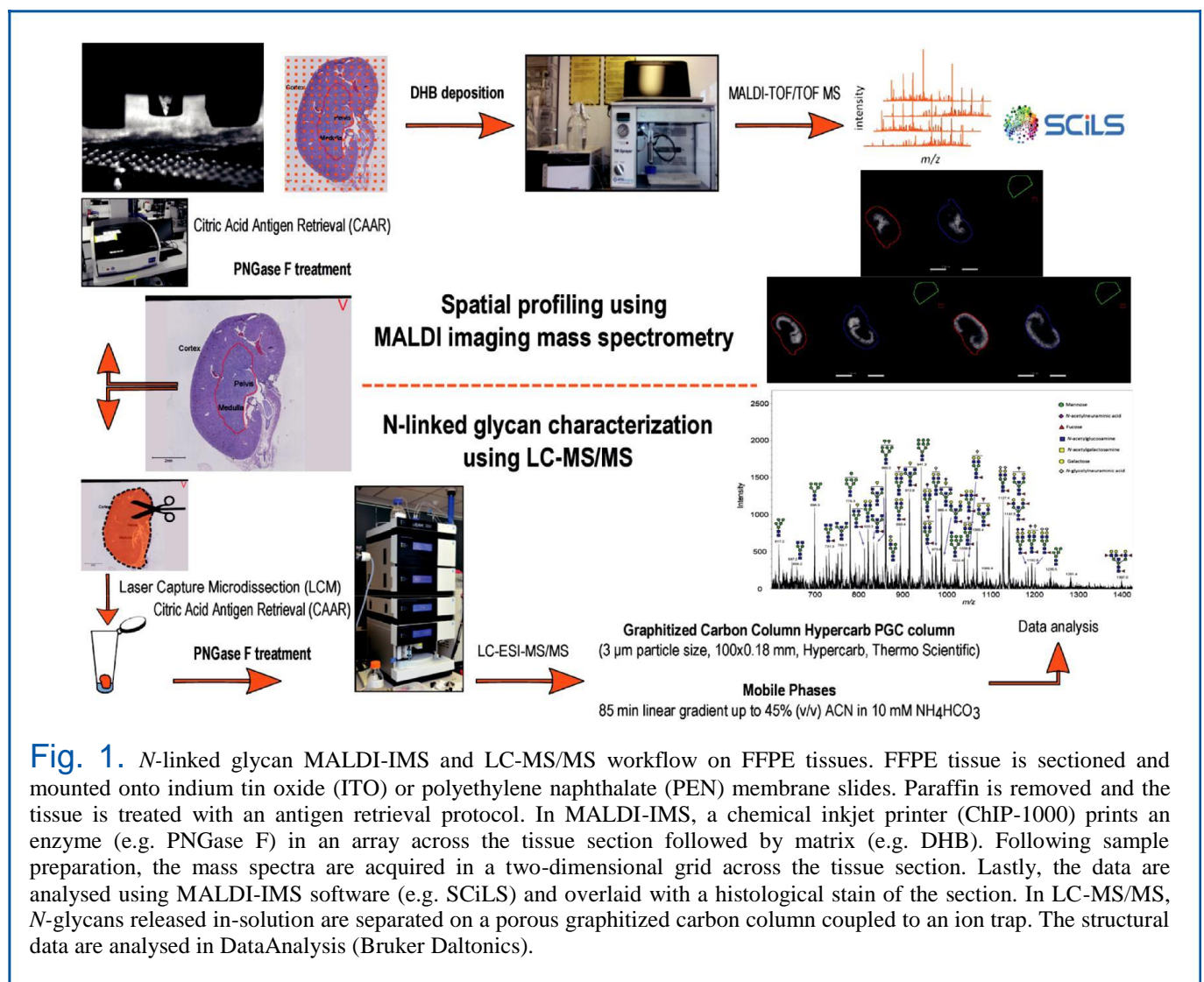
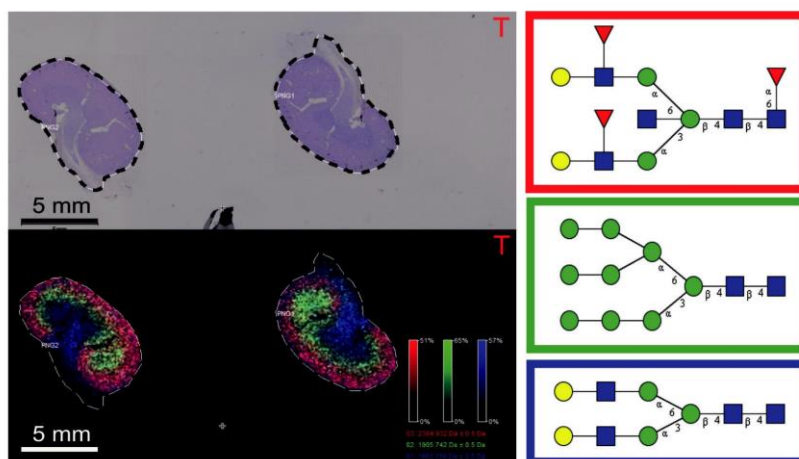


Fig. 1. *N*-linked glycan MALDI-IMS and LC-MS/MS workflow on FFPE tissues. FFPE tissue is sectioned and mounted onto indium tin oxide (ITO) or polyethylene naphthalate (PEN) membrane slides. Paraffin is removed and the tissue is treated with an antigen retrieval protocol. In MALDI-IMS, a chemical inkjet printer (ChIP-1000) prints an enzyme (e.g. PNGase F) in an array across the tissue section followed by matrix (e.g. DHB). Following sample preparation, the mass spectra are acquired in a two-dimensional grid across the tissue section. Lastly, the data are analysed using MALDI-IMS software (e.g. SCiLS) and overlaid with a histological stain of the section. In LC-MS/MS, *N*-glycans released in-solution are separated on a porous graphitized carbon column coupled to an ion trap. The structural data are analysed in DataAnalysis (Bruker Daltonics).

Fig. 2. MALDI imaging mass spectrometry of N-linked glycans released from murine kidney sections. Ion intensity maps for $(\text{Hex})_2(\text{HexNAc})_3(\text{Deoxyhexose})_3 + (\text{Man})_3(\text{GlcNAc})_2$ (m/z 2304.932, red), $(\text{Hex})_6 + (\text{Man})_3(\text{GlcNAc})_2$ (m/z 1905.742, green) and $(\text{Hex})_2(\text{HexNAc})_2 + (\text{Man})_3(\text{GlcNAc})_2$ (m/z 1663.756, blue).



spectra (19). There are several advantages of MALDI-IMS such as: (i) multiple samples can be analysed in a single experiment, (ii) hundreds of molecules and multiple molecule classes can be measured in a single experiment, and (iii) prior knowledge of tissue composition is not essential and antibodies are not required (20).

However, there are also disadvantages in relation to tissue archives. Most MALDI-IMS laboratories use native tissue archives, which are small in sample size and difficult to maintain for long periods of time. To address low sample numbers, multiple groups are turning to archival stored FFPE tissue samples. Hundreds to thousands of FFPE tissue samples, from healthy and diseased individuals, are stored in large pathology repositories worldwide (21). These FFPE tissue samples are pathologically annotated and can be linked to clinical information such as patient diagnosis, treatment and outcome. The advantage is that the formalin-fixation process conserves tissue samples by cross-linking of proteins and even *N*-glycans (11). As a result, FFPE tissues can be stored under ambient conditions for long periods of time without degradation of the proteins and *N*-glycans.

Methods for MALDI-IMS have already been established for analysis of tryptic peptides on FFPE ovarian tumours in our laboratory (20). Our group developed a novel MALDI-IMS method to spatially analyse *N*-glycans on FFPE murine kidney (see Fig. 1 for the workflow) (22). In 2014, other *N*-glycan MALDI-IMS methods were developed concurrently, such as in the Drake group at the Medical University of South Carolina in the USA (23,24). Our group, in collaboration with Professor Nicolle Packer from Macquarie University in Sydney, has developed a more comprehensive approach that extends the application to extract structural information from consecutive sections using LC-MS/MS to confirm the identification of the masses from the MALDI-IMS dataset.

The strength of our novel MALDI-IMS method is exhibited in our proof-of-principle manuscript (also see Fig. 2) (22). In the top panel, consecutive FFPE murine kidney sections have been hematoxylin and eosin (H&E) stained. In the bottom panel, there are ion intensity maps of *N*-glycans identified to be confined to the cortex (red), medulla (green) and pelvis (blue). MALDI-IMS data of

this nature allows us to differentiate between different tissue-types based on the *N*-glycan patterns.

Since publishing our proof-of-principle manuscript, we have investigated the *N*-glycan profile of FFPE ovarian tumours. These are advanced stage (stage III) tumour implants from patients ($n=3$) that were provided by Professor Martin Oehler from the Department of Gynaecological Oncology at the Royal Adelaide Hospital. Following PNGase F treatment and 2,5-DHB deposition, the FFPE tissue sections were analyzed by MALDI-TOF/TOF MS (Bruker Daltonics) and SCiLS 2D software. In parallel, consecutive sections were analyzed by LC-MS/MS to determine structural information for complementary masses. The extracted spectra from different tissue-types (see Fig. 3) exhibit different *N*-glycosylation patterns, therefore allowing tissue-types to be differentiated.

In summary, our group at the Adelaide Proteomics Centre and collaborators from Macquarie University have successfully developed and applied a novel MALDI-IMS

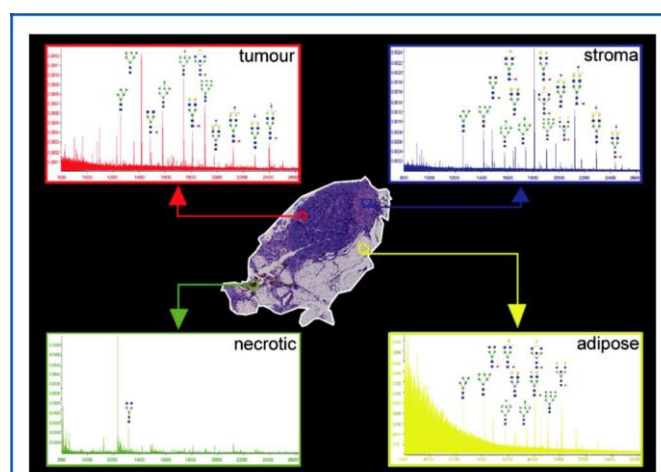


Fig. 3. Spatial profiling of four different tissue-types from an advanced stage ovarian cancer implant (tumour, stroma, necrotic and adipose). Regions of interest were selected in MALDI-IMS software (SCiLS) and sum spectra from these regions were extracted. *N*-linked glycans were structurally identified from complementary LC-MS/MS data.

method to identify *N*-glycans across FFPE tissue sections. However, further work is required to verify whether this technique can be used to discover potential biomarkers in ovarian cancer. For example, tissue-microarrays (TMAs) could be used allowing larger patient cohorts to be studied in a single experiment.

Overall, this novel *N*-glycan MALDI-IMS protocol has enabled the first steps in the Glycomic Quest for the Holy Grail: An early stage biomarker for ovarian cancer.

References

1. Australian Cancer Incidence and Mortality (ACIM) Books – Ovarian Cancer for Australia [cited July 2015]
2. Australian Institute of Health and Welfare in Cancer incidence projections: Australia, 2011 to 2020. Canberra.
3. Coleman, M.P., *et al.* (2011) *Lancet* **377**, 127-138
4. Siegel, R., *et al.* (2012) *CA Cancer J. Clin.* **62**, 220-241
5. Bast, R.C., Jr., Hennessy, B., and Mills, G.B. (2009) *Nat. Rev. Cancer* **9**, 415-428
6. Vang, R., Shih, L.-M., and Kurman, R.J. (2009) *Adv. Anat. Pathol.*, **16**, 267-282
7. Lu, P., Vogel, C., Wang, R., Yao, X., and Marcotte, E.M. (2007) *Nat. Biotechnol.* **25**, 117-124
8. Kim, H., Wu, R., Cho, K.R., Thomas, D.G., Gossner, G., Liu, J.R., Giordano, T.J., Shedden, K.A. Misek, D.E., and Lubman, D.M. (2008) *Proteomics Clin. Appl.* **2**, 571-584
9. Patch, A.M., *et al.* (2015) *Nature* **521**, 489-494
10. Wilkins, M.R., and Appel R.D. Ten years of the proteome. In: Wilkins, M.R., Appel, R.D., Williams, K.L., and Hochstrasser, D.F. (eds.) *Proteome Research: Concepts, Technology and Application (2nd edition)* 2007, Springer, Netherlands
11. Ostasiewicz, P., Zielinska, D.F., Mann, M., and Wisniewski, J.R. (2010) *J. Proteome Res.* **9**, 3688-3700
12. Pan, S., Chen, R., Aebersold, R., and Brentnall T.A. (2011) *Mol. Cell. Proteomics* **10**, R110.003251
13. Apweiler, R., Hermjakob, H., and Sharon, N. (1999) *Biochim. Biophys. Acta* **1473**, 4-8
14. Saldova, R., Struwe, W.B., Wynne, K., Elia, G., Duffy, M.J., and Rudd, P.M. (2013) *Int. J. Mol. Sci.*, **4**, 15636-15654
15. Anugraham, M., Jacob, F., Nixdorf, S., Everest-Dass, A. V., Heinzelmann-Schwarz, V., and Packer, N.H. (2014) *Mol. Cell. Proteomics* **13**, 2213-2232
16. Zhang, X., Wang, Y., Qian, Y., Wu, X., Zhang, Z., Liu, X., Zhao, R., Zhou, L., Ruan, Y., Xu, J., Liu, H., Ren, S., Xu, C., and Gu, J. (2014) *PLoS One* **9**, e87978
17. Hu, Y., Zhou, S., Khalil, S. I., Renteria, C. L., and Mechref, Y. (2013) *Anal. Chem.* **85**, 4074-4079
18. McDonnell, L.A., and Heeren, R.M. (2005) *Mass Spectrom. Rev.* **26**, 606-643
19. Caldwell, R.L., and Caprioli, R.M. (2005) *Mol. Cell. Proteomics* **4**, 394-401
20. Gustafsson, J.O.R., Oehler, M.K., Ruskiewicz, A., McColl, S.R., and Hoffmann, O. (2011) *Int. J. Mol. Sci.* **12**, 773-794
21. Angel, P.M., and Caprioli, R.M. (2013) *Biochemistry* **52**, 3818-3828
22. Gustafsson, O.J.R., Briggs, M.T., Condina, M.R., Winderbaum, L.J., Pelzing, M., McColl, S.R., Everest-Dass, A.A., Packer, N.H., and Hoffmann, P. (2015) *Anal. Bioanal. Chem.* **407**, 2127-2139
23. Toghi Eshghi, S., Yang, S., Wang, X., Shah, P., Li, X., and Zhang, H. (2014) *ACS Chem. Biol.* **9**, 2149-2156
24. Powers, T.W., Neeley, B.A., Shao, Y., Tang, H., Troyer, D.A., Mehta, A.S., Haab, B.B., and Drake, R.R. (2014) *PLoS One* **9**, e106255

9.2 | Statement of Authorship

Title of Paper	Applications of Mass Spectrometry Imaging to Cancer
Publication Status	<input checked="" type="checkbox"/> Published <input type="checkbox"/> Accepted for Publication <input type="checkbox"/> Submitted for Publication <input type="checkbox"/> Unpublished and Unsubmitted work written in manuscript style
Publication Details	G. Arentz, P. Mittal, C. Zhang, Y.-Y. Ho, <u>M. Briggs</u> , L. Winderbaum, M.K. Hoffmann, P. Hoffmann: <i>Applications of Mass Spectrometry Imaging to Cancer</i> . <i>Advances in Cancer Research</i> 01/2017; 134, DOI:10.1016/bs.acr.2016.11.002

Principal Author

Name of Principal Author (Candidate)	Matthew T. Briggs		
Contribution to the Paper	Wrote "Glycan Imaging in Cancer Research"		
Overall percentage (%)	10%		
Certification:	This paper reports on original research I conducted during the period of my Higher Degree by Research candidature and is not subject to any obligations or contractual agreements with a third party that would constrain its inclusion in this thesis. I am the primary author of this paper.		
Signature	_____	Date	05/07/18

Co-Author Contributions

By signing the Statement of Authorship, each author certifies that:

- i. the candidate's stated contribution to the publication is accurate (as detailed above);
- ii. permission is granted for the candidate to include the publication in the thesis; and
- iii. the sum of all co-author contributions is equal to 100% less the candidate's stated contribution.

Name of Co-Author	Georgia Arentz		
Contribution to the Paper	Wrote "Introduction"		
Signature	_____	Date	12/12/17

Name of Co-Author	Parul Mittal		
Contribution to the Paper	Wrote "Protein Imaging in Cancer Research"		
Signature		Date	12/12/17

Name of Co-Author	Chao Zhang		
Contribution to the Paper	Wrote "Practical Considerations for Peptide MSI"		
Signature		Date	18/04/18

Name of Co-Author	Yin-Ying Ho		
Contribution to the Paper	Wrote "Lipid Imaging in Cancer Research"		
Signature		Date	20/12/17

Name of Co-Author	Lyron Winderbaum		
Contribution to the Paper	Wrote "Data Analysis"		
Signature		Date	12/12/17

Name of Co-Author	Manuela Klingler-Hoffmann		
Contribution to the Paper	Wrote "Drug Imaging in Cancer Research" and evaluated the manuscript		
Signature		Date	18/04/18

Name of Co-Author	Peter Hoffmann		
Contribution to the Paper	Wrote "Conclusion" and evaluated the manuscript		
Signature		Date	20/12/17



Applications of Mass Spectrometry Imaging to Cancer

G. Arentz^{*,†}, P. Mittal^{*,†}, C. Zhang^{*,†}, Y.-Y. Ho^{*}, M. Briggs^{*,†,‡},
L. Winderbaum^{*}, M.K. Hoffmann^{*,†}, P. Hoffmann^{*,†,1}

^{*}Adelaide Proteomics Centre, School of Biological Sciences, University of Adelaide, Adelaide, SA, Australia

[†]Institute for Photonics and Advanced Sensing (IPAS), University of Adelaide, Adelaide, SA,

Australia [‡]ARC Centre for Nanoscale BioPhotonics (CNBP), University of Adelaide, Adelaide, SA,

Australia ¹Corresponding author: e-mail address: peter.hoffmann@adelaide.edu.au

Contents

1. Introduction	28
1.1 The Advantages of MSI	29
1.2 The Basic Principles of MSI	30
2. Protein MSI in Cancer Research	33
2.1 Distinguishing Tissue Types by Peptide MSI	36
2.2 Determining Tumor Margins by Peptide MSI	37
2.3 Prediction of Metastasis by Peptide MSI	37
2.4 Analysing Chemoresponse by Peptide MSI	39
2.5 Identification of Diagnostic and Prognostic Markers by Peptide MSI	39
2.6 Characterisation of Intra- and Intertumor Variability by Peptide MSI	41
2.7 Practical Considerations for Proteolytic Peptide MSI: Sample Preparation	42
2.8 Practical Considerations for Peptide MSI: Spatial Resolution	43
2.9 Practical Considerations for Peptide MSI: Mass Analysers	44
2.10 Practical Considerations for Peptide MSI: Identification	44
3. Lipid MSI in Cancer Research	45
3.1 Profiling Lipids in Cancer by DESI-MSI	45
3.2 Profiling Lipids in Cancer by SIMS-MSI	46
4. Glycan MSI in Cancer Research	47
5. Drug Imaging in Cancer Research	50
5.1 MALDI-MSI on Tissue Sections	51
5.2 MALDI-MSI on Whole Body Sections	53
5.3 MALDI-MSI on 3D Tissue Cultures	53
6. Data Analysis	53
6.1 Spatial Information	53
6.2 Preprocessing: Peak Detection	55
6.3 Classification of FFPE-TMAs and the Importance of Dimension Reduction	56
7. Concluding Remarks	57
7.1 The Future of MSI: Molecular Pathology	57
References	57

Abstract

Pathologists play an essential role in the diagnosis and prognosis of benign and cancerous tumors. Clinicians provide tissue samples, for example, from a biopsy, which are then processed and thin sections are placed onto glass slides, followed by staining of the tissue with visible dyes. Upon processing and microscopic examination, a pathology report is provided, which relies on the pathologist's interpretation of the phenotypical presentation of the tissue. Targeted analysis of single proteins provide further insight and together with clinical data these results influence clinical decision making. Recent developments in mass spectrometry facilitate the collection of molecular information about such tissue specimens. These relatively new techniques generate label-free mass spectra across tissue sections providing nonbiased, nontargeted molecular information. At each pixel with spatial coordinates (x/y) a mass spectrum is acquired. The acquired mass spectrums can be visualized as intensity maps displaying the distribution of single m/z values of interest. Based on the sample preparation, proteins, peptides, lipids, small molecules, or glycans can be analyzed. The generated intensity maps/images allow new insights into tumor tissues. The technique has the ability to detect and characterize tumor cells and their environment in a spatial context and combined with histological staining, can be used to aid pathologists and clinicians in the diagnosis and management of cancer. Moreover, such data may help classify patients to aid therapy decisions and predict outcomes. The novel complementary mass spectrometry-based methods described in this chapter will contribute to the transformation of pathology services around the world.

ABBREVIATIONS

CHCA α -cyano-4-hydroxycinnamic acid
DESI desorption electrospray ionization
DHB 2,5-dihydroxybenzoic acid
FFPE formalin-fixed paraffin embedded
FT-ICR Fourier transformed ion cyclotron resonance
IHC immunohistochemistry
LNM lymph node metastasis
MALDI matrix-assisted laser desorption/ionization
MSI mass spectrometry imaging
PCA principle component analysis
SIMS secondary ion mass spectrometry
TOF time-of-flight



1. INTRODUCTION

In order to optimize the treatment outcomes for cancer patients and even provide a cure, several issues regarding the clinical management of disease need to be addressed. Based on pathological and clinical parameters

patients are classified to receive the best possible therapy. The accuracy of this process would be better if a more complete understanding of the molecular events involved in the development and progression of cancer was available. Currently, mass spectrometry imaging (MSI) is being extensively applied to the *in situ* molecular analysis of cancerous cells and tissues with the aim of identifying tumor margins, classifying primary tumor tissues with regards to chemoresponse and metastatic status, identifying diagnostic and prognostic markers, and the analysis of drug response rates and resistance. Elucidation of the spatial location and abundance of peptides, proteins, lipids, glycans, and drug metabolites in relation to cancerous tissues and cells has the potential to significantly improve the diagnosis, staging, and treatment of disease.

1.1 The Advantages of MSI

Interpatient heterogeneity significantly impacts the success of diagnostic and prognostic tests, because it influences the way patients respond to the same treatment. Moreover, proteomic analysis is impacted by intratumor heterogeneity, as tumors are complex structures comprised of a number of different cell types, such as epithelial or endothelial, stromal, vascular, and inflammatory cells. This is particularly important when considering concepts such as innate chemoresistance, metastasis, and stem-cell-like cancer cells, which are believed to consist of a small subset of cells within the bulk of the tumor tissue. Analysis methods that require homogenisation of a sample lose important information about the spatial location of the molecules being studied. Moreover, the information of a potential difference in protein abundance of a small number of cells might not be reflected in the average abundance of the tissue. Certain analysis methods, such as immunohistochemistry (IHC) or fluorescence microscopy, allow for the quantification of compounds within a spatial context. However, these methods are targeted, requiring prior knowledge about the target and the sample in question, and only a small number of molecules can be analyzed simultaneously.

The rapidly evolving technique of MSI allows for the *in situ* analysis of biological samples, combining classical mass spectrometry (MS) with histological tissue analysis. MSI has the capacity to determine the relative intensity and spatial distribution of several hundreds of compounds from cells and tissue while retaining important spatial information (Schwamborn &

Caprioli, 2010). In the context of cancer research this affords the technique the ability to characterize the molecular features of a sample while maintaining morphology and requiring no prior knowledge of the molecular expression profile. The type of molecules detected, or ions in the context of MS, is dependent on the sample preparation, instrumentation, and acquisition protocols used.

1.2 The Basic Principles of MSI

MS analysis includes the processes of analyte ionization, mass analysis, and detection (de Hoffmann & Stroobant, 2007). During ionization analyte molecules become electrically charged and liberated into the gas phase. Once ionized the mass of the charged molecules is determined by analysis in the mass spectrometer; the analyte ions are separated based on their mass-to-charge ratio (m/z) and detected, commonly by a microchannel plate detector. In terms of MSI, there are two basic forms: microprobe mode imaging and microscope mode imaging (Bodzon-Kulakowska & Suder, 2016; Klerk, Maarten Altelaar, Froesch, McDonnell, & Heeren, 2009; Luxembourg, Mize, McDonnell, & Heeren, 2004). In microprobe mode MSI, where information is collected sequentially from each pixel (pixel sizes typically 5–100 μm), each mass spectrum contains information about the m/z and relative intensity of the detected ions at each location. Following data acquisition, the collected information is reconstructed into a molecular image. In microscope mode MSI, spectral information is collected over a relatively large sample area (100–300 μm) simultaneously; in this form of MSI, the ions produced over the analyzed area are measured using a position-sensitive two-dimensional detection system. The information collected by both microprobe and microscope mode can be displayed as ion maps which show the distribution of the detected m/z values and their intensities, thereby characterizing cancer cells or tissues within their environment in a spatial context.

Following MSI the sample morphology is frequently retained and can be histochemically analyzed postdata acquisition (Crecelius et al., 2005; Schwamborn et al., 2007), making it feasible to directly compare MSI results with histological staining. These methods are complementary and have a high potential for aiding pathologists and clinicians in their diagnosis and management of disease (Rodrigo et al., 2014). As indicated earlier, MSI usually requires very little material and, for example,

a single tissue section from an endoscopic biopsy is enough to perform a successful MSI experiment.

For MSI, the ionization methods matrix-assisted laser desorption/ionization (MALDI), secondary ion mass spectrometry (SIMS), and desorption electrospray ionization (DESI) are popular, and are frequently coupled to time-of-flight (TOF) or Fourier transform type mass analyzers. A very brief description of the commonly applied techniques and their capabilities is provided in the following sections.

1.2.1 MALDI-TOF

MALDI-TOF is commonly used for the analysis of proteins, peptides, lipids, metabolites, and glycans (Cho et al., 2015; Signor & Boeri Erba, 2013). The application of MALDI-TOF to imaging MS was first introduced in 1997 (Caprioli, Farmer, & Gile, 1997) and the technique has gained significant popularity over the last two decades. For analysis by MALDI-TOF-MSI, a sample is placed on a conductive surface such as a stainless steel plate or an indium tin oxide-coated glass slide. Commonly fresh frozen or formalin-fixed paraffin-embedded (FFPE) tissue sections 4–10 μm thick are analyzed by MALDI-TOF-MSI, with FFPE tissues requiring additional preparation steps of deparaffinization and antigen retrieval (Ronci et al., 2008). Once the tissue is placed on the slide, depending on the type of analysis being performed, a digestion step may be carried out. For proteolytic peptide analysis, the most common enzyme utilized is trypsin, for glycan analysis a peptide-*N*-glycosidase F (PNGase F) digestion may be employed to release *N*-linked glycan structures from proteins (Gustafsson et al., 2015). The analysis of lipids, metabolites, endogenous peptides, and intact proteins directly from tissue does not require enzyme treatment. Prior to analysis a small organic acid, referred to as the matrix, is suspended in an acidified solvent buffer and deposited over the sample (Goodwin, 2012; Kaletas et al., 2009). During this process the matrix incorporates the analyte molecules, forming crystals. A focussed laser beam can then be applied to the surface in order to induce analyte ionization. The small organic molecules of the matrix mixture are designed to absorb the energy of the focussed laser beam resulting in an explosive desorption of the matrix and analyte crystals. The protons present in the acidified matrix solution also facilitate the analyte ionization. MALDI is a “soft” ionization technique, meaning many analytes may be analyzed without significant fragmentation.

Following ionization the ions are rapidly accelerated through a strong electric field in the ion source, the ions then enter the TOF tube or “drift” region, allowing separation based on velocity and thus m/z . The charged analyte molecules strike the detector and the number of events within a time period are recorded, providing intensity information. By comparing the measured information to calibration standards, the mass of the detected analyte ion can be calculated. The spatial resolution of MALDI-TOF imaging sits at around 20 μm and can accommodate a molecular mass range of over 100 kDa.

1.2.2 MALDI-FT-ICR

MALDI-FT-ICR is routinely applied to the imaging analysis of lipids, drugs, and metabolites. MALDI is carried out as described earlier with the Fourier transform ion cyclotron resonance (FT-ICR) acting as the mass analyser, where the m/z of analyte ions is determined by the cyclotron frequency of the ions within the fixed magnetic field of the instrument (Scigelova, Hornshaw, Giannakopoulos, & Makarov, 2011).

Following ionization the charged molecules are trapped in a Penning trap, which consists of a series of electrodes that use a homogeneous axial magnetic field to capture the molecules radially, and an inhomogeneous quadrupole electric field to confine the molecules axially. Within the Penning trap, a RF electric field is applied in the plane of ion cyclotron motion which excites the ions to move in a larger, synchronous, cyclotron radius. Once the excitation field is removed, the ions are left rotating at their cyclotron frequencies in phase. The ions induce a charge which is detected as an image current by electrode detectors in close proximity. The recorded signal consists of a superposition of sine waves; this information can be used to calculate the masses of the detected ions using a Fourier transform equation. In FT-ICR a superconducting magnet is used to generate a highly stable magnetic field resulting in very high levels of resolution.

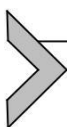
1.2.3 SIMS-TOF

SIMS utilizes beams of primary monoatomic (e.g., Bi $+$, Au $+$) or polyatomic (C $+_{60}$, Bi $+_3$, Cs $+_n$) ions in a vacuum for ionization (Fletcher, Vickerman, & Winograd, 2011). During SIMS the sample surface is bombarded with a beam of primary ions, causing molecules on the surface of the sample to be released, a process referred to as sputtering. During sputtering energy from the primary ions is transferred to the analyte molecules. Around 1% of the sputtered analyte molecules possess an electric

charge; these ions can be detected by a mass analyzer, such as a TOF (as described earlier). The energy of the primary ion beam is typically high compared to the covalent bond energies of the analyte molecules, resulting in their fragmentation. This makes SIMS a “hard” ionization technique, although polyatomic ion beams offer softer ionization than monoatomic ion beams (Bodzón-Kulakowska & Suder, 2016). SIMS requires no matrix and offers higher depth and spatial resolution (<10 μm) as compared to MALDI. However, MALDI is more sensitive as it has access to higher yields of analyte and is able to detect larger molecules (Fletcher, Lockyer, & Vickerman, 2011), with the highest detectable mass range of SIMS sitting at around 1 kDa.

1.2.4 DESI

DESI uses an electrospray source of highly charged aqueous spray droplets under ambient conditions to gently desorb and ionize analyte molecules from the sample surface (Taka’ts, Wiseman, Gologan, & Cooks, 2004). An advantage of DESI is that it allows for the analysis of a sample in its native state. In the ion source an electrospray emitter is used to generate charged microdroplets from a solvent, which create a thin film on the sample surface that dissolves the analyte molecules. Secondary microdroplets are formed from the kinetic impact of the primary droplets, which contain the highly charged solvent and dissolved analyte. These secondary microdroplets are ionized from the sample surface to the mass spectrometer inlet. A DESI source can be coupled to most standard electrospray mass spectrometers (Hsu & Dorrestein, 2015) where following ionization, the analytes are sent via an ion transfer tube to the mass analyser for detection. During ionization little analyte fragmentation occurs, hence DESI is considered a “soft” ionization technique with a spatial resolution of around 50–100 μm and an upper mass range detection limit of around 2 kDa.



2. PROTEIN MSI IN CANCER RESEARCH

Changes in protein function play a crucial role in the development of cancer. Such alterations can be caused by number of events including altered localization, posttranslational modifications (PTMs), and/or abundance levels. Furthermore, the biology of a tumor depends not only on the cancerous cells but also on their interaction with surrounding stroma, blood vessels, and the immune system (Kriegsmann, Kriegsmann, & Casadonte, 2015). The ability to spatially resolve different proteins while simultaneously

acquiring information concerning their relative abundance is particularly important in heterogeneous diseases such as cancer. Therefore, an approach combining high-resolution MS with in situ spatial analysis of the diseased area has the potential to directly identify and quantify proteins and peptides.

When MSI first entered the field of tissue-based research, it was used to analyze the spatial distribution of proteins (Stoeckli, Chaurand, Hallahan, & Caprioli, 2001). Following this ground-breaking research, different imaging methods have been established and applied to a wide range of biological problems. Among the several MSI techniques, MALDI-MSI is one of the most commonly used. MALDI-MSI has the capability of detecting a broad range of compounds present in a tissue section, provided the compound can be ionized and desorbed into gaseous phase during the MALDI process. High-resolution MS, such as MALDI-FT-ICR, has greater strength in the field of low-molecular weight compounds, while MALDI-TOF is used for the analysis of peptides and small proteins up to 25 kDa (Aichler & Walch, 2015). MALDI-MSI of thin tissue sections can result in the detection of over 500 individual protein signals within the mass range of 2–70 kDa that can be directly correlated with specific morphological regions of the tissue (Chaurand, Schwartz, & Caprioli, 2004).

Protocols have been developed for the preparation of tissue sections and matrix application that provide a high level of reproducibility (Gustafsson et al., 2013). The methodology behind protein MSI, via the analysis of their proteolytic peptides, is straightforward; a digestion enzyme is uniformly applied over the entire tissue surface either by a spotting or spray deposition method. Thereafter, using the same application method, internal calibrants and matrix are applied. Data acquisition is then carried out by a MS (Gustafsson et al., 2013), where analyte ionization, mass analysis, and detection occur. This results in the subsequent generation of mass spectrums at regular series of points across the tissue section. The mass spectra produced are then visualized as ion intensity maps; generating two-dimensional distribution maps of the detected mass spectra containing information about the location and the relative intensity of the detected peptides. This visualization is similar in nature to images generated by histological or IHC analysis, but with the advantage that multiple molecules can be examined within a single measurement (Aichler & Walch, 2015) (Fig. 1).

Three-dimensional MALDI-MS images can also be generated by analyzing a number of consecutively cut tissue sections, and following data acquisition, combining the results to generate three-dimensional maps (Andersson, Groseclose, Deutch, & Caprioli, 2008; Sinha et al., 2008).

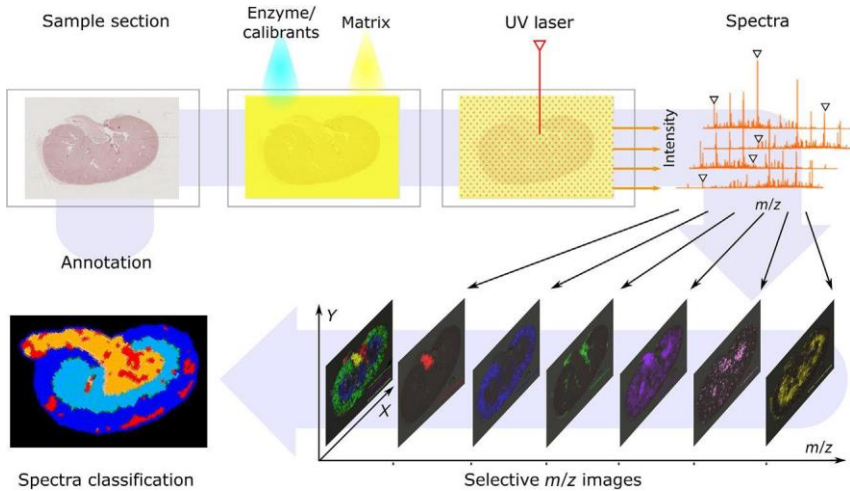


Fig. 1 Workflow of MALDI mass spectrometry imaging.

Recently, methods were developed for the integration of three-dimensional volume reconstructions of spatially resolved MALDI-MSI ion intensity images taken of whole mouse heads with corresponding *in vivo* data provided by magnetic resonance imaging (MRI) (Sinha et al., 2008). The added spatial dimension provides contextual information to the MALDI-MSI data that allow the interrogation of proteomic relationships within a tissue volume. The work displayed a correlation between the *in vivo* MRI and proteomic profiles obtained by MALDI-MSI, with both techniques able to distinguish tumor from healthy tissues (Sinha et al., 2008).

Until recently, MALDI-MSI had been carried out almost exclusively on fresh frozen samples as it was believed proteins were inaccessible from FFPE tissue due to the cross-linking caused by the formalin fixation. However, this limitation has been overcome and equal number of proteins can be identified from both fresh frozen and FFPE tissues (Diehl et al., 2015). The use of FFPE tissues in cancer research is a huge advantage, given that the samples are well preserved by the formalin fixation process and can be stored for long periods of time at room temperature. Another attractive feature is that the samples are often well documented as they have been processed by clinical pathology departments, meaning information on patient treatment response, disease progression, and other relevant clinical data have been cataloged (Gorzolka & Walch, 2014). Additionally, FFPE tissues are well suited for the construction of tissue microarrays (TMAs), where needle core biopsies from multiple tissue samples are assembled into a paraffin block. However,

fresh frozen TMAs have also been studied in a limited context (Fejzo & Slamon, 2010).

One of the main advantages of MALDI-MSI is the technique's ability to detect changes in disease-associated protein expression prior to histological transformation, making it a useful tool in the identification of early stage disease biomarkers (McDonnell et al., 2010). There have been number of cancer studies that have successfully applied peptide imaging to the discovery of potential biomarkers with the capacity to differentiate tumors of various subtypes, stages, and/or degree of metastasis.

2.1 Distinguishing Tissue Types by Peptide MSI

The ability of peptide MSI to distinguish specific types of tissue, such as regions of healthy, cancer, stroma, and vasculature, has been shown multiple times (Mittal, Klingler-Hoffmann, Arentz, Zhang, et al., 2016). Schwamborn et al. performed MSI on prostate cancer specimens and was able to classify the cancerous tissue from normal tissue with 85% sensitivity and 90% specificity, with an overall cross validation accuracy of 88% (Schwamborn et al., 2007). Moreover, MSI of prostate cancer TMAs on a large scale allowed for the immediate prioritization of MSI signals based on associations with clinic-pathological and molecular data (Steurer et al., 2013). A comparison of these signals with clinic-pathological features revealed statistical association with a favorable phenotype such as grade, stage, and relationship with prolonged time to prostate-specific antigen recurrence (Steurer et al., 2013). Peptide MSI experiments have been able to discriminate normal, preinvasive, and invasive lung tumor tissues with an accuracy of 90% (Rahman et al., 2011), to differentiate normal tissue from oral squamous cell carcinoma (Patel et al., 2009), to discriminate normal tissue from gastric cancer tissues (Kim et al., 2010), and have identified mitogen-activated protein kinase/extracellular signal-regulated kinase kinase 2 (MEKK2) as a marker with the capacity to accurately discern cancerous prostate from normal tissue (Cazares et al., 2009).

One of the most challenging aspects of neurochemistry is the detection of endogenous neuropeptides due to their low in vivo concentrations ranging from pico- to femto-molar levels, which makes it difficult to obtain enough material for quantitative analysis (Andersson, Andren, & Caprioli, 2010; Strand, 2003). MALDI-MSI helps overcome this issue as it allows the direct detection of neuropeptides in discrete regions of a brain sections, enabling the study of the physiological and disease-related

metabolic processing of neuropeptides (Andersson et al., 2010). Recently, Andersson et al. has been able to sequence and identify neuropeptides by in situ tandem mass spectrometry (MS/MS) directly off rat brain sections using a MALDI-QTOF mass spectrometer (Andersson et al., 2008).

Furthermore, peptide MALDI-MSI has been employed to differentiate benign regions from malignant in ovarian cancer (Lemaire, Ait Menguellet, et al., 2007) and in thyroid cancer (Pagni et al., 2015). Likewise, biomarkers have been identified that could distinguish Hodgkin's lymphoma from lymphadenitis (Schwamborn et al., 2010).

2.2 Determining Tumor Margins by Peptide MSI

One of the major aims of clinical oncology is to ensure a tumor has been completely removed during surgery to minimize the possibility of disease recurrence (Han et al., 2011). Defining tumor margins also plays a pivotal role in cancer staging, which subsequently influences the administration of treatment. Moreover, the molecular characterization of tumor margins will assist in understanding the process of invasion into surrounding tissues and may help in the clinical management of disease (Agar et al., 2010). MALDI-MSI has been proposed as a valuable tool for gaining information with regards to tumor margins and heterogeneity (Chaurand, Sanders, Jensen, & Caprioli, 2004). Peptide MSI has interestingly revealed histologically normal tissue adjacent to renal cell carcinoma regions, share many molecular characteristics with that of the tumor tissue, providing unprecedented insight into cancer development (Oppenheimer, Mi, Sanders, & Caprioli, 2010). The technique has also been used to identify protein biomarkers for the differentiation of delineated hepatocellular carcinoma from adjacent cirrhotic tissue (Le Faouder et al., 2011). Analysis of ovarian cancer interface zones, the regions between tumor and normal tissues, by MSI revealed a unique peptide profile from both the tumor and normal tissue, and detected plastin 2 and peroxiredoxin 1 as interface markers specific to ovarian cancer (Kang et al., 2010).

2.3 Prediction of Metastasis by Peptide MSI

Metastatic status is often the defining feature in determining if a patient will receive chemotherapy and is currently resolved by the removal and analysis of local lymph nodes, which frequently results in noncancer-related health complications. Identification of primary tumor markers of metastasis

would prevent the unnecessary removal of lymph nodes, thereby reducing patient suffering and associated treatment costs, and allow the introduction of more personalized cancer therapies (Casadonte et al., 2014). However, identification of metastasis based on analysis of the primary tumor tissues is challenging, especially when the primary carcinoma site is unknown (Pavlidis & Pentheroudakis, 2016). A statistical classification model based on peptide MSI data has been developed for determining the metastatic status of primary cancers of pancreatic origin and their metastasis to secondary breast cancer with an overall accuracy of 83% (Casadonte et al., 2014). In another study the HER2 status of gastric cancers could be predicted with 90% accuracy using peptide expression patterns originating from breast cancers (Balluff et al., 2010). These studies display the potential of peptide MSI in the profiling of cancers, independent of their site of origin.

The likelihood of lymph node metastasis (LNM) is one of the most important factors to consider while determining the appropriate treatment for a cancer patient. Several studies have applied MALDI-MSI to the prediction of LNM status. Yanagisawa et al. was able to classify primary lung tumors with and without LNM with an accuracy of 85% (Yanagisawa et al., 2003). Different peptide signatures have been identified with the ability to distinguish melanoma (LNM) from control lymph nodes (Hardesty, Kelley, Mi, Low, & Caprioli, 2011). Similarly, the overexpression of S100A10, thioredoxin, and S100A6, have been shown to be highly associated with LNM in papillary thyroid carcinoma (PTC) (Nipp et al., 2011), and it was suggested the three proteins may be used for risk stratification regarding metastatic potential in PTC. Other protein biomarkers have been suggested for the prediction of LNM in several cancers from peptide MSI experiments, such as S100A8 and S100A9 for gastric adenocarcinoma (Choi et al., 2012), COX7A2, TAGLN2, and S100-A10 for monitoring the Barrett's adenocarcinoma development as well as for predicting regional (LNM) and disease outcome (Elsner et al., 2012).

Recently, it has been shown that the LNM status of primary endometrial tumors could be predicted with an accuracy of 88% using a classification system based on tissue peptide markers detected by MALDI-MSI (Mittal, Klingler-Hoffmann, Arentz, Winderbaum, et al., 2016; Winderbaum, Koch, Mittal, & Hoffmann, 2016). In the study FFPE-TMAs comprised of duplicate tumor tissue cores from endometrial cancer patients diagnosed with and without LNM were analyzed by MALDI-TOF-MSI. An overview of the sample preparation and approach used for the proteomic marker

identification by MALDI-MSI-(top panel) and LC-MS/MS (bottom panel) is outlined in Fig. 2.

2.4 Analysing Chemoresponse by Peptide MSI

Innate and acquired chemoresistance significantly impact the survival rates of late stage cancer patients. Administration of chemotherapy to patients with specific cancer types has traditionally been standardized, despite the knowledge that response can differ significantly among a cohort of patients due to genetic diversity and tumor heterogeneity. Identification of markers or tests that predict resistance to standard chemotherapy regimens would help save patients from damaging, ineffective treatments, and may help determine if an alternative treatment course may be more beneficial.

IHC is one of the most widely applied proteomic techniques in clinical practice. However, IHC is often unable to distinguish the different isoforms of the same protein that may play different role in the disease development. Recent studies using MSI have been able to distinguish two isoforms of the protein defensin. This is of particular interest given the 2 defensin protein isoforms respond differently in breast cancer tumors when exposed to chemotherapy (Bauer et al., 2010). The finding was discovered during the analysis of a breast cancer patient receiving neoadjuvant paclitaxel and radiation therapy, and was one of the first biomarker discovery studies to utilize MALDI-MSI (Bauer et al., 2010). Mitochondrial defects have also been found and linked to chemotherapy response in oesophageal adenocarcinoma patients using peptide MSI (Aichler et al., 2013), displaying the techniques potential to change classifications of tumors and chemoresponse.

2.5 Identification of Diagnostic and Prognostic Markers by Peptide MSI

A high proportion of cancer patients are diagnosed in the later stages of disease, when the cancer has already metastasized to distant lymph nodes or organs. Detecting cancer in the earlier stages of disease, prior to metastasis, would help increase survival rates and reduce the treatment burden for patients. In a genetically engineered mouse model, peptide MSI was used to detected several discriminative peptide masses that could distinguish between intraepithelial neoplasia, intraductal papillary mucinous neoplasm, and normal pancreatic tissue (Gruner et al., 2012). Using MALDI-MSI to analyze TMAs, significant differences between papillary and clear cell renal cell cancer were found (Steurer, Seddiqi, et al., 2014). Analysis of bladder

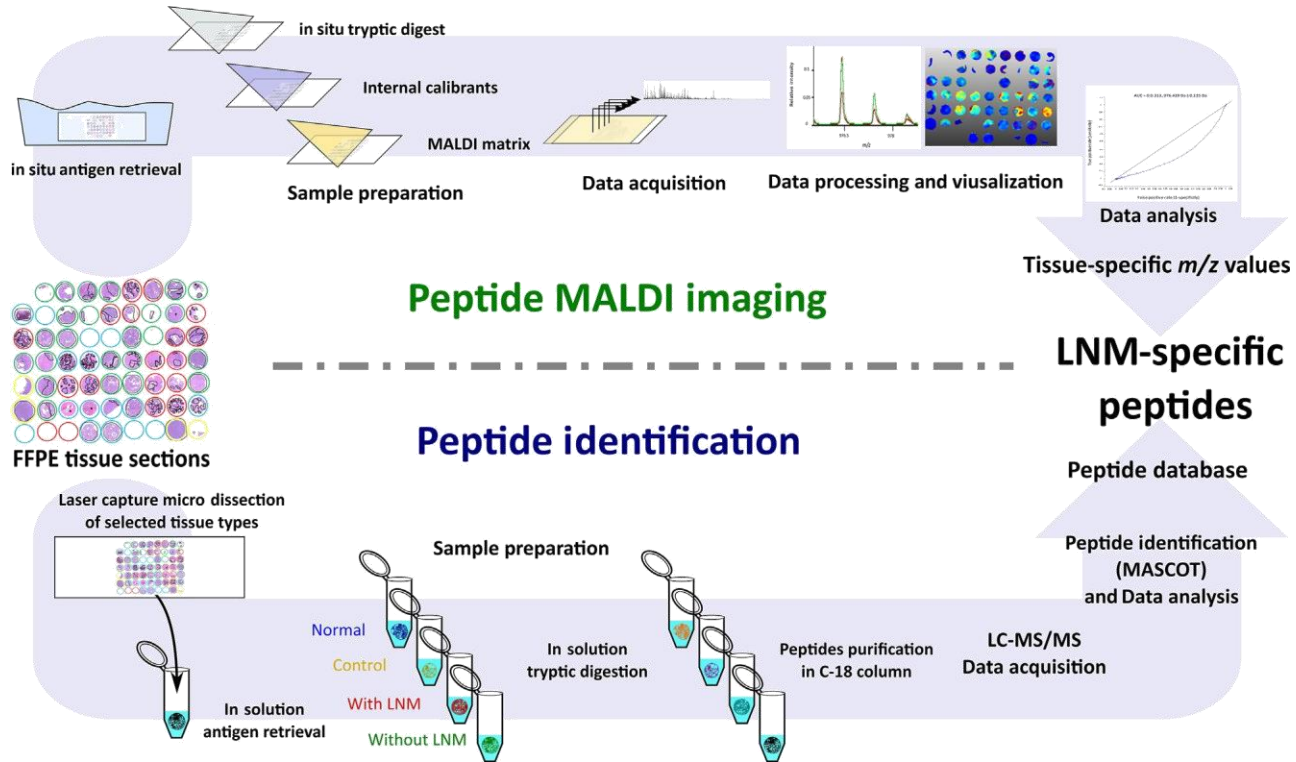


Fig. 2 Workflow for proteomic marker identification by peptide MALDI-MSI and label-free quantification.

cancer TMAs by MSI lead to the identification of multiple signals in the mass spectra associated with unfavorable tumor phenotype and clinical characteristics, such as tumor recurrence, progression, and patient survival time (Steurer, Singer, et al., 2014).

MALDI-MSI has also been used to identify a protein signature that can accurately determine the HER2 status in breast cancer with sensitivity of 83%, for specificity of 92%, and overall accuracy of 89% (Rausser et al., 2010). A seven-protein signature of novel tissue markers was identified as an independent indicator of unfavorable overall survival in intestinal type gastric cancer (Balluff, Rausser, et al., 2011). Other investigators identified histone 4 expression as specific to poorly differentiated gastric cancer tissues by peptide MSI (Morita et al., 2010). A comparison of genomically stable (diploid) and unstable (aneuploid) colon cancer tissues against normal mucosa by MSI identified thymosin beta 4 as an independent prognostic marker for colorectal cancer (Gemoll, Strohkamp, Schillo, Thorns, & Habermann, 2015). Analysis of lung cancer TMAs containing 112 needle core biopsies were used to generate a support vector machine model utilizing MSI information on 73 peptides that could classify adenocarcinomas with an accuracy of 97% and squamous cell carcinomas with an accuracy of 98% (Groseclose, Massion, Chaurand, & Caprioli, 2008).

2.6 Characterisation of Intra- and Intertumor Variability by Peptide MSI

Understanding the spatiotemporal patterns and dynamics of intratumor heterogeneity is crucial for clinical management and designing personalized targeted regimens for cancer patients (Renovanz & Kim, 2014). Balluff et al. showed for the first time that MALDI-MSI of tumor tissues can reveal microscopically indistinct tumor populations that might have adverse impacts in clinical outcome (Balluff et al., 2015). In the proof-of-principal study tumor-specific mass spectra were grouped using an advanced statistically clustering algorithm in order to obtain segmentation maps of molecularly distinct regions. The distinct regions were then statistically compared with patient clinical data to identify phenotypic tumor subpopulations (Balluff et al., 2015). This approach revealed that several of the detected tumor subpopulations are associated with different overall survival characteristics of gastric cancer patients ($p = 0.025$) and the presence of regional metastasis in patients with breast cancer ($p = 0.036$). This approach enables researchers to gain deeper insights into the underlying biological

process and changes of tumor subpopulations on a genetic, metabolic, and proteomic level, which may result in novel targeted therapies (Balluff et al., 2015).

The ability of MALDI-MSI to reveal inter- and intratumoral biomolecular heterogeneity of histologically contiguous tumors has been shown, specifically in the capacity to distinguish different types and grades of myxoid sarcomas (Willems et al., 2010). By applying hierarchical clustering to a gastric cancer MALDI-MSI dataset, it has been demonstrated the different histological regions could be distinguished solely on the basis of their protein and peptide expression profiles (Deininger, Ebert, Futterer, Gerhard, & Rocken, 2008). Ion mobility separation combined with MALDI-MSI has been used to classify prostate cancer TMAs and has identified a number of proteins, including type I collagen and tumor necrosis factor receptor, directly from the tissue that could discriminate different tumor classes (Djidja et al., 2010). Low grade urothelial neoplasia could be separated from high grade urothelial neoplasia with an overall cross validation rate of 97.18% upon analysis of peptide MSI data (Oezdemir et al., 2012). Likewise, based on protein profiling, a grading system for meningioma was developed (Agar et al., 2010). Proteomic signatures associated with breast cancer-activated stromal tissues have been identified by MSI, and hierarchical clustering of the proteomic signals could be used to distinguish the activated intratumoral stroma from the quiescent extratumoral stroma (Dekker et al., 2014). High grade and low grade glioma can also be distinguished by MALDI-MSI (Chaurand et al., 2004).

2.7 Practical Considerations for Proteolytic Peptide MSI: Sample Preparation

MSI of proteolytic peptides in cancer is frequently performed on fresh frozen or FFPE tissues; each sample type has unique advantages and limitations with regards to MSI. The protein component of fresh tissues is easily accessible, especially when compared to FFPE tissues, due to a lack of chemical fixation. Hence, no retrieval steps are required prior to the proteolytic digestion of fresh frozen samples. A disadvantage of fresh frozen tissues, however, is that they require rapid freezing upon collection and storage at extremely low temperatures to inhibit endogenous enzymatic degradation (Fentz, Zornig, Juhl, & David, 2004). Fresh tissues also require solvent washing to remove lipids and other biomolecules that may compete for ionization and interrupt the detection of peptides. Washing steps must be performed carefully, as extensive washing may cause the loss of soluble proteins

(McDonnell et al., 2010; Seeley, Oppenheimer, Mi, Chaurand, & Caprioli, 2008). Two significant advantages of FFPE samples are that they are widely used in modern clinical practice, meaning very large sample banks have often been developed, and that the fixation process allows for storage of the samples at room temperature for indefinite periods of time without loss of morphological information (Wisztorski et al., 2007). The downfall is that formalin fixation results in the formation of methylene bridges between amino residues that causes protein cross-linking (Metz et al., 2004). This cross-linking makes the proteins inaccessible to proteolysis and must be reversed prior to any further preparation steps. Heat-induced antigen retrieval prior to in situ proteolytic digestion is a widely used method for reversing protein cross-links, which allows for the peptide profiling of FFPE tissues that is comparable to fresh frozen tissue analysis (Casadonte & Caprioli, 2011).

2.8 Practical Considerations for Peptide MSI: Spatial Resolution

Currently, MALDI is the most popular ionization method applied in the field of MSI. The success of analyte ionization in a MALDI experiment relies significantly on the matrix used; the type of matrix applied will impact on the mass range of the detectable ions, the intensity of detection, and the minimum spatial resolution achievable (Lemaire et al., 2006). For peptide MALDI-MSI commonly used matrices include α -cyano-4-hydroxycinnamic acid (CHCA) and 2,5-dihydroxybenzoic acid (DHB) (van Hove, Erika, Smith, & Heeren, 2010). The homogeneity of matrix crystallization is a major limiting factor with regard to the spatial resolution that can be achieved by MALDI-MSI, as larger and nonuniform matrix crystals result in lower resolutions. DHB matrix is prone to producing large, needle-like crystals, making CHCA a more suitable matrix as it commonly forms small, homogeneous crystals resulting in higher image resolution (Schwartz, Reyzer, & Caprioli, 2003). The way in which the matrix is applied also has a significant impact on the spatial resolution, with the application of larger size droplets increasing the likelihood of analyte displacement. Instrumentation has been developed that allows matrix solutions to be sprayed or spotted onto the sample surface in a more homogeneous manner compared to manual application (Aerni, Cornett, & Caprioli, 2006). For example, using a matrix spray device CHCA can be applied to form uniform crystals that allow for spatial resolution peptide imaging of $<25 \mu\text{m}$ (McDonnell et al., 2010; Schuerenberg & Deininger, 2010).

Laser specifications also have a significant impact on the spatial resolution achievable. As opposed to the limitations of matrix crystallization, laser beam resolutions can easily reach less than 10 μm , theoretically allowing for pep-tide imaging at the single cell level (Balluff, Schone, Hofler, & Walch, 2011). However, reducing the size of the laser beam concurrently reduces the yield of ionized analytes. Higher frequency lasers and overlapping laser shots can counteract the issue of lower ion yields during detection (Jurchen, Rubakhin, & Sweedler, 2005). Thus, currently matrix is the limiting factor for the spatial resolution achievable in MALDI-MSI.

2.9 Practical Considerations for Peptide MSI: Mass Analysers

The type of mass analyser used for MSI will largely determine the mass resolution and mass range of the detectable ions. TOF mass analysers are commonly coupled to MALDI sources and have high acquisition speeds but typically lower mass resolution (Caprioli et al., 1997). Higher mass accuracy can be achieved through the use of internal or external calibrants. Other commonly used mass analysers include FT-ICR and Orbitraps; these instruments have significantly higher mass accuracy and resolution (Taban et al., 2007).

Internal or external calibrants can be used to improve the mass accuracy of acquired spectra during or after data acquisition (Gobom et al., 2002). Calibrants are often comprised of a small number of specific analytes with known masses that span a specific mass range. Within this mass range, the use of calibrants can significantly increase the mass accuracy of the detected analytes. However, the mass error of any analyte molecules that fall outside the mass range of the calibrants cannot be corrected (Coombes, Koomen, Baggerly, Morris, & Kobayashi, 2005).

2.10 Practical Considerations for Peptide MSI: Identification

Currently, MALDI-MSI enables the discrimination of heterogeneous tis-sue types, but does not allow for the direct identification of the peptide sequences. During data acquisition the intact mass, or the m/z , of the detected peptides is recorded. This allows peptide mass fingerprinting (PMF) to be performed, a process where the intact peptide masses are matched back to a database containing the in silico digested proteome or proteomes of specific species (Pappin, Hojrup, & Bleasby, 1993). Due to a lack of peptide sequence information, often PMF can provide a list of potential peptide identifications but is not able to provide definitive

identifications for those peptides with similar masses. However, the higher the mass accuracy of the instrument used the more likely it is a definitive identification will be gained (Horn, Peters, Klock, Meyers, & Brock, 2004). The use of complementary MS techniques, such as matching data to peptides sequenced by traditional liquid chromatography electrospray ionization tandem mass spectrometry (LC-ESI-MS/MS) or by in situ tandem mass spectrometry (MALDI-MS/MS), can help clarify peptide sequence identifications (Lemaire, Desmons, et al., 2007). However, there can be significant difficulties associated with these options also. Multiple sequence matches are often encountered when matching MSI m/z values back to LC-ESI-MS/MS data obtained from the same sample. Generating high quality in situ MS/MS spectrums is often challenging due to the issue that acquisition of very complex peptide mass spectra directly off tissue results in poor fragmentation and high MS/MS complexity, both of which limit direct peptide sequencing from tissues (Gustafsson et al., 2012).



3. LIPID MSI IN CANCER RESEARCH

3.1 Profiling Lipids in Cancer by DESI-MSI

The soft ionization technique of DESI has been developed for the MSI of small molecules and lipids. DESI uses highly charged solvent droplets traveling at high velocities for analyte ionization in an ambient atmosphere. An advantage of DESI for the analysis of lipids and small molecules is that no sample preparation steps are required, unlike MALDI where matrix deposition is a necessity. A further advantage is that a DESI source can be coupled to most standard mass analysers, such as a FT-ICR, Orbitrap, Ion Trap, or a TOF.

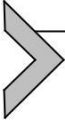
In practice, DESI-MSI has been applied to the study of human cancers for the discrimination of tumor subtypes and grades, as well as for the identification of tumor margins (Calligaris et al., 2014; Eberlin et al., 2014). One particular application used DESI-MSI to generate lipid profiles for the classification of human brain tumors (Eberlin et al., 2012). This study was able to classify the subtype, grade, and tumor concentration of 36 human glioma samples via lipidomics imaging in agreement with the histopathology diagnoses (Eberlin et al., 2012). Lipidomic analysis by DESI-MSI has identified the phospholipids phosphatidylserine (PS), phosphatidylinositol (PI), and phosphatidylethanolamine as biomarkers for distinguishing healthy tissue

from benign and malignant tumor tissues (Abbassi-Ghadi et al., 2014; Dill et al., 2011, 2009; Eberlin et al., 2012).

Discriminatory lipid signatures between cancerous and normal breast tissue have been detected by DESI-MSI (Calligaris et al., 2014), with the delineation of tumor margins possible through the analysis of PI (18:0/20:4). PI (18:0/20:4) has been shown to be abundant at the tumor center and tumor edge, whereas it was absent or weak in normal tissues. This lipid sharply stratifies the tumor margin in agreement the histopathological staining. Using DESI-MSI, another study found PS (20:4/18:0) and PI (18:0/20:4) are significantly lower in concentration in primary tumor tissues and LNMs when compared to normal lymph node tissues (Abbassi-Ghadi et al., 2014). The same lipid, PI (18:0/20:4), was found to be a biomarker for distinguishing benign and malignant breast tumors (Yang et al., 2015). Collectively, the discussed research shows MSI lipid profiling of cancer tissues can be used for classifying tumor types, with high specificity in differentiating histopathologic grade, and in the mapping of tumor margins.

3.2 Profiling Lipids in Cancer by SIMS-MSI

A less popular ionization method for MSI in the lipidomics field is static SIMS. Generally, a static SIMS source is coupled to a TOF (or QTOF) instrument, and is particularly suitable for the analysis of intact molecules such as lipids and metabolites. It uses a beam of energetic primary ions with either monatomic source, such as Cs^+ and Ga^+ for limited mass range of low hundreds Daltons, or cluster ions such as SF_5^+ , Bi_3^+ , and Au_3^+ that have extended the mass range to a couple of thousands Daltons (Lanni, Rubakhin, & Sweedler, 2012). The potential of SIMS-TOF imaging for lipidomics has been shown in rat brain sections, a well-established model system for MSI (Benabdellah et al., 2010; Passarelli & Winograd, 2011; Sjovall, Lausmaa, & Johansson, 2004; Sjovall, Lausmaa, Nygren, Carlsson, & Malmberg, 2003). In the field of cancer lipidomics, it is frequently used in cellular imaging, where single cells or a population of cells are isolated after drug treatment for the characterisation of molecules on the cell surface. For example, lipid composition analysis of individual human breast cancer stem cells (CSCs) reported significantly lower expression levels of palmitoleic acids FA (16:1) as compared to nonstem cancer cells (NSCCs), and is thought to have been successfully characterized from complex clinical specimens using TOF-SIMS (Waki et al., 2014).



4. GLYCAN MSI IN CANCER RESEARCH

Glycosylation is the enzymatic process where oligosaccharides, polysaccharides, and carbohydrates (i.e., glycans) are attached to proteins, lipids, or other organic molecules (Ohtsubo & Marth, 2006). In recent years, the word “glycomics” has emerged to describe the study of glycan structures from an organism’s “glycome.” The mammalian glycome repertoire is comprised of 10 known monosaccharides. These monosaccharides include xylose (Xyl), glucose (Glc), galactose (Gal), mannose (Man), *N*-acetylglucosamine (GlcNAc), *N*-acetylgalactosamine (GalNAc), fucose (Fuc), glucuronic acid (GlcA), iduronic acid (IdoA), and *N*-acetylneuraminic acid (NeuAc or Neu5Ac), a sialic acid (Wuhrer, Deelder, & van der Burgt, 2011). Glycan complexity arises from variation in expression of specific glycosyltransferases, resulting in a diversity of monosaccharide arrangements. Furthermore, modifications such as sulfation, acetylation, or phosphorylation increase the complexity of glycosylation.

The major type of glycosylation is protein glycosylation, where glycans are attached to asparagine residues by their amine group (*N*-linked) or at serine/threonine residues by their hydroxyl group (*O*-linked) (North, Hitchen, Haslam, & Dell, 2009). Protein glycosylation is an important PTM which has relevance in many biological processes such as cell signaling, immune responses, extracellular interaction, and cell adhesion (Varki, 1993). In the tumor microenvironment, aberrant protein glycosylation such as the expression of truncated glycans have been well described in various cancers (Dube & Bertozzi, 2005). These structures may resemble glycomic “fingerprints” which discriminate between healthy and cancerous tissues or potentially discriminate between various cancer subtypes (Abbott et al., 2010).

One of the most common glycosylation changes in various cancers is an increase in branching of *N*-glycans, where large tetra-antennary structures are formed by the expression of *N*-acetylglucosaminyltransferase V (GnT-V) (Lau & Dennis, 2008). The presence of increased branching antennas creates additional sites for the addition of NeuAc by sialyltransferases in various cancers (Bull et al., 2013). Likewise, terminal modifications on glycan structures such as fucosylation on the cancer cell surface can also give rise to the presence of Lewis and sialyl Lewis antigens (sialyl Lea; [Neu5Ac α 2-3Gal β 1-3(Fuca1-4)GlcNAc β] and sialyl Lex; [Neu5Ac α 2-3Gal β 1-4(Fuca1-3)

GlcNAc β]) which have been shown to correlate with tumor progression and metastasis (Nakagoe et al., 2000). It is evident that aberrant glycosylation is indeed a key event in metastasis and therefore the discovery of cancer-specific protein glycosylation markers would be beneficial in the staging and treatment of patients (Drake et al., 2010).

As glycomics gains recognition in this postgenomics era, MS-based methodologies are becoming indispensable and routinely used for the reliable profiling of glycans from clinical samples. Glycan MSI is a recent MS-based development which allows the visualization of the tissue-specific spatial distribution of glycans. *N*-glycans have been the most comprehensively studied type of protein glycosylation, as they can be easily released from proteins by enzymatic cleavage using PNGase F (Jensen, Karlsson, Kolarich, & Packer, 2012). The majority of these studies have applied optimized *N*-glycan MALDI-MSI methods to FFPE tissues, with the most recent focus on various cancer tissues.

One of the first *N*-glycan MALDI-MSI methods to emerge was published in 2013 (Powers et al., 2013). This proof-of-principle paper described the measurement of *N*-glycans by MALDI-MSI across fresh frozen mouse brain tissue. The *m/z* values from the sum spectrum were assigned to *N*-glycans based on further MS structural analysis, for example, high-performance liquid chromatography (HPLC)-MS. The authors concluded that this new approach could lead to novel disease-related targets for biomarker and therapeutic applications. Subsequently, *N*-glycan MALDI-MSI has been successfully applied to the analysis of glioblastoma tumor xenografts compared to normal brain tissues (Toghi Eshghi et al., 2014), where it was found specific *N*-glycans associated with distinct tissue regions. *N*-glycan imaging of FFPE pancreatic and prostate cancers, and a human hepatocellular carcinomas in TMAs found tumor and nontumor regions could be distinguished in the TMA format, enabling high-throughput analysis (Powers et al., 2014).

The use of complimentary MS methods, such as liquid chromatography tandem MS (LC-MS/MS) with MALDI-TOF-MSI, have been developed to enable the mapping of tissue-specific *N*-glycans at high resolution (Gustafsson et al., 2015). The application of these techniques has resulted in several interesting findings. A panel of over 30 *N*-glycans has been detected from FFPE human hepatocellular carcinoma tissues (Powers, Holst, Wuhrer, Mehta, & Drake, 2015), from which the *N*-glycans were extracted and the sialylated species were stabilized by an off-tissue ethylation reaction. *N*-glycan sialylation linkage-specificity was further found to

correlate with the different tissue types analyzed. A novel method for the analysis of *N*-glycan sialylated species (i.e., α 2–3 and α 2–6) by MALDI-MSI in colon carcinoma found sialylated *N*-glycans with α 2–3 linkage were observed in stroma, tumor, and necrotic regions, while sialylated *N*-glycans with α 2–6 linkage were observed in necrotic, collagen-rich, and red blood cell regions (Holst et al., 2016).

The analysis of FFPE stage III ovarian cancer tissues found high mannose structure (Man5 + Man3GlcNAc2) in the tumor regions, while triantennary complex structures (Hex3HexNAc3Deoxyhexose1 + Man3GlcNAc2) were observed in the stromal regions (Fig. 3). This observation was consistent between not only the patients investigated, but also between each *N*-glycan family. The tissue analyzed in the study had been annotated by a pathologist, and it was found specific glycan structures were differentially detected in specific tissue regions, such as tumor, stroma, and adipose tissue.

In summary, *N*-glycan MALDI-MSI has developed immensely in recent times, with improvements in areas such as sensitivity and mass accuracy,

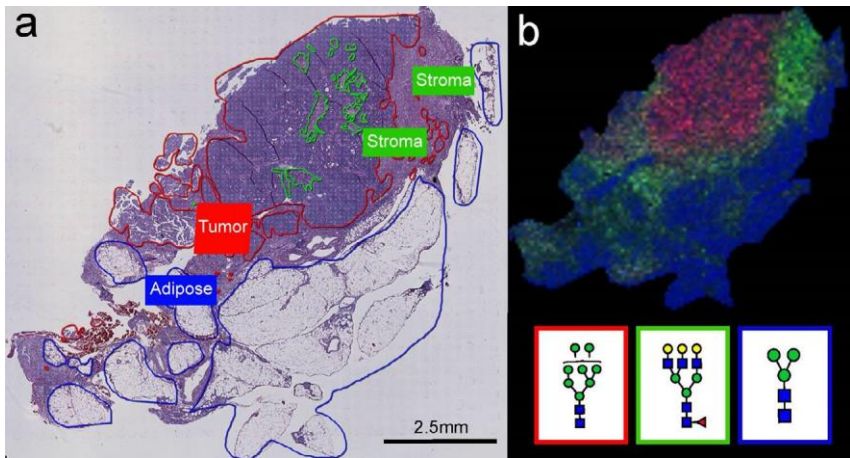
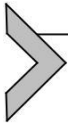


Fig. 3 Glycan analysis of ovarian cancer. The formalin-fixed paraffin-embedded stage III ovarian cancer section was treated with antigen retrieval prior to printing of 15 nL/spot dialyzed PNGase F with 250 μ m spacing. 2,5-DHB (20 mg/mL) was sprayed onto the sections and MS spectra were acquired by oversampling at 100 μ m intervals using a MALDI-TOF/TOF MS instrument. (A) Haematoxylin and eosin stain of the ovarian cancer section with tumor (red), stroma (green), and adipose (blue) regions annotated by a pathologist. (B) An ion intensity map of m/z 1743.7 (red), m/z 2174.9 (green), and m/z 933.3 (blue) on the ovarian cancer section. Yellow circle, galactose (Gal); green circle, mannose (Man); blue square, *N*-acetylglucosamine (GlcNAc); red triangle, fucose (Fuc).

compositional analysis by complementary techniques (i.e., LC-MS/MS and lectin histochemistry staining), and identification of linkage-specific sialylated species by in situ derivatization methods. However, further work in the field is required to properly answer clinical questions and discover cancer-specific markers. TMAs have not yet been fully utilized in *N*-glycan MSI experiments, but offer promise in providing researchers and clinicians with high-throughput data for analysis.



5. DRUG IMAGING IN CANCER RESEARCH

Quantification of drugs and their metabolites is crucial in oncology where drug distribution within the tumor tissue is thought to play a pivotal role in response to therapy and could partly explain the variable response rates observed among patients with similar tumor types (Minchinton & Tannock, 2006). Traditionally, autoradiography has been used to visualize the localization of a drug. However, this technique suffers from some significant limitations. One of them is that the synthesis of the radiolabeled drug is an expensive and time-consuming process. Second, the technique does not provide information on the molecular structure. Hence, metabolites either cannot be distinguished from the parent drug or are not detected if the radiolabel is lost in a metabolic process (Kertesz et al., 2008). The other clinically used noninvasive drug imaging techniques are positron emission tomography and MRI. These techniques can provide information on the drug distribution but suffers from the limitation of low spatial resolution. Due to the relatively simple sample preparation steps required for MSI the technique has rapidly emerged as an alternative to the conventional methods of analysis. MSI allows detailed distribution analysis of the parent drug and its metabolites in a single experiment and without any labeling of the targeted compound in contrast to conventional immunohistochemical methods. Such drug characterization in situ, by both spatial and temporal behaviors within tissue compartments, provides a new understanding of the dynamic processes impacting drug uptake and metabolism at the local sites targeted by a drug therapy (Kwon et al., 2015). Multiple MSI techniques including MALDI-MSI, SIMS, and nanostructure initiator mass spectrometry (NIMS) have been used to analyze the distribution of the drug and metabolites. However, MALDI-MSI is the most frequently used method for looking at anticancer drug distribution in tumor samples.

5.1 MALDI-MSI on Tissue Sections

MALDI-MSI was used for the first time in 2003 to directly analyze and image pharmaceutical compounds in intact tissues (Reyzer, Hsieh, Ng, Korfmacher, & Caprioli, 2003). From then, the technique has been applied to the imaging of a number of drugs. Prideaux et al. applied MALDI-MRM-MSI to visualize the distribution of the second line tuberculosis drug moxifloxacin at a range of time points after dosing in tuberculosis-infected rabbits, which was further validated by quantitative LC-MS/MS of lung and granuloma extracts from adjacent biopsies taken from the same animals (Prideaux et al., 2011). Drug distribution within the granulomas was observed to be inhomogeneous, and very low levels were observed in the caseum in comparison to the cellular granuloma regions (Prideaux et al., 2011). Fehniger et al. measured the occurrence of inhaled bronchodilator, ipratropium, within human bronchial biopsies obtained by fiber optic bronchoscopy shortly after dosing exposure and showed the drug is rapidly absorbed into the airway wall (Fehniger et al., 2011). Nilson et al. provided the first evidence that compounds administered by inhaled delivery at standard pharmacological dosage can be quantitatively detected by MALDI-MSI with accuracy and precision (Nilsson et al., 2010). The distribution of the inhaled drug tiotropium was tracked and quantified in the lungs of dosed rats and a concentration gradient (80 fmol–5 pmol) away from the central airways into the lung parenchyma and pleura was observed (Nilsson et al., 2010). Hsieh et al. visualized the spatial distribution of astemizole (withdrawn in most countries due to its side effects) and its primary metabolite in rat brain tissues and showed that the drug alone is likely to be responsible for the associated central nervous system side effects upon elevated exposure (Hsieh, Li, & Korfmacher, 2010). Using MALDI-MSI the specific distribution of unlabeled chloroquine was examined in the retinas of rats and was found to be similar to auto-radiograms results reported previously (Yamada, Hidefumi, Shion, Oshikata, & Haramaki, 2011).

Atkinson et al. showed the distribution of the bioreductive anticancer drug AQ4N (banoxatrone), its active metabolite AQ4, and ATP in treated human tumor xenografts (Atkinson, Loadman, Sutton, Patterson, & Clench, 2007). The distribution of ATP was found similar to that of AQ4N, i.e., in regions of abundant ATP there was no evidence of conversion of AQ4N into AQ4, indicating that the cytotoxic metabolite AQ4 is confined to hypoxic regions of the tumor as intended (Atkinson et al., 2007). Using

MALDI-FT-ICR, Cornett et al. imaged the antitumor drug imatinib and two of its metabolites from a mouse brain glioma and showed the metabolites to be more abundant in tumor region compared to normal, which is consistent with other imaging studies of the drug (Cornett, Frappier, & Caprioli, 2008). In order to better understand the penetration of the anti-cancer drug oxaliplatin, MALDI-MSI of tissue sections from treated rat kidneys was performed and it was observed that the drug and its metabolites were localized exclusively in the kidney cortex, suggesting the drug did not penetrate deeply into the organ (Bouslimani, Bec, Glueckmann, Hirtz, & Larroque, 2010). Sugihara et al. demonstrated the first data on the localization of personalized medicine (vemurafenib) within tumor compartments of malignant melanoma (MM). In a proof-of-concept in vitro study the overexpression and localization of the drug in the MM was shown using MS fragment ion signatures (Sugihara et al., 2014). Using MALDI-MSI, it has been shown the drug irinotecan reaches tumors mainly through microvessels whereas the conversion of the drug into its active form SN-38 in tumors of colorectal cancer was poor compared to normal tissue (Buck et al., 2015). The distribution of tamoxifen in both ER-positive and ER-negative breast cancer tumor tissues as analyzed by MALDI-MSI detected the drug at significantly lower intensities in tumor cells compared with stroma in ER-negative samples (Vegvári et al., 2016). Aikawa et al. employed a quantitative MSI method (a combination of MALDI-MSI and LC-MS/MS) in a preclinical mouse model to evaluate the intrabrain distribution of an anticancer drug (Aikawa et al., 2016). While no differences were observed between the mice for the drug concentration, diffuse drug distribution was found in the brain of the knockout mice vs wild mice (Aikawa et al., 2016).

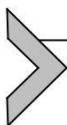
To remove the background signals from matrix degradation observed in MALDI-MSI, the method nanoparticle-assisted laser desorption ionization (n-PALDI) was developed which utilises nanoparticles as matrixes. It was found the protocol could be used to investigate the distribution of anticancer agents in primary tumors and in metastasis, to ascertain whether resistance is related to inadequate drug penetration in poorly vascularized parts of the tumor (Morosi et al., 2013). Using the n-PALDI protocol, the different distribution of paclitaxel in tumor and normal tissues was visualized and related to the dosage-schedules and pathological features of the tumors (Morosi et al., 2013).

5.2 MALDI-MSI on Whole Body Sections

Rohner et al. first demonstrated the MALDI-MSI of drugs in whole body animal sections in 2005 (Rohner, Staab, & Stoeckli, 2005). Since then, a wide range of drugs have been imaged in whole body animal sections, allowing the label-free tracking of both endogenous and exogenous compounds with spatial resolution and molecular specificity (Khatib-Shahidi, Andersson, Herman, Gillespie, & Caprioli, 2006). MALDI-MSI has been used to simultaneously detect drugs and their individual metabolite distributions at various time points across whole body tissue sections (Khatib-Shahidi et al., 2006). Stoeckli et al. measured the distribution of a ^{14}C labeled compound (dosed intratracheally) in whole rat tissue sections using MALDI-MSI and whole body autoradiography (WBA) which displayed good quantitative agreement between both techniques (Stoeckli, Staab, & Schweitzer, 2007). Trim et al. compared the distribution of vinblastine within whole body sections using MALDI-MSI and WBA which displayed MALDI-MSI to be advantageous by separating the drug from an endogenous isobaric lipid (Trim et al., 2008).

5.3 MALDI-MSI on 3D Tissue Cultures

Liu et al. applied MALDI-MSI to the analysis of 3D spheroids in order to assess the distribution of pharmaceuticals and their metabolites. As a proof-of-concept study, MALDI-MSI was applied to in HCT 116 colon carcinoma multicellular spheroids to analyze the distribution of irinotecan, showing the time-dependent penetration of the drug and three metabolites (Liu, Weaver, & Hummon, 2013).



6. DATA ANALYSIS

6.1 Spatial Information

The main advantage of MSI over other methods is the access it provides to spatial information. Possibly the most common approach to leveraging the spatial information in MSI data is simply in displaying results as spatial plots. Fig. 4 shows the results of several analyses of such data. These analyses are blind to the spatial information in the data but their results have spatial patterns that can be easily seen when plotted. Plotting such results next to a stained image of the tissue allows for the molecular information in the MSI data

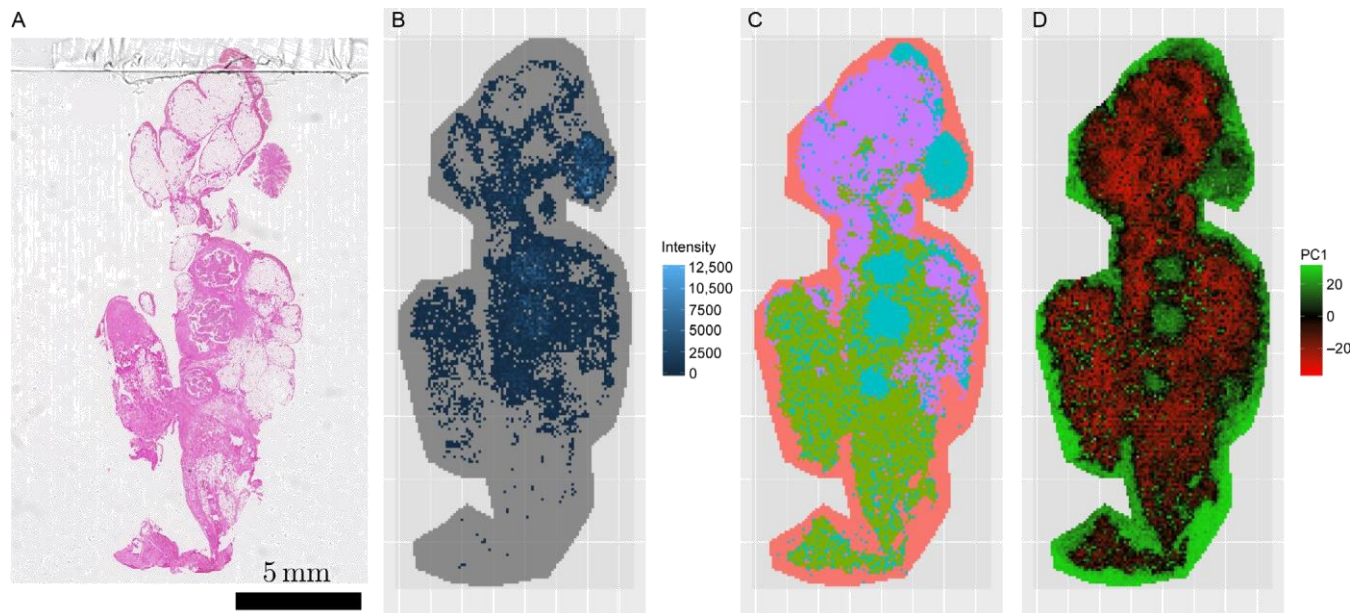


Fig. 4 Results of various analyses of tryptic peptide MALDI-MSI data collected from the same section of tissue. (A) H&E stained section of several primary serous ovarian tumors embedded in surrounding stromal tissue. (B) Intensity of a single peptide peak at $m/z = 1628.8$ confirmed as belong to heterogeneous nuclear ribonucleoprotein A1 which has been shown to be of interest in the past (Chen, Zhang, & Manley, 2010; Lee et al., 2010). (C) Results of 4-means clustering on the log-intensities including all measured m/z values. (D) Results of the first principle component including all measured m/z values on the log-intensities.

to be correlated to the histology of the tissue, thereby allowing biologically relevant use of the spatial information. Such results can even be overlaid directly with stained images (Walch, Rauser, Deininger, & Hofler, 2008), and used to partially automate and aid in histological annotations in an unbiased manner (Cornett et al., 2006). A popular alternative to the k-means clustering shown in Fig. 4 is the so-called semisupervised hierarchical clustering approach applied by Deininger et al. (2008). These semisupervised methods allow the user to manipulate the clustering results until they agree with the observed histology. Jones et al. (2011) demonstrated how multiple approaches to multivariate analysis, such as k-means and principle component analysis (PCA) (Fig. 4), could be combined in an automated manner to produce more reliable partitioning of spatial regions based on the multivariate MSI data.

Spatial information can also be applied to the partitioning of data in a histology driven fashion. To use Fig. 4 as an example, one could use the histology shown in the H&E stain to distinguish different tissue types such as tumor and surrounding stroma, and then by matching the image to the acquired region, partition the spectra into groups representing specific tissue. These groups of spectra could then be compared in an attempt to detect molecular differences between tissue types—this is also a very common approach used in the analysis of MSI data. Using this technique Oppenheimer et al. (2010) demonstrated that histologically healthy tissues within a margin of tumor tissues share molecular characteristics, and hypothesized that this phenomena could be involved in tumor recurrence postresection. Such information could be used by surgeons to identify an appropriate margin to excise the tissue surrounding a tumor.

6.2 Preprocessing: Peak Detection

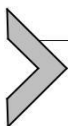
MSI data have a uniquely complicated structure due to the spatial information it contains, and additionally can be computationally challenging due to the sheer amount of information recorded during acquisition. The data therefore require novel approaches to analysis when compared to other, more traditional forms of mass spectrometry (Jones, Deininger, Hogendoorn, Deelder, & McDonnell, 2012). Furthermore, the appropriate approach will vary depending on the application. One approach to addressing the quantity of data is to perform some, preferably computationally fast, data reduction early in the data analysis workflow and then work

with the reduced data. This allows for analyses to be performed quickly, but also means that all further analyses will be affected by the choices made in the data reduction step. The most simplistic approach to data reduction is centroiding—essentially reducing spectra to their local maxima. Centroiding is perhaps the most simplistic approach to peak detection. Essentially centroiding involves reducing the acquired spectra to their local maxima, allowing peaks in the spectra to be identified, information relevant to these peaks to be stored and the remainder of the “noise” to be removed. [Yang, He, and Yu \(2009\)](#) provide a good overview of peak detection in the context of MALDI-MS. Wavelet approaches to peak detection, such as those suggested by [Du, Kibbe, and Lin \(2006\)](#), [Lange, Gropl, Reinert, Kohlbacher, and Hildebrandt \(2006\)](#), show some promise but have not yet made it into mainstream software packages, and so do not currently see much use. Regardless, peak detection prior to further analysis is a useful tool as it can reduce the volume of data by as much as three orders of magnitude. However, care must be taken when interpreting final results; it is important to be aware that all analyses will be affected by any peak detection steps and that a quality control analysis of the data following peak detection should be implemented to ensure its performance.

6.3 Classification of FFPE-TMAs and the Importance of Dimension Reduction

The application of MSI to FFPE-TMAs for classification of various diagnostic and prognostic clinical factors is a particularly promising field of research. The ability to use FFPE tissue allows access to large archives including tissue samples and associated patient meta data ([Hood et al., 2005](#)). The use of TMAs with MSI facilitates the collection of label-free and untargeted mass data from large numbers of patients ([Groseclose et al., 2008](#)), which in turn allows for classification problems to be considered. One of the key obstacles to the classification of such data is that, due to the untargeted nature of MSI, the resulting data are of high-dimensionality. The natural approach to address the dimensionality of such data is to perform some dimension reduction prior to classification. [Mascini et al. \(2015\)](#) proposed the use PCA for dimension reduction prior to classification. PCA is a classical multivariate approach that preserves the maximum amount of variability in the dimension-reduced data. [Winderbaum et al. \(2016\)](#) proposed using a cross correlation analysis (CCA) to rank MSI variables based on their contribution to the highest multivariate correlation to the clinical variable and to reduce the dimension of the data by restricting to only the most highly ranked MSI

variables. Either way, dimension reduction prior to classification is crucial. In order to apply these ideas in clinical practice, large cohort studies and/or clinical trials would need to be carried out to validate the performance of these MS-based classifiers. To date most studies have been exploratory, using small samples of patients as a proof of principle, with a study by [Steurer et al. \(2013\)](#) being a notable exception. Dependent on large scale validation studies, classification of MSI data could potentially be used in the individualisation of treatments, predicting factors such as LNM or potentially even chemotherapy response.



7. CONCLUDING REMARKS

7.1 The Future of MSI: Molecular Pathology

For over 100 years clinical pathology has relied upon a description of morphology by trained specialists for tumor classification and grading. The information that can be gained from such an analyses is limited, however, and is often purely descriptive. During the last decade mass spectrometers have found their way from physics and biochemistry research laboratories into clinical pathology laboratories, bringing together researchers from a wide spectrum of disciplines, such as physics, biochemistry, medicine, pathology, and mathematics. A key feature of MSI is the ability to discern molecular signatures of disease with the additional bonus that the features can be directly related back to the tissue morphology. In the context of clinical oncology, the application of MSI has the potential to shift traditional pathology from descriptive morphological analyses to detailed molecular analyses. As such, the introduction of MSI equipment into pathology laboratories will extend their capabilities and revolutionize management and treatment of cancer.

REFERENCES

- Abbassi-Ghadi, N., Veselkov, K., Kumar, S., Huang, J., Jones, E., Strittmatter, N., et al. (2014). Discrimination of lymph node metastases using desorption electrospray ionisation-mass spectrometry imaging. *Chemical Communications (Cambridge, England)*, 50(28), 3661–3664.
- Abbott, K. L., Lim, J. M., Wells, L., Benigno, B. B., McDonald, J. F., & Pierce, M. (2010). Identification of candidate biomarkers with cancer-specific glycosylation in the tissue and serum of endometrioid ovarian cancer patients by glycoproteomic analysis. *Proteomics*, 10(3), 470–481.
- Aerni, H.-R., Cornett, D. S., & Caprioli, R. M. (2006). Automated acoustic matrix deposition for MALDI sample preparation. *Analytical Chemistry*, 78(3), 827–834.

- Agar, N. Y., Malcolm, J. G., Mohan, V., Yang, H. W., Johnson, M. D., Tannenbaum, A., et al. (2010). Imaging of meningioma progression by matrix-assisted laser desorption ionization time-of-flight mass spectrometry. *Analytical Chemistry*, 82(7), 2621–2625.
- Aichler, M., Elsner, M., Ludyga, N., Feuchtinger, A., Zangen, V., Maier, S. K., et al. (2013). Clinical response to chemotherapy in oesophageal adenocarcinoma patients is linked to defects in mitochondria. *The Journal of Pathology*, 230(4), 410–419.
- Aichler, M., & Walch, A. (2015). MALDI Imaging mass spectrometry: Current frontiers and perspectives in pathology research and practice. *Laboratory Investigation*, 95(4), 422–431.
- Aikawa, H., Hayashi, M., Ryu, S., Yamashita, M., Ohtsuka, N., Nishidate, M., et al. (2016). Visualizing spatial distribution of alectinib in murine brain using quantitative mass spectrometry imaging. *Scientific Reports*, 6, 23749.
- Andersson, M., Andren, P., & Caprioli, R. M. (2010). MALDI imaging and profiling mass spectrometry in neuroproteomics. In O. Alzate (Ed.), *Neuroproteomics*. Boca Raton, FL: CRC Press/Taylor & Francis.
- Andersson, M., Groseclose, M. R., Deutch, A. Y., & Caprioli, R. M. (2008). Imaging mass spectrometry of proteins and peptides: 3D volume reconstruction. *Nature Methods*, 5(1), 101–108.
- Atkinson, S. J., Loadman, P. M., Sutton, C., Patterson, L. H., & Clench, M. R. (2007). Examination of the distribution of the bioreductive drug AQ4N and its active metabolite AQ4 in solid tumours by imaging matrix-assisted laser desorption/ionisation mass spectrometry. *Rapid Communications in Mass Spectrometry*, 21(7), 1271–1276.
- Balluff, B., Elsner, M., Kowarsch, A., Rauser, S., Meding, S., Schuhmacher, C., et al. (2010). Classification of HER2/neu status in gastric cancer using a breast-cancer derived proteomic classifier. *Journal of Proteome Research*, 9(12), 6317–6322.
- Balluff, B., Frese, C. K., Maier, S. K., Schone, C., Kuster, B., Schmitt, M., et al. (2015). De novo discovery of phenotypic intratumour heterogeneity using imaging mass spectrometry. *The Journal of Pathology*, 235(1), 3–13.
- Balluff, B., Rauser, S., Meding, S., Elsner, M., Schone, C., Feuchtinger, A., et al. (2011). MALDI imaging identifies prognostic seven-protein signature of novel tissue markers in intestinal-type gastric cancer. *The American Journal of Pathology*, 179(6), 2720–2729.
- Balluff, B., Schone, C., Hofler, H., & Walch, A. (2011). MALDI imaging mass spectrometry for direct tissue analysis: Technological advancements and recent applications. *Histochemistry and Cell Biology*, 136(3), 227–244.
- Bauer, J. A., Chakravarthy, A. B., Rosenbluth, J. M., Mi, D., Seeley, E. H., De Matos Granja-Ingram, N., et al. (2010). Identification of markers of taxane sensitivity using proteomic and genomic analyses of breast tumors from patients receiving neoadjuvant paclitaxel and radiation. *Clinical Cancer Research*, 16(2), 681–690.
- Benabdellah, F., Seyer, A., Quinton, L., Touboul, D., Brunelle, A., & Laprevote, O. (2010). Mass spectrometry imaging of rat brain sections: Nanomolar sensitivity with MALDI versus nanometer resolution by TOF-SIMS. *Analytical and Bioanalytical Chemistry*, 396(1), 151–162.
- Bodzon-Kulakowska, A., & Suder, P. (2016). Imaging mass spectrometry: Instrumentation, applications, and combination with other visualization techniques. *Mass Spectrometry Reviews*, 35(1), 147–169.
- Bouslimani, A., Bec, N., Glueckmann, M., Hirtz, C., & Larroque, C. (2010). Matrix-assisted laser desorption/ionization imaging mass spectrometry of oxaliplatin derivatives in heated intraoperative chemotherapy (HIPEC)-like treated rat kidney. *Rapid Communications in Mass Spectrometry*, 24(4), 415–421.
- Buck, A., Halbritter, S., Spath, C., Feuchtinger, A., Aichler, M., Zitzelsberger, H., et al. (2015). Distribution and quantification of irinotecan and its active metabolite SN-38

- in colon cancer murine model systems using MALDI MSI. *Analytical and Bioanalytical Chemistry*, 407(8), 2107–2116.
- Bull, C., Boltje, T. J., Wassink, M., de Graaf, A. M., van Delft, F. L., den Brok, M. H., et al. (2013). Targeting aberrant sialylation in cancer cells using a fluorinated sialic acid analog impairs adhesion, migration, and in vivo tumor growth. *Molecular Cancer Therapeutics*, 12(10), 1935–1946.
- Calligaris, D., Caragacianu, D., Liu, X., Norton, I., Thompson, C. J., Richardson, A. L., et al. (2014). Application of desorption electrospray ionization mass spectrometry imaging in breast cancer margin analysis. *Proceedings of the National Academy of Sciences of the United States of America*, 111(42), 15184–15189.
- Caprioli, R. M., Farmer, T. B., & Gile, J. (1997). Molecular imaging of biological samples: Localization of peptides and proteins using MALDI-TOF MS. *Analytical Chemistry*, 69(23), 4751–4760.
- Casadonte, R., & Caprioli, R. M. (2011). Proteomic analysis of formalin-fixed paraffin-embedded tissue by MALDI imaging mass spectrometry. *Nature Protocols*, 6(11), 1695–1709.
- Casadonte, R., Kriegsmann, M., Zweynert, F., Friedrich, K., Bretton, G., Otto, M., et al. (2014). Imaging mass spectrometry to discriminate breast from pancreatic cancer metastasis in formalin-fixed paraffin-embedded tissues. *Proteomics*, 14(7–8), 956–964.
- Cazares, L. H., Troyer, D., Mendrinós, S., Lance, R. A., Nyalwidhe, J. O., Beydoun, H. A., et al. (2009). Imaging mass spectrometry of a specific fragment of mitogen-activated protein kinase/extracellular signal-regulated kinase kinase 2 discriminates cancer from uninvolved prostate tissue. *Clinical Cancer Research*, 15(17), 5541–5551.
- Chaurand, P., Sanders, M. E., Jensen, R. A., & Caprioli, R. M. (2004). Proteomics in diagnostic pathology: Profiling and imaging proteins directly in tissue sections. *The American Journal of Pathology*, 165(4), 1057–1068.
- Chaurand, P., Schwartz, S. A., & Caprioli, R. M. (2004). Assessing protein patterns in disease using imaging mass spectrometry. *Journal of Proteome Research*, 3(2), 245–252.
- Chen, M., Zhang, J., & Manley, J. L. (2010). Turning on a fuel switch of cancer: hnRNP proteins regulate alternative splicing of pyruvate kinase mRNA. *Cancer Research*, 70(22), 8977–8980.
- Cho, Y. T., Su, H., Wu, W. J., Wu, D. C., Hou, M. F., Kuo, C. H., et al. (2015). Biomarker characterization by MALDI-TOF/MS. *Advances in Clinical Chemistry*, 69, 209–254.
- Choi, J. H., Shin, N. R., Moon, H. J., Kwon, C. H., Kim, G. H., Song, G. A., et al. (2012). Identification of S100A8 and S100A9 as negative regulators for lymph node metastasis of gastric adenocarcinoma. *Histology and Histopathology*, 27(11), 1439–1448.
- Coombes, K. R., Koomen, J. M., Baggerly, K. A., Morris, J. S., & Kobayashi, R. (2005). Understanding the characteristics of mass spectrometry data through the use of simulation. *Cancer Informatics*, 1, 41–52.
- Cornett, D. S., Frappier, S. L., & Caprioli, R. M. (2008). MALDI-FTICR imaging mass spectrometry of drugs and metabolites in tissue. *Analytical Chemistry*, 80(14), 5648–5653.
- Cornett, D. S., Mobley, J. A., Dias, E. C., Andersson, M., Arteaga, C. L., Sanders, M. E., et al. (2006). A novel histology-directed strategy for MALDI-MS tissue profiling that improves throughput and cellular specificity in human breast cancer. *Molecular & Cellular Proteomics*, 5(10), 1975–1983.
- Crecelius, A. C., Cornett, D. S., Caprioli, R. M., Williams, B., Dawant, B. M., & Bodenheimer, B. (2005). Three-dimensional visualization of protein expression in mouse brain structures using imaging mass spectrometry. *Journal of the American Society for Mass Spectrometry*, 16(7), 1093–1099.
- de Hoffmann, E., & Stroobant, V. (2007). *Mass spectrometry: Principles and applications* (3rd ed.). England: Wiley.

- Deininger, S.-O., Ebert, M. P., Futterer, A., Gerhard, M., & Rocken, C. (2008). MALDI imaging combined with hierarchical clustering as a new tool for the interpretation of complex human cancers. *Journal of Proteome Research*, 7(12), 5230–5236.
- Dekker, T. J. A., Balluff, B. D., Jones, E. A., Schone, C. D., Schmitt, M., Aubele, M., et al. (2014). Multicenter matrix-assisted laser desorption/ionization mass spectrometry imaging (MALDI MSI) identifies proteomic differences in breast-cancer-associated stroma. *Journal of Proteome Research*, 13(11), 4730–4738.
- Diehl, H. C., Beine, B., Elm, J., Trede, D., Ahrens, M., Eisenacher, M., et al. (2015). The challenge of on-tissue digestion for MALDI MSI—A comparison of different protocols to improve imaging experiments. *Analytical and Bioanalytical Chemistry*, 407(8), 2223–2243.
- Dill, A. L., Eberlin, L. S., Costa, A. B., Zheng, C., Ifa, D. R., Cheng, L., et al. (2011). Multivariate statistical identification of human bladder carcinomas using ambient ionization imaging mass spectrometry. *Chemistry*, 17(10), 2897–2902.
- Dill, A. L., Ifa, D. R., Manicke, N. E., Costa, A. B., Ramos-Vara, J. A., Knapp, D. W., et al. (2009). Lipid profiles of canine invasive transitional cell carcinoma of the urinary bladder and adjacent normal tissue by desorption electrospray ionization imaging mass spectrometry. *Analytical Chemistry*, 81(21), 8758–8764.
- Djidja, M.-C., Claude, E., Snel, M. F., Francese, S., Scriven, P., Carolan, V., et al. (2010). Novel molecular tumour classification using MALDI–mass spectrometry imaging of tissue micro-array. *Analytical and Bioanalytical Chemistry*, 397(2), 587–601.
- Drake, P. M., Cho, W., Li, B., Prakobphol, A., Johansen, E., Anderson, N. L., et al. (2010). Sweetening the pot: adding glycosylation to the biomarker discovery equation. *Clinical Chemistry*, 56(2), 223–236.
- Du, P., Kibbe, W. A., & Lin, S. M. (2006). Improved peak detection in mass spectrum by incorporating continuous wavelet transform-based pattern matching. *Bioinformatics*, 22(17), 2059–2065.
- Dube, D. H., & Bertozzi, C. R. (2005). Glycans in cancer and inflammation—Potential for therapeutics and diagnostics. *Nature Reviews. Drug Discovery*, 4(6), 477–488.
- Eberlin, L. S., Norton, I., Dill, A. L., Golby, A. J., Ligon, K. L., Santagata, S., et al. (2012). Classifying human brain tumors by lipid imaging with mass spectrometry. *Cancer Research*, 72(3), 645–654.
- Eberlin, L. S., Tibshirani, R. J., Zhang, J., Longacre, T. A., Berry, G. J., Bingham, D. B., et al. (2014). Molecular assessment of surgical-resection margins of gastric cancer by mass-spectrometric imaging. *Proceedings of the National Academy of Sciences of the United States of America*, 111(7), 2436–2441.
- Elsner, M., Rauser, S., Maier, S., Schone, C., Balluff, B., Meding, S., et al. (2012). MALDI imaging mass spectrometry reveals COX7A2, TAGLN2 and S100-A10 as novel prognostic markers in Barrett's adenocarcinoma. *Journal of Proteomics*, 75(15), 4693–4704.
- Fehniger, T. E., Vegvari, A., Rezeli, M., Prikk, K., Ross, P., Dahlback, M., et al. (2011). Direct demonstration of tissue uptake of an inhaled drug: Proof-of-principle study using matrix-assisted laser desorption ionization mass spectrometry imaging. *Analytical Chemistry*, 83(21), 8329–8336.
- Fejzo, M. S., & Slamon, D. J. (2010). Tissue microarrays from frozen tissues-OCT technique. *Methods in Molecular Biology*, 664, 73–80.
- Fentz, J. S., Zornig, C., Juhl, H. H., & David, K. A. (2004). Tissue ischemia time affects gene and protein expression patterns within minutes following surgical tumor excision. *Biotechniques*, 36(6), 1030–1037.
- Fletcher, J. S., Lockyer, N. P., & Vickerman, J. C. (2011). Developments in molecular SIMS depth profiling and 3D imaging of biological systems using polyatomic primary ions. *Mass Spectrometry Reviews*, 30(1), 142–174.

- Fletcher, J. S., Vickerman, J. C., & Winograd, N. (2011). Label free biochemical 2D and 3D imaging using secondary ion mass spectrometry. *Current Opinion in Chemical Biology*, 15(5), 733–740.
- Gemoll, T., Strohkamp, S., Schillo, K., Thorns, C., & Habermann, J. K. (2015). MALDI-imaging reveals thymosin beta-4 as an independent prognostic marker for colorectal cancer. *Oncotarget*, 6(41), 43869–43880.
- Gobom, J., Mueller, M., Egelhofer, V., Theiss, D., Lehrach, H., & Nordhoff, E. (2002). A calibration method that simplifies and improves accurate determination of peptide molecular masses by MALDI-TOF MS. *Analytical Chemistry*, 74(15), 3915–3923.
- Goodwin, R. J. (2012). Sample preparation for mass spectrometry imaging: Small mistakes can lead to big consequences. *Journal of Proteomics*, 75(16), 4893–4911.
- Gorzolka, K., & Walch, A. (2014). MALDI mass spectrometry imaging of formalin-fixed paraffin-embedded tissues in clinical research. *Histology and Histopathology*, 29(11), 1365–1376.
- Groseclose, M. R., Massion, P. P., Chaurand, P., & Caprioli, R. M. (2008). High-throughput proteomic analysis of formalin-fixed paraffin-embedded tissue micro-arrays using MALDI imaging mass spectrometry. *Proteomics*, 8(18), 3715–3724.
- Gruner, B. M., Hahne, H., Mazur, P. K., Trajkovic-Arsic, M., Maier, S., Esposito, I., et al. (2012). MALDI imaging mass spectrometry for in situ proteomic analysis of preneoplastic lesions in pancreatic cancer. *PLoS One*, 7(6), e39424.
- Gustafsson, O. J., Briggs, M. T., Condina, M. R., Winderbaum, L. J., Pelzing, M., McColl, S. R., et al. (2015). MALDI imaging mass spectrometry of *N*-linked glycans on formalin-fixed paraffin-embedded murine kidney. *Analytical and Bioanalytical Chemistry*, 407(8), 2127–2139.
- Gustafsson, J. O., Eddes, J. S., Meding, S., Koudelka, T., Oehler, M. K., McColl, S. R., et al. (2012). Internal calibrants allow high accuracy peptide matching between MALDI imaging MS and LC-MS/MS. *Journal of Proteomics*, 75(16), 5093–5105.
- Gustafsson, O. J., Eddes, J. S., Meding, S., McColl, S. R., Oehler, M. K., & Hoffmann, P. (2013). Matrix-assisted laser desorption/ionization imaging protocol for in situ characterization of tryptic peptide identity and distribution in formalin-fixed tissue. *Rapid Communications in Mass Spectrometry*, 27(6), 655–670.
- Han, E. C., Lee, Y.-S., Liao, W.-S., Liu, Y.-C., Liao, H.-Y., & Jeng, L.-B. (2011). Direct tissue analysis by MALDI-TOF mass spectrometry in human hepatocellular carcinoma. *Clinica Chimica Acta*, 412(3–4), 230–239.
- Hardesty, W. M., Kelley, M. C., Mi, D., Low, R. L., & Caprioli, R. M. (2011). Protein signatures for survival and recurrence in metastatic melanoma. *Journal of Proteomics*, 74(7), 1002–1014.
- Holst, S., Heijs, B., de Haan, N., van Zeijl, R. J., Briare-de Bruijn, I. H., van Pelt, G. W., et al. (2016). Linkage-specific in situ sialic acid derivatization for *N*-glycan mass spectrometry imaging of formalin-fixed paraffin-embedded tissues. *Analytical Chemistry*, 88(11), 5904–5913.
- Hood, B. L., Darfler, M. M., Guiel, T. G., Furusato, B., Lucas, D. A., Ringeisen, B. R., et al. (2005). Proteomic analysis of formalin-fixed prostate cancer tissue. *Molecular & Cellular Proteomics*, 4(11), 1741–1753.
- Horn, D. M., Peters, E. C., Klock, H., Meyers, A., & Brock, A. (2004). Improved protein identification using automated high mass measurement accuracy MALDI FT-ICR MS peptide mass fingerprinting. *International Journal of Mass Spectrometry*, 238(2), 189–196.
- Hsieh, Y., Li, F., & Korfmacher, W. A. (2010). Mapping pharmaceuticals in rat brain sections using MALDI imaging mass spectrometry. *Methods in Molecular Biology*, 656, 147–158.
- Hsu, C. C., & Dorrestein, P. C. (2015). Visualizing life with ambient mass spectrometry. *Current Opinion in Biotechnology*, 31, 24–34.

- Jensen, P. H., Karlsson, N. G., Kolarich, D., & Packer, N. H. (2012). Structural analysis of *N*- and *O*-glycans released from glycoproteins. *Nature Protocols*, 7(7), 1299–1310.
- Jones, E. A., Deininger, S.-O., Hogendoorn, P. C., Deelder, A. M., & McDonnell, L. A. (2012). Imaging mass spectrometry statistical analysis. *Journal of Proteomics*, 75(16), 4962–4989.
- Jones, E. A., van Remoortere, A., van Zeijl, R. J. M., Hogendoorn, P. C. W., Bovee, J. V. M. G., Deelder, A. M., et al. (2011). Multiple statistical analysis techniques corroborate intratumor heterogeneity in imaging mass spectrometry datasets of myxofibrosarcoma. *PLoS One*, 6(9), e24913.
- Jurchen, J. C., Rubakhin, S. S., & Sweedler, J. V. (2005). MALDI-MS imaging of features smaller than the size of the laser beam. *Journal of the American Society for Mass Spectrometry*, 16(10), 1654–1659.
- Kaletas, B. K., van der Wiel, I. M., Stauber, J., Guzel, C., Kros, J. M., Luiders, T. M., et al. (2009). Sample preparation issues for tissue imaging by imaging MS. *Proteomics*, 9(10), 2622–2633.
- Kang, S., Shim, H. S., Lee, J. S., Kim, D. S., Kim, H. Y., Hong, S. H., et al. (2010). Molecular proteomics imaging of tumor interfaces by mass spectrometry. *Journal of Proteome Research*, 9(2), 1157–1164.
- Kertesz, V., Berkel, V., Gary, J., Vavrek, M., Koeplinger, K. A., Schneider, B. B., et al. (2008). Comparison of drug distribution images from whole-body thin tissue sections obtained using desorption electrospray ionization tandem mass spectrometry and autoradiography. *Analytical Chemistry*, 80(13), 5168–5177.
- Khatib-Shahidi, S., Andersson, M., Herman, J. L., Gillespie, T. A., & Caprioli, R. M. (2006). Direct molecular analysis of whole-body animal tissue sections by imaging MALDI mass spectrometry. *Analytical Chemistry*, 78(18), 6448–6456.
- Kim, H. K., Reyzer, M. L., Choi, I. J., Kim, C. G., Kim, H. S., Oshima, A., et al. (2010). Gastric cancer-specific protein profile identified using endoscopic biopsy samples via MALDI mass spectrometry. *Journal of Proteome Research*, 9(8), 4123–4130.
- Klerk, L. A., Maarten Altelaar, A. F., Froesch, M., McDonnell, L. A., & Heeren, R. M. A. (2009). Fast and automated large-area imaging MALDI mass spectrometry in microprobe and microscope mode. *International Journal of Mass Spectrometry*, 285(1–2), 19–25.
- Kriegsmann, J., Kriegsmann, M., & Casadonte, R. (2015). MALDI TOF imaging mass spectrometry in clinical pathology: A valuable tool for cancer diagnostics (review). *International Journal of Oncology*, 46(3), 893–906.
- Kwon, H. J., Kim, Y., Sugihara, Y., Baldetorp, B., Welinder, C., Watanabe, K., et al. (2015). Drug compound characterization by mass spectrometry imaging in cancer tissue. *Archives of Pharmacal Research*, 38(9), 1718–1727.
- Lange, E., Gropl, C., Reinert, K., Kohlbacher, O., & Hildebrandt, A. (2006). High-accuracy peak picking of proteomics data using wavelet techniques. *Pacific Symposium on Biocomputing*, 11, 243–254. Paper presented at the Pacific Symposium on Biocomputing.
- Lanni, E. J., Rubakhin, S. S., & Sweedler, J. V. (2012). Mass spectrometry imaging and profiling of single cells. *Journal of Proteomics*, 75(16), 5036–5051.
- Lau, K. S., & Dennis, J. W. (2008). *N*-Glycans in cancer progression. *Glycobiology*, 18(10), 750–760.
- Le Faouder, J., Laouirem, S., Chapelle, M., Albuquerque, M., Belghiti, J., Degos, F., et al. (2011). Imaging mass spectrometry provides fingerprints for distinguishing hepatocellular carcinoma from cirrhosis. *Journal of Proteome Research*, 10(8), 3755–3765.
- Lee, D. H., Chung, K., Song, J.-A., Kim, T.-h., Kang, H., Huh, J. H., et al. (2010). Proteomic identification of paclitaxel-resistance associated hnRNP A2 and GDI 2 proteins in human ovarian cancer cells. *Journal of Proteome Research*, 9(11), 5668–5676.
- Lemaire, R., Ait Menguellet, S., Stauber, J., Marchaudon, V., Lucot, J.-P., Collinet, P., et al. (2007). Specific MALDI imaging and profiling for biomarker hunting and validation: Fragment of the 11S proteasome activator complex, Reg alpha fragment, is a new potential ovary cancer biomarker. *Journal of Proteome Research*, 6(11), 4127–4134.

- Lemaire, R., Desmons, A., Tabet, J. C., Day, R., Salzet, M., & Fournier, I. (2007). Direct analysis and MALDI imaging of formalin-fixed, paraffin-embedded tissue sections. *Journal of Proteome Research*, 6(4), 1295–1305.
- Lemaire, R., Tabet, J. C., Ducoroy, P., Hendra, J. B., Salzet, M., & Fournier, I. (2006). Solid ionic matrixes for direct tissue analysis and MALDI imaging. *Analytical Chemistry*, 78(3), 809–819.
- Liu, X., Weaver, E. M., & Hummon, A. B. (2013). Evaluation of therapeutics in three-dimensional cell culture systems by MALDI imaging mass spectrometry. *Analytical Chemistry*, 85(13), 6295–6302.
- Luxembourg, S. L., Mize, T. H., McDonnell, L. A., & Heeren, R. M. (2004). High-spatial resolution mass spectrometric imaging of peptide and protein distributions on a surface. *Analytical Chemistry*, 76(18), 5339–5344.
- Mascini, N. E., Eijkel, G. B., ter Brugge, P., Jonkers, J., Wesseling, J., & Heeren, R. M. A. (2015). The use of mass spectrometry imaging to predict treatment response of patient-derived xenograft models of triple-negative breast cancer. *Journal of Proteome Research*, 14(2), 1069–1075.
- McDonnell, L. A., Corthals, G. L., Willems, S. M., van Remoortere, A., van Zeijl, R. J. M., & Deelder, A. M. (2010). Peptide and protein imaging mass spectrometry in cancer research. *Journal of Proteomics*, 73(10), 1921–1944.
- Metz, B., Kersten, G. F. A., Hoogerhout, P., Brugghe, H. F., Timmermans, H. A. M., De Jong, A. D., et al. (2004). Identification of formaldehyde-induced modifications in proteins reactions with model peptides. *Journal of Biological Chemistry*, 279(8), 6235–6243.
- Minchinton, A. I., & Tannock, I. F. (2006). Drug penetration in solid tumours. *Nature Reviews. Cancer*, 6(8), 583–592. <http://dx.doi.org/10.1038/nrc1893>.
- Mittal, P., Klingler-Hoffmann, M., Arentz, G., Winderbaum, L., Lokman, N. A., Zhang, C., et al. (2016). Maldi imaging of primary endometrial cancers reveals proteins associated with lymph node metastasis. *Proteomics*, 16, 1793–1801.
- Mittal, P., Klingler-Hoffmann, M., Arentz, G., Zhang, C., Kaur, G., Oehler, M. K., et al. (2016). Proteomics of endometrial cancer diagnosis, treatment, and prognosis. *Proteomics. Clinical Applications*, 10(3), 217–229.
- Morita, Y., Ikegami, K., Goto-Inoue, N., Hayasaka, T., Zaima, N., Tanaka, H., et al. (2010). Imaging mass spectrometry of gastric carcinoma in formalin-fixed paraffin-embedded tissue microarray. *Cancer Science*, 101(1), 267–273.
- Morosi, L., Spinelli, P., Zucchetti, M., Pretto, F., Carrà, A., D’Incalci, M., et al. (2013). Determination of paclitaxel distribution in solid tumors by nano-particle assisted laser desorption ionization mass spectrometry imaging. *PLoS One*, 8(8), e72532.
- Nakagoe, T., Fukushima, K., Nanashima, A., Sawai, T., Tsuji, T., Jibiki, M., et al. (2000). Expression of Lewis(a), sialyl Lewis(a), Lewis(x) and sialyl Lewis(x) antigens as prognostic factors in patients with colorectal cancer. *Canadian Journal of Gastroenterology*, 14(9), 753–760.
- Nilsson, A., Fehniger, T. E., Gustavsson, L., Andersson, M., Kenne, K., Marko-Varga, G., et al. (2010). Fine mapping the spatial distribution and concentration of unlabeled drugs within tissue micro-compartments using imaging mass spectrometry. *PLoS One*, 5(7), e11411.
- Nipp, M., Elsner, M., Balluff, B., Meding, S., Sarioglu, H., Ueffing, M., et al. (2011). S100-A10, thioredoxin, and S100-A6 as biomarkers of papillary thyroid carcinoma with lymph node metastasis identified by MALDI imaging. *Journal of Molecular Medicine*, 90(2), 163–174.
- North, S. J., Hitchen, P. G., Haslam, S. M., & Dell, A. (2009). Mass spectrometry in the analysis of *N*-linked and *O*-linked glycans. *Current Opinion in Structural Biology*, 19(5), 498–506.
- Oezdemir, R. F., Gaisa, N. T., Lindemann-Docter, K., Gostek, S., Weiskirchen, R., Ahrens, M., et al. (2012). Proteomic tissue profiling for the improvement of

- grading of noninvasive papillary urothelial neoplasia. *Clinical Biochemistry*, 45(1–2), 7–11.
- Ohtsubo, K., & Marth, J. D. (2006). Glycosylation in cellular mechanisms of health and disease. *Cell*, 126(5), 855–867.
- Oppenheimer, S. R., Mi, D., Sanders, M. E., & Caprioli, R. M. (2010). Molecular analysis of tumor margins by MALDI mass spectrometry in renal carcinoma. *Journal of Proteome Research*, 9(5), 2182–2190.
- Pagni, F., Mainini, V., Garancini, M., Bono, F., Vanzati, A., Giardini, V., et al. (2015). Proteomics for the diagnosis of thyroid lesions: Preliminary report. *Cytopathology*, 26(5), 318–324.
- Pappin, D. J. C., Hojrup, P., & Bleasby, A. J. (1993). Rapid identification of proteins by peptide-mass fingerprinting. *Current Biology*, 3(6), 327–332.
- Passarelli, M. K., & Winograd, N. (2011). Lipid imaging with time-of-flight secondary ion mass spectrometry (ToF-SIMS). *Biochimica et Biophysica Acta*, 1811(11), 976–990.
- Patel, S. A., Barnes, A., Loftus, N., Martin, R., Sloan, P., Thakker, N., et al. (2009). Imaging mass spectrometry using chemical inkjet printing reveals differential protein expression in human oral squamous cell carcinoma. *Analyst*, 134(2), 301–307. <http://dx.doi.org/10.1039/B812533C>.
- Pavlidis, N., & Pentheroudakis, G. (2016). Cancer of unknown primary site. *The Lancet*, 379(9824), 1428–1435.
- Powers, T. W., Holst, S., Wuhler, M., Mehta, A. S., & Drake, R. R. (2015). Two-dimensional *N*-glycan distribution mapping of hepatocellular carcinoma tissues by MALDI-imaging mass spectrometry. *Biomolecules*, 4, 2554–2572.
- Powers, T. W., Jones, E. E., Betesh, L. R., Romano, P. R., Gao, P., Copland, J. A., et al. (2013). Matrix assisted laser desorption ionization imaging mass spectrometry workflow for spatial profiling analysis of *N*-linked glycan expression in tissues. *Analytical Chemistry*, 85(20), 9799–9806.
- Powers, T. W., Neely, B. A., Shao, Y., Tang, H., Troyer, D. A., Mehta, A. S., et al. (2014). MALDI imaging mass spectrometry profiling of *N*-glycans in formalin-fixed paraffin embedded clinical tissue blocks and tissue microarrays. *PLoS One*, 9(9), e106255.
- Prideaux, B., Dartois, V., Staab, D., Weiner, D. M., Goh, A., Via, L. E., et al. (2011). High-sensitivity MALDI-MRM-MS imaging of moxifloxacin distribution in tuberculosis-infected rabbit lungs and granulomatous lesions. *Analytical Chemistry*, 83(6), 2112–2118.
- Rahman, S. M., Gonzalez, A. L., Li, M., Seeley, E. H., Zimmerman, L. J., Zhang, X. J., et al. (2011). Lung cancer diagnosis from proteomic analysis of preinvasive lesions. *Cancer Research*, 71(8), 3009–3017.
- Rauser, S., Marquardt, C., Balluff, B., Deininger, S.-O., Albers, C., Belau, E., et al. (2010). Classification of HER2 receptor status in breast cancer tissues by MALDI imaging mass spectrometry. *Journal of Proteome Research*, 9(4), 1854–1863.
- Renovanz, M., & Kim, E. L. (2014). Intratumoral heterogeneity, its contribution to therapy resistance and methodological caveats to assessment. *Frontiers in Oncology*, 4, 142.
- Reyzer, M. L., Hsieh, Y., Ng, K., Korfmacher, W. A., & Caprioli, R. M. (2003). Direct analysis of drug candidates in tissue by matrix-assisted laser desorption/ionization mass spectrometry. *Journal of Mass Spectrometry*, 38(10), 1081–1092.
- Rodrigo, M. A., Zitka, O., Krizkova, S., Moullick, A., Adam, V., & Kizek, R. (2014). MALDI-TOF MS as evolving cancer diagnostic tool: A review. *Journal of Pharmaceutical and Biomedical Analysis*, 95, 245–255.
- Rohner, T. C., Staab, D., & Stoeckli, M. (2005). MALDI mass spectrometric imaging of biological tissue sections. *Mechanisms of Ageing and Development*, 126(1), 177–185.

- Ronci, M., Bonanno, E., Colantoni, A., Pieroni, L., Di Ilio, C., Spagnoli, L. G., et al. (2008). Protein unlocking procedures of formalin-fixed paraffin-embedded tissues: Application to MALDI-TOF imaging MS investigations. *Proteomics*, 8(18), 3702–3714.
- Schuerenberg, M., & Deininger, S.-O. (2010). Matrix application with ImagePrep. *Imaging mass spectrometry* (pp. 87–91). New York, USA: Springer.
- Schwamborn, K., & Caprioli, R. M. (2010). Molecular imaging by mass spectrometry—Looking beyond classical histology. *Nature Reviews. Cancer*, 10(9), 639–646. <http://dx.doi.org/10.1038/nrc2917>.
- Schwamborn, K., Krieg, R. C., Jirak, P., Ott, G., Knuchel, R., Rosenwald, A., et al. (2010). Application of MALDI imaging for the diagnosis of classical Hodgkin lymphoma. *Journal of Cancer Research and Clinical Oncology*, 136(11), 1651–1655.
- Schwamborn, K., Krieg, R. C., Reska, M., Jakse, G., Knuechel, R., & Wellmann, A. (2007). Identifying prostate carcinoma by MALDI-Imaging. *International Journal of Molecular Medicine*, 20(2), 155–159.
- Schwartz, S. A., Reyzer, M. L., & Caprioli, R. M. (2003). Direct tissue analysis using matrix-assisted laser desorption/ionization mass spectrometry: Practical aspects of sample preparation. *Journal of Mass Spectrometry*, 38(7), 699–708.
- Scigelova, M., Hornshaw, M., Giannakopoulos, A., & Makarov, A. (2011). Fourier transform mass spectrometry. *Molecular & Cellular Proteomics*, 10(7). M111.009431.
- Seeley, E. H., Oppenheimer, S. R., Mi, D., Chaurand, P., & Caprioli, R. M. (2008). Enhancement of protein sensitivity for MALDI imaging mass spectrometry after chemical treatment of tissue sections. *Journal of the American Society for Mass Spectrometry*, 19(8), 1069–1077.
- Signor, L., & Boeri Erba, E. (2013). Matrix-assisted laser desorption/ionization time of flight (MALDI-TOF) mass spectrometric analysis of intact proteins larger than 100 kDa. *Journal of Visualized Experiments*, 79, e506351.
- Sinha, T. K., Khatib-Shahidi, S., Yankeelov, T. E., Mapara, K., Ehtesham, M., Cornett, D. S., et al. (2008). Integrating spatially resolved three-dimensional MALDI IMS with in vivo magnetic resonance imaging. *Nature Methods*, 5(1), 57–59. <http://dx.doi.org/10.1038/nmeth1147>.
- Sjovall, P., Lausmaa, J., & Johansson, B. (2004). Mass spectrometric imaging of lipids in brain tissue. *Analytical Chemistry*, 76(15), 4271–4278.
- Sjovall, P., Lausmaa, J., Nygren, H., Carlsson, L., & Malmberg, P. (2003). Imaging of membrane lipids in single cells by imprint-imaging time-of-flight secondary ion mass spectrometry. *Analytical Chemistry*, 75(14), 3429–3434.
- Steurer, S., Borkowski, C., Odinga, S., Buchholz, M., Koop, C., Huland, H., et al. (2013). MALDI mass spectrometric imaging based identification of clinically relevant signals in prostate cancer using large-scale tissue microarrays. *International Journal of Cancer*, 133(4), 920–928.
- Steurer, S., Seddiqi, A. S., Singer, J. M., Bahar, A. S., Eichelberg, C., Rink, M., et al. (2014). MALDI imaging on tissue microarrays identifies molecular features associated with renal cell cancer phenotype. *Anticancer Research*, 34(5), 2255–2261.
- Steurer, S., Singer, J. M., Rink, M., Chun, F., Dahlem, R., Simon, R., et al. (2014). MALDI imaging-based identification of prognostically relevant signals in bladder cancer using large-scale tissue microarrays. *Urologic Oncology*, 32(8), 1225–1233.
- Stoekli, M., Chaurand, P., Hallahan, D. E., & Caprioli, R. M. (2001). Imaging mass spectrometry: A new technology for the analysis of protein expression in mammalian tissues. *Nature Medicine*, 7(4), 493–496.
- Stoekli, M., Staab, D., & Schweitzer, A. (2007). Compound and metabolite distribution measured by MALDI mass spectrometric imaging in whole-body tissue sections. *International Journal of Mass Spectrometry*, 260(2–3), 195–202.
- Strand, F. L. (2003). Neuropeptides: General characteristics and neuropharmaceutical potential in treating CNS disorders. *Progress in Drug Research*, 61, 1–37.

- Sugihara, Y., Vegvari, A., Welinder, C., Jonsson, G., Ingvar, C., Lundgren, L., et al. (2014). A new look at drugs targeting malignant melanoma—An application for mass spectrometry imaging. *Proteomics*, 14(17–18), 1963–1970.
- Taban, I. M., Altaalar, A. F., van der Burgt, Y. E., McDonnell, L. A., Heeren, R. M., Fuchser, J., et al. (2007). Imaging of peptides in the rat brain using MALDI-FTICR mass spectrometry. *Journal of the American Society for Mass Spectrometry*, 18(1), 145–151.
- Taka'cs, Z., Wiseman, J. M., Gologan, B., & Cooks, R. G. (2004). Mass spectrometry sampling under ambient conditions with desorption electrospray ionization. *Science*, 306(5695), 471–473.
- Toghi Eshghi, S., Yang, S., Wang, X., Shah, P., Li, X., & Zhang, H. (2014). Imaging of *N*-linked glycans from formalin-fixed paraffin-embedded tissue sections using MALDI mass spectrometry. *ACS Chemical Biology*, 9(9), 2149–2156.
- Trim, P. J., Henson, C. M., Avery, J. L., McEwen, A., Snel, M. F., Claude, E., et al. (2008). Matrix-assisted laser desorption/ionization-ion mobility separation-mass spectrometry imaging of vinblastine in whole body tissue sections. *Analytical Chemistry*, 80(22), 8628–8634.
- Hove, A., Erika, R., Smith, D. F., & Heeren, R. M. A. (2010). A concise review of mass spectrometry imaging. *Journal of Chromatography. A*, 1217(25), 3946–3954.
- Varki, A. (1993). Biological roles of oligosaccharides: All of the theories are correct. *Glycobiology*, 3(2), 97–130.
- Vegvari, A., Shavkunov, A. S., Fehniger, T. E., Grabau, D., Nimeus, E., & Marko-Varga, G. (2016). Localization of tamoxifen in human breast cancer tumors by MALDI mass spectrometry imaging. *Clinical and Translational Medicine*, 5(1), 1–8.
- Waki, M., Ide, Y., Ishizaki, I., Nagata, Y., Masaki, N., Sugiyama, E., et al. (2014). Single-cell time-of-flight secondary ion mass spectrometry reveals that human breast cancer stem cells have significantly lower content of palmitoleic acid compared to their counterpart non-stem cancer cells. *Biochimie*, 107(Pt. A), 73–77.
- Walch, A., Rauser, S., Deininger, S.-O., & Hofler, H. (2008). MALDI imaging mass spectrometry for direct tissue analysis: A new frontier for molecular histology. *Histochemistry and Cell Biology*, 130(3), 421–434.
- Willems, S. M., van Remoortere, A., van Zeijl, R., Deelder, A. M., McDonnell, L. A., & Hogendoorn, P. C. W. (2010). Imaging mass spectrometry of myxoid sarcomas identifies proteins and lipids specific to tumour type and grade, and reveals biochemical intra-tumour heterogeneity. *The Journal of Pathology*, 222(4), 400–409.
- Winderbaum, L., Koch, I., Mittal, P., & Hoffmann, P. (2016). Classification of MALDI-MS imaging data of tissue microarrays using canonical correlation analysis based variable selection. *Proteomics*, 16, 1731–1735.
- Wisztorski, M., Lemaire, R., Stauber, J., Menguélet, S. A., Croix, D., Mathe, O. J., et al. (2007). New developments in MALDI imaging for pathology proteomic studies. *Current Pharmaceutical Design*, 13(32), 3317–3324.
- Wuhrer, M., Deelder, A. M., & van der Burgt, Y. E. (2011). Mass spectrometric glycan rearrangements. *Mass Spectrometry Reviews*, 30(4), 664–680.
- Yamada, Y., Hidefumi, K., Shion, H., Oshikata, M., & Haramaki, Y. (2011). Distribution of chloroquine in ocular tissue of pigmented rat using matrix-assisted laser desorption/ionization imaging quadrupole time-of-flight tandem mass spectrometry. *Rapid Communications in Mass Spectrometry*, 25(11), 1600–1608.
- Yanagisawa, K., Yu, S., Xu, B. J., Massion, P. P., Larsen, P. H., White, B. C., et al. (2003). Proteomic patterns of tumour subsets in non-small-cell lung cancer. *The Lancet*, 362(9382), 433–439.
- Yang, L., Cui, X., Zhang, N., Li, M., Bai, Y., Han, X., et al. (2015). Comprehensive lipid profiling of plasma in patients with benign breast tumor and breast cancer reveals novel biomarkers. *Analytical and Bioanalytical Chemistry*, 407(17), 5065–5077.
- Yang, C., He, Z., & Yu, W. (2009). Comparison of public peak detection algorithms for MALDI mass spectrometry data analysis. *BMC Bioinformatics*, 10(1), 4.